Theoretical Study of Actinide Oxides

A thesis submitted to the University of Manchester for the degree of

Doctor of Philosophy

in the Faculty of Science and Engineering

2020

Jia-Li Chen

Department of Chemistry, School of Natural Sciences

Blank page

Contents

Abstract

The development of nuclear power brings much attention to the actinides, as they are the most important part of nuclear power production. The first generation of nuclear fuel is uranium dioxide (UO_2), and it remains the most used fuel, so there are many research works studying UO_2, to gain better understanding and hence safe handling. However, the burning of UO_2 accumulates considerable amounts of highly-radioactive nuclear wastes, including used U and plutonium (Pu). Reprocessing of spent fuel in the UK over the last few decades has led to the country having the largest civil stockpile of separated Pu (currently stored as plutonium dioxide: PuO_2). Minor actinides, include neptunium (Np), americium (Am), and curium (Cm), also accumulate during the reprocessing of spent UO_2 fuel. There are two acknowledged ways to deal with these highly-radioactive nuclear wastes, reusing as mixed oxides (MOX) nuclear fuel or deep geological long-term storage.

A closed fuel cycle is fulfilled by reusing highly-radioactive actinides from spent fuel, to decrease highly-radioactive wastes. Therefore, actinide MOX are important for the future development of nuclear power. Regarding deep geological disposal of highly-radioactive nuclear wastes, what happens in the stockpile, especially chemical processes, are important for the safe long-term storage; thus, understanding possible chemical reactions on PuO_2 surfaces is crucial.

In this thesis, uranium and other actinides (Np, Pu, Am, and Cm) MOX have been extensively studied computationally using periodic boundary condition density functional theory, and the influence of other actinides on UO_2 has been investigated, mainly focusing on surface properties and water adsorption behaviour. However, for a better discussion of MOX, sufficient knowledge of pure actinide oxides is essential for the comparison, so the study of minor actinide dioxides (NpO_2, AmO_2, and CmO_2) are presented before MOX; bulk and surface properties are simulated. Then, turning to civil stockpiles of separated Pu, the influence of Am, which has been found in the PuO_2 stockpiles, and the residual molecule hydrogen chloride (HCl) have been investigated respectively.

Declaration

No portion of the work referred to in this thesis has been submitted in support of an application for another degree or qualification of this or any other university or other institute of learning.

Copyright statement

i. The author of this thesis (including any appendices and/or schedules to this thesis) owns certain copyright or related rights in it (the “Copyright”) and she has given The University of Manchester certain rights to use such Copyright, including for administrative purposes.

ii. Copies of this thesis, either in full or in extracts and whether in hard or electronic copy, may be made only in accordance with the Copyright, Designs and Patents Act 1988 (as amended) and regulations issued under it or, where appropriate, in accordance with licensing agreements which the University has from time to time. This page must form part of any such copies made.

iii. The ownership of certain Copyright, patents, designs, trademarks and other intellectual property (the “Intellectual Property”) and any reproductions of copyright works in the thesis, for example graphs and tables (“Reproductions”), which may be described in this thesis, may not be owned by the author and may be owned by third parties. Such Intellectual Property and Reproductions cannot and must not be made available for use without the prior written permission of the owner(s) of the relevant Intellectual Property and/or Reproductions.

iv. Further information on the conditions under which disclosure, publication and commercialisation of this thesis, the Copyright and any Intellectual Property and/or Reproductions described in it may take place is available in the University IP Policy (see http://documents.manchester.ac.uk/DocuInfo.aspx?DocID=2442 0), in any relevant Thesis restriction declarations deposited in the University Library, The University Library’s regulations (see http://www.library.manchester.ac.uk/about/regulations/) and in The University’s policy on Presentation of Theses

Introduction

Energy has always played a pivotal role in the development of human beings. Burning wood to keep warm, thousands of years ago, was a turning point in human evolution, and since then biofuels (produced from biomass, e.g. wood) have continued to be an important energy source (particularly in developing countries). However, as shown in Figure 1.1, it was the discovery of coal (along with other fossil fuels such as oil and natural gas) that saw energy use increase dramatically across the world. Today fossil fuels are still the dominant energy source globally, however as they are non-renewable, dependency on them is an issue. In fact, one of the most crucial problems we face now, and in the future, is the energy crisis. Fossil fuels are overdeveloped and the resource is declining, additionally, the burning of fossil fuels has severe negative environmental impacts, e.g. emission of greenhouse gases and formation of acid rains. Therefore, new sources of clean energy are urgently needed. Renewable energies derived from sunlight, wind, tidal, and geothermal heat, have captured increasing attention, as they are abundant, and use of them is environmentally friendly. However, the main problem with our current renewable energy sources is they are restricted by weather and/or geography. Thus, due to the instability of renewable energies and the increasing demand for energy, humans still depend on fossil fuels (Figure 1.1), and finding a reliable substitute for fossil fuels is the key to resolving the energy crisis and climate change. One option is nuclear energy; it can release 1 million times more energy per atom than fossil fuels, through fission, and does not generate any greenhouse gases directly. For this reason, nuclear power offers a viable substitute for fossil fuels and a solution for mitigating climate change.

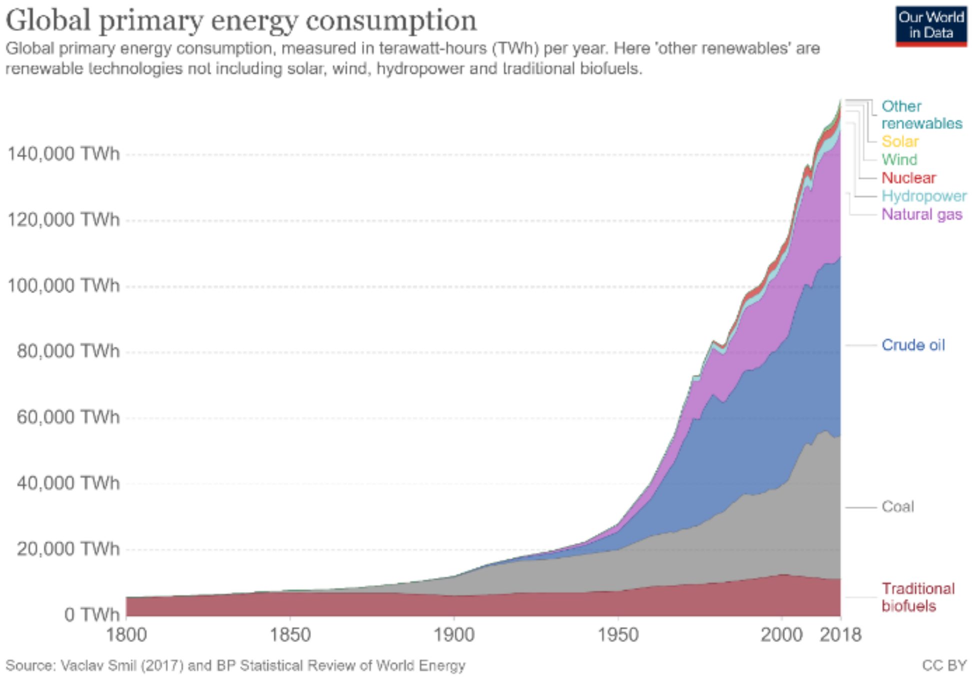

Figure 1.1: Global primary energy consumption.[1]

1.1 Nuclear energy

Nuclear energy can be traced back to the discovery of uranium by Martin Klaproth in 1789. Ionising radiation was discovered six years later, followed later by the concept of 'radioactivity', proposed by Pierre and Marie Curie in 1896. The neutron (n or n^0), a subatomic particle with no electric charge and a mass slightly greater than a proton, was discovered by James Chadwick in 1932; it is a vital component of nuclear power, used to induce nuclear fission. Atomic fission was demonstrated by Otto Hahn and Fritz Strassmann at the end of 1938; they found new lighter elements, barium, and other elements with about half the mass of uranium after uranium atoms were bombarded by neutrons. The first nuclear reactor, Chicago Pile-1, was a research reactor and was created in 1942 after the discovery of nuclear chain reaction. Nuclear power was developed to power submarines and aircraft carriers with the first nuclear-powered submarine being placed in the sea in 1954. Later that decade, the world's first commercial nuclear power station, Calder Hall, was opened in Windscale, England. The initial capacity of Calder Hall was 50

MW (million watts) per reactor. As highlighted in Figure 1.2, since 1957 nuclear energy has rapidly developed.

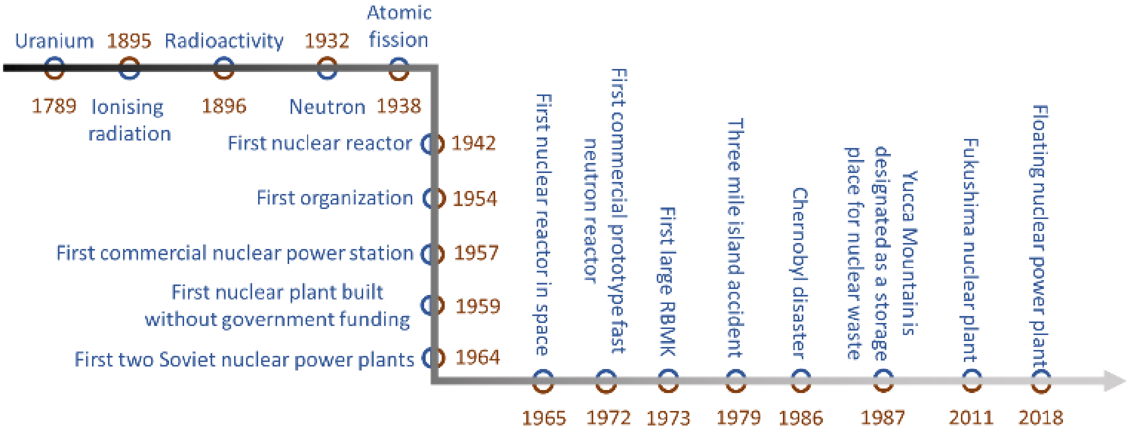

Figure 1.2: Important time points in nuclear power history.

Nuclear energy is the energy released from nuclear reactions, and it is then transformed into electricity, to be stored and transported to where it is needed. Nowadays, about 440 nuclear reactors are active and provide 10% of the world's electricity, which makes nuclear the world's second-largest source of low-carbon power. About 50 more reactors, which could provide 15% of existing capacity, will open in the near future. The rapid development of nuclear energy (Figure 1.3) is due to its compelling advantages. The most obvious advantage is that, as mentioned above, nuclear energy possesses a much higher energy density per atom than other energy sources. Thus, nuclear reactors require less fuel than other power plants, and as a result, can produce electricity at a lower cost than fossil fuels and renewables. Another advantage is that nuclear is a clean energy source; the use of nuclear energy over fossil fuels reduces carbon emissions. However, it is key to note that the construction of power plants, processing of the fuel, and dealing with radioactive waste are costly. This in part is because nuclear wastes, especially highly radioactive waste, are very harmful to humans, animals, and the environment, and as such should be handled and disposed of carefully. Nuclear accidents have resulted in disasters across the world, such as: the three mile island accident (which is the worst nuclear accident in the United States' commercial reactor history), the distressing Chernobyl disaster in Ukraine on 26 April 1986 (which is considered as the worst nuclear disaster), and the Fukushima Daiichi nuclear disaster in Japan on 11 March 2011. Each accident is a painful lesson; with the harmful effects on humans still being witnessed today. The debate on nuclear safety is key to the development of the technology.

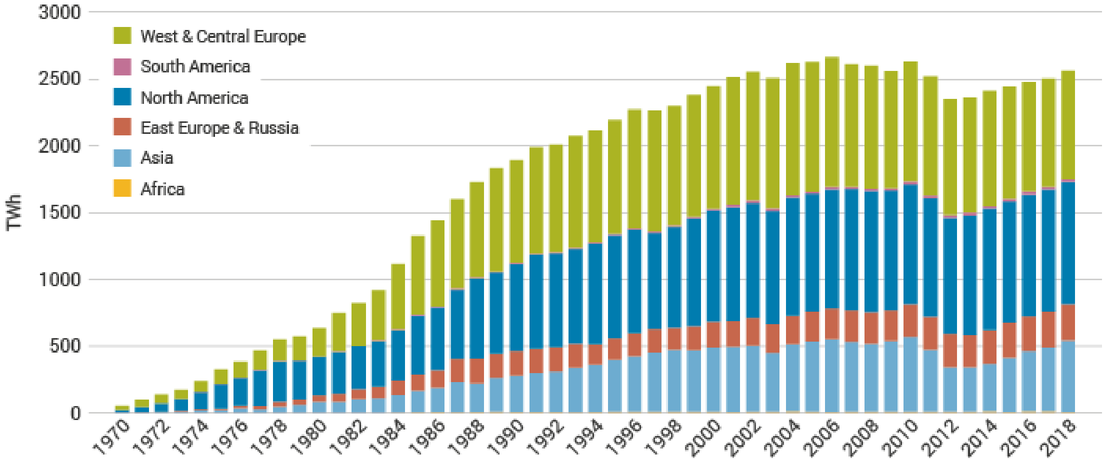

Source: World Nuclear Association and IAEA Power Reactor Information Service (PRIS)

Figure 1.3: The production of nuclear energy worldwide from 1970 to 2018.[2]

The UK has a long history of nuclear energy use and development. As mentioned above the world's first commercial nuclear station was built in this country, and since then many more nuclear plants have been built. At the peak, in 1997, nuclear energy provided 26% of the nation's electricity. However, since this date, many reactors have closed, with the UK government stating they would slow down the production of nuclear power stations in 2002. This decision was followed by heated debates between nuclear supporters and opponents and was subsequently reversed in 2006 (in an aim to reduce UK greenhouse gas emissions). Thus, in the same year as the 'U'-turn, the design of new nuclear plants started. Currently, there are 7 nuclear stations in the UK with 15 active nuclear reactors (Figure 1.4), including 14 advanced gas-cooled reactors (AGR) and 1 pressurised water reactor (PWR). The government has stated that 95 Gigawatts (GW) of new generating capacity will be constructed by 2035, which is equivalent to 90% of the grid's current capacity. Despite the recent investment, it is clear that nuclear energy is a politically controversial topic in the UK, and thus its development has not been consistent in the last 40 years.

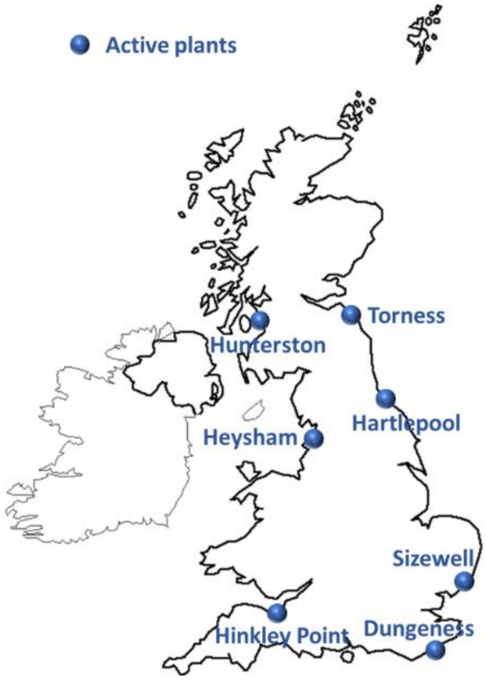

Figure 1.4: Existing nuclear power stations in the UK.

1.2 Nuclear reactors

Nuclear reactors convert nuclear energy into electricity, which can be integrated into electricity grids. The core of nuclear reactors contains the fuel and control rods. Nuclear fuel is compressed into small pellets, which are bundled into a fuel rod. Energy is created by bombarding fuel rods with neutrons, to induce fission; however, if left uncontrolled this can lead to fierce chain reactions. Thus, control rods, made from neutron-absorbing materials, are used in reactors to control fission speed. Control rods can be inserted or withdrawn in active reactors, in order to adjust the fission to a suitable speed, moreover, if unsafe conditions are detected, reactors use the control rods in their automatic and manual systems to shut down the fission reaction. Another important part of nuclear reactors is the cooling system. Coolant is transferred to the core of reactors through pressure vessels, to cool down the core and store the heat released from fission reactions, then the heated coolant flows to the steam generator, which makes steam from the coolant. The steam produced by the coolant can power up the connected turbine and generate electricity. Finally, containment protects reactors from outside intrusion, and protects the outside from the effects of radiation. Since the 1950s, nuclear reactors have been developed and improved, resulting in five generations of reactor today. The generation one reactors are precursors; most current reactors are generation two, such as: light water graphite-moderated reactor (LWGR), pressurised water reactor (PWR), and boiling water reactor (BWR). Generation three reactors have developments in efficiency and safety from their generation two reactors, whilst generation four reactors are still under research and will not be available before 2030 for commercial construction, generation five reactors are still only theoretically possible.

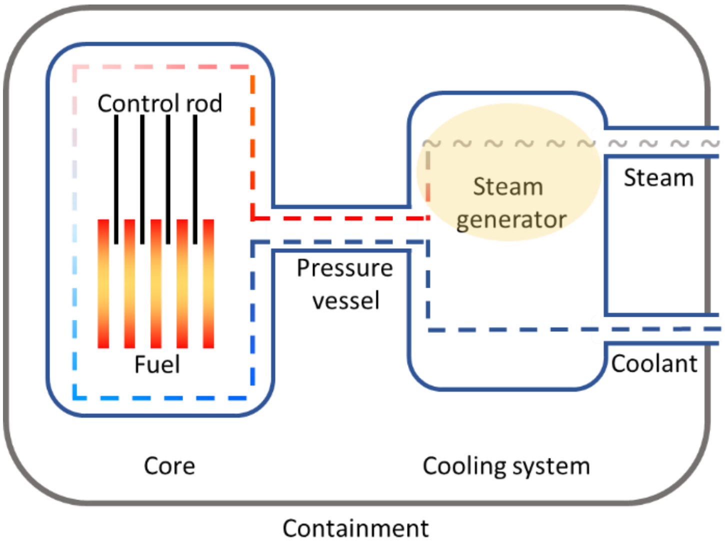

Figure 1.5: Schematic diagram of a nuclear reactor.

1.3 Nuclear fuel

Nuclear fuel is the heart of the reactor and powers the whole system. Heavy fissile actinide elements, such as uranium-233 (^{233}U), uranium-235 (^{235}U), and plutonium-239 (^{239}Pu), are effective constituents of most nuclear fuels, and the form of the actinide dictates the type of nuclear fuel used. The most popular nuclear fuel is actinide oxides, including traditional nuclear fuel, uranium dioxide (UO_2), and mixed oxides (MOX) fuel. UO_2 (Figure 1.6 (a)) is made from uranium hexafluoride (UF_6) or uranium trioxide (UO_3), then UO_2 powder (Figure 1.6 (b)) may be further processed or conditioned. The last step is then to mould this powder into pellets (Figure 1.6 (c)). MOX, as the name suggests, contains more than one oxide of fissile elements. The most common MOX fuel is uranium-plutonium mixed dioxide (U-Pu MOX). Minor actinides, neptunium, americium, and curium, can also be added to U-Pu MOX to obtain a closed fuel cycle (where spent fuel is reprocessed, and partly reused). Non-oxide ceramic fuels, such as uranium nitride and uranium carbide, have high heat conductivities and melting points, but a good understanding of them is still lacking. Metal fuels (uranium alloys) also have high heat conductivities, but they cannot survive high temperatures. Minor actinides can also be recycled into metal fuels – metal actinide fuel. There are also some other kinds of nuclear fuel, like molten salt fuels, and aqueous solutions of uranyl salts.

Figure 1.6: (a) Cubic structure of UO_2; (b) UO_2 powder; (c) UO_2 pellet.[3]

Oxide fuel is a typical nuclear fuel, hence oxide fuel will be discussed extensively in the following sections. Previous work on pure UO_2 will be reviewed firstly (1.3.1). To have a good understanding of MOX fuel, knowledge of every oxide in it should be clear, and there are numerous studies that have investigated plutonium dioxides (PuO_2), neptunium dioxides (NpO_2), americium dioxides (AmO_2), and curium dioxides (CmO_2). Pu is the most accumulated highly radioactive nuclear wastes, so it is at the core of handling nuclear wastes and will be discussed in the section on nuclear waste (1.4.1). Therefore, the next step is reviewing works about minor actinides dioxides (MAnO$_2$) viz., NpO$_2$, AmO$_2$, and CmO$_2$ (1.3.2). After works about actinide oxides, uranium and other actinides (Np, Pu, Am, or Cm) mixed dioxides (MOX) will be discussed (1.3.3). Uranium and plutonium mixed dioxide (U-Pu MOX) is the most studied MOX, as it is the most common MOX fuel. Uranium and minor actinide mixed dioxides, including U-Np MOX, U-Am MOX, and U-Cm MOX, are simplified forms of minor actinide-containing U-Pu MOX (U-Pu-MAn MOX), and hopefully, investigation of U-MAn MOX promotes a better understanding of U-Pu-MAn MOX. Finally, a summary of previous works about the most complicated oxides is presented: U-Pu-MAn MOX (1.3.4).

1.3.1 Uranium dioxide (UO$_2$)

Uranium dioxide (UO$_2$), as a traditional nuclear fuel and the most used one, has attracted researchers' attention. Thermophysical properties,[4-5] such as thermodynamic[6-13] and transport properties[14-19], have been widely studied, as they are important parameters for fuel performance (regarding its efficiency and safety). Many works on the thermophysical properties of UO$_2$ focus on the fuel operational temperature range,[6, 13, 18] as it is the most important temperature range, although there are some works interested in very high temperatures,[5-6, 10, 12-15] for example, Ronchi *et al*. have studied thermal conductivity of UO$_2$ up to 2900 K,[14] as high temperatures are relevant to accident conditions. Furthermore, studying a wide range of temperature provides a better understanding of thermophysical properties, and can hopefully and potentially provide a mechanism to explain thermophysical phenomena, thus, there are also plenty of works investigating low temperature thermophysical properties of UO$_2$.[6, 9, 16, 19]

Fundamental properties of UO$_2$, such as local structure, oxidation of UO$_2$, and diffusion of U, O, and fission gas in UO$_2$, are essential to the investigation of thermophysical properties. The geometry[20-25], electronic structure[26-32], and magnetism[33-40] of UO$_2$ have been studied with spectroscopy. It is widely acknowledged that UO$_2$ has the face-centered cubic (*fcc*) fluorite structure with tetravalent U; the cubic unit cell contains 4 U atoms and 8 O atoms, with the U atoms in *fcc* lattice sites and the O atoms occupying (±1/4, ±1/4, ±1/4) positions around each cubic corner U atom (Figure 1.6 (a)). It is antiferromagnetic (AFM) at low temperature below 30.8 K, which is the first-order phase transition temperature.[34]

A UO_2 fuel pellet undergoes severe structural changes under irradiation conditions, such as defect accumulations, fission gas bubble growth and redistribution, and grain subdivision. Therefore, as well as stoichiometric UO_2, non-stoichiometric UO_2 has also attracted attention. Point defects in UO_2,[41-50] including uranium and oxygen vacancies, interstitials, Frenkel pairs, and Schottky defects, have been studied and compared for the formation energies. Hyper-stoichiometric UO_{2+x} is also of great interest.[51-55] Because UO_2 has a large number of octahedral holes and U can form oxidation states from U(III) to U(VI), UO_2 can accommodate large amounts of interstitial oxygen to form the hyper-stoichiometric UO_{2+x}. To better understand the stability of UO_2, oxidation of hyper-stoichiometric UO_{2+x}, which can maintain the *fcc* structure with $x < 0.23$, has also attracted much attention.[53, 55] Further oxidation of UO_2 causes phase transition, leading to different structures such as the tetragonal U_3O_7 or orthorhombic U_3O_8.[53, 55-56]

Self-diffusion of U and O in stoichiometric and non-stoichiometric UO_2 has been studied and compared,[57-63] focusing on diffusion pathways and coefficients, as well as activation energy, as it is important to the understanding of sintering, creep, and corrosion phenomena in nuclear fuel. Extensive research had also been carried out to investigate the diffusion characteristics of fission products, mainly the noble gases He, Kr, and Xe.[64-65]

Exposed UO_2 surfaces are ubiquitous in nuclear reactors, for example in the gap between the fuel and cladding, and grain boundaries. Surface properties are also important for the storage of spent UO_2 fuel. Surface structure and properties have been investigated experimentally with X-ray diffraction (XRD), X-ray photoelectron spectroscopy (XPS), X-ray absorption near-edge structure (XANES), extended X-ray absorption fine structure (EXAFS), Raman spectra, and atomic force microscopy.[66-79] UO_2 surfaces are highly oriented along the {111} direction,[66] and different oxidation states of U have been found (mostly U^{4+} and U^{5+} ions with some U^{6+} ions).[67] Oxidation of UO_2 surfaces is an important interfacial process.[71-79] Different oxidation conditions have been studied in previously published works, including exposed surfaces[71], gas medium[74], and temperature[76]. The oxidation is universal and prevails regardless of which surface is exposed, and the gas medium influences the oxidation rate, for example, H_2O/H_2 and CO_2/CO mix gas have been studied by Dobrov *et al*. and Carter *et al*., respectively,[71-72] increasing partial pressure of H_2 will hinder oxidation while increasing partial pressure of CO_2 will promote oxidation. Oxidation of UO_2 was found to have a strong temperature dependence.[76] To get a better understanding of UO_2 surfaces properties, small molecules have been extensively used as a probe to investigate adsorptions and interactions on UO_2 surfaces.[80-89] The most common probe is water, as its adsorption and dissociation on the UO_2 surfaces are also important for the long-term storage of UO_2.[80, 82, 85-86]

There are also lots of theoretical works on UO_2, as simulations can provide a deeper understanding of the mechanisms behind the phenomena we are interested in. Atomistic simulation, e.g. molecular dynamics (MD), has been widely applied in the simulation of thermal properties of UO_2, such as thermal conductivity,[90-97] diffusion coefficient[98-99], and thermal expansivity[100]; previous atomistic results show a good agreement with experimental data, as well as providing predictions for untested thermal properties. However, first-principles calculations, with density functional theory (DFT) being the most widely used method for nuclear fuel modelling, are more relevant to this work. Unfortunately, the local density approximation (LDA) and generalized gradient approximation (GGA) functionals wrongly describe UO_2 as a metal (due to the strong correlations of *f* electrons).[101-103] There are several methods proposed to handle this problem, such as hybrid density functionals,[104-108] self-interaction correction (SIC),[109] and dynamical mean-field theory (DMFT);[110-111] however, they are computationally expensive. On the other hand, the Hubbard model-based DFT method (DFT + *U*) has been widely applied to the simulation of UO_2, as it has much higher computational efficiency than the above-mentioned methods. Many studies, using DFT + *U*, have simulated UO_2 properties, such as surface and bulk properties[103, 109, 112-114], defect formation[45, 49], He diffusion in UO_2[115-116], and oxidation of UO_2[117]. The DFT + *U* simulations give much more reasonable results of electronic structure, which fits experimental findings better than pure DFT.

However, the DFT + *U* method is not perfect, as it brings the problem of metastable states because of the degeneracy of the *f* orbitals. The DFT + *U* optimization is easily trapped in a metastable state and it can be hard to reach the true ground state. Thus methods, such as occupation matrix control (OMC)[118] and *U*-ramping[119], have been developed to help the DFT + *U* optimization reach the true ground state. The DFT + *U* + OMC method has been applied to simulations of UO_2 bulk and surfaces,[120-121] and it always allows one to reach the lowest energy states. But as one should consider all possible initial occupation matrices, the DFT + *U* + OMC method is very time consuming and complicated for a system with an enormous number of electronic configurations. *U*-ramping only works when the *U* value does not change the orbital ordering.[119] Besides these simulation methods, there are still some other settings that affect the calculated results, such as magnetic ordering and spin-orbit coupling (SOC).[122-123] Table 1.1 summarizes the lattice constant and bandgap of UO_2 calculated with different methods and compares them with experimental data. As we can see from the table, the DFT + *U* simulated results are in agreement with the experiment. Therefore, the DFT + *U* method is currently the most commonly used method to simulate UO_2, with the collinear 1*k* AFM state. As mentioned above, hybrid DFT can overcome the drawback of LDA and GGA functionals but is time consuming for periodic DFT. Thus embedded cluster approaches such as the periodic electrostatic embedded cluster method (PEECM) are another good way to reduce computational time and can treat of UO_2 with hybrid DFT.[108, 124]

Table 1.1: Lattice parameter and bandgap of UO_2 from different theoretical simulation methods and experiments.

Method	Lattice parameter (Å)	Bandgap (eV)
DFT[101-103]	5.289 – 5.445	0.00
DFT + *U*[60, 118, 123, 125-128]	5.440 – 5.520	2.03 – 2.40
Hybrid DFT[106-108]	4.05 – 5.454	2.78 – 3.20
Experiment[129-135]	5.470 – 5.473	2.00 – 2.50

Defect formation and small molecule adsorption on UO_2 surfaces are much more complicated than bulk calculations, thus most surface simulations are done with the DFT + *U* method. There are a number of papers published about UO_2 surfaces and water adsorption.[108, 114, 121, 124, 136-142] Oxygen vacancy formation on the UO_2 {111}, {110}, and {100} surfaces has been calculated with hybrid DFT (PBE0) and the DFT + U method,[124] these two methods are basically in agreement with each other and predict similar behaviour for water adsorption on stoichiometric and oxygen vacancy UO_2 surfaces. Both single and multiple water adsorptions on UO_2 surfaces have been simulated with DFT + U by Tegner *et al.*[141-142] Bo *et al.* studied water dissociation and H_2 formation on UO_2 surfaces,[139-140] and Pegg *et al.* investigated the interaction between H_2 and UO_2 surfaces.[143-144] Overall, UO_2 has been intensively studied over the last decades, and the study of UO_2 not only gives us a better understanding of the material itself, but is also a good reference for the study of other actinides.

1.3.2 Minor actinide dioxides ($MAnO_2$)

Neptunium (Np) is an important actinide accumulated during the UO_2 nuclear fuel cycle. ^{237}Np is one of the important long-lived isotopes; it is formed predominantly from ^{235}U, and the alpha decay of ^{241}Am leads to further accumulation of Np in highly radioactive nuclear wastes. Np is mainly present as the dioxide, i.e. stoichiometric, substoichiometric, and hyperstoichiometric NpO_2.[145] Similar to UO_2, NpO_2 has the *fcc* crystal structure with space group *Fm-3m*,[129] but understanding the properties and behaviour of NpO_2 has proved to be much more difficult, e.g. magnetic ordering.[146-156] For example, Foumier *et al.* observed a phase transition at about 25.5 K for NpO_2 cooling from room temperature,[146] whereas Caciuffo *et al.* did not find any magnetic order by neutron diffraction.[152] Numerous studies have tried to find the mechanism behind the phase transition of NpO_2, and have concluded that the phase transition is due to octupole moments of Γ_5 symmetry (Figure 1.7).[155] The basic chemical and thermal properties of NpO_2, such as heat capacity,[157-160] bandgap,[161-162] evaporation behaviour,[163-164] have also attracted a lot of attention. There are fewer theoretical studies (compared to experimental) on NpO_2,[106, 108, 123, 143-144, 165-179] however, there are still some examples such as Wang *et al.* who have performed systematic DFT + U calculations to investigate the electronic structure, mechanical properties, and phonon-dispersion curves of NpO_2;[166] their work demonstrated that DFT + U method is able to give a good simulation of NpO_2.

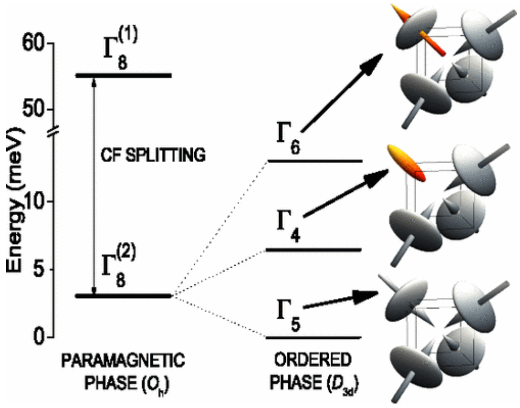

Figure 1.7: Schematic energy spectra of Np (IV) ions in NpO_2 from Ref. 151. Left side is the paramagnetic phase with a bare crystal-field (CF) gap of 55 meV present between the two Γ_8 quartets; right side is the ordered phase where the ground CF quartet is split into two Γ_5 and Γ_6 singlets and a Γ_4 doublet. Ellipsoids and arrows represent the electric quadrupole and magnetic triakontadipole, respectively.

There are a few studies that focus on the surfaces of NpO_2, such as that by Naegele *et al.* who studied the oxidation of Np on the surface.[180] They found that Np_2O_3 naturally forms on the surfaces, but does not exist in the bulk. They demonstrated that with further oxidation of the surfaces this Np_2O_3 species completely disappears to leave just the NpO_2; however reduction of the surface leads to a stable Np_2O_3 structure.[181] Therefore, Np_2O_3 could exist on NpO_2 surfaces. Theoretical simulations of NpO_2 surfaces are mainly interested in surface properties and water adsorptions. Bo *et al.* simulated NpO_2 {111}, {110}, and {100} surfaces and further investigated oxygen vacancy formation, as well as water adsorption on stoichiometric and defect surfaces.[169] Hydrogen adsorption on NpO_2 surfaces has been studied by Pegg and co-workers,[143-144] and there is also a simulation work studying hydroxyl adsorption.[179]

Americium (Am) has high and lasting radiotoxicity and is the second most-produced MAn in the UO_2 fuel cycle. Beta-decay of ^{241}Pu generates ^{241}Am, which decays to ^{237}Np by alpha emission. The ^{243}Am isotope is also present in the spent fuel, but in much smaller concentrations. The first Am compound that was thoroughly characterized was AmO_2, though Am (III) is more stable than Am (IV). AmO_2 also has the *fcc* crystal structure, and is commonly reduced to Am_2O_3 with a body centered cubic (*bcc*) structure between 600 and 800 K, and exists as Am_2O_3 at higher temperatures but with different crystal structure over different temperature ranges.[182] However, Am_2O_3 is not thermodynamically stable in air, and is slowly oxidized and transfers to the *fcc* AmO_2.[183] Similar to UO_2 and NpO_2, a low temperature phase transition has been discovered in AmO_2 (at 8.5 K);[184] this has been attributed to AFM ordering, but the crystalline electric field ground state of Am (IV) has been suggested to be a Γ_7 doublet, which is nondipolar ordering, in AmO_2.[184-187] Further investigations have found that the ground state can be easily converted into Γ_8 quartet, due to the competition between SOC and Coulomb interactions.[188-190]

Theoretical studies of americium oxides mainly focus on bulk properties.[106, 123, 171, 173-174, 176-177, 191-196] Kovac *et al*. analysed the electronic structure of AmO_2 molecules in the gas phase with a accuracy theoretical method (CASPT2),[196] and they found that AmO_2 with five unpaired electrons has the lowest energy. Teterin and co-workers have studied the electronic structure of solid-state AmO_2 by combining X-Ray spectroscopy and theoretical simulation;[191, 193] detailed composition of molecular orbitals are plotted, and they conclude that Am 5f electrons partially delocalize within the outer valence band and the rest of the 5*f* electrons are localized. Many efforts have been made to investigate the structure, electronic and thermodynamic properties. The latest work is a DFT + *U* study of AmO_2 by Noutack *et al*.,[194] which suggests that transverse 3*k* AFM is the ground state magnetic order of AmO_2, but longitudinal 1*k* AFM order without SOC is a reasonable approximation for DFT + *U* calculation of AmO_2 bulk properties. There is no theoretical work studying AmO_2 surfaces.

Curium dioxide (CmO_2) is still somewhat of a mystery. An expansion of the lattice parameter was found at room temperature within a few days after the discovery of CmO_2 as a compound, and the presence of oxygen and its partial pressure have an obvious influence on the expansion.[197-198] Unsurprisingly, the curium-oxygen phase diagram shows a rich variety of compounds, for example, curium sesquioxide has five polymorphic forms. The simplest oxide structure is CmO_2, and similar to other AnO_2 structures it only has the *fcc* crystal structure; neutron powder diffraction measurement shows the lattice constant is 0.5364 nm.[199] Knowledge of CmO_2 electronic structure mainly comes from theoretical simulations. Asprey and co-workers found evidence for tetravalent Cm.[198] Gubanov *et al*. calculated the electronic structure of a CmO_8^{12-} cluster;[200] their results show that the effects of covalent mixing of the 5*f* orbital with oxygen ligands are larger in CmO_2 than in UO_2. Prodan and co-workers investigated solid-state AnO_2, including CmO_2, with screened hybrid density functional theory.[106] From PuO_2 to CmO_2, they found the *f* electrons change from delocalized to localized, which is the driving force for An(IV) atoms to reduce to An (III) (this is especially true for CmO_2, where Cm borrows oxygen spin and approaches the stable half-filled f^7 subshell).

The magnetic structure of CmO_2 is still unclear. As Cm is tetravalent, a nonmagnetic ground state should be found for CmO_2, but an effective moment of about 3.4 μ_B has been observed from neutron diffraction.[199] There are two different explanations for the moment found in CmO_2; one attributes the moment to Cm (III) impurity, while the other attributes it to a low-lying excited state of Cm (IV). Niikura *et al*. found that the excitation energy between the ground and magnetic excited states of AmO_2 is small, due to the combined effect of Coulomb interactions, SOC, and crystalline electric field potential; the result demonstrated the possibility of low-lying excited states contributing to the moment found in CmO_2.[201] Huang and co-workers recently simulated bulk CmO_2 and further studied the magnetic properties;[202] they conclude that the ground state electronic structure of Cm is an intermediate configuration between Cm (III) and Cm (IV), which causes the moment detected in CmO_2.

Overall, further investigations into $MAnO_2$ are needed. In particular, more work is required to understand the AmO_2 and CmO_2 structures, especially their surface chemistry. Although we know more about NpO_2, a better understanding of its surfaces is required too.

1.3.3 Uranium and actinide mixed dioxides (U-An MOX)

U-Pu MOX fuel has been used in light water reactors around the world for decades, and the development of sodium-cooled fast reactors has given new life to the prospect of future U-Pu MOX fuel usage. The most important characteristic of U-Pu MOX fuel is the Pu to metal (Pu/M, M = U and Pu) ratio. MOX with Pu up to 4% is added into thermal reactors as fuel, and slightly higher Pu (7%) fuel can be used in light water reactors. MOX fuel for fast reactors is designed to have much higher Pu, ranging from 20% to 40%. For example, U-Pu MOX, which contains up to 30% Pu, has been used for a while in conventional fast breeder reactors, and sodium bonded MOX test pins that contain up to 40% Pu are commonly used. However, due to the temperature gradient in MOX fuel, redistribution of U and Pu occurs at the early stage of irradiation, therefore, the Pu content in MOX fuel can increase from 10-70% compared to the initial fabricated ratio.[203-205] Hence, studies of U-Pu MOX have considered a wide range of Pu content. For instance, thermal properties, such as burnup, thermal conductivity, and so on, have been investigated against the Pu content.[206-211] There are also works focused on the Pu isotope (^{238}Pu and ^{239}Pu) ratio to all Pu in U-Pu MOX,[212-215] as it is crucial for the use of MOX in reactors.

Another important quantity in U-Pu MOX is the O to metal (O/M, M = U and Pu) ratio, which influences fuel-clad compatibility,[216-217] thermal conductivity,[218] melting point[219] and fission product behaviour[220]. For example, the O/M ratio is not allowed to exceed 2.00 at the beginning of the fission process, to reduce fuel cladding chemical interaction.[216-217] Another example of previous work concerns the melting point; the melting temperature of MOX decreases with an increase in the O/M ratio.[219] The O/M ratio can be adjusted during the sintering process, where the MOX is reduced under a mixed atmosphere of hydrogen and inert gas. But, during irradiation, due to the generation of fission products and redistribution of O, U, and Pu, the O/M ratio of the U-Pu MOX will change. In the centre of the pellet, the O/M ratio is lowered to at least 1.92 by O defects and Pu redistribution.[221-222] Therefore, to have an insightful understanding of the O/M ratio of U-Pu MOX, the oxidation of MOX has attracted the attention of researchers.[223-228] The oxidation of (U, Pu)O_2 is slowed down by higher Pu/M ratios.[226-227] On the other hand, the oxidation of (U, Pu)O_{2-x} ($x > 0$) is diffusion controlled, and is mainly related to anion vacancy migration; the presence of anion sublattice defects in samples with higher Pu/M ratio favours the oxidation.[226-227] Self-irradiation induced defects will also decrease the oxidation kinetics of MOX.[224] Spontaneous oxidation of biphasic MOX has been observed by Vauchy *et al.*;[223] this oxidation process is driven by water chemisorption, thus it is influenced by the moisture content of the atmosphere rather than its O_2 concentration. Some works study the diffusion of O, U, Pu, and irradiation products, like He, in MOX, which is also, directly and indirectly, related to the O/M ratio of U-Pu MOX.

The crystal structure of U-Pu MOX is affected by many factors; the most commonly studied factors being the previously mentioned Pu/M and O/M ratio. It is widely acknowledged that UO_2 and PuO_2 have an *fcc* crystal structure, and it has been revealed that the solid solution of (U, Pu)O_2 also possesses this same crystal structure.[229-232] Also, it is apparent that the lattice parameter for (U, Pu)O_2 changes linearly with the ratio of Pu/M, from pure UO_2 to PuO_2.[206] Whilst it is necessary to take into consideration the O/M ratio, temperature, and atmosphere to accurately model a real system, there has been work on these compounds. For example, a study by Sari and co-workers which looks at the ternary system of U-Pu-O at room temperature for O/M of 2.00, found MOX remains a single phase fcc with a Pu/M ratio less than 20%.[233] Two phases are found for MOX with Pu/M ratio larger than 20%, one phase is *fcc*, another phase related to Pu/M ratio.[233] A later study by Vigier *et al*. also found that substoichiometric $(U_{0.3}Pu_{0.7})O_{2-x}$ is biphasic and confirmed the presence of trivalent Pu in the sample.[229] Stable hyperstoichiometric U-Pu MOX has also been detected in experiments. A single *fcc* phase $(U_{0.3}Pu_{0.7})O_{2.15}$ was obtained by Sali *et al*. from the oxidation of (U, Pu)C, and they found that the mean valency of U was +5.[234] Martin and co-workers revealed that (U, Pu)O_{2+x} with Pu/M ratio of 30% or lower has a disordered hyperstoichiometric structure.[232]

Theoretical simulations of U-Pu MOX can be divided into two groups, one being molecular dynamics simulations with a focus on thermal properties,[97, 235-241] and the other one is DFT simulations with focus on chemical properties. As the core in this thesis is more focused on DFT calculations, this will be discussed in detail. Gryaznov *et al*. simulated (U, Pu)O_2 bulk with the Pu/M ratio range from 12.5 to 87.5% with the DFT + *U* method,[242] indicating that the antiferromagnetic (AFM) state is more stable than the ferromagnetic (FM) state for low Pu concentration. The lattice parameters Gryaznov *et al*. obtain for (U, Pu)O_2 also obey Vegard's law.[242] The (U, Pu)O_2 bulk was also studied by Dorado and co-workers, but with 12.5-25% Pu.[243] They found that the presence of Pu in MOX creates an electronic state above the Fermi level and decreases the bandgap of pure UO_2. Yang *et al*. investigated electronic properties of (U, Pu)O_2 with 25%, 50%, and 75% Pu with the DFT + *U* method;[244] they found that Pu-O and U-O bonds in MOX are more ionic than in pure PuO_2 and UO_2. Recently, Njifon and co-workers studied $U_{0.5}Pu_{0.5}O_2$ also using the DFT + *U* method,[245] and they found that small variation of the *U* parameter for Pu does not impact significantly the properties of MOX. As with the study by Gryaznov *et al*., they found a narrow bandgap for MOX. The above studies are all focused on stoichiometric MOX, whereas Ma *et al*. systematically simulated $U_{0.5}Pu_{0.5}O_{2.25}$, $U_{0.5}Pu_{0.5}O_{2}$, and $U_{0.5}Pu_{0.5}O_{1.75}$ with hybrid DFT.[246] Their results support the presence of an AFM ground state for all the MOX structures they studied, and there was only distortion for O in the hyper and hypo-stoichiometric ($U_{0.5}Pu_{0.5}O_{2.25}$ and $U_{0.5}Pu_{0.5}O_{2}$, respectively) bulk when compared with the stoichiometric one.

Much less attention has been paid to U-Np MOX than U-Pu MOX. The phase diagram of the U-Np-O system has been studied in several works, for example, Paul and co-workers studied the phase diagram in an O_2 atmosphere between 1373 and 1823 K.[247] Martel *et al*. investigated the structure of $U_{1-x}Np_{x}O_2$ (x = 0.01, 0.05, 0.20, 0.50, 0.75, 0.85) using X-ray spectroscopy,[248] confirming that the lattice parameter of U-Np MOX obeys Vegard's law, and that U and Np remain tetravalent in MOX. Chollet and co-workers compared stoichiometric ($U_{0.9}Np_{0.1}O_2$) and hyperstoichiometric ($U_{0.9}Np_{0.1}O_{2+x}$) MOX,[249] and found Np remains tetravalent with a coordination number of eight in the fluorite structure (even in an oxidizing atmosphere, as any excess charge on the oxygen is supported by U). Martel *et al*. found that the AFM order of U-Np MOX is stable in a large applied magnetic field.[250] The stability of the AFM order was also confirmed by theoretical simulation, as a negative formation enthalpy of AFM U-Np MOX was obtained with DFT + U calculations by Ghosh and co-workers.[251-252] Among limited works on U-Np MOX, several studies have been interested in thermal properties.[253]

U-Am MOX has attracted more interest than U-Np MOX, due to the interesting structural and electronic properties of this compound.[254-268] Prieur *et al*. found U-Am MOX with 10%, 15%, and 20% Am content possess Fm-3m crystal structure.[265] This structure is also maintained for MOX with higher Am content (30%, 40%, and 50%).[261] In fact, the fluorite structure is still stable under high α self-irradiation of ^{241}Am and is independent of the synthesis processes used.[262, 266] Lebreton and co-workers confirmed again that no significant deviations of the cation sublattice were evidenced for high Am content MOX, while the oxygen sublattice presents deviations from the fluorite structure.[259]

The electronic structure of U-Am MOX is much different from U-Pu and U-Np MOX. Bartscher *et al*. found that, under nitrogen atmosphere, U (IV) is oxidised by Am (IV) in a phosphoric acid solution.[254] Since this study there has been a lot of work undertaken to find out the charge state of U and Am in U-Am MOX solid solution. For example, Prieur and co-workers investigated the charge state of U and Am in U-Am MOX with low Am content (< 20%);[264] they found only trivalent Am and a mixed charge state (tetravalent and pentavalent) for U. This finding had been further supported by Lebreton's work, which also concludes that the charge states of Am and U are unaffected by sintering atmosphere.[260] Another work of Prieur found that self-irradiation does not affect the charge distribution.[266] For U-Am MOX with high Am content (< 50%), only trivalent Am was found, and only pentavalent U was found for $U_{0.5}Am_{0.5}O_{2-x}$.[260] Prieur and co-workers further studied the relationship between trivalent Am and pentavalent U in MOX, and found that Am(III) and U(V) are present in almost equimolar proportions.[264] Once more, Caisso *et al*. proved the existence of trivalent Am in U_3O_8,[256] and Epifano and co-workers confirmed trivalent state Am in $(U, Am)_4O_9$ and $(U, Am)_3O_8$.[257]

At the time of writing, there are no published work studied the U-Cm MOX system, while there are some works that studied Cm bearing U-Pu MOX. Thus, Cm in UO_2 matrix will be discussed below (1.3.4).

Overall, theoretical works on U-Pu MOX are still in their early stages. Fortunately, previous DFT + *U* simulations provide promising results, but further theoretical simulations are required to provide a deeper understanding of U-Pu MOX. Am acts differently in UO_2 than Np and Pu, so the presence of Am in MOX fuel will bring more uncertainty, more work is required to safely recycle and burn Am in nuclear fuel. Cm is again more complex to model than Am. In the real activated pellet, the situation is very complicated, thus, further investigations are needed for U-An MOX.

1.3.4 Minor actinide bearing uranium and plutonium mixed oxide (MAn-MOX)

Np-MOX is more suitable for fast reactors than light water commercial reactors. During operation the content of ^{237}Np increases slightly in both types of reactors, however, this increase does not exceed 0.08wt.% in U-Pu MOX.[269-270] Ng and co-workers suggest that Np may pose a proliferation risk to MOX fuel.[271] However, recycling Np into U-Pu MOX is still attractive. Morimoto *et al*. studied the thermal conductivities (λ) of Np-MOX,[272] and they found that the thermal conductivity could be expressed as $\lambda = (A + BT)^{-1}$ up to 1400 K (where T is temperature, and A and B are material-related constants; the A values increased linearly with increasing Np content). This finding is also supported by Prieur and co-workers;[273] they also found that the thermal conductivity of Np-MOX is lower than UO_2 and the melting temperature of Np-MOX is 3020 K. The oxygen potential increases with increasing Np content but this effect is smaller than Pu.[272] However, Kato *et al*. believe that addition of a small percentage of Np has a negligibly small effect on MOX properties,[274] such as lattice parameters, melting temperatures, thermal conductivities, and oxygen potentials.

The Am-MOX lattice parameter decreases with increasing Am content (< 15%), whilst Am content has little influence on thermal conductivity and heat capacity.[275] Morimoto and co-workers further studied the influence of Am content on the thermal conductivity of Am-MOX,[276] and they found that $\lambda = (A + BT)^{-1}$ up to 1400 K (where T is temperature, and A and B are material-related constants; the A value increased linearly with increasing Am content, while the B-value decreased slightly with increasing Am content). This result is in agreement with Prieur's work.[273] Morimoto *et al*. also found that Am in U-Pu MOX has a significant effect on the O/M ratio.[276] Hirooka and co-workers believe that Am inclusion, in terms of substituting U, significantly increased the O potential at the same O/M ratio. The increase in O potential was larger than with the addition of Pu at the same rate, and they attribute this to the higher O potential of AmO_{2-x} than that of PuO_{2-x}.[277] Am was found to be trivalent and embedded in the form of $\{AmO_8\}^{13-}$ or $\{AmO_7\}^{11-}$ in Am-MOX in Degueldre's work.[278] Meanwhile, Vanchy and co-workers found that, for $U_{0.54}Pu_{0.45}Am_{0.01}O_{2-x}$, Am exhibits a mixed-valence III/IV charge state when the MOX has U and Pu distribution heterogeneities and is only tetravalent when the MOX is homogeneous.[279] Their later work confirmed that the reduction of Am (IV) to Am (III) is completed before any reduction of Pu (IV), and U remains tetravalent.[280] Maeda *et al*. studied the redistribution behaviour after irradiation of Am-MOX,[281] and they found Am and Pu have similar redistribution tendency, as well as an increase in Am and Pu content around the central void.

There are a limited number of studies on Cm-MOX.[282-285] Osaka and co-workers analysed irradiated MOX fuel in an experimental fast reactor,[285] and found that Cm content reaches equilibrium above burnup of 100 GWd/t, except for ^{247}Cm. Additionally, they found the accumulation of ^{244}Cm in the irradiated MOX fuel becomes larger even at a low burnup.[284] Degueldre and co-workers proved that Cm in Cm-MOX is trivalently embedded in the form of $\{CmO_8\}^{13-}$ or $\{CmO_7\}^{11-}$ within the fluorite structures of the UO_2 matrix. [283]

Overall, knowledge about MAn-MOX is dominated by studies looking at fabrication in gloveboxes and behaviour in experimental reactors, with very few theoretical simulations available. Some interesting phenomena have been observed for MAn-MOX, but further work is needed to explain the underlying mechanisms.

1.4 Nuclear waste

Nuclear waste can be divided into three types according to their radioactivity: low-level, intermediate-level, and high-level waste (Figure 1.8). About 90% of nuclear waste is low-level, such as tools and work clothing. Used filters, and components of reactors are classed as intermediate-level waste, which accounts for 7% of nuclear waste. Spent nuclear fuel is classed as high-level waste; despite only accounting for 3% of total nuclear waste, it is the most concerning category. 96% of spent nuclear fuel is the remaining U, including ^{238}U, ^{235}U, and ^{236}U, and the rest of the nuclear fuel is composed of 1% Pu, 3% fission products of U and Pu, and very small amounts of minor actinides. U can be reused as UO_2 fuel, but one disadvantage to reprocessing spent fuel, is that Pu can accumulate. As a consequence of this, reprocessing has led to the largest civil stockpile of separated Pu (stored as PuO_2) in the UK over the last few decades. To develop either a long-term storage plan for Pu or reuse it as U-Pu MOX fuel, a sufficient understanding of PuO_2 is required. What is more, up to about 6% Am is found in the oldest PuO_2 stockpiles in the UK, thus for safe storage of PuO_2, an understanding of aged PuO_2 and how its structure may change over time is important. Therefore, in this section, works that focused on pure PuO_2 (1.4.1) and the simplified aged PuO_2 system: Pu-Am MOX (1.4.2) will be discussed.

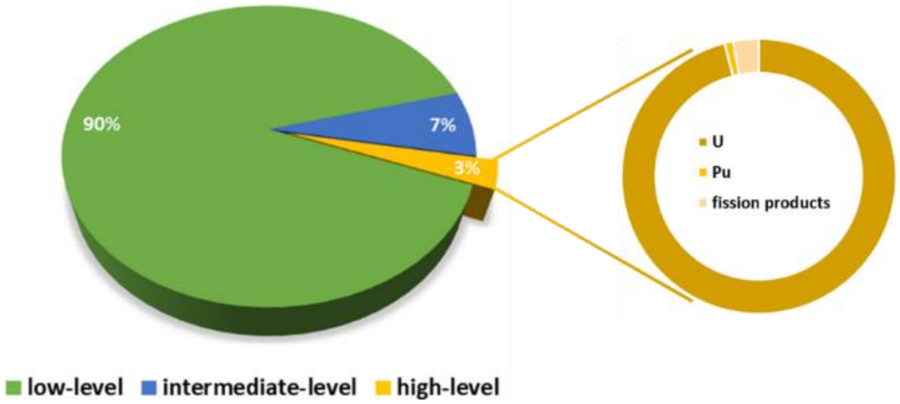

Figure 1.8: Composition of spent UO_2 nuclear fuel.

1.4.1 Plutonium dioxide (PuO_2)

Plutonium dioxide (PuO_2) has the *fcc* fluorite like structure, belonging to the *Fm-3m* space group.[286-287] In PuO_2, the Pu 5*f* electrons directly participate in chemical bond formation, whilst the 6*p* electrons contribute noticeably to the formation of the occupied part of the valence bands.[288] The ground-state magnetic structure of PuO_2 remains debatable, with experimental studies supporting the presence of a diamagnetic (DM) ground state,[289-291] whilst theoretical methods indicate either a collinear ferromagnetic (FM) or antiferromagnetic (AFM) ground state.[292-297] Pu is extracted from spent nuclear fuel and has the potential to be reused as U-Pu MOX fuel, thus there is a lot of work involved in investigating the performance of PuO_2 as nuclear fuel (mainly focused on thermal properties, such as heat capacity, thermal conduction, and so on).[298-310] To better predict PuO_2 performance as a nuclear fuel, the influence of fission products and irradiation generation defects has also been investigated in previous studies.[311-314]

Additionally, as it is important to safely store PuO_2 long-term, there has been a lot of attention paid to the corrosion of PuO_2 over time. In these studies, the properties and adsorption of small molecules on PuO_2 surfaces have been intensively examined. For example, experimental results show that PuO_2 is active under an atmosphere containing hydrogen, oxygen, and water.[315] Formation of PuO_{2+x} at temperatures below 200 °C has been detected after dissociative water adsorption, and this structure shows evidence of extensive hydroxylation and spectroscopic features that are consistent with higher Pu oxidation states (such as Pu(V)).[315] Gouder and co-workers also support the idea that PuO_{2+x} contains additional OH^- rather than O^{2-}.[316] Stakebake *et al*. found that the reaction of dry oxygen with the PuO_2 surfaces is slow and the extent is limited after a few hours.[317-318] Therefore, water adsorption on PuO_2 surfaces is important. Stakebake and co-workers studied the surface interaction between water and PuO_2,[319-320] dividing the adsorption of water into three steps: the first step was chemisorption which involves adsorption and dissociation of water; the second step was quasi-chemisorption with molecularly adsorbed water; the last step was physisorption. Haschke *et al*. further divided ten molecular layers of water on the PuO_2 surface into five distinctly different types, ranging from strong dissociative chemisorption to molecular condensation.[321]

Theoretical simulations of PuO_2 have focused on bulk and surface properties, as well as water adsorption. The lattice parameter, bandgap, and the electronic state of PuO_2 from DFT + U simulation are in agreement with experimental results, thus suggesting that the DFT + U method can provide reasonable predictions for PuO_2.[322-330] Surface properties, such as surface stability, oxidation, and defect formation, have been compared for different PuO_2 surfaces.[331-334] Both molecular and dissociative forms of water adsorption have been widely studied on a range of different PuO_2 surfaces (such as the {111}, {110} and {100} surfaces.[124, 141-142, 335-337] The relative stability of both forms of water adsorption is dependent on which surface type is being studied. Tegner and co-workers simulated a full water adsorption layer on PuO_2 {111}, {110} and {100} surfaces, and found a mix of molecular and dissociative adsorption on the {111} surface, but fully dissociative adsorption on the {110} and {100} surfaces.[142] They further studied multiple water layers on PuO_2 surfaces, and found significant variation in the per-layer adsorption energies.[141]

Other small molecules (such as HCl, NO_x, and CO_2) also exist in PuO_2 stockpiles. Thus, the interactions between these small molecules and the PuO_2 surface are also important to understand the true nature of long-term corrosion. Experiments on HCl desorption from chloride-contaminated PuO_2 suggest HCl is adsorbed to the surface in a range of different forms, including strong evidence for co-adsorption of HCl and water on PuO_2 surfaces.[338] Sims *et al*. found that hydrogen production from PuO_2 is affected not only by monolayers of water but also by the presence of other adsorbates, such as NO_x and CO_2.[339] Few theoretical works studied HCl and CO_2 adsorption on PuO_2 surfaces.[340-342] For example, Collard and co-workers systematically investigated HCl adsorption on stoichiometric and oxygen vacancy PuO_2 surfaces.[341] However, the understanding of the behaviour of other small molecules on PuO_2 surfaces is still lacking, along with knowledge on the co-adsorption of water and other small molecules. As the behaviour of small molecules on the PuO_2 surfaces is important for its long-term storage, further studies are required.

1.4.2 Plutonium and americium mixed oxide (Pu-Am MOX)

Separation of Am from aged PuO_2 is important for the reuse of Pu in U-Pu MOX fuel, thus several studies have been devoted to understanding this process.[343-344] Additionally, the influence of Am contamination in PuO_2 is also very important for the long-term storage of nuclear waste. Solid solutions of $(Pu_{0.91}Am_{0.09})O_{2-x}$ possess a single-phase fluorite structure, with an O/M ratio ranging between 1.90 - 2.00 and a phase transition temperature of around 950°C (which is slightly lower than that of AmO_{2-x}),[345] Higher Am contents (20%, 50%, and 80%) were studied by Jankowiak and co-workers,[346] and they observed a fast lattice parameter expansion rate (which increases with Am content), followed by stabilisation at a maximum value (which increases with Pu content). Vauchy *et al.* compared lattice expansion of Pu-Am MOX with a wide range of Am contents (from 1.8% to 100%),[347] they confirmed the presence of a single *fcc* phase for all MOX samples and a linear lattice thermal expansion behaviour below 1100 K. Ellinger *et al.* found that the lattice parameter of Pu-Am MOX has a positive deviation from Vegard's law.[348]

Several studies have investigated the valence states of Pu and Am in MOX, and concluded that Am is reduced from a tetravalent to a trivalent state when the O/M ratio of Pu-Am MOX deviates from the stoichiometric value.[349-351] For example Prieur *et al.* confirm the presence of Am in $(Pu_{0.8}Am_{0.2})O_{2-x}$ as well as finding that Pu remains tetravalent.[351] The same valence state relationship of Pu and Am in MOX is also found in $(Pu_{1-y}Am_{y})O_{2-x}$ (y = 0.018, 0.077, 0.21, 0.49, 0.80, and 1.00).[347] So far experimental study of Pu-Am MOX's magnetic properties has been restricted to one paper by Tokunaga *et al.*,[352] who found that the effective moment of the Am ions in MOX is comparable with Am in AmO_2. A theoretical simulation of $Pu_{0.5}Am_{0.5}O_2$ suggests that the ground state is AFM.[353] Overall, limited work has been published on Pu-Am MOX, thus we know little about the true chemistry of Pu-Am MOX, and hence much more investigation into this system is required.

1.5 Conclusions, aims and objectives

In conclusion, due to the importance of actinide oxides and actinide mixed oxides in the development of nuclear power, a lot of studies have investigated both actinide and mixed oxides. However, there is still not enough of understanding of these materials to support further development of nuclear fuel and long-term disposal of nuclear waste. This is primarily due to the fact that most previous work on these systems has been mainly focused on uranium dioxide (UO_2), plutonium dioxides (PuO_2), and uranium and plutonium mixed oxides (U-Pu MOX), along with a little work on minor actinide dioxides ($MAnO_2$), uranium and minor actinide mixed oxides (U-MAn MOX), and plutonium and americium mixed oxides (Pu-Am MOX). What is more, previous work on PuO_2 surfaces has been mainly interested in water adsorption, thus the behaviour of other small molecules on PuO_2 surfaces is unclear.

This thesis, firstly, aims to have a comprehensive understanding of all actinides in nuclear cycles. Theoretical works Extended from UO_2 and PuO_2 to minor and later actinides, providing a systematic comparison of the bulk and surface properties of AnO_2 from UO_2 to CmO_2. Secondly, exploring the behaviour of recycled actinides (from Np to Cm) in UO_2 is essential knowledge, to provide essential knowledge for recycling all high radioactive actinides from spent fuel and fulfilling a close nuclear fuel cycle. Finally, moving on to the issue of the UK PuO_2 stockpile. Am build-up and HCl molecule have been considered in PuO_2 stockpile, in order to find out the influence of Am and HCl on long-term storage of PuO_2.

Four works are presented in this thesis (after a review of the background to the theoretical methods). Firstly, the DFT + *U* simulation of $MAnO_2$ bulk and surface, as well as water adsorption on the $MAnO_2$ surface, which will provide a systematic comparison of the bulk and surface properties of AnO_2 from UO_2 to CmO_2. Secondly, the surface properties of U-An MOX (An = Np, Pu, Am, or Cm) are investigated with the DFT + *U* method. This study will discuss the results of a range of different types of substitution positions in the UO_2 matrix, along with a comparison of a range of An to U ratios. Thirdly, the DFT + *U* method was used once more to simulate Pu-Am MOX - with Am in a range of positions in the PuO_2 matrix. In this work, surface O vacancies and water adsorption behaviour on Pu-Am MOX and PuO_2 and AmO_2 surfaces are compared. Finally, the co-adsorption of HCl and H_2O on the PuO_2 surfaces will investigated with the use of hybrid DFT within the PEECM. In this study, HCl adsorption on PuO_2 surfaces with single, multiple, and one molecular layer of H_2O have been considered.

The four works presented in this thesis are all published or accepted. The first one is 'Computational Study of the Bulk and Surface Properties of the Minor Actinide Dioxides $MAnO_2$ (MAn = Np, Am, Cm); Water Adsorption on Stoichiometric and Reduced {111}, {110} and {100} Surfaces' (Jia-Li Chen and Nikolas Kaltsoyannis, J. Phys. Chem. C 2019, 123, 25, 15540–15550, https://doi.org/10.1021/acs.jpcc.9b02324). The second one is 'DFT + U study of $U_{1-y}An_yO_{2-x}$ (An = Np, Pu, Am and Cm) {111}, {110} and {100} surfaces' (Jia-Li Chen and Nikolas Kaltsoyannis, Appl. Surf. Sci. 2021, 537, 147972, https://doi.org/10.1016/j.apsusc.2020.147972). The third one is 'Computational Study of Plutonium-Americium Mixed Oxides ($Pu_{0.92}Am_{0.08}O_{2-x}$); Water Adsorption on {111}, {110} and {100} Surfaces' (Jia-Li Chen and Nikolas Kaltsoyannis, J. Phys. Chem. C 2020, 124, 12, 6646–6658, https://doi.org/10.1021/acs.jpcc.9b11601). I am the first author for the first three works, and my supervisor is the only co-author, I responsible for all investigation, methodology, formal analysis, software, writing (review and editing). The fourth one is 'Embedded Cluster and Periodic Boundary Condition Study of the Co-Adsorption of HCl and H_2O on PuO_2 Surfaces' (Jonathan Collard, Jia-Li Chen, Helen Steele and Nikolas Kaltsoyannis, J. Nucl. Mater. accepted). I am the second author for the fourth work, Jonathan Collard did most of the simulations in this work and wrote the most part of the paper, I responsible for the gas phase and periodic boundary simulation in this work. The appendices are the supporting information for the 4 published papers.

Reference

1. global primary energy consumption. *https://www.bp.com/en/global/corporate/energy-economics/statistical-review-of-world-energy/primary-energy.html* **2017**.

2. World nuclear association and IAEA power reactor information service (PRIS). https://www.world-nuclear.org/ **2018**.

3. Uranium dioxide. https://www.wikiwand.com/en/Uranium_dioxide.

4. Fink, J. K., Thermophysical properties of uranium dioxide. *J. Nucl. Mater.* **2000**, *279*, 1-18.

5. Pavlov, T. R.; Wenman, M. R.; Vlahovic, L.; Robba, D.; Konings, R. J. M.; Van Uffelen, P.; Grimes, R. W., Measurement and interpretation of the thermo-physical properties of UO_2 at high temperatures: The viral effect of oxygen defects. *Acta Mater.* **2017**, *139*, 138-154.

6. Peng, S.; Grimvall, G., Heat-capacity of actinide dioxides. *J. Nucl. Mater.* **1994**, *210*, 115-122.

7. Baichi, M.; Chatillon, C.; Ducros, G.; Froment, K., Thermodynamics of the O-U system: III - Critical assessment of phase diagram data in the U-UO_{2+x} composition range. *J. Nucl. Mater.* **2006**, *349*, 57-82.

8. Nerikar, P. V.; Liu, X. Y.; Uberuaga, B. P.; Stanek, C. R.; Phillpot, S. R.; Sinnott, S. B., Thermodynamics of fission products in $UO_{2\ +/-\ x}$. *J. Phys. Condens. Matter.* **2009**, *21*.

9. Wang, B. T.; Zhang, P.; Lizarraga, R.; Di Marco, I.; Eriksson, O., Phonon spectrum, thermodynamic properties, and pressure-temperature phase diagram of uranium dioxide. *Phys. Rev. B* **2013**, *88*.

10. Baldinozzi, G.; Desgranges, L.; Petot, C., A statistical approach of the thermodynamic properties of UO_2 at high temperature. *Nucl. Instrum. Methods Phys. Res., B* **2014**, *327*, 68-73.

11. Bottin, F.; Geneste, G.; Jomard, G., Thermodynamic stability of the UO_2 surfaces: Interplay between over-stoichiometry and polarity compensation. *Phys. Rev. B* **2016**, *93*.

12. Guthrie, M.; Benmore, C. J.; Skinner, L. B.; Alderman, O. L. G.; Weber, J. K. R.; Parise, J. B.; Williamson, M., Thermal expansion in UO_2 determined by high-energy X-ray diffraction. *J. Nucl. Mater.* **2016**, *479*, 19-22.

13. Aristova, N. M.; Belov, G. V.; Morozov, I. V.; Sineva, M. A., Thermodynamic properties of condensed uranium dioxide. *High Temp.* **2018**, *56*, 652-661.

14. Ronchi, C.; Sheindlin, M.; Musella, M.; Hyland, G. J., Thermal conductivity of uranium dioxide up to 2900 K from simultaneous measurement of the heat capacity and thermal diffusivity. *J. Appl. Phys.* **1999**, *85*, 776-789.

15. Ronchi, C.; Sheindlin, M.; Staicu, D.; Kinoshita, M., Effect of burn-up on the thermal conductivity of uranium dioxide up to 100.000 MWdt(-1). *J. Nucl. Mater.* **2004**, *327*, 58-76.

16. Gofryk, K., et al., Anisotropic thermal conductivity in uranium dioxide. *Nat. Commun.* **2014**, *5*.

17. Deng, B.; Chernatynskiy, A.; Sinnott, S. B.; Phillpot, S. R., Thermal transport at (001) twist grain boundaries in UO_2. *J. Nucl. Mater.* **2016**, *479*, 167-173.

18. Vlahovic, L.; Staicu, D.; Kust, A.; Konings, R. J. M., Thermal diffusivity of UO_2 up to the melting point. *J. Nucl. Mater.* **2018**, *499*, 504-511.

19. Shrestha, K.; Yao, T.; Lian, J.; Antonio, D.; Sessim, M.; Tonks, M. R.; Gofryk, K., The grain-size effect on thermal conductivity of uranium dioxide. *J. Appl. Phys.* **2019**, *126*.

20. Conradson, S. D.; Manara, D.; Wastin, F.; Clark, D. L.; Lander, G. H.; Morales, L. A.; Rebizant, J.; Rondinella, V. V., Local structure and charge distribution in the UO_2-U_4O_9 system. *Inorg. Chem.* **2004**, *43*, 6922-6935.

21. Andreev, E. I.; Glavin, K. V.; Ivanov, A. V.; Malovik, V. V.; Martynov, V. V.; Panov, V. S., Some results uranium dioxide powder structure investigation. *Russ. J. Non-Ferr. Met.* **2009**, *50*, 281-285.

22. Kim, J. G.; Park, Y. S.; Ha, Y. K.; Song, K., Infrared spectra of uranium oxides measured by ATR-FTIR. *J. Nucl. Sci. Technol.* **2009**, *46*, 1188-1192.

23. Skinner, L. B., et al., Molten uranium dioxide structure and dynamics. *Science* **2014**, *346*, 984-987.

24. Jiang, A. K.; Zhao, Y. W.; Long, Z.; Zhang, L.; Hu, Y.; Zeng, R. G.; Zhang, Y. Z.; Xiao, H.; Zhu, K. W.; Liu, K. Z., EXELFs analysis of lattice structure of uranium dioxide. *Acta. Phys. Sin.* **2017**, *33*, 364-369.

25. Desgranges, L.; Ma, Y.; Garcia, P.; Baldinozzi, G.; Simeone, D.; Fischer, H. E., Understanding local structure versus long-range structure: The case of UO_2. *Chem. Eur. J.* **2018**, *24*, 2085-2088.

26. Jollet, F.; Petit, T.; Gota, S.; Thromat, N.; GautierSoyer, M.; Pasturel, A., The electronic structure of uranium dioxide: an oxygen K-edge X-ray absorption study. *J. Phys. Condens. Matter.* **1997**, *9*, 9393-9401.

27. Kang, S. H.; Lee, J. H.; Yoo, H. I.; Kim, H. S.; Lee, Y. W., Non-stoichiometry, electrical conductivity and defect structure of hyper-stoichiometric UO_{2+x} at 1000 degrees C. *J. Nucl. Mater.* **2000**, *277*, 339-345.

28. Aguiar, J. A.; Asta, M.; Gronbech-Jensen, N.; Browning, N. D., Studying the electronic structure of uranium dioxide. *Microsc. Microanal.* **2009**, *15*, 1380-1381.

29. Wang, J. W.; Ewing, R. C.; Becker, U., Electronic structure and stability of hyperstoichiometric UO_{2+x} under pressure. *Phys. Rev. B* **2013**, *88*.

30. Tobin, J. G.; Yu, S. W.; Qiao, R.; Yang, W. L.; Booth, C. H.; Shuh, D. K.; Duffin, A. M.; Sokaras, D.; Nordlund, D.; Weng, T. C., Covalency in oxidized uranium. *Phys. Rev. B* **2015**, *92*.

31. Butorin, S. M.; Modin, A.; Vegelius, J. R.; Kvashnina, K. O.; Shuh, D. K., Probing chemical bonding in uranium dioxide by means of high-resolution X-ray absorption spectroscopy. *J. Phys. Chem. C* **2016**, *120*, 29397-29404.

32. Maslakov, K. I.; Teterin, Y. A.; Ryzhkov, M. V.; Popel, A. J.; Teterin, A. Y.; Ivanov, K. E.; Kalmykov, S. N.; Petrov, V. G.; Farnan, I., The nature of the chemical bond in UO_2. *Int. J. Quantum Chem.* **2019**, *119*.

33. Casado, J. M.; Harding, J. H.; Hyland, G. J., Small-polaron hopping in Mott-Insulating UO_2. *J. Phys. Condens. Matter.* **1994**, *6*, 4685-4698.

34. Caciuffo, R.; Amoretti, G.; Santini, P.; Lander, G. H.; Kulda, J.; Du Plessis, P. D., Magnetic excitations and dynamical Jahn-Teller distortions in UO_2. *Phys. Rev. B* **1999**, *59*, 13892-13900.

35. Boettger, J. C., Predicted spin-orbit coupling effect on the magnetic ordering of crystalline uranium dioxide. *Eur. Phys. J. B.* **2003**, *36*, 15-20.

36. Sakai, H.; Kato, H.; Tokunaga, Y.; Kambe, S.; Walstedt, R. E.; Nakamura, A.; Tateiwa, N.; Kobayashi, C., Magnetism of uranium dioxide UO_2 under high pressure. *J. Magn. Magn. Mater.* **2004**, *272*, E413-E414.

37. Caciuffo, R.; Santini, P.; Carretta, S.; Amoretti, G.; Hiess, A.; Magnani, N.; Regnault, L. P.; Lander, G. H., Multipolar, magnetic, and vibrational lattice dynamics in the low-temperature phase of uranium dioxide. *Phys. Rev. B* **2011**, *84*.

38. Tereshina, E. A.; Danis, S.; Springell, R.; Bao, Z.; Havela, L.; Caciuffo, R., Crystal structure and magnetic properties of UO_2/permalloy thin films. *Thin Solid Films* **2015**, *591*, 271-275.

39. Jaime, M., et al., Piezomagnetism and magnetoelastic memory in uranium dioxide. *Nat. Commun.* **2017**, *8*.

40. Lander, G. H.; Caciuffo, R., The fifty years it has taken to understand the dynamics of UO_2 in its ordered state. *J. Phys. Condens. Matter.* **2020**, *32*.

41. Petit, T.; Lemaignan, C.; Jollet, F.; Bigot, B.; Pasturel, A., Point defects in uranium dioxide. *Philos. Mag. B* **1998**, *77*, 779-786.

42. Crocombette, J. P.; Jollet, F.; Nga, L. N.; Petit, T., Plane-wave pseudopotential study of point defects in uranium dioxide. *Phys. Rev. B* **2001**, *64*.

43. Freyss, M.; Petit, T.; Crocombette, J. P., Point defects in uranium dioxide: Ab initio pseudopotential approach in the generalized gradient approximation. *J. Nucl. Mater.* **2005**, *347*, 44-51.

44. Iwasawa, M.; Chen, Y.; Kaneta, Y.; Ohnuma, T.; Geng, H. Y.; Kinoshita, M., First-principles calculation of point defects in uranium dioxide. *Mater. Trans.* **2006**, *47*, 2651-2657.

45. Geng, H. Y.; Chen, Y.; Kaneta, Y.; Iwasawa, M.; Ohnuma, T.; Kinoshita, M., Point defects and clustering in uranium dioxide by LSDA+U calculations. *Phys. Rev. B* **2008**, *77*.

46. Geng, H. Y.; Chen, Y.; Kaneta, Y.; Kinoshita, M., Ab initio investigation on oxygen defect clusters in $UO_{(2+x)}$. *Appl. Phys. Lett.* **2008**, *93*.

47. Yu, J. G.; Devanathan, R.; Weber, W. J., First-principles study of defects and phase transition in UO_2. *J. Phys. Condens. Matter.* **2009**, *21*.

48. Dorado, B.; Jomard, G.; Freyss, M.; Bertolus, M., Stability of oxygen point defects in UO_2 by first-principles DFT plus U calculations: Occupation matrix control and Jahn-Teller distortion. *Phys. Rev. B* **2010**, *82*.

49. Vathonne, E.; Wiktor, J.; Freyss, M.; Jomard, G.; Bertolus, M., DFT plus U investigation of charged point defects and clusters in UO_2. *J. Phys. Condens. Matter.* **2014**, *26*.

50. Cooper, M. W. D.; Murphy, S. T.; Andersson, D. A., The defect chemistry of $UO_{2\ +/-\ x}$ from atomistic simulations. *J. Nucl. Mater.* **2018**, *504*, 251-260.

51. Nakajima, K.; Arai, Y., Investigation of vaporization behavior of hyper-stoichiometric uranium dioxide by Knudsen effusion mass spectrometry. *J. Nucl. Mater.* **2003**, *317*, 243-251.

52. He, H. M.; Ding, Z. F.; Shoesmith, D. W., The determination of electrochemical reactivity and sustainability on individual hyper-stoichiometric UO_{2+x} grains by Raman microspectroscopy and scanning electrochemical microscopy. *Electrochem. commun.* **2009**, *11*, 1724-1727.

53. He, H. M.; Shoesmith, D., Raman spectroscopic studies of defect structures and phase transition in hyper-stoichiometric UO_{2+x}. *Phys. Chem. Chem. Phys.* **2010**, *12*, 8108-8117.

54. Pakhomov, E. P., Interaction of oxygen with uranium dioxide and its defect structure. *High Temp.* **2011**, *49*, 390-397.

55. Elorrieta, J. M.; Bonales, L. J.; Rodriguez-Villagra, N.; Baonza, V. G.; Cobos, J., A detailed Raman and X-ray study of UO_2+x oxides and related structure transitions. *Phys. Chem. Chem. Phys.* **2016**, *18*, 28209-28216.

56. McEachern, R. J.; Taylor, P., A review of the oxidation of uranium dioxide at temperatures below 400 degrees C. *J. Nucl. Mater.* **1998**, *254*, 87-121.

57. Belle, J., Oxygen and uranium diffusion in uranium dioxide (a review). *J. Nucl. Mater.* **1969**, *30*, 3-15.

58. Murch, G.; Bradhurst, D.; De Bruin, H., Oxygen self-diffusion in non-stoichiometric uranium dioxide. *Philos. Mag.* **1975**, *32*, 1141-1150.

59. Kupryazhkin, A. Y.; Zhiganov, A.; Risovany, D.; Nekrassov, K.; Risovany, V.; Golovanov, V., Simulation of diffusion of oxygen and uranium in uranium dioxide nanocrystals. *J. Nucl. Mater.* **2008**, *372*, 233-238.

60. Dorado, B.; Durinck, J.; Garcia, P.; Freyss, M.; Bertolus, M., An atomistic approach to self-diffusion in uranium dioxide. *J. Nucl. Mater.* **2010**, *400*, 103-106.

61. Williams, N. R.; Molinari, M.; Parker, S. C.; Storr, M. T., Atomistic investigation of the structure and transport properties of tilt grain boundaries of UO_2. *J. Nucl. Mater.* **2015**, *458*, 45-55.

62. Shea, J. H., An improved model of fission gas atom transport in irradiated uranium dioxide. *J. Nucl. Mater.* **2018**, *501*, 302-311.

63. Bernhardt, J. R.; Han, X. C.; Heuser, B. J., Oxygen-18 tracer measurements of anion diffusion in uranium dioxide thin films. *JOM* **2019**, *71*, 4808-4816.

64. Catlow, C. R. A., Fission gas diffusion in uranium dioxide. *Proc. R. Soc. Lond. A.* **1978**, *364*, 473-497.

65. Torres, E.; Kaloni, T., Thermal conductivity and diffusion mechanisms of noble gases in uranium dioxide: A DFT+ U study. *J. Nucl. Mater.* **2019**, *521*, 137-145.

66. Chen, Q. Y.; Lai, X. C.; Bai, B.; Chu, M. F., Structural characterization and optical properties of UO_2 thin films by magnetron sputtering. *Appl. Surf. Sci.* **2010**, *256*, 3047-3050.

67. Ilton, E. S.; Bagus, P. S., XPS determination of uranium oxidation states. *Surf. Interface Anal.* **2011**, *43*, 1549-1560.

68. Maslakov, K. I.; Teterin, Y. A.; Popel, A. J.; Teterin, A. Y.; Ivanov, K. E.; Kalmykov, S. N.; Petrov, V. G.; Springell, R.; Scott, T. B.; Farnan, I., XPS study of the surface chemistry of UO_2 (111) single crystal film. *Appl. Surf. Sci.* **2018**, *433*, 582-588.

69. Maslova, O. A.; Iltis, X.; Desgranges, L.; Ammar, M. R.; Genevois, C.; de Bilbao, E.; Canizares, A.; Barannikova, S. A.; Leontyev, I. N.; Simon, P., Characterization of an UO_2 ceramic via Raman imaging and electron back-scattering diffraction. *Mater. Charact.* **2019**, *147*, 280-285.

70. Spurgeon, S. R.; Sassi, M.; Ophus, C.; Stubbs, J. E.; Ilton, E. S.; Buck, E. C., Nanoscale oxygen defect gradients in UO_{2+x} surfaces. *PNAS* **2019**, *116*, 17181-17186.

71. Carter, R.; Lay, K., Surface-controlled oxidation-reduction of UO_2. *J. Nucl. Mater.* **1970**, *36*, 77-86.

72. Dobrov, B. V.; Likhanskii, V. V.; Ozrin, V. D.; Solodov, A. A., Modeling of the oxidation of uranium dioxide in a steam atmosphere. *At. Energy* **1997**, *82*, 109-115.

73. Dobrov, B.; Likhanskii, V.; Ozrin, V.; Solodov, A.; Kissane, M.; Manenc, H., Kinetics of UO_2 oxidation in steam atmosphere. *J. Nucl. Mater.* **1998**, *255*, 59-66.

74. Rakitskaya, E. M.; Panov, A. S., The behavior of uranium dioxide in various gases. *At. Energy* **2000**, *89*, 890-894.

75. Manara, D.; Renker, B., Raman spectra of stoichiometric and hyperstoichiometric uranium dioxide. *J. Nucl. Mater.* **2003**, *321*, 233-237.

76. Espriu-Gascon, A.; Llorca, J.; Dominguez, M.; Gimenez, J.; Casas, I.; de Pablo, J., UO_2 surface oxidation by mixtures of water vapor and hydrogen as a function of temperature. *J. Nucl. Mater.* **2015**, *467*, 240-243.

77. Stubbs, J. E.; Chaka, A. M.; Ilton, E. S.; Biwer, C. A.; Engelhard, M. H.; Bargar, J. R.; Eng, P. J., UO_2 oxidative corrosion by nonclassical diffusion. *Phys. Rev. Lett.* **2015**, *114*.

78. Stubbs, J. E.; Biwer, C. K.; Chaka, A. M.; Ilton, E. S.; Du, Y. G.; Bargar, J. R.; Eng, P. J., Oxidative corrosion of the UO_2 (001) surface by nonclassical diffusion. *Langmuir* **2017**, *33*, 13189-13196.

79. Tracy, C. L.; Chen, C. H.; Park, S.; Davisson, M. L.; Ewing, R. C., Measurement of UO_2 surface oxidation using grazing-incidence X-ray diffraction: Implications for nuclear forensics. *J. Nucl. Mater.* **2018**, *502*, 68-75.

80. Lahalle, M. P.; Guillaumont, R.; Allen, G. C., Surface behaviour of uranium-dioxide after immersion in mineral water studies by X-ray photoelectron-spectroscopy. *J. Chem. Soc., Faraday Trans.* **1990**, *86*, 2641-2644.

81. Chong, S. V.; Griffiths, T. R.; Idriss, H., Ethanol reactions over the UO_2(111) single crystal: Effect of the Madelung potential on the reaction selectivity. *Surf. Sci.* **2000**, *444*, 187-198.

82. Hedhili, M. N.; Yakshinskiy, B. V.; Madey, T. E., Interaction of water vapor with UO_2 (001). *Surf. Sci.* **2000**, *445*, 512-525.

83. Chong, S. V.; Idriss, H., The reactions of carboxylic acids on UO_2 (111) single crystal surfaces. Effect of gas-phase acidity and surface defects. *Surf. Sci.* **2002**, *504*, 145-158.

84. Schlereth, T. W.; Hedhili, M. N.; Yakshinskiy, B. V.; Gouder, T.; Madey, T. E., Adsorption and reaction of SO_2 with a polycrystalline UO_2 film: Promotion of S-O bond cleavage by creation of O-defects and Na or Ca coadsorption. *J. Phys. Chem. B* **2005**, *109*, 20895-20905.

85. Cohen, S.; Mintz, M. H.; Zalkind, S.; Seibert, A.; Gouder, T.; Shamir, N., Water chemisorption on a sputter deposited uranium dioxide film - Effect of defects. *Solid State Ion.* **2014**, *263*, 39-45.

86. Springell, R., et al., Water corrosion of spent nuclear fuel: Radiolysis driven dissolution at the UO_2/water interface. *Faraday Discuss.* **2015**, *180*, 301-311.

87. Bright, E. L.; Rennie, S.; Siberry, A.; Samani, K.; Clarke, K.; Goddard, D. T.; Springell, R., Comparing the corrosion of uranium nitride and uranium dioxide surfaces with H_2O_2. *J. Nucl. Mater.* **2019**, *518*, 202-207.

88. Guo, X. F.; Wu, D.; Ushakov, S. V.; Shvareva, T.; Xu, H. W.; Navrotsky, A., Energetics of hydration on uranium oxide and peroxide surfaces. *J. Mater. Res.* **2019**, *34*, 3319-3325.

89. Mudiyanselage, K.; Burrell, A. K.; Senanayake, S. D.; Idriss, H., XPS and NEXAFS study of the reactions of acetic acid and acetaldehyde over UO_2(100) thin film. *Surf. Sci.* **2019**, *680*, 107-112.

90. Higuchi, S., A molecular dynamics study of the thermal conductivity of UO_2 with impurities. *J. Nucl. Sci. Technol.* **1998**, *35*, 833-835.

91. Motoyama, S.; Ichikawa, Y.; Hiwatari, Y.; Oe, A., Thermal conductivity of uranium dioxide by nonequilibrium molecular dynamics simulation. *Phys. Rev. B* **1999**, *60*, 292-298.

92. Phillpot, S. R.; El-Azab, A.; Chernatynskiy, A.; Tulenko, J. S., Thermal conductivity of UO_2 fuel: predicting fuel performance from simulation. *JOM* **2011**, *63*, 77-83.

93. Nichenko, S.; Staicu, D., Molecular dynamics study of the effects of non-stoichiometry and oxygen Frenkel pairs on the thermal conductivity of uranium dioxide. *J. Nucl. Mater.* **2013**, *433*, 297-304.

94. Chen, T. Y.; Chen, D.; Sencer, B. H.; Shao, L., Molecular dynamics simulations of grain boundary thermal resistance in UO_2. *J. Nucl. Mater.* **2014**, *452*, 364-369.

95. Kim, H.; Kim, M. H.; Kaviany, M., Lattice thermal conductivity of UO_2 using ab-initio and classical molecular dynamics. *J. Appl. Phys.* **2014**, *115*.

96. Nichenko, S.; Staicu, D., Thermal conductivity of porous UO_2: Molecular dynamics study. *J. Nucl. Mater.* **2014**, *454*, 315-322.

97. Maxwell, C. I.; Pencer, J., Molecular dynamics modelling of the thermal conductivity of off-stoichiometric $UO_{2+/-x}$ and $(U_yPu_{1-y})O_{2+/-x}$ using equilibrium molecular dynamics. *Ann. Nucl. Energy* **2019**, *131*, 317-324.

98. Goel, P.; Choudhury, N.; Chaplot, S. L., Atomistic modeling of the vibrational and thermodynamic properties of uranium dioxide, UO_2. *J. Nucl. Mater.* **2008**, *377*, 438-443.

99. Wang, X. Y.; Wu, B.; Gao, F.; Li, X.; Sun, X.; Khaleel, M. A.; Akinlalu, A. V.; Liu, L., Molecular dynamics simulation of thermodynamic properties in uranium dioxide. *Nucl. Sci. Eng.* **2014**, *176*, 360-369.

100. Basak, C. B.; Sengupta, A. K.; Kamath, H. S., Classical molecular dynamics simulation of UO_2 to predict thermophysical properties. *J. Alloys Compd.* **2003**, *360*, 210-216.

101. Kelly, P. J.; Brooks, M., Electronic structure and ground-state properties of the actinide dioxides. *J. Chem. Soc., Faraday Trans.* **1987**, *83*, 1189-1203.

102. Petit, T.; Morel, B.; Lemaignan, C.; Pasturel, A.; Bigot, B., Cohesive properties of UO_2. *Philos. Mag. B* **1996**, *73*, 893-904.

103. Dudarev, S. L.; Manh, D. N.; Sutton, A. P., Effect of Mott-Hubbard correlations on the electronic structure and structural stability of uranium dioxide. *Philos. Mag. B* **1997**, *75*, 613-628.

104. Kudin, K. N.; Scuseria, G. E.; Martin, R. L., Hybrid density-functional theory and the insulating gap of UO_2. *Phys. Rev. Lett.* **2002**, *89*, 266402.

105. Hoover, M. E.; Atta-Fynn, R.; Ray, A. K., Surface properties of uranium dioxide from first principles. *J. Nucl. Mater.* **2014**, *452*, 479-485.

106. Prodan, I. D.; Scuseria, G. E.; Martin, R. L., Covalency in the actinide dioxides: Systematic study of the electronic properties using screened hybrid density functional theory. *Phys. Rev. B* **2007**, *76*.

107. Jollet, F.; Jomard, G.; Amadon, B.; Crocombette, J. P.; Torumba, D., Hybrid functional for correlated electrons in the projector augmented-wave formalism: Study of multiple minima for actinide oxides. *Phys. Rev. B* **2009**, *80*.

108. Wellington, J. P. W.; Kerridge, A.; Austin, J.; Kaltsoyannis, N., Electronic structure of bulk AnO_2 (An = U, Np, Pu) and water adsorption on the (111) and (110) surfaces of UO_2 and PuO_2 from hybrid density functional theory within the periodic electrostatic embedded cluster method. *J. Nucl. Mater.* **2016**, *482*, 124-134.

109. Dudarev, S. L.; Botton, G. A.; Savrasov, S. Y.; Szotek, Z.; Temmerman, W. M.; Sutton, A. P., Electronic structure and elastic properties of strongly correlated metal oxides from first principles: LSDA+U, SIC-LSDA and EELS study of UO_2 and NiO. *Phys. Status Solidi a* **1998**, *166*, 429-443.

110. Georges, A.; Kotliar, G.; Krauth, W.; Rozenberg, M. J., Dynamical mean-field theory of strongly correlated fermion systems and the limit of infinite dimensions. *Rev. Mod. Phys.* **1996**, *68*, 13.

111. Kotliar, G.; Savrasov, S. Y.; Haule, K.; Oudovenko, V. S.; Parcollet, O.; Marianetti, C., Electronic structure calculations with dynamical mean-field theory. *Rev. Mod. Phys.* **2006**, *78*, 865.

112. Geng, H. Y.; Chen, Y.; Kaneta, Y.; Kinoshita, M., Structural behavior of uranium dioxide under pressure by LSDA+U calculations. *Phys. Rev. B* **2007**, *75*.

113. Weck, P. F.; Kim, E.; Jove-Colon, C. F.; Sassani, D. C., On the role of strong electron correlations in the surface properties and chemistry of uranium dioxide. *Dalton Trans.* **2013**, *42*, 4570-4578.

114. Pegg, J. T.; Shields, A. E.; Storr, M. T.; Scanlon, D. O.; de Leeuw, N. H., Noncollinear relativistic DFT plus U calculations of actinide dioxide surfaces. *J. Phys. Chem. C* **2019**, *123*, 356-366.

115. Gryaznov, D.; Heifets, E.; Kotomin, E., Ab initio DFT plus U study of He atom incorporation into UO_2 crystals. *Phys. Chem. Chem. Phys.* **2009**, *11*, 7241-7247.

116. Liu, X. Y.; Andersson, D. A., Revisiting the diffusion mechanism of helium in UO_2: A DFT+ U study. *J. Nucl. Mater.* **2018**, *498*, 373-377.

117. Chaka, A. M.; Oxford, G. A. E.; Stubbs, J. E.; Eng, P. J.; Bargar, J. R., Density-functional theory investigation of oxidative corrosion of UO_2. *Comput. Theor. Chem.* **2012**, *987*, 90-102.

118. Dorado, B.; Amadon, B.; Freyss, M.; Bertolus, M., DFT plus U calculations of the ground state and metastable states of uranium dioxide. *Phys. Rev. B* **2009**, *79*.

119. Meredig, B.; Thompson, A.; Hansen, H.; Wolverton, C.; Van de Walle, A., Method for locating low-energy solutions within DFT+ U. *Phys. Rev. B* **2010**, *82*, 195128.

120. Krack, M., On the ground state electronic structure of uranium dioxide. *Phys. Scr.* **2015**, *90*.

121. Rabone, J.; Krack, M., A procedure for bypassing metastable states in local basis set DFT+U calculations and its application to uranium dioxide surfaces. *Comput. Mater. Sci.* **2013**, *71*, 157-164.

122. Laskowski, R.; Madsen, G. K. H.; Blaha, P.; Schwarz, K., Magnetic structure and electric-field gradients of uranium dioxide: An ab initio study. *Phys. Rev. B* **2004**, *69*.

123. Pegg, J. T.; Aparicio-Angles, X.; Storr, M.; de Leeuw, N. H., DFT plus U study of the structures and properties of the actinide dioxides. *J. Nucl. Mater.* **2017**, *492*, 269-278.

124. Wellington, J. P. W.; Tegner, B. E.; Collard, J.; Kerridge, A.; Kaltsoyannis, N., Oxygen vacancy formation and water adsorption on reduced AnO_2 {111}, {110}, and {100} surfaces (An = U, Pu): A computational study. *J. Phys. Chem. C* **2018**, *122*, 7149-7165.

125. Sui, P. F.; Dai, Z. H.; Zhang, X. L.; Zhao, Y. C., Electronic structure and optical properties in uranium dioxide: The first principle calculations. *Chin. Phys. Lett.* **2015**, *32*.

126. Nerikar, P.; Watanabe, T.; Tulenko, J. S.; Phillpot, S. R.; Sinnott, S. B., Energetics of intrinsic point defects in uranium dioxide from electronic-structure calculations. *J. Nucl. Mater.* **2009**, *384*, 61-69.

127. Gupta, F.; Brillant, G.; Pasturel, A., Correlation effects and energetics of point defects in uranium dioxide: a first principle investigation. *Philos. Mag.* **2007**, *87*, 2561-2569.

128. Geng, H. Y.; Chen, Y.; Kaneta, Y.; Iwasawa, M.; Ohnuma, T.; Kinoshita, M., Point defects and clustering in uranium dioxide by LSDA+ U calculations. *Physical Review B* **2008**, *77*, 104120.

129. Yamashita, T.; Nitani, N.; Tsuji, T.; Inagaki, H., Thermal expansions of NpO_2 and some other actinide dioxides. *J. Nucl. Mater.* **1997**, *245*, 72-78.

130. Idiri, M.; Le Bihan, T.; Heathman, S.; Rebizant, J., Behavior of actinide dioxides under pressure: UO_2 and ThO_2. *Phys. Rev. B* **2004**, *70*, 014113.

131. Crowhurst, J.; Jeffries, J.; Åberg, D.; Zaug, J.; Dai, Z.; Siekhaus, W.; Teslich, N.; Holliday, K.; Knight, K.; Nelson, A., A combined theoretical and experimental investigation of uranium dioxide under high static pressure. *J. Phys. Condens. Matter.* **2015**, *27*, 265401.

132. Schoenes, J., Electronic transitions, crystal field effects and phonons in UO_2. *Phys. Rep.* **1980**, *63*, 301-336.

133. Yu, S.-W.; Tobin, J.; Crowhurst, J.; Sharma, S.; Dewhurst, J.; Olalde-Velasco, P.; Yang, W.; Siekhaus, W., F-f origin of the insulating state in uranium dioxide: X-ray absorption experiments and first-principles calculations. *Phys. Rev. B* **2011**, *83*, 165102.

134. Schoenes, J., Optical properties and electronic structure of UO_2. *J. Appl. Phys.* **1978**, *49*, 1463-1465.

135. Yamashita, T.; Nitani, N.; Tsuji, T.; Kato, T., Thermal expansion of neptunium-uranium mixed oxides. *J. Nucl. Mater.* **1997**, *247*, 90-93.

136. Hoover, M. E.; Atta-Fynn, R.; Ray, A. K., Surface properties of uranium dioxide from first principles. *Journal of Nuclear Materials* **2014**, *452*, 479-485.

137. Sattonnay, G.; Tetot, R., Bulk, surface and point defect properties in UO_2 from a tight-binding variable-charge model. *J. Phys. Condens. Matter.* **2013**, *25*.

138. Tian, X. F.; Wang, H.; Xiao, H. X.; Gao, T., Adsorption of water on UO_2 (111) surface: Density functional theory calculations. *Comput. Mater. Sci.* **2014**, *91*, 364-371.

139. Bo, T.; Lan, J. H.; Zhao, Y. L.; Zhang, Y. J.; He, C. H.; Chai, Z. F.; Shi, W. Q., First-principles study of water adsorption and dissociation on the UO_2 (111), (110) and (100) surfaces. *J. Nucl. Mater.* **2014**, *454*, 446-454.

140. Bo, T.; Lan, J. H.; Wang, C. Z.; Zhao, Y. L.; He, C. H.; Zhang, Y. J.; Chai, Z. F.; Shi, W. Q., First-principles study of water reaction and H_2 formation on UO_2 (111) and (110) single crystal surfaces. *J. Phys. Chem. C* **2014**, *118*, 21935-21944.

141. Tegner, B. E.; Kaltsoyannis, N., Multiple water layers on AnO_2 {111},{110}, and {100} surfaces (An= U, Pu): A computational study. *J. Vac. Sci. Technol. A* **2018**, *36*, 041402.

142. Tegner, B. E.; Molinari, M.; Kerridge, A.; Parker, S. C.; Kaltsoyannis, N., Water adsorption on AnO_2 {111},{110}, and {100} surfaces (An= U and Pu): A density functional theory+ U study. *J. Phys. Chem. C* **2017**, *121*, 1675-1682.

143. Pegg, J. T.; Shields, A. E.; Storr, M. T.; Scanlon, D. O.; de Leeuw, N. H., Interaction of hydrogen with actinide dioxide (011) surfaces. *J. Chem. Phys.* **2020**, *153*.

144. Pegg, J. T.; Shields, A. E.; Storr, M. T.; Scanlon, D. O.; de Leeuw, N. H., Interaction of hydrogen with actinide dioxide (111) surfaces. *J. Chem. Phys.* **2019**, *150*.

145. Smith, A. L.; Colle, J. Y.; Benes, O.; Konings, R. J. M.; Sundman, B.; Gueneau, C., Thermodynamic assessment of the neptunium-oxygen system: Mass spectrometric studies and thermodynamic modelling. *J. Chem. Thermodyn.* **2016**, *103*, 257-275.

146. Fournier, J. M.; Blaise, A.; Amoretti, G.; Caciuffo, R.; Larroque, J.; Hutchings, M. T.; Osborn, R.; Taylor, A. D., HIigh-energy-neutron spectroscopy of crystal-field excitations in NpO_2. *Phys. Rev. B* **1991**, *43*, 1142-1145.

147. Amoretti, G.; Blaise, A.; Caciuffo, R.; Dicola, D.; Fournier, J. M.; Hutchings, M. T.; Lander, G. H.; Osborn, R.; Severing, A.; Taylor, A. D., Neutron-scattering investigation of the electronic ground state of neptunium dioxide. *J. Phys. Condens. Matter.* **1992**, *4*, 3459-3478.

148. Kopmann, W.; Litterst, F. J.; Klauss, H. H.; Hillberg, M.; Wagener, W.; Kalvius, G. M.; Schreier, E.; Burghart, F. J.; Rebizant, J.; Lander, G. H., Magnetic order in NpO_2 and UO_2 studied by muon spin rotation. *J. Alloys Compd.* **1998**, *271*, 463-466.

149. Mannix, D.; Lander, G. H.; Rebizant, J.; Caciuffo, R.; Bernhoeft, N.; Lidstrom, E.; Vettier, C., Unusual magnetism of NpO_2: A study with resonant X-ray scattering. *Phys. Rev. B* **1999**, *60*, 15187-15193.

150. Santini, P.; Amoretti, G., Magnetic-octupole order in neptunium dioxide? *Phys. Rev. Lett.* **2000**, *85*, 5481-5481.

151. Paixao, J. A.; Detlefs, C.; Longfield, M. J.; Caciuffo, R.; Santini, P.; Bernhoeft, N.; Rebizant, J.; Lander, G. H., Triple-(q)over-right-arrow octupolar ordering in NpO_2. *Phys. Rev. Lett.* **2002**, *89*.

152. Caciuffo, R.; Paixao, J. A.; Detlefs, C.; Longfield, M. J.; Santini, P.; Bernhoeft, N.; Rebizant, J.; Lander, G. H., Multipolar ordering in NpO_2 below 25 K. *J. Phys. Condens. Matter.* **2003**, *15*, S2287-S2296.

153. Nagao, T.; Igarashi, J., Resonant X-ray scattering spectra from multipole ordering: Np M-4,M-5 edges in NpO_2. *Phys. Rev. B* **2005**, *72*.

154. Santini, P.; Carretta, S.; Magnani, N.; Amoretti, G.; Caciuffo, R., Hidden order and low-energy excitations in NpO_2. *Phys. Rev. Lett.* **2006**, *97*.

155. Magnani, N.; Carretta, S.; Caciuffo, R.; Santini, P.; Amoretti, G.; Hiess, A.; Rebizant, J.; Lander, G. H., Inelastic neutron scattering study of the multipolar order parameter in NpO_2. *Phys. Rev. B* **2008**, *78*.

156. Lovesey, S. W.; Detlefs, C.; Rodriguez-Fernandez, A., Neptunium multipoles and resonant X-ray Bragg diffraction by neptunium dioxide (NpO_2). *J. Phys. Condens. Matter.* **2012**, *24*.

157. Westrum, E. F.; Hatcher, J. B.; Osborne, D. W., The entropy and low temperature heat capacity of neptunium dioxide. *J. Chem. Phys.* **1953**, *21*, 419-423.

158. Serizawa, H.; Arai, Y.; Nakajima, K., The estimation of the heat capacity of NpO_2. *J. Chem. Thermodyn.* **2001**, *33*, 615-628.

159. Benes, O.; Gotcu-Freis, P.; Schworer, F.; Konings, R. J. M.; Fanghanel, T., The high temperature heat capacity of NpO_2. *J. Chem. Thermodyn.* **2011**, *43*, 651-655.

160. Konings, R. J. M.; Benes, O., The heat capacity of NpO_2 at high temperatures: The effect of oxygen Frenkel pair formation. *J. Phys. Chem. Solids* **2013**, *74*, 653-655.

161. McCleskey, T. M., et al., Optical band gap of NpO_2 and PuO_2 from optical absorbance of epitaxial films. *J. Appl. Phys.* **2013**, *113*.

162. Teterin, Y. A.; Teterin, A. Y.; Ivanov, K. E.; Ryzhkov, M. V.; Maslakov, K. I.; Kalmykov, S. N.; Petrov, V. G.; Enina, D. A., X-ray photoelectron spectra structure and chemical bond nature in NpO_2. *Phys. Rev. B* **2014**, *89*.

163. Ackermann, R. J.; Faircloth, R. L.; Rauh, E. G.; Thorn, R. J., Evaporation behaviour of neptunium dioxide. *J. Inorg. Nucl. Chem.* **1966**, *28*, 111-+.

164. Gotcu-Freis, P.; Colle, J. Y.; Hiernaut, J. P.; Konings, R. J. M., (Solid plus gas) equilibrium studies for neptunium dioxide. *J. Chem. Thermodyn.* **2011**, *43*, 492-498.

165. Kurosaki, K.; Imamura, M.; Sato, I.; Namekawa, T.; Uno, M.; Yamanaka, S., Molecular dynamics studies of neptunium dioxide. *J. Alloys Compd.* **2005**, *387*, 9-14.

166. Wang, B. T.; Shi, H. L.; Li, W. D.; Zhang, P., First-principles LDA plus U and GGA plus U study of neptunium dioxide. *Phys. Rev. B* **2010**, *81*.

167. Yun, Y.; Rusz, J.; Suzuki, M. T.; Oppeneer, P. M., First-principles investigation of higher oxides of uranium and neptunium: U_3O_8 and Np_2O_5. *Phys. Rev. B* **2011**, *83*.

168. Arima, T.; Yoshida, K.; Matsumoto, T.; Inagaki, Y.; Idemitsu, K., Thermal conductivities of ThO_2, NpO_2 and their related oxides: Molecular dynamics study. *J. Nucl. Mater.* **2014**, *445*, 175-180.

169. Bo, T.; Lan, J. H.; Zhao, Y. L.; Zhang, Y. J.; He, C. H.; Chai, Z. F.; Shi, W. Q., Surface properties of NpO_2 and water reacting with stoichiometric and reduced NpO_2 (111), (110), and (100) surfaces from ab initio atomistic thermodynamics. *Surf. Sci.* **2016**, *644*, 153-164.

170. Andersson, D. A.; Lezama, J.; Uberuaga, B. P.; Deo, C.; Conradson, S. D., Cooperativity among defect sites in AO_{2+x} and A_4O_9 (A=U,Np,Pu): Density functional calculations. *Phys. Rev. B* **2009**, *79*.

171. Cooper, M. W. D.; Rushton, M. J. D.; Grimes, R. W., A many-body potential approach to modelling the thermomechanical properties of actinide oxides. *J. Phys. Condens. Matter.* **2014**, *26*.

172. Eser, E.; Koc, H.; Gokbulut, M.; Gursoy, G., Estimations of heat capacities for actinide dioxide: UO_2, NpO_2, ThO_2, And PuO_2. *Nucl. Eng. Technol.* **2014**, *46*, 863-868.

173. Gaigalas, G.; Gaidamauskas, E.; Rudzikas, Z.; Magnani, N.; Caciuffo, R., Ab initio calculations of crystal-field for actinide dioxides. *Lith. J. Phys.* **2009**, *49*, 403-413.

174. Magnani, N.; Suzuki, M. T.; Oppeneer, P. M., First-principles theory of multipolar order in actinide dioxides. *C. R. Phys.* **2014**, *15*, 580-586.

175. Pegg, J. T.; Shields, A. E.; Storr, M. T.; Wills, A. S.; Scanlon, D. O.; de Leeuw, N. H., Magnetic structure of UO_2 and NpO_2 by first-principle methods. *Phys. Chem. Chem. Phys.* **2019**, *21*, 760-771.

176. Petit, L.; Svane, A.; Szotek, Z.; Temmerman, W. M.; Stocks, G. M., Electronic structure and ionicity of actinide oxides from first principles. *Phys. Rev. B* **2010**, *81*.

177. Suzuki, M. T.; Magnani, N.; Oppeneer, P. M., Microscopic theory of the insulating electronic ground states of the actinide dioxides AnO_2 (An= U, Np, Pu, Am, and Cm). *Phys. Rev. B* **2013**, *88*.

178. Yang, Y.; Zhang, P., Chemical bonds and vibrational properties of ordered (U, Np, Pu) mixed oxides. *J. Appl. Phys.* **2013**, *113*.

179. Rak, Z.; Ewing, R. C.; Becker, U., Hydroxylation-induced surface stability of AnO_2 (An = U, Np, Pu) from first-principles. *Surf. Sci.* **2013**, *608*, 180-187.

180. Naegele, J. R.; Cox, L. E.; Ward, J. W., Photoelectro-spectroscopy (UPS XPS) study of Np_2O_3 formation on the surface of neptunium metal. *Inorganica Chim. Acta* **1987**, *139*, 327-329.

181. Cakir, P.; Eloirdi, R.; Huber, F.; Konings, R. J. M.; Gouder, T., Surface reduction of neptunium dioxide and uranium mixed oxides with plutonium and thorium by photocatalytic reaction with Ice. *J. Phys. Chem. C* **2015**, *119*, 1330-1337.

182. Lebreton, F.; Belin, R. C.; Delahaye, T.; Blanchart, P., In-situ X-ray diffraction study of phase transformations in the Am-O system. *J. Solid State Chem.* **2012**, *196*, 217-224.

183. Horlait, D.; Caraballo, R.; Lebreton, F.; Jegou, C.; Roussel, P.; Delahaye, T., Self-irradiation and oxidation effects on americium sesquioxide and Raman spectroscopy studies of americium oxides. *J. Solid State Chem.* **2014**, *217*, 159-168.

184. Karraker, D., Magnetic susceptibility of $^{243}AmO_2$. *J. Chem. Phys.* **1975**, *63*, 3174-3175.

185. Magnani, N.; Santini, P.; Amoretti, G.; Caciuffo, R., Perturbative approach to J mixing in f-electron systems: Application to actinide dioxides. *Phys. Rev. B* **2005**, *71*, 054405.

186. Abraham, M.; Boatner, L.; Finch, C.; Reynolds, R., Electron-paramagnetic-resonance investigations of 5 f^5 Configuration Ions in Cubic Single Crystals: Pu $^{3+}$ in ThO_2 and $SrCl_2$, and Am $^{4+}$ in ThO_2. *Phys. Rev. B* **1971**, *3*, 2864.

187. Kolbe, W.; Edelstein, N.; Finch, C.; Abraham, M., Electron paramagnetic resonance of $^{239}Pu^{3+}$ and $^{243}Am^{4+}$ in CeO_2 and of $^{241}Pu^{3+}$ in ThO_2. *J. Chem. Phys.* **1974**, *60*, 607-609.

188. Tokunaga, Y.; Nishi, T.; Nakada, M.; Itoh, A.; Sakai, H.; Kambe, S.; Homma, Y.; Honda, F.; Aoki, D.; Walstedt, R. E., Self-radiation effects and glassy nature of magnetic transition in AmO_2 revealed by O-17-NMR. *Phys. Rev. B* **2014**, *89*.

189. Tokunaga, Y.; Nishi, T.; Kambe, S.; Nakada, M.; Itoh, A.; Homma, Y.; Sakai, H.; Chudo, H., NMR evidence for the 8.5K phase transition in americium dioxide. *J. Phys. Soc. Jpn.* **2010**, *79*.

190. Hotta, T., Microscopic analysis of multipole susceptibility of actinide dioxides: A scenario of multipole ordering in AmO_2. *Phys. Rev. B* **2009**, *80*.

191. Teterin, Y. A.; Maslakov, K. I.; Ryzhkov, M. V.; Teterin, A. Y.; Ivanov, K. E.; Kalmykov, S. N.; Petrov, V. G., X-ray photoelectron spectra structure and chemical bonding in AmO_2. *Nucl. Technol. Radiat. Prot.* **2015**, *30*, 83-98.

192. Uchida, T.; Arima, T.; Idemitsu, K.; Inagaki, Y., Thermal conductivities of americium dioxide and sesquioxide by molecular dynamics simulations. *Comput. Mater. Sci.* **2009**, *45*, 229-234.

193. Teterin, Y. A.; Maslakov, K. I.; Ryzhkov, M. V.; Teterin, A. Y.; Ivanov, K. E.; Kalmykov, S. N.; Petrov, V. G., Nature of chemical bond in AmO_2. *Radiochemistry* **2015**, *57*, 565-574.

194. Noutack, M. S. T.; Geneste, G.; Jomard, G.; Freyss, M., First-principles investigation of the bulk properties of americium dioxide and sesquioxides. *Phys. Rev. Mater.* **2019**, *3*.

195. Lu, Y.; Yang, Y.; Zheng, F. W.; Wang, B. T.; Zhang, P., Electronic, mechanical, and thermodynamic properties of americium dioxide. *J. Nucl. Mater.* **2013**, *441*, 411-420.

196. Kovacs, A.; Konings, R. J. M.; Raab, J.; Gagliardi, L., A theoretical study of AmO_n and CmO_n (n=1, 2). *Phys. Chem. Chem. Phys.* **2008**, *10*, 1114-1117.

197. Noé, M.; Fuger, J., Self-radiation effects on the lattice parameter of $^{244}CmO_2$. *Inorg. Nucl. Chem. Lett.* **1971**, *7*, 421-430.

198. Asprey, L. B.; Ellinger, F. H.; Fried, S.; Zachariasen, W. H., Evidence for quadrivalent curium - X-ray data on curium oxides. *JACS* **1955**, *77*, 1707-1708.

199. Morss, L.; Richardson Jr, J.; Williams, C.; Lander, G.; Lawson, A.; Edelstein, N.; Shalimoff, G., Powder neutron diffraction and magnetic susceptibility of $^{248}CmO_2$. *J. Less Common Met.* **1989**, *156*, 273-289.

200. Gubanov, V. A.; Chirkov, A. K., Electronic-structure and ESCA spectra of curium dioxide. *Inorg. Nucl. Chem. Lett.* **1978**, *14*, 139-142.

201. Niikura, F.; Hotta, T., Magnetic behavior of curium dioxide with a nonmagnetic ground state. *Phys. Rev. B* **2011**, *83*.

202. Huang, L.; Chen, R. F.; Lu, H. Y., Reexaming the ground state and magnetic properties of curium dioxide. *Phys. Rev. B* **2020**, *102*.

203. Bober, M.; Sari, C.; Schumacher, G., Redistribution of uranium and plutonium during evaporation processe in mixed oxide fuel. *J. Nucl. Mater.* **1971**, *40*, 341-+.

204. Bober, M.; Sari, C.; Schumacher, G., Redistribution of plutonium and uranium in mIixed (U, Pu) oxide fuel materials in a thernal gradient. *J. Nucl. Mater.* **1971**, *39*, 265-+.

205. Parrish, R.; Aitkaliyeva, A., A review of microstructural features in fast reactor mixed oxide fuels. *J. Nucl. Mater.* **2018**, *510*, 644-660.

206. Vauchy, R.; Robisson, A. C.; Audubert, F.; Hodaj, F., Ceramic processing of uranium-plutonium mixed oxide fuels $(U_{1-y}Pu_y)O_2$ with high plutonium content. *Ceram. Int.* **2014**, *40*, 10991-10999.

207. Kandan, R.; Babu, R.; Nagarajan, K.; Rao, P. R. V., Calorimetric measurements on plutonium rich $(U,Pu)O_2$ solid solutions. *Thermochim. Acta* **2008**, *472*, 46-49.

208. Kandan, R.; Babu, R.; Nagarajan, K.; Rao, P. R. V., Calorimetric measurements on uranium-plutonium mixed oxides. *J. Nucl. Mater.* **2004**, *324*, 215-219.

209. Kameyama, T.; Sasahara, A.; Matsumura, T., Analyses of burnup at plutonium spots in uranium-plutonium mixed oxide fuels in light water reactors by neutron transport and burnup calculations. *J. Nucl. Sci. Technol.* **1997**, *34*, 551-558.

210. Fujino, T.; Yamashita, T.; Ohuchi, K.; Naito, K.; Tsuji, T., High-temperature electrical-conductivity and conduction mechanism of $(U, Pu)O_{2+/-X}$ at low-oxygen partial pressures. *J. Nucl. Mater.* **1993**, *202*, 154-162.

211. De Bruycker, F.; Boboridis, K.; Konings, R. J. M.; Rini, M.; Eloirdi, R.; Gueneau, C.; Dupin, N.; Manara, D., On the melting behaviour of uranium/plutonium mixed dioxides with high-Pu content: A laser heating study. *J. Nucl. Mater.* **2011**, *419*, 186-193.

212. Lee, C. G.; Suzuki, D.; Saito-Kokubu, Y.; Esaka, F.; Magara, M.; Kimura, T., Simultaneous determination of plutonium and uranium isotope ratios in individual plutonium-uranium mixed particles by thermal ionization mass spectrometry. *Int. J. Mass Spectrom.* **2012**, *314*, 57-62.

213. Esaka, F.; Suzuki, D.; Miyamoto, Y.; Magara, M., Determination of plutonium isotope ratios in individual uranium-plutonium mixed particles with inductively coupled plasma mass spectrometry. *J. Radioanal. Nucl. Chem.* **2015**, *306*, 393-399.

214. Esaka, F.; Yasuda, K.; Suzuki, D.; Miyamoto, Y.; Magara, M., Analysis of plutonium isotope ratios including Pu-238/Pu-239 in individual U-Pu mixed oxide particles by means of a combination of alpha spectrometry and ICP-MS. *Talanta* **2017**, *165*, 122-127.

215. Willingham, D.; Groopman, E.; Sangely, L., U-Pu mixed oxide particle analysis by NAUTILUS and implications for next-generation verification challenges. *JASMS* **2020**, *31*, 1647-1655.

216. Viswanathan, R., Fuel clad chemical interactions in fast reactor MOX fuels. *J. Nucl. Mater.* **2014**, *444*, 101-111.

217. Verma, R.; Mahajan, V. K., Interaction between uranium-pluronium mixed-oxide and zircaloy-2. *J. Nucl. Mater.* **1979**, *79*, 252-254.

218. Inoue, M., Thermal conductivity of uranium-plutonium oxide fuel for fast reactors. *J. Nucl. Mater.* **2000**, *282*, 186-195.

219. Matsumoto, T.; Arima, T.; Inagaki, Y.; Idemitsu, K.; Kato, M.; Uchida, T., Investigation of O/M ratio effect on thermal conductivity of oxide nuclear fuels by non-equilibrium molecular dynamics calculation. *J. Nucl. Mater.* **2013**, *440*, 580-585.

220. Katsuyama, K.; Ishimi, A.; Maeda, K.; Nagamine, T.; Asaga, T., Helium release from the uranium-plutonium mixed oxide (MOX) fuel irradiated to high burn-up in a fast breeder reactor (FBR). *J. Nucl. Mater.* **2010**, *401*, 86-90.

221. Teske, K.; Nebelung, C.; Kapshukov, II; Sudakov, L. V.; Bevz, A. S., Determination of the oxygen coefficient for hyperstoichiometric uranium plutonium mixed-oxide by a solid-electrolyte-based coulometric technique. *J. Nucl. Mater.* **1989**, *168*, 97-100.

222. Hiyama, T., Determination of oxygen-to-metal atomic ratio in mixed oxide fuel by non-dispersive infrared spectrophotometry after fusion in an inert gas atmosphere. *Anal. Chim. Acta.* **1999**, *402*, 297-302.

223. Vauchy, R.; Robisson, A. C.; Belin, R. C.; Martin, P. M.; Scheinost, A. C.; Hodaj, F., Room-temperature oxidation of hypostoichiometric uranium plutonium mixed oxides $U_{1-y}Pu_yO_{2-x}$ - A depth-selective approach. *J. Nucl. Mater.* **2015**, *465*, 349-357.

224. Strach, M.; Belin, R. C.; Richaud, J. C.; Rogez, J., High temperature X-ray diffraction study of the oxidation products and kinetics of uranium-plutonium mixed oxides. *Inorg. Chem.* **2014**, *53*, 12757-12766.

225. Sampath, S.; Hadap, R. G.; Swamy, R. K.; Chackraburtty, D. M., Studies on kinetics of oxidation of uranium-plutonium mixed oxides under controlled oxygen potential. *Thermochim. Acta* **1979**, *32*, 326-330.

226. Jegou, C.; Gennisson, M.; Peuget, S.; Desgranges, L.; Guimbretiere, G.; Magnin, M.; Talip, Z.; Simon, P., Raman micro-spectroscopy of UOX and MOX spent nuclear fuel characterization and oxidation resistance of the high burn-up structure. *J. Nucl. Mater.* **2015**, *458*, 343-349.

227. Jegou, C.; Caraballo, R.; Peuget, S.; Roudil, D.; Desgranges, L.; Magnin, M., Raman spectroscopy characterization of actinide oxides $(U_{1-y}Pu_y)O_2$ Resistance to oxidation by the laser beam and examination of defects. *J. Nucl. Mater.* **2010**, *405*, 235-243.

228. Strach, M.; Belin, R. C.; Richaud, J.-C.; Rogez, J., Influence of phase separation on the oxidation of $(U,Pu)O_{2-x}$. *J. Phys. Chem. C* **2015**, *119*, 23159-23167.

229. Vigier, J. F.; Martin, P. M.; Martel, L.; Prieur, D.; Scheinost, A. C.; Somers, J., Structural investigation of $(U_{0.7}Pu_{0.3})O_{2-x}$ mixed oxides. *Inorg. Chem.* **2015**, *54*, 5358-5365.

230. Talip, Z.; Peuget, S.; Magnin, M.; Tribet, M.; Valot, C.; Vauchy, R.; Jegou, C., Characterization of un-irradiated MIMAS MOX fuel by Raman spectroscopy and EPMA. *J. Nucl. Mater.* **2018**, *499*, 88-97.

231. Talip, Z.; Peuget, S.; Magnin, M.; Berardo, L.; Valot, C.; Vauchy, R.; Jegou, C., Raman microspectroscopic studies of unirradiated homogeneous $(U_{0.76}Pu_{0.24})O_{2+x}$: the effects of Pu

content, non-stoichiometry, self-radiation damage and secondary phases. *J. Raman Spectrosc.* **2017**, *48*, 765-772.

232. Martin, P.; Grandjean, S.; Valot, C.; Carlot, G.; Ripert, M.; Blanc, P.; Hennig, C., XAS study of $(U_{1-y}Pu_y)O_2$ solid solutions. *J. Alloys Compd.* **2007**, *444-445*, 410-414.

233. Sari, C.; Benedict, U.; Blank, H., A study of the ternary system $U0_2$-$Pu0_2$-Pu_20_3. *J. Nucl. Mater.* **1970**, *35*, 267-277.

234. Sali, S. K.; Kulkarni, N. K.; Phatak, R.; Agarwal, R., Oxidation behaviour of plutonium rich (U, Pu)C and (U, Pu)O_2. *J. Nucl. Mater.* **2016**, *479*, 623-632.

235. Terentyev, D., Molecular dynamics study of oxygen transport and thermal properties of mixed oxide fuels. *Comput. Mater. Sci.* **2007**, *40*, 319-326.

236. Takoukam-Takoundjou, C.; Bourasseau, E.; Lachet, V., Study of thermodynamic properties of $U_{1-y}Pu_yO_2$ MOX fuel using classical molecular Monte Carlo simulations. *J. Nucl. Mater.* **2020**, *534*.

237. Potashnikov, S. I.; Boyarchenkov, A. S.; Nekrasov, K. A.; Kupryazhkin, A. Y., High-precision molecular dynamics simulation of UO_2-PuO_2: Pair potentials comparison in UO_2. *J. Nucl. Mater.* **2011**, *419*, 217-225.

238. Parfitt, D. C.; Cooper, M. W. D.; Rushton, M. J. D.; Christopoulos, S. R. G.; Fitzpatricka, M. E.; Chroneos, A., Thermodynamic calculations of oxygen self-diffusion in mixed-oxide nuclear fuels. *RSC Adv.* **2016**, *6*, 74018-74027.

239. Ma, J. J.; Zheng, J. J.; Wan, M. J.; Duc, J. G.; Yang, J. W.; Jiang, G., Molecular dynamical study of physical properties of $(U_{0.75}Pu_{0.25})O_{2-x}$. *J. Nucl. Mater.* **2014**, *452*, 230-234.

240. Cooper, M. W. D.; Stanek, C. K.; Liu, X. Y.; Andersson, D. A., A comment on the thermal conductivity of (U,Pu)O_2 and (U,Th)O_2 by molecular dynamics with adjustment for phonon-spin scattering. *MRS Adv.* **2016**, *1*, 2483-2487.

241. Arima, T.; Yamasaki, S.; Inagaki, Y.; Idemitsu, K., Evaluation of thermal conductivity of hypostoichiometric (U, Pu)O_{2-x} solid solution by molecular dynamics simulation at temperatures up to 2000 K. *J. Alloys Compd.* **2006**, *415*, 43-50.

242. Gryaznov, D.; Rashkeev, S.; Kotomin, E. A.; Heifets, E.; Zhukovskii, Y., Helium behavior in oxide nuclear fuels: First principles modeling. *Nucl. Instrum. Methods Phys. Res., B* **2010**, *268*, 3090-3094.

243. Dorado, B.; Garcia, P., First-principles DFT plus U modeling of actinide-based alloys: Application to paramagnetic phases of UO_2 and (U,Pu) mixed oxides. *Phys. Rev. B* **2013**, *87*.

244. Yang, Y.; Wang, B. T.; Zhang, P., Electronic and mechanical properties of ordered (Pu, U)O_2 compounds: A density functional theory plus U study. *J. Nucl. Mater.* **2013**, *433*, 345-350.

245. Njifon, I. C.; Bertolus, M.; Hayn, R.; Freyss, M., Electronic structure investigation of the bulk properties of uranium-plutonium mixed oxides (U, Pu)O_2. *Inorg. Chem.* **2018**, *57*, 10974-10983.

246. Ma, L.; Ray, A. K., An ab initio study of $PuO_{2\pm0.25}$, $UO_{2\pm0.25}$, and $U_{0.5}Pu_{0.5}O_{2\pm0.25}$. *Eur. Phys. J. B.* **2011**, *81*, 103.

247. Paul, R.; Keller, C., Phasengleichgewichte in den systemen UO_2-$UO_{2.67}$-ThO_2 und UO_{2+x}-NPO_2. *J. Nucl. Mater.* **1971**, *41*, 133-142.

248. Martel, L.; Vigier, J. F.; Prieur, D.; Nourry, S.; Guiot, A.; Dardenne, K.; Boshoven, J.; Somers, J., Structural investigation of uranium-neptunium mixed oxides using XRD, XANES, and O-17 MAS NMR. *J. Phys. Chem. C* **2014**, *118*, 27640-27647.

249. Chollet, M.; Martin, P.; Degueldre, C.; Poonoosamy, J.; Belin, R. C.; Hennig, C., Neptunium characterization in uranium dioxide fuel: Combining a XAFS and a thermodynamic approach. *J. Alloys Compd.* **2016**, *662*, 448-454.

250. Martel, L.; Hen, A.; Tokunaga, Y.; Kinnart, F.; Magnani, N.; Colineau, E.; Griveau, J. C.; Caciuffo, R., Magnetization, specific heat, O-17 NMR, and N-237(P) Mossbauer study of $U_{0.15}Np_{0.85}O_2$. *Phys. Rev. B* **2018**, *98*.

251. Ghosh, P. S.; Arya, A.; Kuganathan, N.; Grimes, R. W., Thermal and diffusional properties of (Th,Np)O_2 and (U,Np)O_2 mixed oxides. *J. Nucl. Mater.* **2019**, *521*, 89-98.

252. Ghosh, P. S.; Kuganathan, N.; Arya, A.; Grimes, R. W., Phase stability, electronic structures and elastic properties of (U,Np)O_2 and (Th,Np)O_2 mixed oxides. *Phys. Chem. Chem. Phys.* **2018**, *20*, 18707-18717.

253. Chollet, M.; Prieur, D.; Bohler, R.; Belin, R.; Manara, D., The melting behaviour of uranium/neptunium mixed oxides. *J. Chem. Thermodyn.* **2015**, *89*, 27-34.

254. Bartscher, W., Detemination of the oxygen-metal-ratio of uranium-americium mixed oxides. *Fresenius Z. Anal. Chem.* **1982**, *310*, 413-414.

255. Caisso, M.; Picart, S.; Belin, R. C.; Lebreton, F.; Martin, P. M.; Dardenne, K.; Rothe, J.; Neuville, D. R.; Delahaye, T.; Ayral, A., In situ characterization of uranium and americium oxide solid solution formation for CRMP process: First combination of in situ XRD and XANES measurements. *Dalton Trans.* **2015**, *44*, 6391-6399.

256. Caisso, M.; Roussel, P.; Den Auwer, C.; Picart, S.; Hennig, C.; Scheinost, A. C.; Delahaye, T.; Ayral, A., Evidence of Trivalent Am substitution into U_3O_8. *Inorg. Chem.* **2016**, *55*, 10438-10444.

257. Epifano, E.; Vauchy, R.; Lebreton, E.; Lauwerier, R.; Joly, A.; Scheinost, A.; Gueneau, B. C.; Valot, C.; Martin, P. M., On the O-rich domain of the U-Am-O phase diagram. *J. Nucl. Mater.* **2020**, *531*.

258. Horlait, D.; Lebreton, F.; Roussel, P.; Delahaye, T., XRD monitoring of a self-irradiation in uranium-americium mixed oxides. *Inorg. Chem.* **2013**, *52*, 14196-14204.

259. Lebreton, F.; Belin, R. C.; Prieur, D.; Delahaye, T.; Blanchart, P., In situ study of the solid-state formation of $U_{1-x}Am_xO_{2 +/-delta}$ solid solution. *Inorg. Chem.* **2012**, *51*, 9369-9375.

260. Lebreton, F.; Horlait, D.; Caraballo, R.; Martin, P. M.; Scheinost, A. C.; Rossberg, A.; Jegou, C.; Delahaye, T., Peculiar behavior of $(U,Am)O_{2-delta}$ compounds for high americium contents evidenced by XRD, XAS, and Raman spectroscopy. *Inorg. Chem.* **2015**, *54*, 9749-9760.

261. Lebreton, F.; Horlait, D.; Delahaye, T.; Blanchart, P., Fabrication and characterization of $U_{1-x}Am_xO_{2+delta}$ compounds with high americium contents (x=0.3, 0.4 and 0.5). *J. Nucl. Mater.* **2013**, *439*, 99-102.

262. Lebreton, F.; Martin, P. M.; Horlait, D.; Bes, R.; Scheinost, A. C.; Rossberg, A.; Delahaye, T.; Blanchart, P., New insight into self-irradiation effects on local and long-range structure of uranium-americium mixed oxides (through XAS and XRD). *Inorg. Chem.* **2014**, *53*, 9531-9540.

263. Nishi, T.; Nakada, M.; Hirata, M., Lattice parameter functions of $(Am_yU_{1-y})O_{2-x}$ based on XRD and XANES measurements. *J. Solid State Chem.* **2017**, *256*, 252-255.

264. Prieur, D.; Lebreton, F.; Martin, P. M.; Caisso, M.; Butzbach, R.; Somers, J.; Delahaye, T., Comparative XRPD and XAS study of the impact of the synthesis process on the electronic and structural environments of uranium-americium mixed oxides. *J. Solid State Chem.* **2015**, *230*, 8-13.

265. Prieur, D.; Martin, P. M.; Jankowiak, A.; Gavilan, E.; Scheinost, A. C.; Herlet, N.; Dehaudt, P.; Blanchart, P., Local structure and charge distribution in mixed uranium-americium oxides: Effects of oxygen potential and Am content. *Inorg. Chem.* **2011**, *50*, 12437-12445.

266. Prieur, D.; Martin, P. M.; Lebreton, F.; Delahaye, T.; Jankowiak, A.; Laval, J. P.; Scheinost, A. C.; Dehaudt, P.; Blanchart, P., Alpha self-irradiation effect on the local structure of the $U_{0.85}Am_{0.15}O_{2 +/- x}$ solid solution. *J. Solid State Chem.* **2012**, *194*, 206-211.

267. Ramond, L.; Horlait, D.; Delahaye, T.; Jouan, G.; Gauthe, A.; Arab-Chapelet, B.; Picart, S., Dilatometric study of a co-converted $(U,Am)O_2$ powder. *J. Eur. Ceram. Soc.* **2016**, *36*, 1775-1782.

268. Remy, E.; Picart, S.; Delahaye, T.; Jobelin, I.; Lebreton, F.; Horlait, D.; Bisel, I.; Blanchart, P.; Ayral, A., Fabrication of uranium-americium mixed oxide pellet from microsphere precursors: Application of CRMP process. *J. Nucl. Mater.* **2014**, *453*, 214-219.

269. Koyama, S.; Otsuka, Y.; Osaka, M.; Morozumi, K.; Konno, K.; Kajitani, M.; Mitsugashira, T., Analysis of minor actinides in mixed oxide fuel irradiated in fast reactor, (I) - Determination of neptunium-237. *J. Nucl. Sci. Technol.* **1998**, *35*, 406-410.

270. Sus, F.; Parus, J. L.; Raab, W., Determination of neptunium in plutonium and mixed uranium-plutonium samples by isotope dilution gamma-spectrometry with Am-243 as a spike. *J. Radioanal. Nucl. Chem.-Articles* **1996**, *211*, 363-374.

271. Ng, S.; Greneche, D.; Guesdon, B.; Vinoche, R.; Delpech, M.; Dolci, F.; Golfier, H.; Poinot-Salanon, C., Neptunium in the fuel cycle: Nonproliferation benefits versus industrial drawbacks. *Nucl. Technol.* **2008**, *164*, 13-19.

272. Morimoto, K.; Kato, M.; Ogasawara, M.; Kashimura, M., Thermal conductivity of (U,Pu,Np)O_2 solid solutions. *J. Nucl. Mater.* **2009**, *389*, 179-185.

273. Prieur, D.; Belin, R.; Manara, D.; Staicu, D.; Richaud, J.-C.; Vigier, J.-F.; Scheinost, A.; Somers, J.; Martin, P., Linear thermal expansion, thermal diffusivity and melting temperature of Am-MOX and Np-MOX. *J. Alloys Compd.* **2015**, *637*, 326-331.

274. Kato, M.; Maeda, K.; Ozawa, T.; Kashimura, M.; Kihara, Y., Physical properties and irradiation behavior analysis of Np-and Am-bearing MOX fuels. *J. Nucl. Sci. Technol.* **2011**, *48*, 646-653.

275. Kurosaki, K.; Adachi, J.; Katayama, M.; Osaka, M.; Tanaka, K.; Uno, M.; Yamanaka, S., Molecular dynamics studies of americium-containing mixed oxide fuels. *J. Nucl. Sci. Technol.* **2006**, *43*, 1224-1227.

276. Morimoto, K.; Kato, M.; Ogasawara, M.; Kashimura, M., Thermal conductivities of hypostoichiometric (U, Pu, Am)O_{2-x} oxide. *J. Nucl. Mater.* **2008**, *374*, 378-385.

277. Hirooka, S.; Matsumoto, T.; Kato, M.; Sunaoshi, T.; Uno, H.; Yamada, T., Oxygen potential measurement of (U, Pu, Am)$O_{2\pm x}$ and (U, Pu, Am, Np)$O_{2\pm x}$. *J. Nucl. Mater.* **2020**, *542*, 152424.

278. Degueldre, C.; Cozzo, C.; Martin, M.; Grolimund, D.; Mieszczynski, C., Americium characterization by X-ray fluorescence and absorption spectroscopy in plutonium uranium mixed oxide. *J. Solid State Chem.* **2013**, *202*, 315-319.

279. Vauchy, R.; Robisson, A. C.; Martin, P. M.; Belin, R. C.; Aufore, L.; Scheinost, A. C.; Hodaj, F., Impact of the cation distribution homogeneity on the americium oxidation state in the $U_{0.54}Pu_{0.45}Am_{0.01}O_{2-x}$ mixed oxide. *J. Nucl. Mater.* **2015**, *456*, 115-119.

280. Vauchy, R.; Belin, R. C.; Robisson, A. C.; Lebreton, F.; Aufore, L.; Scheinost, A. C.; Martin, P. M., Actinide oxidation state and O/M ratio in hypostoichiometric uranium-plutonium-americium $U_{0.750}Pu_{0.246}Am_{0.004}O_{2-x}$ mixed oxides. *Inorg. Chem.* **2016**, *55*, 2123-2132.

281. Maeda, K.; Katsuyama, K.; Ikusawa, Y.; Maeda, S., Short-term irradiation behavior of low-density americium-doped uranium-plutonium mixed oxide fuels irradiated in a fast reactor. *J. Nucl. Mater.* **2011**, *416*, 158-165.

282. Artisyuk, V.; Chmelev, A.; Saito, M.; Suzuki, M.; Fujii-E, Y., Cm-244 transmutation in accelerator-driven system. *J. Nucl. Sci. Technol.* **1999**, *36*, 1135-1140.

283. Degueldre, C.; Borca, C.; Cozzo, C., Curium analysis in plutonium uranium mixed oxide by X-ray fluorescence and absorption fine structure spectroscopy. *Talanta* **2013**, *115*, 986-991.

284. Osaka, M.; Koyama, S.; Mitsugashira, T., Analysis of curium in mixed oxide fuel irradiated in the experimental fast reactor JOYO for the evaluation of its transmutation behavior. *J. Nucl. Sci. Technol.* **2004**, *41*, 907-914.

285. Osaka, M.; Koyama, S.; Morozumi, K.; Namekawa, T.; Mitsugashira, T., Analysis of curium isotopes in mixed oxide fuel irradiated in fast reactor. *J. Nucl. Sci. Technol.* **2001**, *38*, 912-914.

286. Dias, R. M. A.; Chackrab.Dm, Evaluation of crystallinity and surface area measurements of plutonium dioxide samples. *J. Appl. Crystallogr.* **1971**, *4*, 74-&.

287. Noe, M.; Fuger, J., Self-radiation effects on the lattice parameter of $^{238}PuO_2$. *Inorg. Nucl. Chem. Lett.* **1974**, *10*, 7-19.

288. Teterin, Y. A.; Maslakov, K. I.; Teterin, A. Y.; Ivanov, K. E.; Ryzhkov, M. V.; Petrov, V. G.; Enina, D. A.; Kalmykov, S. N., Electronic structure and chemical bonding in PuO_2. *Phys. Rev. B* **2013**, *87*.

289. Kern, S.; Loong, C.-K.; Goodman, G.; Cort, B.; Lander, G., Crystal-field spectroscopy of PuO_2: Further complications in actinide dioxides. *J. Phys. Condens. Matter.* **1990**, *2*, 1933.

290. Raphael, G.; Lallement, R., Susceptibilite magnetique de PuO_2. *Solid State Commun.* **1968**, *6*, 383-385.

291. Tokunaga, Y.; Sakai, H.; Fujimoto, T.; Kambe, S.; Walstedt, R.; Ikushima, K.; Yasuoka, H.; Aoki, D.; Homma, Y.; Haga, Y., NMR studies of actinide dioxides. *J. Alloys Compd.* **2007**, *444*, 241-245.

292. Wen, X.-D.; Martin, R. L.; Scuseria, G. E.; Rudin, S. P.; Batista, E. R., A screened hybrid dft study of actinide oxides, nitrides, and carbides. *J. Phys. Chem. C* **2013**, *117*, 13122-13128.

293. Sun, B.; Liu, H.; Song, H.; Zhang, G.; Zheng, H.; Zhao, X.; Zhang, P., First-principles study of surface properties of PuO_2: Effects of thickness and O-vacancy on surface stability and chemical activity. *J. Nucl. Mater.* **2012**, *426*, 139-147.

294. Prodan, I. D.; Scuseria, G. E.; Martin, R. L., Covalency in the actinide dioxides: Systematic study of the electronic properties using screened hybrid density functional theory. *Physical Review B* **2007**, *76*, 033101.

295. Pegg, J. T.; Shields, A. E.; Storr, M. T.; Wills, A. S.; Scanlon, D. O.; de Leeuw, N. H., Hidden magnetic order in plutonium dioxide nuclear fuel. *Phys. Chem. Chem. Phys.* **2018**, *20*, 20943-20951.

296. Jomard, G.; Bottin, F., Thermodynamic stability of PuO_2 surfaces: Influence of electronic correlations. *Phys. Rev. B* **2011**, *84*, 195469.

297. Gryaznov, D.; Heifets, E.; Sedmidubsky, D., Density functional theory calculations on magnetic properties of actinide compounds. *Phys. Chem. Chem. Phys.* **2010**, *12*, 12273-12278.

298. Wan, M. J.; Zhang, L.; Du, J. G.; Huang, D. H.; Wang, L. L.; Jiang, G., The MD simulation of thermal properties of plutonium dioxide. *Physica B Condens. Matter* **2012**, *407*, 4595-4599.

299. Sandenaw, T. A., Heat capacity of plutonium dioxide below 325 K. *J. Nucl. Mater.* **1963**, *10*, 165-172.

300. Nakamura, H.; Machida, M., First-principles calculation study on phonon thermal conductivity of thorium and plutonium dioxides: Intrinsic anharmonic phonon-phonon and extrinsic grain-boundary-phonon scattering effects. *J. Nucl. Mater.* **2019**, *519*, 45-51.

301. Kruger, O. L.; Savage, H., Heat capacity and thermodynamic properties of plutonium dioxide. *J. Chem. Phys.* **1968**, *49*, 4540-&.

302. Kato, M.; Uchida, T.; Matsumoto, T.; Sunaoshi, T.; Nakamura, H.; Machida, M., Thermal expansion measurement and heat capacity evaluation of hypo-stoichiometric $PuO_{2.00}$. *J. Nucl. Mater.* **2014**, *451*, 78-81.

303. Gunay, S. D.; Akgenc, B.; Tasseven, C., Modeling superionic behavior of plutonium dioxide. *High Temp. Mater. Process.* **2016**, *35*, 999-1004.

304. Gueneau, C.; Chatillon, C.; Sundman, B., Thermodynamic modelling of the plutonium-oxygen system. *J. Nucl. Mater.* **2008**, *378*, 257-272.

305. Golovnin, I. S., Properties of plutonium dioxide as nuclear fuel. *At. Energy* **2000**, *89*, 627-637.

306. De Bruycker, F.; Boboridis, K.; Poml, P.; Eloirdi, R.; Konings, R. J. M.; Manara, D., The melting behaviour of plutonium dioxide: A laser-heating study. *J. Nucl. Mater.* **2011**, *416*, 166-172.

307. Chu, M. F.; Meng, D. Q.; Xiao, S.; Wang, W.; Chen, Q. Y., Evaluation of thermal properties of PuO_2 and alpha-Pu_2O_3 by atomic simulation. *J. Alloys Compd.* **2012**, *539*, 7-11.

308. Chernikov, A. S.; Permyakov, L. N.; Kurbakov, S. D.; Cherkasov, A. S.; Degal'tsev, Y. G.; Lyshov, L. L.; Makarov, V. M., HTGR nuclear fuel based on plutonium oxide microspheres. *At. Energy* **2000**, *88*, 30-34.

309. Bielenberg, P. A.; Prenger, F. C.; Veirs, D. K.; Jones, G. F., Effects of pressure on thermal transport in plutonium oxide powder. *Int. J. Heat Mass Transf.* **2006**, *49*, 3229-3239.

310. Ackermann, R. J.; Faircloth, R. L.; Rand, M. H., A thermodynamic study of the vaporization behavior of the substoichiometric plutonium dioxide phase. *J. Phys. Chem.* **1966**, *70*, 3698-+.

311. Wang, L. F.; Sun, B.; Liu, H. F.; Lin, D. Y.; Song, H. F., Thermodynamics and kinetics of intrinsic point defects in plutonium dioxides. *J. Nucl. Mater.* **2019**, *526*.

312. Tang, J.; Qiu, R. Z.; Chen, J. F.; Ao, B. Y., Diffusion behavior of hydrogen in oxygen saturated and unsaturated plutonium dioxide: An ab initio molecular dynamics study. *J. Alloys Compd.* **2020**, *834*.

313. Seitov, D. D.; Nekrasov, K. A.; Kupryazhkin, A. Y.; Gupta, S. K.; Usseinov, A. B., The impact of the collision cascades on the xenon and helium clusters in PuO_2 crystals. A molecular dynamics simulation. *Nucl. Instrum. Methods Phys. Res., B* **2020**, *476*, 26-31.

314. Ronchi, C.; Hiernaut, J. P., Helium diffusion in uranium and plutonium oxides. *J. Nucl. Mater.* **2004**, *325*, 1-12.

315. Haschke, J. M.; Allen, T. H.; Morales, L. A., Reactions of plutonium dioxide with water and hydrogen-oxygen mixtures: Mechanisms for corrosion of uranium and plutonium. *J. Alloys Compd.* **2001**, *314*, 78-91.

316. Gouder, T.; Seibert, A.; Havela, L.; Rebizant, J., Search for higher oxides of Pu: A photoemission study. *Surf. Sci.* **2007**, *601*, L77-L80.

317. Stakebake, J. L., Low temperature adsorption of oxygen on plutonium dioxide. *J. Nucl. Mater.* **1967**, *23*, 154-+.

318. Stakebake, J. L.; Dringman, M. R., Adsorption of oxygen of sintered plutonium dioxide. *J. Nucl. Mater.* **1967**, *23*, 349-+.

319. Stakebake, J. L., A thermal desorption study of the surface interactions between water and plutonium dioxide. *J. Phys. Chem.* **1973**, *77*, 581-586.

320. Stakebake, J. L.; Steward, L. M., Water vapor adsorption on plutonium dioxide. *J. Colloid Interface Sci.* **1973**, *42*, 328-333.

321. Haschke, J. M.; Ricketts, T. E., Adsorption of water on plutonium dioxide. *J. Alloys Compd.* **1997**, *252*, 148-156.

322. Petit, L.; Svane, A.; Szotek, Z.; Temmerman, W. M., First-principles calculations of $PuO_{2\,+/-\,x}$. *Science* **2003**, *301*, 498-501.

323. Prodan, I. D.; Scuseria, G. E.; Sordo, J. A.; Kudin, K. N.; Martin, R. L., Lattice defects and magnetic ordering in plutonium oxides: A hybrid density-functional-theory study of strongly correlated materials. *J. Chem. Phys.* **2005**, *123*.

324. Konashi, K.; Matsui, H.; Kawazoe, Y.; Kato, M.; Minamoto, S., Defect structure of nonstoichiometric plutonium oxide. *J. Phys. Soc. Japan* **2006**, *75*, 143-145.

325. Zhang, P.; Wang, B. T.; Zhao, X. G., Ground-state properties and high-pressure behavior of plutonium dioxide: Density functional theory calculations. *Phys. Rev. B* **2010**, *82*.

326. Sun, B.; Liu, H. F.; Song, H. F.; Zhang, G. C.; Zheng, H.; Zhao, X. G.; Zhang, P., The environmental dependence of redox energetics of PuO_2 and alpha-Pu_2O_3: A quantitative solution from DFT+U. *Phys. Lett. A* **2012**, *376*, 2672-2676.

327. Yang, Y.; Lu, Y.; Zhang, P., Optical properties of PuO_2 and alpha-Pu_2O_3 by GGA + U plus QA studies. *J. Nucl. Mater.* **2014**, *452*, 414-418.

328. Lu, Y.; Yang, Y.; Zhang, P., Charge states of point defects in plutonium oxide: A first-principles study. *J. Alloys Compd.* **2015**, *649*, 544-552.

329. Nakamura, H.; Machida, M.; Kato, M., First-principles calculation of phonon and schottky heat capacities of plutonium dioxide. *J. Phys. Soc. Japan* **2015**, *84*.

330. Chen, J.; Meng, D. Q.; Chen, Q. Y.; Luo, W. H., Electronic structure and optical properties of plutonium dioxide from first-principles calculations. *Rare Met.* **2016**, *35*, 643-648.

331. Wu, X.; Ray, A. K., A density functional study of plutonium dioxide. *Eur. Phys. J. B.* **2001**, *19*, 345-351.

332. Korzhavyi, P. A.; Vitos, L.; Andersson, D. A.; Johansson, B., Oxidation of plutonium dioxide. *Nat. Mater.* **2004**, *3*, 225-228.

333. Ao, B. Y.; Qiu, R. Z.; Lu, H. Y.; Ye, X. Q.; Shi, P.; Chen, P. H.; Wang, X. L., New insights into the formation of hyperstoichiometric plutonium oxides. *J. Phys. Chem. C* **2015**, *119*, 101-108.

334. Moten, S. A.; Atta-Fynn, R.; Ray, A. K.; Huda, M. N., Size effects on the electronic and magnetic properties of PuO_2 (111) surface. *J. Nucl. Mater.* **2016**, *468*, 37-45.

335. Wu, X. Y.; Ray, A. K., Density-functional study of water adsorption on the PuO_2 (110) surface. *Phys. Rev. B* **2002**, *65*.

336. Jomard, G.; Bottin, F.; Geneste, G., Water adsorption and dissociation on the PuO_2 (110) surface. *J. Nucl. Mater.* **2014**, *451*, 28-34.

337. Zhang, C.; Yang, Y.; Zhang, P., Dissociation mechanism of water molecules on the PuO_2(110) surface: An ab initio molecular dynamics study. *J. Phys. Chem. C* **2018**, *122*, 371-376.

338. Webb, K., et al., Thermal processing of chloride-contaminated plutonium dioxide. *ACS Omega* **2019**, *4*, 12524-12536.

339. Sims, H. E.; Webb, K. J.; Brown, J.; Morris, D.; Taylor, R. J., Hydrogen yields from water on the surface of plutonium dioxide. *J. Nucl. Mater.* **2013**, *437*, 359-364.

340. Meng, D. Q.; Luo, W. H.; Li, G.; Chen, H. C., Density functional study of CO_2 adsorption on Pu(100) surface. *Acta. Phys. Sin.* **2009**, *58*, 8224-8229.

341. Collard, J.; Steele, H.; Kaltsoyannis, N., Computational study of HCl adsorption on stoichiometric and oxygen vacancy PuO_2 {111}, {110} and {100} surfaces. *J. Nucl. Mater.* **2020**, *530*.

342. Zhang, L.; Sun, B.; Zhang, Q. L.; Liu, H. F.; Liu, K. Z.; Song, H. F., Polaron modulation mechanism of H_2O and CO_2 adsorption on PuO_2(111) surface. *Appl. Surf. Sci.* **2020**, *516*.

343. Brown, J., et al., Americium and plutonium purification by extraction (the AMPPEX process): Development of a new method to separate Am-241 from aged plutonium dioxide for use in space power systems. *Prog. Nucl. Energy* **2018**, *106*, 396-416.

344. Cota-Sanchez, G.; Leeder, K.; Bureau, D.; Watson, M.; MacCready, C.; Turgeon, D.; Woods, D., Separation of americium from aged plutonium dioxide. *CNL Nucl. Rev.* **2018**, *7*, 165-175.

345. Miwa, S.; Osaka, M.; Yoshimochi, H.; Tanaka, K.; Kurosaki, K.; Uno, M.; Yamanaka, S., Phase behavior of PuO_{2-x} with addition of 9% Am. *J. Alloys Compd.* **2007**, *444*, 610-613.

346. Jankowiak, A.; Maillard, C.; Donnet, L., Structural study of $Pu_{1-x}Am_xO_2$ (x=0.2; 0.5; 0.8) obtained by oxalate co-conversion. *J. Nucl. Mater.* **2009**, *393*, 87-91.

347. Vauchy, R.; Joly, A.; Valot, C., Lattice thermal expansion of $Pu_{1-y}Am_yO_{2-x}$ plutonium-americium mixed oxides. *J. Appl. Crystallogr.* **2017**, *50*, 1782-1790.

348. Ellinger, F. H.; Johnson, K. A.; Struebing, V. O., The plutonium-americium system. *J. Nucl. Mater.* **1966**, *20*, 83-86.

349. Jankowiak, A.; Jorion, F.; Maillard, C.; Donnet, L., Preparation and characterization of $Pu_{0.5}Am_{0.5}O_{2-x}$-MgO ceramic/ceramic composites. *Nucl. Sci. Eng.* **2008**, *160*, 378-384.

350. Belin, R. C.; Martin, P. M.; Lechelle, J.; Reynaud, M.; Scheinost, A. C., Role of cation interactions in the reduction pProcess in plutonium-americium mixed oxides. *Inorg. Chem.* **2013**, *52*, 2966-2972.

351. Prieur, D.; Carvajal-Nunez, U.; Vitova, T.; Somers, J., Local and electronic structure of americium-bearing PuO_2. *Eur. J. Inorg. Chem.* **2013**, 1518-1524.

352. Tokunaga, Y.; Osaka, M.; Kambe, S.; Miwa, S.; Sakai, H.; Chudo, H.; Homma, Y.; Shiokawa, Y., O-17 NMR study in $(Pu_{0.91}Am_{0.09})O_2$. *J. Nucl. Mater.* **2010**, *396*, 107-111.

353. Ma, L.; Atta-Fynn, R.; Ray, A. K., Elemental and mied actinide dioxides: An ab initio study. *J. Theor. Comput. Chem.* **2012**, *11*, 611-629.

Theoretical background

Quantum chemistry is a subject that investigates and solves chemical problems with the method of quantum mechanics; the essence is to solve the Schrödinger equation. However, it is hard to get analytical solutions for multi-electron systems. Hartree-Fock (HF) and density functional theory (DFT) are well known approximate theories for solving the many-body Hamiltonian.

2.1 Hartree–Fock theory (HF)

The many-body wavefunction is given by an antisymmetrised product of single-particle orbitals in the Hartree-Fock theory.[1-4] The Schrödinger equation for a system, such as isolated atom, molecule, nanoparticle, or extended system, is given by:

$$\widehat{H}(R,r)\Psi(R,r) = E\Psi(R,r) \tag{2.1}$$

Where *R*, *r,* and *E* are the coordinates of the nucleus and electrons in the system and total energy of the system, respectively. The Hamiltonian operator $\widehat{H}(R,r)$ for a system without any external fields is given by:

$$\widehat{H}(R,r) = \widehat{T}_n + \widehat{T}_e + \widehat{V}_{n,e} + \widehat{V}_{e,e} + \widehat{V}_{n,n} \tag{2.2}$$

Where *n* and *e* represent nucleus and electrons, respectively, *T* and *V* are kinetic energy and Coulomb potential, respectively. According to the Born-Oppenheimer approximation,[5] which was proposed by Born and Oppenheimer in 1927, the total wavefunction $\Psi(R,r)$ can be described as the following:

$$\Psi(R,r) = \Phi_e(r,R) \cdot \chi_n(R) \tag{2.3}$$

Where $\Phi_e(r,R)$ is the electronic wavefunction and $\chi_n(R)$ is the nuclear wavefunction. Therefore, the total Schrödinger equation can be divided into electronic and nuclear Schrödinger equations.

$$\widehat{H}_e\Phi_e(r,R) = E_e(R)\Phi_e(r,R) \tag{2.4}$$

$$\widehat{H}_n\chi_n(R) = E\chi_n(R) \tag{2.5}$$

Where,

$$\hat{H}_e = \hat{T}_e + \hat{V}_{n,e} + \hat{V}_{e,e} + \hat{V}_{n,n} \tag{2.6}$$

$$\hat{H}_n = \hat{T}_n + E_e(R) \tag{2.7}$$

The electronic Hamiltonian operator is much more complicated than the nuclear one, containing the no-electron term, $\hat{V}_{n,n}$, the one-electron terms, $\hat{T}_e$ and $\hat{V}_{n,e}$, and the two-electron term, $\hat{V}_{e,e}$. If we ignore the two-electron term, the electronic Schrödinger equation will be a product of single-electron orbitals. In order to take the electron-electron repulsion effect (two-electron term) into the one-electron Schrödinger equation, the Fock operator was introduced:

$$\hat{F} = -\frac{1}{2}\nabla^2 - \sum_{I}^{N} \frac{Z_I}{r_{iI}} + \sum_{j}^{occ} (2\hat{J}_j - \hat{K}_j) \tag{2.8}$$

The first term is the kinetic energy of the electrons. The second term is the Coulomb potential between the electron and nuclei, the *N* and *Z* mark the total number of nuclei in the system and the charge of nuclei I, respectively. $\hat{J}_j$ and $\hat{K}_j$ are the Coulomb and exchange operators. The Fock operator acts on orbitals ϕ_i and gives the Hartree-Fock equation:

$$\hat{F}\phi_i = \epsilon_i \phi_i \tag{2.9}$$

Where, ϵ_i is the orbital energy.

$$\hat{J}_j \phi_i = \int \frac{1}{r_{ij}} \phi_j^* \, \phi_j dr_j \cdot \phi_i \tag{2.10}$$

$$\hat{K}_j \phi_i = \int \frac{1}{r_{ij}} \phi_j^* \, \phi_i dr_j \cdot \phi_j \tag{2.11}$$

A Hartree-Fock simulation starts with guess ϕ_i, then the $\hat{J}_j$, $\hat{K}_j$, and $\hat{F}$ operators are constructed. By solving the Hartree-Fock equation, new orbitals and orbital energies are obtained, then the Hartree-Fock equation is solved again with a newly constructed $\hat{F}$ operator, and this procedure is repeated until self-consistency is reached.

2.2 Density functional theory (DFT)

In 1927, Thomas and Fermi proposed a method that describes a system with a given electronic density; it is the Thomas-Fermi model and the prototype of density functional theory (DFT).[6-7] Exchange correlation energy was introduced to the Thomas-Fermi model by Dirac in 1929, then the Thomas-Fermi-Dirac theory was born.[8] Like Hartree-Fock theory, DFT belongs to ab initio methods, so it is also called a first-principles method. It has been widely used in physics and chemistry, due to the following advantage over wavefunction methods such as HF theory; DFT converts the multi-dimensional problem of the electronic wavefunction to the three-dimensional problem of electron density, consequently, convergence speed is increased, while the computation time is decreased.

The Hohenberg-Kohn theorem provides a stable mathematical basis for the DFT. It was proposed in 1964 and contains two parts.[9] Theorem 1: The external potential $V_{ext}(r)$, and hence the total energy, is a unique function of the electron density. Therefore, the energy $\mathrm{E}[\rho(r)]$ is a functional of electron density ρ:

$$E[\rho(r)] = T[\rho(r)] + V_{ee}[\rho(r)] + \int \rho(r)V_{ext}(r)dr \tag{2.12}$$

$$= F[\rho(r)] + \int \rho(r)V_{ext}(r)dr \tag{2.13}$$

Where,

$$F[\rho(r)] = T[\rho(r)] + V_{ee}[\rho(r)] \tag{2.14}$$

Theorem 2: The ground state energy can be obtained variationally: the density that minimises the total energy is the exact ground state density. It means that when $\rho'(r) \geq 0$ and $\int \rho'(r)dr = N$, $E[\rho'(r)] \geq E_0$, where *N* represents the total number of electrons, and E_0 is the energy of the ground state.

After the existence of $E[\rho(r)]$ was proved by the Hohenberg-Kohn theorem, Kohn and Sham proposed the equation of $E[\rho(r)]$ in 1965:[10]

$$F[\rho(r)] = T_s[\rho(r)] + E_H[\rho(r)] + E_{xc}[\rho(r)] \tag{2.15}$$

Where,

$$F_s[\rho(r)] = \sum_{i=1}^{N} \int \varphi_i{}^{*} \left(-\frac{h}{2m}\nabla^2\right) \varphi_i dr \tag{2.16}$$

$$E_H[\rho(r)] = \frac{1}{2}\int \frac{\rho(r)\rho(r')}{|r-r'|} dr dr' \tag{2.17}$$

$$E_{xc}[\rho(r)] = F[\rho(r)] - T_s[\rho(r)] - E_H[\rho(r)] \tag{2.18}$$

Where T_s is kinetic energy of electrons which do not interact with each other, φ_i is wavefunction, E_H is the Coulomb energy, and E_{xc} is the exchange correlation. Obviously, this is a fictitious system, as the influence of other electrons in the system on the considered electrons cannot be ignored. However, by introducing this T_s, the kinetic energy can be calculated exactly, and the only term that cannot be calculated exactly is $E_{xc}[\rho(r)]$; this is where approximations come into DFT.

For a system containing N electrons:

$$N = \int \rho(r) dr \tag{2.19}$$

$$\rho(r) = \int \varphi_i{}^{*}\varphi_i dr \tag{2.20}$$

According to the Hohenberg and Kohn theorem, the minimum energy is the unique functional of the ground state density.

$$F[\rho(r)] + \int V_{ext}\,\rho(r) dr \geq E_0 \tag{2.21}$$

Where $V_{\mathrm{ext}}(r)$ is the external potential, and E_0 is the energy of the ground state. Kohn and Sham further introduce a Lagrange multiplier μ that constrains the number of electrons to *N*:

$$\frac{\delta}{\delta\rho(r)}\left[F\rho(r) + \int V_{ext}\,\rho(r)dr + \mu\left(N - \int \rho(r)dr\right)\right] = 0 \tag{2.22}$$

So we can get:

$$\frac{\delta T_s[\rho(r)]}{\delta\rho(r)} = -\frac{h^2\nabla^2}{2m} \tag{2.23}$$

$$\frac{\delta}{\delta\rho(\mathrm{r})}\left[\int V_{ext}\,\rho(\mathrm{r})dr\right] = V_{ext}(r) \tag{2.24}$$

$$\frac{\delta}{\delta\rho(r)}E_H[\rho(r)] = \int \frac{\rho(r)}{|r-r'|}dr = V_H(r) \tag{2.25}$$

$$\frac{\delta}{\delta\rho(r)}E_{xc}[\rho(r)] = V_{xc}(r) \tag{2.26}$$

Where $V_{\mathrm{ext}}(r)$ is the external potential, $V_H(r)$ is the Hartree potential, $V_{xc}(r)$ is the exchange correlation potential.

The ground state can be found by solving the one-electron Schrödinger equations:

$$\left[-\frac{h^2\nabla^2}{2m} + V_{ext}(r) + V_{Har}(r) + V_{xc}(r)\right]\varphi_i = \varepsilon_i\varphi_i \tag{2.27}$$

Or

$$\left[-\frac{h^2\nabla^2}{2m} + V_{KS}(r)\right]\varphi_i = \varepsilon_i\varphi_i \tag{2.28}$$

Where $V_{KS}(r)$ is the Kohn-Sham potential. It is related to the electron density, which is itself obtained by solving the Kohn-Sham equation, thus we must solve the Kohn-Sham equation through self-consistent loops. The Kohn-Sham equation converts a multi-electron system to a single-electron problems. Though it is similar to the Hartree-Fock method, DFT is much simpler.

The key point in solving the Kohn-Sham equation is knowledge of the exchange correlation parts ($V_{xc}(r)$ or $\mathrm{E}_{\mathrm{xc}}[\rho(r)]$). Approximations, such as the local density approximation (LDA), the generalized gradient approximation (GGA), the Meta-GGA, the generalized random phase approximation (RPA), and so on, are made to solve the equation. Perdew proposed the Jacob's ladder (Figure 2.1) in 2001.[11] He divides the different approximations by the number and kind of their local iterm and gives some outlook for the DFT method.

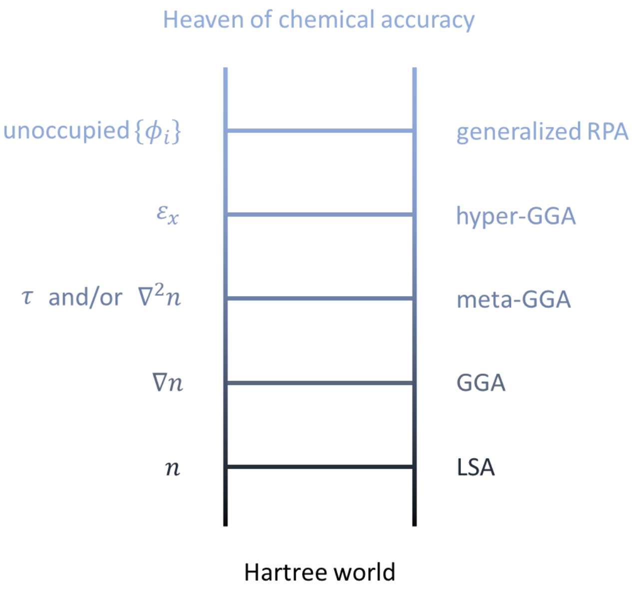

Figure 2.1: The 'Jacob's ladder' of functional approximations, in the Hartree world, there is no electron correlation.[11]

The Local density approximation (LDA) is the simplest approximation for $\mathrm{E_{xc}}[\rho(r)]$ and is the lowest rung of Jacob's ladder.[10] It supposes that the electron density is averaged at all points, so the $\mathrm{E_{xc}}[\rho(r)]$ only depends on electron density and can be expressed as:

$$E_{xc}^{LDA}[\rho(r)] = \int d^3r\, \varepsilon_{xc}^{LDA} \rho(r) \tag{2.29}$$

This kind of approximation can deal with some systems,[12] such as metals, but LDA has some unavoidable disadvantages. For example, the LDA method overestimates the interaction between atoms and leads to an underestimate in the length of bonds. Also, the LDA method overestimates binding energy. Furthermore, the LDA method is unable to describe some magnetic systems correctly. LDA is also not good at dealing with systems that contain weak interactions, such as Van der Waals forces, hydrogen bonding, and so on.

The Generalized gradient approximation (GGA) is on the second rung of Jacob's ladder.[13-16] It improves the LDA method by introducing a new parameter, the gradient of the electron density ($\nabla\rho(\mathrm{r})$)

$$E_{xc}^{GGA}(\rho_{\alpha,}\rho_{\beta}) = \int d^3r\ \rho(r)\varepsilon_{xc}^{\mathrm{GGA}}[\,\rho(r), \nabla\mathrm{\rho(r)}] \tag{2.30}$$

Because of this improvement, GGA corrects the overestimate of bonding in the LDA, and GGA can predict the correct ground state for transition metals, such as Fe and Cr, where LDA fails.[17-18] However, the GGA method is still not good enough to get accurate band gaps for pure transition metals as well as their compounds. PBE, PW91, and BLYP are popular GGA methods.

Meta-GGA, such as TPSS, and hybrid functionals are in the third and fourth stages of Jacob's ladder, respectively.[19] Meta-GGA contains the second derivative of electron density. Hybrid functionals have a mixed exchange of HF and DFT and are one of the most popular types of functionals.

$$E_{xc} = \mathrm{\alpha} E_x^{HF} + (1 - \mathrm{\alpha})E_x^{approx} + E_c^{approx} \tag{2.31}$$

Where α is a independent parameter, E_x^{HF} is the HF exchange energy, E_x^{approx} is the exchange energy of one of the approximations of DFT, E_c^{approx} is the correlation energy of one of the approximations of DFT. B3LYP, B3P86, MPW1K, O3LYP, X3LYP, PBE0, and so on are typical hybrid functionals.[20-26] Lately, a series of highly accurate functions were developed by introducing a kinetic energy correction, such as BMK, M05, M06, M05-2X, M06-2X, M06-HF, and so on.[27-31]

2.3 Relativistic effects

Relativistic effects in quantum chemistry are the discrepancies between results calculated with and without the consideration of Einstein's relativity. Relativistic effects do not normally need to be taken into account for calculations on light elements, but may count for the heavier elements, such as lanthanides and actinides, which are the focus of this thesis. Relativistic effects in chemistry can be described with perturbations or small corrections to the Schrödinger equation. By using the Dirac one-electron Hamiltonian,[32] the difference between the Hamiltonian with and without relativistic effects can be written as:

$$\widehat{H}^R = \widehat{H}^{UR} - \frac{p^4}{8c^2} + \frac{\Delta v}{8c^2} + \frac{1}{2c^2}\frac{1}{r}\frac{dv}{dr}\hat{l} \cdot \hat{s} \tag{2.32}$$

Where $\widehat{H}^R$ is the Hamiltonian with relativistic effects, $\widehat{H}^{UR}$ is the Hamiltonian without relativistic effects, c is the speed of light, p and v are momentum and velocity of the electron, respectively, and $\hat{\boldsymbol{l}}$ and $\hat{\boldsymbol{s}}$ are angular and spin momentum operators. According to this equation, relativistic effects can be divided into three parts: mass-velocity ($\frac{p^4}{8c^2}$), Darwin ($\frac{\Delta v}{8c^2}$) and spin-orbit coupling ($\frac{1}{2c^2}\frac{1}{r}\frac{dv}{dr}\hat{l} \cdot \hat{s}$). Mass-velocity accounts for the variation of the mass with the velocity; it leads to contraction and stabilization of *s* and *p* orbitals, and expansion and destabilization of *d* and *f* orbitals, where Hubbard *U* is introduced to stabilized *d* and *f* orbitals. The Darwin effect is the non-local interaction between electrons and the Coulomb field. Spin-orbit coupling is the interaction between electron spin magnetic moment and the magnetic field which comes from the motion of the electron in the electrostatic field of the nucleus.

2.4 Modified DFT

Traditional DFT methods, such as LDA, GGA, and meta-GGA, sometimes fail to describe correctly systems containing actinides. For example, UO_2 is predicted to be a ferromagnetic metal with the LDA calculation, but it is known exprimentally to be an antiferromagnetic semiconductor.[33] Actinides are strongly correlated atoms with partially occupied *f*-states. The self-interaction error is severe for actinide systems considered with traditional DFT, which does not consider self-coulomb repulsion and just approximates it with the exchange correlation energy (E_{xc}). However, E_{xc} at point r only depends on the density, derivatives of the density, and the kinetic energy at that point. The cancellation of self-coulomb repulsion in E_{xc} is incomplete. What is more, above mentioned relativistic effect, especially on 5*f* orbitals of actinides, also leads to the failure of traditional DFT. Several methods are developed to overcome this self-interaction error; three popular ways are discussed here, they are DFT + *U*,[34-38] self-interaction correction (SIC),[39] and hybrid DFT.[20-31]

2.4.1 DFT + *U*

The first method is by applying the Hubbard *U* parameter. After the Hubbard *U* parameter was proposed by Anisimov and co-workers,[34-36] two kinds of approaches were developed for the DFT + *U* method by Liechtenstein *et al.* and Dudarev *et al.* in 1995 and 1998, respectively.[37-38] Dudarev approach is simpler than the Liechtenstein approach and can give a reasonably good description, so the Dudarev's approach is used in this thesis and will be discussed in the following. The DFT + *U* method divides electrons into two parts, delocalized electrons, and localized electrons. For delocalized electrons, which are s and p electrons, the traditional DFT is able to gain accurate results. For localized electrons, which are d and f electrons, an additional term is added to describe the self-coulomb interaction.

$$E_{DFT+U} = E_{DFT} + \frac{U-J}{2}\sum\nolimits_{\sigma}[Tr\rho^{\sigma} - Tr(\rho^{\sigma}\rho^{\sigma})] \tag{2.33}$$

U and *J* averaged screened Coulomb and exchange energy, respectively. The DFT + *U* method shifts a selected orbital space in energy, and adjusts their occupation, and introduces a bandgap, so the *U* and *J* parameters must be chosen carefully. The DFT + *U* method can describe actinide oxides accurately with a suitable effective *U* ($U_{eff} = U - J$) parameter, and it is the most popular method for calculations of actinide oxides.

2.4.2 Self-interaction correction (SIC)

The second method is the self-interaction correction (SIC),[39] which is the simplest method and explicitly eliminates the self-interaction error.

$$E_{xc}^{SIC} = E_{xc}^{approx} - \sum_{i}(\frac{1}{2}\int\frac{\rho_i(\mathrm{r})\rho_i(r')}{|r-r'|} + E_{xc}^{approx}(\rho_i)) \tag{2.34}$$

The SIC approximation can describe strongly correlated systems, successfully. But it is quite complicated to apply in metal oxide systems, as one should single out orbitals that need special treatment.

2.4.3 Hybrid DFT

The third method is hybrid DFT, discussed above. Hybrid DFT shows significant improvement in the calculation of *d* and *f* states but is unable to address all the problems of open-shell systems and is very expensive for periodic calculation. Heyd, Scuseria, and Enzerhof developed a screened hybrid method HSE.[40] The HSE does not consider HF exchange energy in the long-range, but takes PBEh hybrid for short-range and PBE for long-range.

$$E_{xc}^{HSE} = aE_{x}^{HF,SR} + (1-a)E_{x}^{PBE,SR} + E_{x}^{PBE,LR} + E_{c}^{PBE} \tag{2.35}$$

Where a = 0.25. HSE is good at treating solid state systems and studying semiconductors and insulators.

2.5 Pseudopotentials

The popularity of DFT is due to its low cost and reliable accuracy. Another way to reduce computational costs, but keep the accuracy, is to use pseudopotentials, what is more, pseudopotential method also accounts for the most important relativistic effects (mass-velocity and Darwin terms) in heavy elements calculation. The general idea of a pseudopotential is to replace the core electrons and nucleus of an atom with an effective pseudopotential, calculating valence electrons with normal explicit methods. A successful pseudopotential will predict the same energies above a certain cutoff radius r_c as an all-electron calculation (Figure 2.2), so r_c is an important parameter, pseudopotentials with larger r_c have more rapid convergence and less accuracy. There are three common pseudopotentials: norm-conserving pseudopotentials (NCPP), ultra-soft pseudopotentials (USPP), and the projector-augmented-wave method (PAW).

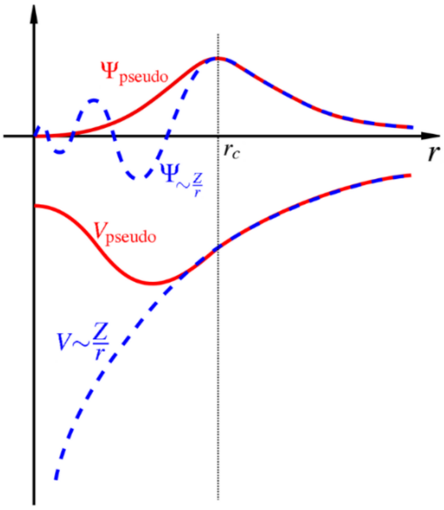

Figure 2.2: A sketch of pseudopotential, blue lines are the potential of the nucleus calculated with all-electron basis, red lines are the potential calculated with the pseudopotential method, r_c is the cutoff radius.[41]

Norm-conserving pseudopotentials (NCPP) were introduced by Haman *et al.* in 1979,[42] and can be written as:

$$V_l^{ps} = \left[1 - f\left(\frac{r}{r_c}\right)\right] V(r) + cf\left(\frac{r}{r_c}\right) \tag{2.36}$$

Where l is angular momentum. For each l, a cutoff radius r_c is chosen, typically from 0.5 to 1.0 × the radius of the outermost peak of the valence wave function. $f(x)$ is a cutoff function which approaches 0 as $x \to \infty$, and approaches 1 as $x \to 0$. The NCPP has paved the way for accurate calculations of solid-state properties within the LDA using plane-wave functions, but is not good at dealing with highly localized valence orbitals.

Ultra-soft pseudopotential (USPP) is introduced by Vanderbilt *et al.* in 1990.[43] They constructed a pseudo-wave function and the pseudopotential is:

$$V^{us} = V_{loc} + \sum_{lm} D_{lm} |\beta_l\rangle\langle\beta_m| \tag{2.37}$$

Where V_{loc} is local pseudopotential operator, β is a projector, lm angular momentum.

$$D_{lm} = B_{lm} + \varepsilon_m Q_{lm} \tag{2.38}$$

$$B_{lm} = \int_0^R dr u_l^*(r) \left[\varepsilon_m + \frac{1}{2}\frac{d^2}{dr^2} - \frac{l(l+1)}{2r^2} - V_{loc}\right] u_m(r) \tag{2.39}$$

$$Q_{lm} = \langle\psi_l|\psi_m\rangle_R - \langle\phi_l|\phi_m\rangle_R \tag{2.40}$$

Where ε_m is orbital energy, $u(r)$ is radial wave function, ψ is all-electron wave function, and ϕ is pseudo-wave function. USPP has been widely used for the 3d transition metals, as it saves computational time and improves accuracy, but there are lots of parameters, so extensive tests are needed to obtain suitable parameters.

The projector-augmented-wave method (PAW) was introduced by Blöchl *et al.* in 1994.[44] They combined pseudopotential and linear augmented plane-wave methods. The pseudopotential wavefunction (Φ) can be transferred to the all-electron wavefunction (Ψ) with the linear transformation (Γ):

$$\Gamma = 1 + \sum_i (|\psi_i\rangle - |\phi_i\rangle)\langle p_i| \tag{2.41}$$

Where ψ_i is an all-electron partial wave, and ϕ_i is a pseudopotential partial wave and obeys the following equations within some augmentation region (Ω_R) enclosing the atom:

$$|\psi_i\rangle = \Gamma|\phi_i\rangle \tag{2.42}$$

$$\Psi = \sum_i |\psi_i\rangle c_i \tag{2.43}$$

$$\Phi = \sum_i |\phi_i\rangle c_i \tag{2.44}$$

p_i are projector functions, and there is exactly one projector function for each pseudopotential partial wave. c_i are expansion coefficients, which are scalar products:

$$c_i = \langle p_i|\Phi\rangle \tag{2.45}$$

Overall, the PAW orbitals (φ_n) can be written as:

$$\varphi_n = \Phi_n + \sum_i (|\psi_i\rangle - |\phi_i\rangle)\langle p_i|\Phi_n\rangle \tag{2.46}$$

The PAW method avoids the disadvantages of USPP, and the construction of PAW datasets is easier.

2.6 Periodic boundary conditions (PBCs) and VASP

For solids, the infinite number of electrons within the solid should be taken into consideration for theoretical simulation. The Bloch theorem simplifies infinite systems according to the translational symmetry of the solid. Bloch theorem states that, in a periodic system, the solution of the one-electron Schrödinger equation can be written as:

$$\varphi(r + \tau) = \varphi(r)e^{ik\tau} \tag{2.47}$$

Where *k* is a vector in reciprocal space, τ is a translational vector leaving the Hamiltonian invariant. Therefore, wave vectors with different k are equivalent, in other words, they represent the same set of Bloch states. By restricting a set of k, every Bloch state in the first Brillouin zone has a unique k. Thus, the first Brillouin zone can describe all of the Bloch states without redundancy.

The Vienna Ab initio Simulation Package (VASP) is a powerful computer program for materials modelling at the atomic scale; it is good at electronic structure calculations, quantum-mechanical molecular dynamics, and so on.[45-48] Several popular methods are implemented in VASP to gain an approximate solution to the many-body Schrödinger equation. DFT is available in VASP, solving the Kohn-Sham equations with LDA, GGA, and meta-GGA functionals and so on. VASP can deal with magnetic systems, collinear and non-collinear, and considers spin-orbit coupling, so it is a good choice for the simulation of actinide systems.

In VASP, the electronic charge density and the local potential are expressed in plane-wave basis sets. The Bloch theorem can be expressed as follows:

$$\varphi_{n,k}(r+\tau) = \varphi_{n,k}(r)e^{ik\tau} \tag{2.48}$$

Where k is a vector in reciprocal space, integer number n is the band index, τ is a translational vector leaving the Hamiltonian invariant. Introducing the cell periodic part $\mu_{n,k}(r)$ of the wavefunctions

$$\varphi_{n,k}(r) = \mu_{n,k}(r)e^{ikr} \tag{2.49}$$

Using Fourier transformation, all functions are expanded in plane waves:

$$\mu_{n,k}(r) = \frac{1}{\Omega^{\frac{1}{2}}}\sum_{G} C_{Gnk}\, e^{iGr} \tag{2.50}$$

$$\varphi_{n,k}(r) = \frac{1}{\Omega^{\frac{1}{2}}}\sum_{G} C_{Gnk}\, e^{i(G+k)r} \tag{2.51}$$

Where C is the expansion coefficient, and G represents the first Brillouin zone

$$\Omega = a_y \cdot a_x \times a_z \tag{2.52}$$

Where a_x, a_y, and a_z is the lattice parameter along x, y, and z directions in real space, respectively.

In practice only those plane waves are included which satisfy

$$\frac{h^2}{8\pi^2 m_e}|G+k|^2 < E_{cutoff} \tag{2.53}$$

Excepting H and Li, the number of plane waves would exceed any practical limit, so instead of using the exact potential, the interactions between the electrons and ions are described using pseudopotentials. Three kinds of potential are implemented in VASP, norm-conserving, and ultra-soft pseudopotentials, and the projector-augmented-wave method (PAW).

2.7 Periodic electrostatic embedded cluster method (PEECM)

It is too expensive to use hybrid DFT in VASP for periodic bulk and surfaces. The TURBOMOLE program can do so with the periodic electrostatic embedded cluster method (PEECM).[49] The periodic system is divided into three parts with the PEECM (Figure 2.3). The most important part is the inner part that contains the defect or active site and which is described by a quantum mechanical (QM) method, usually DFT. Surrounding the QM cluster is the intermediate region. In the intermediate region, all cations are replaced by all-electron effective core potentials (ECPs), and all anions are represented by point charges. In the outer part, all ions are set as corresponding point charges. The intermediate region connects the QM cluster and point charge region, and avoids over-polarisation of the electron density in the QM cluster by positive charges in the point charge region. Hybrid DFT methods are available in TURBOMOLE for the QM cluster. Theoretical simulation of the AnO_2 system with PEECM has proved to be successful;[50-51] the structural and electronic properties for AnO_2 (U, Np, and Pu) are similar to experimental results, and give the correct pattern of water adsorption on AnO_2 (U and Pu) surfaces.

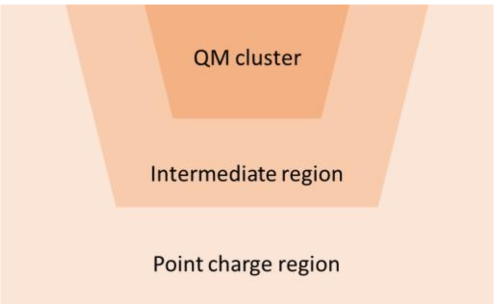

Figure 2.3: Schematic diagram of the periodic electrostatic embedded cluster method (PEECM)

2.8 Temperature effects

To investigate the desorption of molecules from surfaces, molecular thermodynamics was employed to predict the relationship between desorption temperature and the partial pressure of the molecules concerned.

$$\gamma_{s,mol} = \gamma_{s,clean} + C\left(E_{ads}(T) - RTln\frac{p}{p_0}\right) \tag{2.54}$$

Where, $\gamma_{s,clean}$ is energy of clean surfaces; $\gamma_{s,mol}$ is the energy of molecule adsorbed surfaces; *C* is the coverage; *p* is the partial pressure of molecules; p_0 is the partial pressure of the molecule in its standard state (298.1K, 101.3 KPa); *R* is the gas constant; *T* is temperatures; $E_{ads}(T)$ is the temperature-dependent adsorption energy.

$$E_{ads}(T) = E_{ads}^{DFT} + TS(T) \tag{2.55}$$

Where, E_{ads}^{DFT} is the adsorption energy calculated from the DFT simulation, *S(T)* is the temperature-dependent entropy of the molecule. The entropies of molecules of interest can be found in the NIST-JANAF Thermochemical Tables.[52] For example, figure 2.4 gives the entropy of H_2O from those tables. Ignoring the influence of pressure, the *S(T)* of water can be expressed as follows:

$$S(T) = 65.086T^{0.1852} \tag{2.56}$$

Therefore, for water molecule:

$$E_{ads}(T) = E_{ads}^{DFT} + 65.086T^{1.1852} \tag{2.57}$$

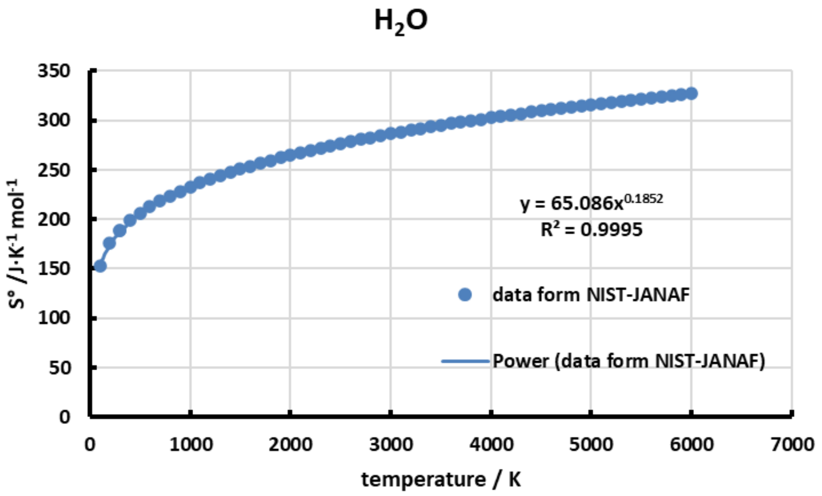

Figure 2.4: Plot of the entropy of water under standard pressure against temperature.

The adsorption and desorption preference of a molecule can be inspected by compare $\gamma_{s,clean}$ and $\gamma_{s,mol}$, if $\gamma_{s,mol} \geq \gamma_{s,clean}$, the molecule will desorb, while prefer to adsorb, if $\gamma_{s,mol} < \gamma_{s,clean}$. In other words, thermal desorption of a molecule will occur when:

$$ln\frac{p}{p_0} \leq \frac{1}{R}\left(\frac{E_{ads}^{DFT}}{T} - S(T)\right) \tag{2.58}$$

Reference

1. Hartree, D., In The Wave Mechanics of an Atom with a Non-Coulomb Central Field. Part III. Term Values and Intensities in Series in Optical Spectra, *Proceedings of the Cambridge Philosophical Society*, **1928**, *24*, 426-437.

2. Hartree, D. R., The Wave Mechanics of an Atom with a Non-Coulomb Central Field. Part I. Theory and Methods. *Proceedings of the Cambridge Philosophical Society*, **1928**, *24*, 89-110.

3. Hartree, D. R., In The Wave Mechanics of an Atom with a Non-Coulomb Central Field. Part II. Some Results and Discussion, *Proceedings of the Cambridge Philosophical Society*, **1928**, *24*, 111-132.

4. Hartree, D., In The Wave Mechanics of an Atom with a Non-Coulomb Central Field. Part IV. Further Results Relating to Terms of the Optical Spectrum, *Proceedings of the Cambridge Philosophical Society*, **1928**, *25*, 310-314.

5. Born, M.; Oppenheimer, R., Zur Quantentheorie Der Molekeln. *Annalen der physik* **1927**, *389*, 457-484.

6. Fermi, E., Atti Accad. Naz. Lincei, Cl. *Sci. Fis. Mat. Nat* **1927**.

7. Thomas, L. H., In The Calculation of Atomic Fields, Mathematical Proceedings of the Cambridge Philosophical Society, Cambridge University Press: 1927; pp 542-548.

8. Dirac, P. A. M., Quantum Mechanics of Many-Electron Systems. *Proceedings of the Royal Society of London. Series A, Containing Papers of a Mathematical and Physical Character* **1929**, *123*, 714-733.

9. Hohenberg, P.; Kohn, W., Inhomogeneous Electron Gas Physical Review 136. *B864* **1964**.

10. Kohn, W.; Sham, L. J., Self-Consistent Equations Including Exchange and Correlation Effects. *Physical review* **1965**, *140*, A1133.

11. Perdew, J. P.; Ruzsinszky, A.; Tao, J.; Staroverov, V. N.; Scuseria, G. E.; Csonka, G. I., Prescription for the Design and Selection of Density Functional Approximations: More Constraint Satisfaction with Fewer Fits. *The Journal of chemical physics* **2005**, *123*, 062201.

12. Dreizler, R. M.; Gross, E. K., *Density Functional Theory: An Approach to the Quantum Many-Body Problem*; Springer Science & Business Media, 2012.

13. Becke, A. D., Density-Functional Exchange-Energy Approximation with Correct Asymptotic Behavior. *Physical review A* **1988**, *38*, 3098.

14. Lee, C.; Yang, W.; Parr, R. G., Development of the Colle-Salvetti Correlation-Energy Formula into a Functional of the Electron Density. *Physical review B* **1988**, *37*, 785.

15. Perdew, J. P.; Chevary, J. A.; Vosko, S. H.; Jackson, K. A.; Pederson, M. R.; Singh, D. J.; Fiolhais, C., Atoms, Molecules, Solids, and Surfaces: Applications of the Generalized Gradient Approximation for Exchange and Correlation. *Physical review B* **1992**, *46*, 6671.

16. Perdew, J. P.; Burke, K.; Ernzerhof, M., Generalized Gradient Approximation Made Simple. *Physical review letters* **1996**, *77*, 3865.

17. Moroni, E.; Kresse, G.; Hafner, J.; Furthmüller, J., Ultrasoft Pseudopotentials Applied to Magnetic Fe, Co, and Ni: From Atoms to Solids. *Physical Review B* **1997**, *56*, 15629.

18. Hafner, R.; Spisak, D.; Lorenz, R.; Hafner, J., Ab Initio Local-Spin-Density Study of Oscillatory Exchange Coupling in Fe/Au Multilayers. *Journal of Physics: Condensed Matter* **2002**, *14*, 4297.

19. Tao, J.; Perdew, J.; Ruzsinszky, A.; Scuseria, G.; Csonka, G.; Staroverov, V., Meta-Generalized Gradient Approximation: Non-Empirical Construction and Performance of a Density Functional. *Philosophical Magazine* **2007**, *87*, 1071-1084.

20. Perdew, J. P., Erratum: Density-Functional Approximation for the Correlation Energy of the Inhomogeneous Electron Gas. *Physical Review B* **1986**, *34*, 7406.

21. Becke, A. D., Density ‐ Functional Thermochemistry. I. The Effect of the Exchange ‐ Only Gradient Correction. *The Journal of chemical physics* **1992**, *96*, 2155-2160.

22. Becke, A. D., Density ‐ Functional Thermochemistry. Iv. A New Dynamical Correlation Functional and Implications for Exact ‐ Exchange Mixing. *The Journal of chemical physics* **1996**, *104*, 1040-1046.

23. Adamo, C.; Barone, V., Exchange Functionals with Improved Long-Range Behavior and Adiabatic Connection Methods without Adjustable Parameters: The M Pw and M Pw1pw Models. *The Journal of chemical physics* **1998**, *108*, 664-675.

24. Lynch, B. J.; Fast, P. L.; Harris, M.; Truhlar, D. G., Adiabatic Connection for Kinetics. *The Journal of Physical Chemistry A* **2000**, *104*, 4811-4815.

25. Handy, N. C.; Cohen, A. J., Left-Right Correlation Energy. *Molecular Physics* **2001**, *99*, 403-412.

26. Xu, X.; Goddard, W. A., The X3lyp Extended Density Functional for Accurate Descriptions of Nonbond Interactions, Spin States, and Thermochemical Properties. *Proceedings of the National Academy of Sciences* **2004**, *101*, 2673-2677.

27. Boese, A. D.; Martin, J. M., Development of Density Functionals for Thermochemical Kinetics. *The Journal of chemical physics* **2004**, *121*, 3405-3416.

28. Hohenstein, E. G.; Chill, S. T.; Sherrill, C. D., Assessment of the Performance of the M05− 2x and M06− 2x Exchange-Correlation Functionals for Noncovalent Interactions in Biomolecules. *Journal of Chemical Theory and Computation* **2008**, *4*, 1996-2000.

29. Riley, K. E.; Pitonák, M.; Jurecka, P.; Hobza, P., Stabilization and Structure Calculations for Noncovalent Interactions in Extended Molecular Systems Based on Wave Function and Density Functional Theories. *Chemical Reviews* **2010**, *110*, 5023-5063.

30. Cohen, A. J.; Mori-Sánchez, P.; Yang, W., Challenges for Density Functional Theory. *Chemical reviews* **2012**, *112*, 289-320.

31. Ferrighi, L.; Pan, Y.-x.; Grönbeck, H.; Hammer, B., Study of Alkylthiolate Self-Assembled Monolayers on Au (111) Using a Semilocal Meta-Gga Density Functional. *The Journal of Physical Chemistry C* **2012**, *116*, 7374-7379.

32. Reiher, M.; Wolf, A., Exact Decoupling of the Dirac Hamiltonian. I. General Theory. *The Journal of chemical physics* **2004**, *121*, 2037-2047.

33. Kudin, K. N.; Scuseria, G. E.; Martin, R. L., Hybrid Density-Functional Theory and the Insulating Gap of U O 2. *Physical review letters* **2002**, *89*, 266402.

34. Anisimov, V. I.; Zaanen, J.; Andersen, O. K., Band Theory and Mott Insulators: Hubbard U Instead of Stoner I. *Physical Review B* **1991**, *44*, 943.

35. Anisimov, V.; Gunnarsson, O., Density-Functional Calculation of Effective Coulomb Interactions in Metals. *Physical Review B* **1991**, *43*, 7570.

36. Anisimov, V. I.; Solovyev, I.; Korotin, M.; Czyżyk, M.; Sawatzky, G., Density-Functional Theory and Nio Photoemission Spectra. *Physical Review B* **1993**, *48*, 16929.

37. Liechtenstein, A.; Anisimov, V. I.; Zaanen, J., Density-Functional Theory and Strong Interactions: Orbital Ordering in Mott-Hubbard Insulators. *Physical Review B* **1995**, *52*, R5467.

38. Dudarev, S.; Botton, G.; Savrasov, S.; Humphreys, C.; Sutton, A., Electron-Energy-Loss Spectra and the Structural Stability of Nickel Oxide: An Lsda+ U Study. *Physical Review B* **1998**, *57*, 1505.

39. Perdew, J. P.; Zunger, A., Self-Interaction Correction to Density-Functional Approximations for Many-Electron Systems. *Physical Review B* **1981**, *23*, 5048.

40. Heyd, J.; Peralta, J. E.; Scuseria, G. E.; Martin, R. L., Energy Band Gaps and Lattice Parameters Evaluated with the Heyd-Scuseria-Ernzerhof Screened Hybrid Functional. *The Journal of chemical physics* **2005**, *123*, 174101.

41. Hamann, D.; Schlüter, M.; Chiang, C., Norm-Conserving Pseudopotentials. *Physical Review Letters* **1979**, *43*, 1494.

42. Vanderbilt, D., Soft Self-Consistent Pseudopotentials in a Generalized Eigenvalue Formalism. *Physical review B* **1990**, *41*, 7892.

43. Blöchl, P. E., Projector Augmented-Wave Method. *Physical review B* **1994**, *50*, 17953.

44. Kresse, G.; Hafner, J., Ab Initio Molecular-Dynamics Simulation of the Liquid-Metal–Amorphous-Semiconductor Transition in Germanium. *Physical Review B* **1994**, *49*, 14251.

45. Kresse, G.; Furthmüller, J., Efficiency of Ab-Initio Total Energy Calculations for Metals and Semiconductors Using a Plane-Wave Basis Set. *Computational materials science* **1996**, *6*, 15-50.

46. Kresse, G.; Furthmüller, J., Efficient Iterative Schemes for Ab Initio Total-Energy Calculations Using a Plane-Wave Basis Set. *Physical review B* **1996**, *54*, 11169.

47. Kresse, W. G.; Marsman, M., Vasp The. **2013**.

48. Burow, A. M., The Howto of the Periodic Electrostatic Embedded Cluster Method (Peecm). **2011**.

49. Wellington, J. P. W.; Kerridge, A.; Austin, J.; Kaltsoyannis, N., Electronic Structure of Bulk Ano(2) (an = U, Np, Pu) and Water Adsorption on the (111) and (110) Surfaces of Uo2 and Puo2 from Hybrid Density Functional Theory within the Periodic Electrostatic Embedded Cluster Method. *Journal of Nuclear Materials* **2016**, *482*, 124-134.

50. Wellington, J. P. W.; Tegner, B. E.; Collard, J.; Kerridge, A.; Kaltsoyannis, N., Oxygen Vacancy Formation and Water Adsorption on Reduced Ano(2){111}, {110}, and {100} Surfaces (an = U, Pu): A Computational Study. *Journal of Physical Chemistry C* **2018**, *122*, 7149-7165.

51. Nist-Janaf Thermochemical Tables. *https://janaf.nist.gov/* **1998**.

Computational Study of the Bulk and Surface Properties of the Minor Actinide Dioxides $MAnO_2$ (MAn = Np, Am, Cm); Water Adsorption on Stoichiometric and Reduced {111}, {110} and {100} Surfaces.

Jia-Li Chen and Nikolas Kaltsoyannis

Abstract

Hubbard *U*-corrected generalised gradient approximation density functional theory is used to study bulk and surface properties of the minor actinide dioxides NpO_2, AmO_2 and CmO_2. Comparison of lattice parameters, band gaps and densities of states with experimental data indicates that PBE + *U* (*U* = 4.50 eV, *J* = 0.50 eV) is the best approach of those considered. Stoichiometric and oxygen vacancy defect {111}, {110} and {100} surfaces are investigated, including the molecular and dissociative adsorptions of water. Comparison with previous work from our group on UO_2 and PuO_2 leads to the conclusion that oxygen defect generation energy is essentially linearly correlated with An(IV)/(III) redox potential across the AnO_2 series from U to Cm. The geometries of water adsorption are similar across the series, while adsorption energies generally decrease, with the exception of certain PuO_2 surfaces, in agreement with very hygroscopic nature of PuO_2. Surface defects promote dissociative water adsorption.

3.1 Introduction

Nuclear fuel is typically formed of uranium dioxide, UO_2. Over the fuel's lifetime, plutonium is generated from the uranium by neutron capture and β decay nuclear reactions. During reprocessing of the spent fuel, the plutonium is separated from the remaining uranium, which can then be reused in new fuel. Several decades of spent fuel reprocessing in the UK has led to the accumulation of more than 100 tonnes of Pu, which is currently stored as PuO_2 powders in multi-layer steel canisters. There is evidence for the generation of gas within some of these canisters, and possible causes include the reaction of water with PuO_2

surfaces. Given the difficulties associated with studying such chemistry experimentally we, and others, have been using computational methods to probe the interactions between water and the surfaces of both PuO_2 and UO_2.[1-9] In this contribution we extend this work to the dioxides of the elements neighbour U and Pu in the actinide series, the so-called minor actinides (MAn) Np, Am and Cm. Not only is this work of fundamental interest, but as ^{241}Pu decays to ^{241}Am, so Am concentrations of up to 8 atom% may arise in older PuO_2 samples. Although the dioxides are not the only stable oxides of these elements, *e.g.* Pu, Am and Cm sesquioxides are known, the dioxides are the most relevant for the nuclear fuel cycle.[10]

Experimental study of $MAnO_2$ is limited by the intense radioactivity of Np, Am and Cm. Experimental studies of bulk $MAnO_2$, which have the calcium fluorite (CaF_2) structure with *Fm-3m* symmetry,[11-13] have focused on heat capacity, thermal expansion, and vaporisation behaviour,[14-18] as well as the band structure.[19-24] The actinide 5f and 6d orbitals, and the O 2p orbitals, contribute to the valence and conduction bands of both dioxides, and the valence band of NpO_2 has more actinide character than that in AmO_2.[19, 22] Theoretical studies of bulk $MAnO_2$ have employed modified density functional theory (DFT) methods, such as DFT + U and screened hybrid DFT, to give reasonable results.[25-27] For example, the lattice constants of $MAnO_2$ calculated with the PBE + U method are close to experimental data,[13, 28-29] and calculations correctly predict the band structure and insulating behaviour.[27, 30]

There are even fewer reports of the surface properties of $MAnO_2$. Decades ago, Naegele and co-workers investigated the oxidation process of the surface of Np metal,[31] concluding that NpO_2 is formed, with a thin surface layer of Np_2O_3. More recently, Cakir *et al.* studied the photo-catalysis reaction between water ice and NpO_2 surfaces,[32] and found that under certain conditions Np^{4+} can be reduced to Np^{3+} on the top of the NpO_2 surface. Computationally, Bo and co-workers have studied water adsorption on stoichiometric and reduced NpO_2 surfaces, as well as the surface properties of NpO_2.[33] Other previous theoretical simulation concluded that adsorption of hydroxyls stabilises NpO_2 surfaces.[34] To the best of our knowledge, the surface properties of AmO_2 and CmO_2 have not been reported experimentally or theoretically. Thus, in the present paper, we study computationally three low index surfaces of $MAnO_2$ (MAn = Np, Am, Cm), including the adsorption of water on stoichiometric and oxygen vacancy surfaces. We organize the paper as follows: we begin with a brief description of the DFT + U computational methodology used, followed by some results for the bulk dioxides. We then discuss the structures and energies of stoichiometric and reduced {111}, {110}, and {100} surfaces, and present molecular and dissociative water adsorption geometries and energies on those surfaces. We make extensive comparison between the PBE and PBESol functionals, and explore the effects of the Hubbard U parameter on the properties of AmO_2. Throughout, we compare our data to our previous results on UO_2 and PuO_2,[6-7, 9] and establish trends in bulk and surface properties, and water adsorptions, on all AnO_2 from U to Cm.

3.2 Computational details

All calculations were performed using density functional theory (DFT), as implemented in the Vienna Ab-initio Simulation Package (VASP), version 5.4.1.[35-38] Two exchange-correlation functionals have been employed, the generalized gradient approximation functional of Perdew, Burke, and Ernzerhof (PBE), and PBE revised for solids (PBESol).[39-40] A Hubbard U correction was employed for the 5f electrons;[41] values of U are discussed in the main text. Plane wave basis sets and projector-augmented wave pseudopotentials were used to describe the ions.[42] A plane wave cutoff of 650 eV was adopted for all calculations. Monkhorst-Pack (MP) grids were employed for the k-space integration;[43] a minimum MP grid of $5 \times 5 \times 1$ k points for the Brillouin zone sampling for the surface simulations and $11 \times 11 \times 11$ for the bulk calculations. Electronic and ionic self-consistency thresholds were 0.0001 eV/Å and 0.001 eV/Å, respectively. A 1k colinear magnetic ordering with a net magnetic moment of zero was used; this allows the total system to be treated as antiferromagnetic and hence to reach the correct ground state.[44-46] Spin−orbit coupling has been neglected; earlier results by Rák and co-workers indicate that spin−orbit coupling has only a very small effect on surface stability,[34] and we have not included spin-orbit effects in our previous studies of water adsorption onto UO_2 and PuO_2 surfaces.[7-8]

The bulk model employed is $MAnO_2$ contains 4 MAn and 8 O. The $MAnO_2$ surfaces are constructed using repeating slabs of 24 $MAnO_2$ units arranged in six layers, each with 18 Å of vacuum between each slab. Each surface is 2 × 2, and the defect and water coverage is one-quarter monolayer. Defects and adsorbates are introduced on both sides of the slab to minimize dipole effects. All the periodic images were made using VESTA.[47]

Surface energies E_{surf} are calculated according to equation (3.1):

$$E_{\mathrm{surf}} = \frac{1}{2S}\left(E_{\mathrm{slab}} - NE_{\mathrm{bulk}}\right) \tag{3.1}$$

where S is the surface area of the slab, E_{slab} is the energy of the relaxed stoichiometric slab that contains N $\mathrm{MAnO_2}$ formula units, so $N = 6$, and E_{bulk} is the bulk energy.

E_{reduce}, the surface oxygen defect generation energy, was calculated using equation (3.2):

$$E_{\mathrm{reduce}} = \frac{1}{2}\left(E_{\mathrm{red,slab}} + E_{\mathrm{O_2}} - E_{\mathrm{slab}}\right) \tag{3.2}$$

where $E_{\mathrm{red,slab}}$ is the energy of the relaxed reduced slab of the same surface as the stoichiometric slabs, and E_{O2} is the energy of a single oxygen molecule in a box with a 20 Å side. The factor of 1/2 is due to the reduced slab having one vacancy on each side.

The adsorption energy of water on stoichiometric and reduced slabs is given by equations (3.3) and (3.4) respectively:

$$E_{\mathrm{ads}} = \frac{1}{2}\left[E_{\mathrm{slab+H2O}} - \left(E_{\mathrm{slab}} + 2E_{\mathrm{H_2O}}\right)\right] \tag{3.3}$$

$$E_{\mathrm{ads}} = \frac{1}{2}\left[E_{\mathrm{red,slab+H2O}} - \left(E_{\mathrm{red,slab}} + 2E_{\mathrm{H_2O}}\right)\right] \tag{3.4}$$

where $E_{\mathrm{slab+mol}}$ and $E_{\mathrm{red,slab+mol}}$ are the energies of the stoichiometric and reduced slab with an adsorbed water molecule, respectively, and E_{H2O} is the energy of a water molecule in the gas phase, calculated as single water molecule in a periodic box with a 20 Å side. The factor of 1/2 is due to adsorbing water on both sides of every slab.

3.3 Results and discussion

3.3.1 Bulk properties of $MAnO_2$

We begin by establishing key computational parameters through comparison with experimental results for the bulk properties of $MAnO_2$. Previous studies within our group on UO_2 and PuO_2 showed the PBE functional to give reliable results.[6-7, 9] However, it has been recently shown that PBESol can give more accurate lattice constants and band gaps than PBE for AnO_2 bulk.[25] Thus, PBESol was compared with PBE for calculations of NpO_2 (NpO_2 is the most studied system of the three minor actinides, with sufficient data to allow meaningful comparison.)

In our previous work, we used the PBE + U method to obtain reliable bulk and surface properties of UO_2 and PuO_2, with U_{eff} equal to 4.00 eV (U = 4.50 eV, J = 0.5 eV). This includes the energies of water adsorption, which we showed to be only very minorly (< 0.05 eV) affected on changing U by up to 3 eV.[7] Here, we also employ the Hubbard U correction, and have optimised the bulk properties of $MAnO_2$ with different U_{eff} from 0.00 to 7.00 eV (Appendix 1, Figures A3.1- A3.3). Using U_{eff} = 4.00 eV, we obtain reasonable lattice constants and band gaps for NpO_2 and AmO_2 (Table 3.1). The same value for U_{eff} leads to a rather larger overestimation of the lattice parameter for CmO_2 (no experimental data exist for the band gap of CmO_2), but we employ this value throughout as it facilitates direct comparison of our results for the bulk and surface properties of AnO_2 from U to Cm. Table 3.1: Lattice constants and band gaps for bulk $MAnO_2$.

As well as the band gap, the density of states (DOS) is an important electronic property of bulk $MAnO_2$. Thus, the DOS of bulk $MAnO_2$ were calculated, and are presented in Figure 3.1. Clear trends can be found. Comparing (a), (b) and (c) in Figure 3.1, we find that the contribution of the MAn states (5f and 6d) to the valence band decreases from Np to Cm, while the contribution of O 2p increases, such that the valence band of CmO_2 is formed only of O 2p. The conduction band is constructed mainly from An 5f states for all $MAnO_2$. Hence, across the series there is a change from Mott-Hubbard insulator to charge transfer insulator, in agreement with previous conclusions.[25, 27] There is a small intermediate band in the DOS of AmO_2 (between +1.3 and +2.0 eV), which is constructed mainly from Am 5f states, in agreement with previous studies.[25, 27]

Table 3.1 Shows that both PBE and PBESol give reasonable predictions for the NpO_2 bulk with U_{eff} = 4.00 eV; a better band gap is predicted by PBE and a better lattice constant is predicted by PBESol. For AmO_2, we tested two values of U_{eff} (4.00 and 6.15 eV (U = 6.50 eV, J = 0.35 eV)) for reasons which will be explained below. The larger U_{eff} produces a significantly larger lattice constant and band gap *vs* experiment, once again illustrating that U_{eff} can have a significant influence on theoretical simulation of the bulk properties of actinide solids.

Table 3.1: Lattice constants and band gaps for bulk $MAnO_2$

$MAnO_2$	Method	U_{eff} (eV)	Lattice constant (Å)		Band gap (eV)	
			Calculation	Expt.	Calculation	Expt.
NpO_2	PBE	4.00	5.498	5.434[48]	2.57	2.85-3.10[20, 30]
	PBESol		5.436		2.47	
AmO_2	PBE	4.00	5.427	5.372-5.379[12, 49-50]	1.34	1.3[30]
		6.15	5.536		3.17	
CmO_2	PBE	4.00	5.507	5.359[23, 51]	3.11	-

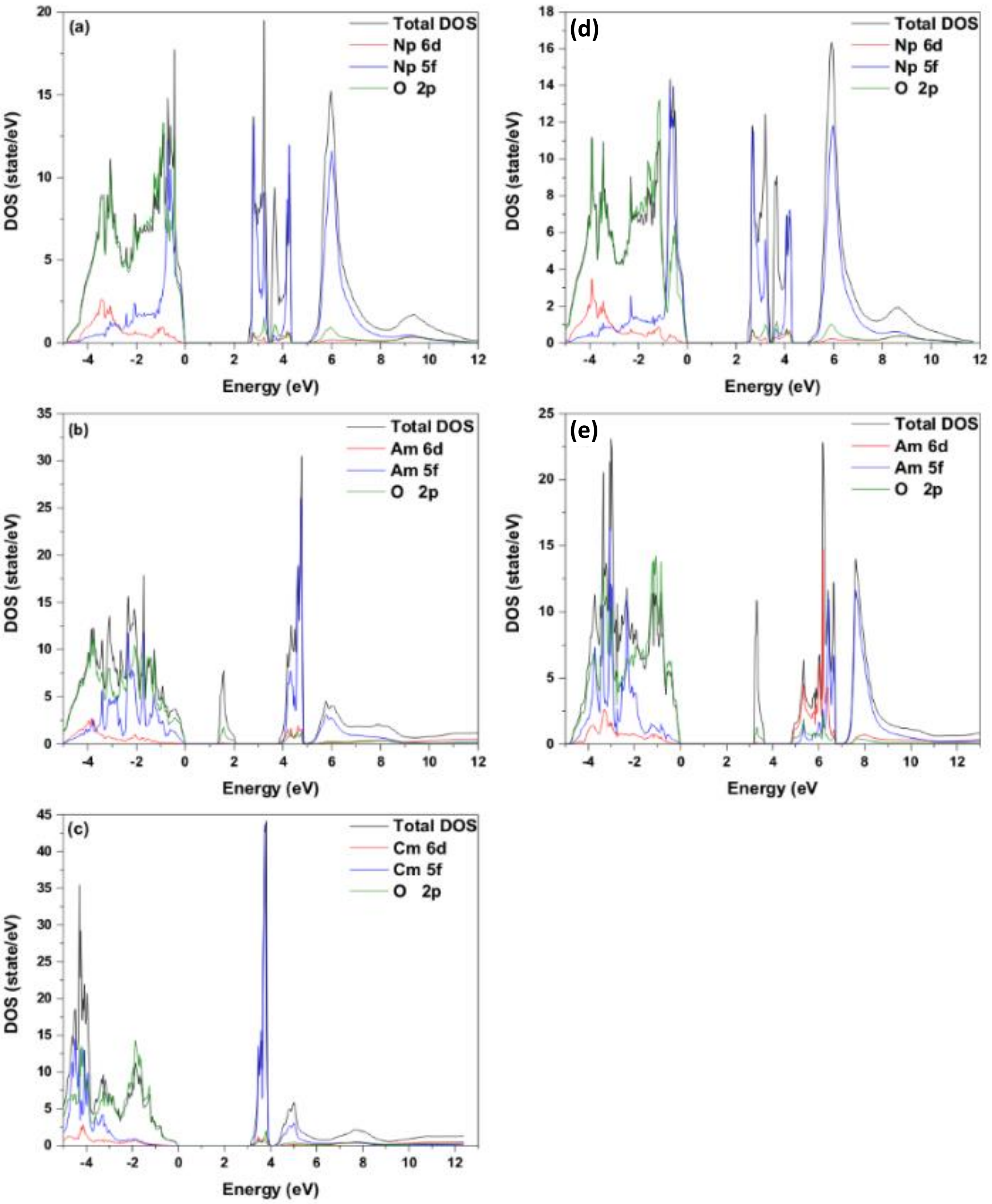

Figure 3.1: The density of states for $MAnO_2$ with different functionals and *U* values: (a) NpO_2 with PBE and U_{eff} = 4.00 eV; (b) AmO_2 with PBE and U_{eff} = 4.00 eV; (c) CmO_2 with PBE and U_{eff} = 4.00 eV; (d) NpO_2 with PBESol and U_{eff} = 4.00 eV; (e) AmO_2 with PBE and U_{eff} = 6.15 eV.

The DOS of NpO_2 calculated with PBESol is presented in Figure 3.1 (d); it is very similar to the PBE data. The valence band is composed of Np 5f, 6d and O 2p states, while the conduction band is made up predominantly of Np 5f states. In AmO_2, the valence band is formed by the overlap of Am 5f and 6d states with O 2p, and the contribution of O 2p is slightly larger with U_{eff} = 6.15 eV. The conduction band is similar for both U_{eff} values and is mainly comprised of Am 5f states, but the composition of the higher unoccupied states differs substantially between the two U_{eff} values (compare Figure 3.1(b) and (e)). When U_{eff} = 4.00 eV, Am 5f states make up the unoccupied states between 4 eV and 6 eV, whereas when U_{eff} = 6.15 eV, O 2p states contribute most to the unoccupied states, which now lie between 6 eV and 8 eV. Therefore, the U_{eff} value has a significant effect on the energy and distribution of the unoccupied states of AmO_2.

3.3.2 Surface properties of $MAnO_2$

Three low Miller index surfaces, {111}, {110}, {100} have been studied. We choose these for a variety of reasons, not least because they have been investigated in previous work by us,[6-9] and others.[1, 5, 33, 52] For dioxides with the fluorite structure, such as the present targets and CeO_2, the {111} surface is the most stable, while {100} has a high surface energy; the stability of the {110} lies in between {111} and {100}.[53] Furthermore, the morphologies of the three surfaces are different. While both {111} and {100} are flat, {111} is terminated by actinides and oxygen but {100} is terminated only by oxygen. The {110} surface is terminated by actinide and oxygen, but the actinides in both the first and second layers are exposed, *i.e.* the {110} surface is ridged. Side views of these three surfaces are presented in Figure 3.2 (for NpO_2 calculated at the PBE+U level) and top views in Figure 3.3 (a) – (c), equivalent images for AmO_2 and CmO_2 are given in Figure A3.4 and A3.5.

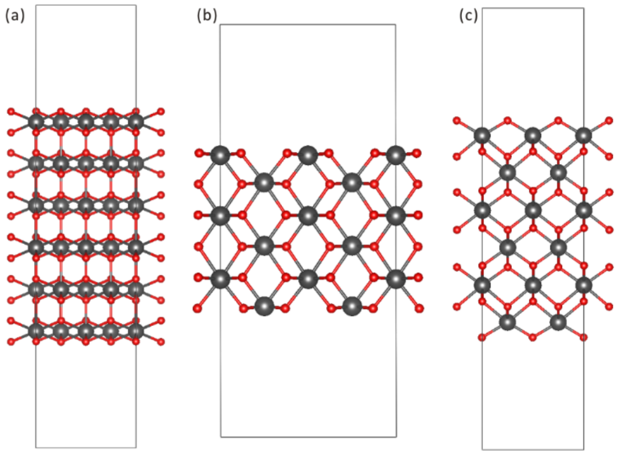

Figure 3.2: Side views of (a) {111}, (b) {110} and (c) {100} NpO_2 surfaces. Dark grey and red spheres represent neptunium and oxygen atoms, respectively.

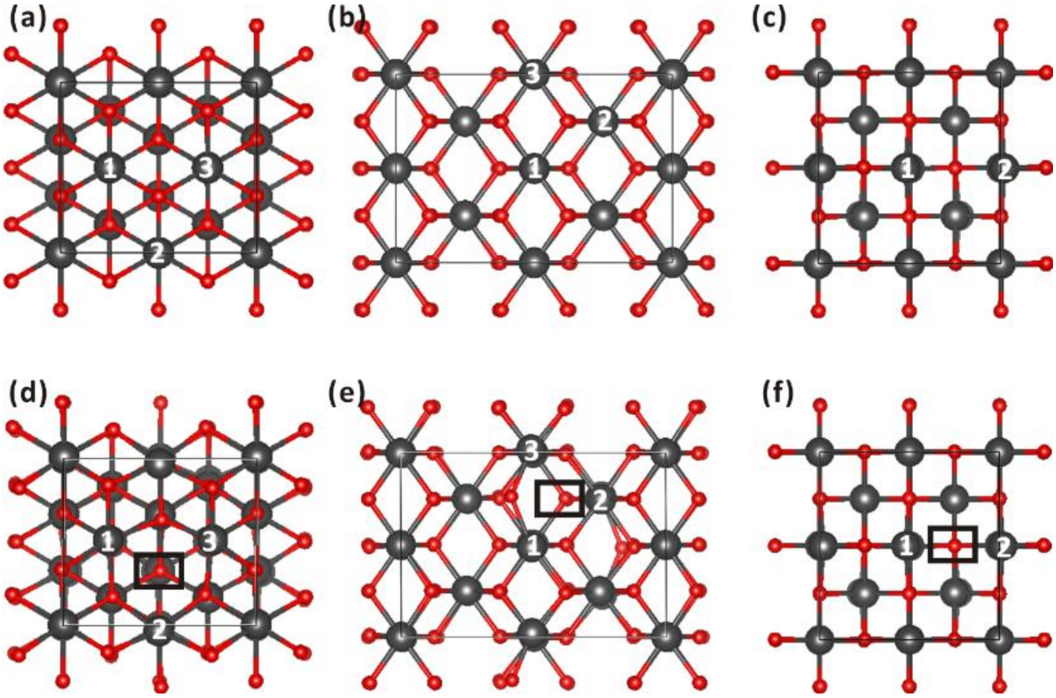

Figure 3.3: Top view of stoichiometric (a) {111}, (b) {110}, (c) {100} and reduced (d) {111}, (e) {110}, (f) {100} NpO_2 surfaces calculated at the PBE+U level (the corresponding PBESol images, not shown, are very similar). Dark grey and red spheres represent neptunium and oxygen atoms, respectively, black squares mark the position of oxygen vacancy defects, and the labelled Np atoms were bonded to the removed oxygen.

Table 3.2: Surface energies (J·m^{-2}) and oxygen defect generation energy (eV) for $MAnO_2$ {111}, {110} and {100} surfaces.

$MAnO_2$	Method	U_{eff}	Surface energy, E_{surf}			Oxygen defect generation energy, E_{reduce}		
			{111}	{110}	{100}	{111}	{110}	{100}
NpO_2	PBE	4.00	0.68	1.14	1.57	4.65	3.83	3.76
	PBESol		1.13	1.66	1.83	4.20	2.90	4.46
AmO_2	PBE	4.00	-0.37	0.43	0.53	1.04	0.50	0.31
		6.15	0.29	0.88	1.10	-0.52	-2.50	-2.07
CmO_2	PBE	4.00	0.35	0.78	0.90	-0.28	-0.49	-0.53

The energies of the {111}, {110} and {100} surfaces of NpO_2, AmO_2 and CmO_2 are listed in Table 3.2. For NpO_2, both the PBE and PBESol methods predict the correct sequence of surface energies, {111} < {110} < {100}; noticeably higher surface energies are obtained with PBESol. PBE predicts surfaces energies in good agreement with Bo et al.'s work (0.81, 1.14, and 1.67 J·m^{-2} for the {111}, {110} and {100} surfaces respectively[33]). PBE with U_{eff} = 4.00 eV give an unphysical prediction of the surface energy for AmO_2 {111} (-0.37 J·m^{-2}); a negative surface energy implies that the surface is more stable than the bulk, and hence that a bulk solid would disintegrate.[54] This energy becomes gradually less negative on increasing U_{eff}, becoming positive (0.29 J·m^{-2}) when U_{eff} = 6.15 eV (U = 6.50 eV, J = 0.35 eV). Hence calculations on AmO_2 were carried out with two values of U_{eff}, as noted in the section above on bulk properties. However, the higher U_{eff} yields bulk data which are further away from experiment than U_{eff} = 4.00 (Table 3.1) especially for the band gap, suggesting that different U values are required for the correct prediction of bulk properties and surface energies using the DFT + U method. We note that, for AmO_2, both U_{eff} yield very similar surface geometries, and the same sequence of surface energies. Predictions for the CmO_2 surfaces are reasonable at the PBE+U (U_{eff} = 4.00 eV) level, with the correct energy sequence for the three low Miller index surfaces and surface energies (Table 3.2) in a reasonable range when compared with the surface energies of UO_2, NpO_2 and PuO_2.

There has been a number of periodic DFT studies of oxygen vacancies in UO_2 and PuO_2,[5, 9, 55-57] whereas $MAnO_2$ have not been studied, and so we have calculated oxygen vacancy defects on $MAnO_2$ surfaces. Representative examples of oxygen vacancy surface geometries are shown for NpO_2 in Figure 3.3 (d) – (f), and the geometries for reduced AmO_2 and CmO_2 surfaces are presented in Figure A3.4 and A3.5. The creation of the vacancy distorts all the surfaces in a similar way, *i.e.* the surrounding minor actinide atoms move away from the defect, while surrounding oxygen atoms move towards it. This is as found for reduced UO_2 and PuO_2 surfaces in our previous work.[9] Given the relative stability of the three target surfaces, it should be hardest to create an oxygen vacancy in the most stable {111} surface, and easiest in the {100}. This is indeed found for NpO_2 at the PBE+U level (Table 3.2), but PBESol predicts the highest oxygen vacancy formation energy for the {100} surface. This, coupled with the observation that the surface energies of NpO_2 are more similar to those of UO_2 (0.65, 1.05, and 1.33 $J \cdot m^{-2}$) and PuO_2 (0.66, 1.13, and 1.59 $J \cdot m^{-2}$) at the PBE+U level, lead us to recommend this approach for the calculation of the surface properties.

Although more reasonable surface energies are obtained for AmO_2 with U_{eff} = 6.15 eV than with U_{eff} = 4.00 eV, the oxygen defect generation energies predicted with U_{eff} = 6.15 eV are all negative, and their order is incorrect. By contrast, U_{eff} = 4.00 eV yields positive defect generation energies and the correct energy sequence for reduced AmO_2 surfaces. U_{eff} = 4.00 eV is clearly more suitable than the larger value for reduced AmO_2 surfaces. U_{eff} = 4.00 eV predicts the correct energy sequence for oxygen vacancy formation in CmO_2 surfaces (Table 3.2), although all energies are negative. Note that the oxygen defect generation energy for bulk CmO_2 has been previously reported to be much lower than the other AnO_2 (An = U, Np, Pu, Am, Bk, Cf),[10] less than 1 eV, so our U_{eff} = 4.00 eV trend from NpO_2 to CmO_2 is likely to be at least qualitatively correct.

We have previously suggested that the oxygen defect generation energy for AnO_2 surfaces is related to the redox potential of An(IV).[9] We here combine our new data on $MAnO_2$ with those we previously acquired on UO_2 and PuO_2 to produce Figure 3.4, which plots the oxygen vacancy formation energy (at the PBE+U level with U_{eff} = 4.00 eV) against the An(IV)/An(III) couple. There is clearly a very strong linear relationship between these quantities; R^2 values for the {111}, {110} and {100} surfaces are 0.986, 0.981 and 0.976, respectively, supporting our previous suggestion.

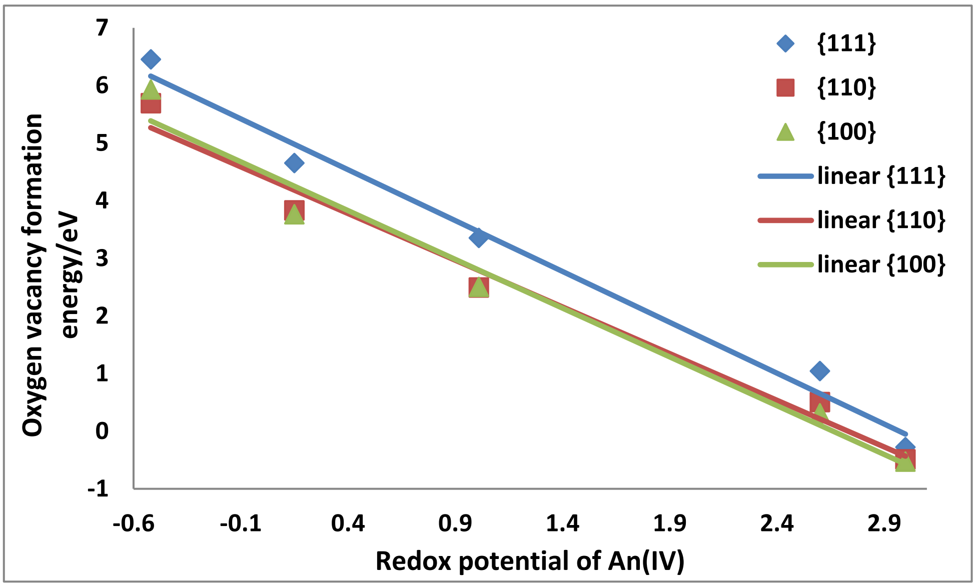

Figure 3.4: The relation between the oxygen vacancy formation energy for AnO_2 (An = U, Np, Pu, Am, and Cm) surfaces and the redox potential of An(IV)/(III). The oxygen vacancy formation energies are calculated at the PBE + U (U_{eff} = 4.00 eV) level.

The creation of a neutral oxygen vacancy leaves behind two electrons, and it is important to establish their localisation properties; we do this by analysing the difference between the spin density in the stoichiometric and reduced slabs, and the data are collected in Table 3.3. For NpO_2, the two electrons mainly locate on two surface Np are adjacent to the defect, labelled ‘1’ and ‘2’ in Figure 3.3, and the spin density of the rest of the Np in the three slabs is not much altered from the stoichiometric case. For the AmO_2 surfaces, more than half of the two electrons are located on the same two surface atoms as see enhanced spin density in NpO_2, and there are slightly larger changes in the spin densities of the other Am in the slab than in the Np case. In contrast, the distribution of electrons on the reduced CmO_2 surfaces is very different from NpO_2 and AmO_2, as the two additional electrons are spread throughout the slabs, with no clear localisation. We have previously studied electron localisation on reduced UO_2 and PuO_2 surfaces, using the PBE0 functional within an embedded cluster approach.[9] In general, the results are similar to those reported here for NpO_2, with large spin density increases on two (or, in the case of UO_2 {111} and {110}, three) metal atoms neighbour the oxygen vacancy. There is thus a trend across the AnO_2 series towards increasingly delocalised behaviour on oxygen vacancy formation. This may well reflect the increasing preference of the metal atoms to exist in the +III oxidation state, such that by CmO_2 all the metal centres participate in accommodating the two electrons left behind on oxygen vacancy formation.

Table 3.3: Difference in the spin density (au) of the actinides between stoichiometric and reduced $MAnO_2$ surfaces. The atom labelling refers to Figure 3.3. All data are calculated at the PBE + *U* (U_{eff} = 4.00 eV) level.

$MAnO_2$	Label of An	Difference in An spin density		
		{111}	{110}	{100}
NpO_2	1	0.880	0.834	0.874
	2	0.953	0.860	0.878
	Rest Np	0.001-0.036	0.000-0.036	0.000-0.018
AmO_2	1	0.568	0.519	0.570
	2	0.569	0.703	0.628
	Rest Am	0.003-0.132	0.006-0.077	0.000-0.066
CmO_2	All Cm	0.003-0.119	0.003-0.155	0.000-0.208

3.3.3 Water adsorption on stoichiometric surfaces

We now move on to consider water adsorption on $MAnO_2$ surfaces with a coverage of 1/4 of a monolayer (*i.e.* a single water molecule adsorbing on one of the four actinides in the surface layer of our unit cells). If the water stays as an intact molecule during the adsorption process it is termed molecular adsorption, whereas dissociative adsorption breaks an O–H bond and results in one adsorbed hydrogen atom and one adsorbed hydroxyl group. The geometries found here for water adsorption on NpO_2, AmO_2 and CmO_2 surfaces are similar to one another, and to those previously reported for UO_2 and PuO_2 surfaces.[6-7, 9] Optimized structures calculated at the PBE + *U* level for molecular and dissociative adsorption on NpO_2 surfaces are presented in Figure 3.5 (a) – (c) and (d) – (f) respectively; the structures on AmO_2 surfaces and on the CmO_2 surfaces are presented in Figure A3.6 and A3.7. Bond lengths are collected in Tables A3.1 – A3.3. PBE + *U* and PBESol + *U* predict very similar bond lengths for molecular and dissociative adsorption on NpO_2 surfaces (Table A3.1), and different U_{eff} also have little effect on the structures of molecular and dissociative adsorption on AmO_2 surfaces (Table A3.2).

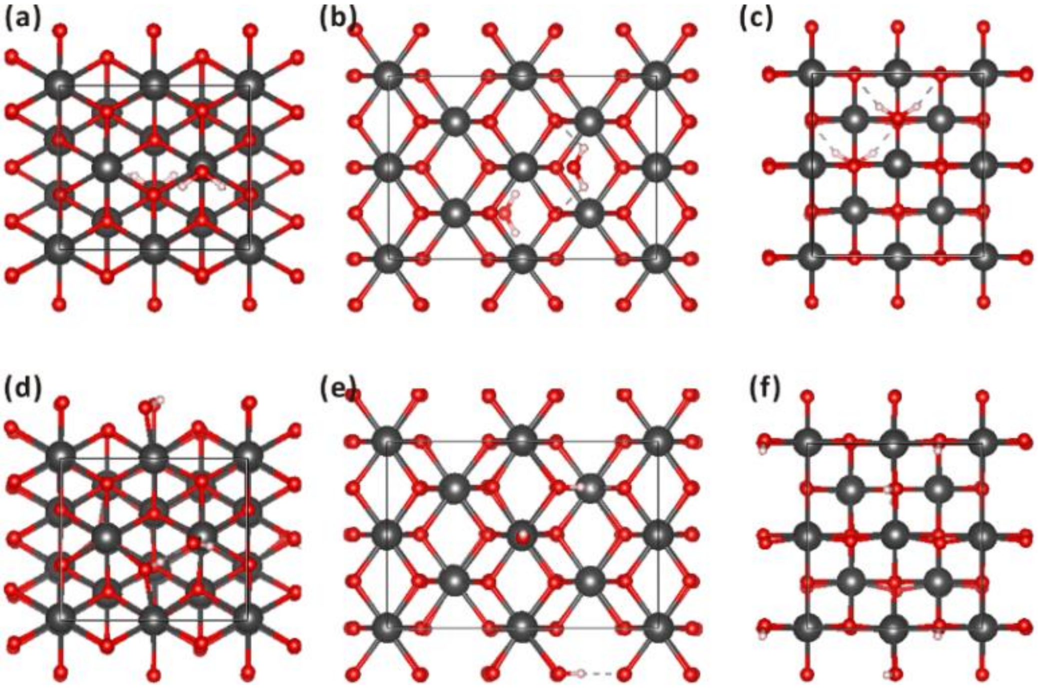

Figure 3.5: Top view of molecular (a) {111}, (b) {110}, (c) {100} and dissociative (d) {111}, (e) {110}, (f) {100} water adsorption on stoichiometric NpO_2 surfaces calculated at the PBE + *U* level. Water adsorbs on both sides of the slab with 25% coverage. Dark grey, red and white spheres represent neptunium, oxygen and hydrogen atoms, respectively.

In molecular adsorption, the oxygen of water (O_w) approaches surface An (An_s) with the two hydrogen atoms (H_w) interacting with surface oxygens (O_s). The interaction between H_w and O_s on the {110} and {100} surfaces is stronger than on the {111}, at least as evidenced by the distance between H_w and O_s on {110} and {100} being shorter than on {111} (Table A3.1 – A3.3). For dissociative adsorption, on the {111} surface there is an obvious hydrogen bond between the adsorbed hydrogen atom and adsorbed hydroxyl, while on {110}, the adsorbed hydrogen interacts with another surface oxygen and forms a hydrogen bond, the adsorbed hydroxyl being almost perpendicular to the surface. On the {100} surface, the adsorbed hydrogen atom points towards the adsorbed hydroxyl, but no clear hydrogen bond is formed. Similar dissociative adsorption structures have previously been reported on NpO_2 surfaces.[33]

The energies of molecular and dissociative water adsorption on stoichiometric $MAnO_2$ surfaces are summarized in Table 3.4. On NpO_2, PBE + *U* and PBESol + *U* predict similar dissociative adsorption energies, but very different molecular adsorption energies. We have previously found molecular water adsorption energies on UO_2 and PuO_2 surfaces to be around -1 eV (from both periodic DFT + *U*[7] and embedded cluster hybrid DFT[6]), and it is clear that the molecular adsorption energies on NpO_2 are well beyond this range at the PBESol + *U* level. Furthermore, molecular water adsorption on UO_2 and PuO_2 {100} is slightly stronger than on {110}, whereas here the PBESol + *U* method predicts much lower energy on NpO_2 {110} than on {100}. We therefore favour PBE over PBESol for water adsorption calculations. At this level, dissociative and molecular water adsorption on NpO_2 {111} are very close in energy, while dissociative adsorption is much more favourable than molecular adsorption on {110} and {100}. This trend is similar to our previous findings for UO_2 and PuO_2.[6-7]

For AmO_2, U_{eff} = 6.15 eV predicts unreasonably large energies for dissociative water adsorption on the {110} and {100} surfaces; U_{eff} = 4.00 eV gives much more sensible values. On AmO_2 {111}, molecular water adsorption is slightly more stable than dissociative adsorption, while the reverse is true on {110} and {100}, a similar, though less exaggerated, trend to NpO_2. Our calculations reveal little difference between molecular and dissociative adsorption energies on the CmO_2 surfaces, the largest difference being 0.22 eV for dissociative *vs* molecular adsorption on {100}.

Table 3.4: Molecular and dissociative water adsorption energies (eV) on stoichiometric NpO_2, AmO_2 and CmO_2 surfaces.

AnO_2	Method	U_{eff} (eV)	Molecular adsorption			Dissociative adsorption		
			{111}	{110}	{100}	{111}	{110}	{100}
NpO_2	PBE	4.00	-0.25	-0.62	-0.66	-0.27	-1.20	-1.48
	PBESol		-2.35	-3.66	-2.17	-0.28	-1.15	-1.80
AmO_2	PBE	4.00	-0.41	-0.60	-0.77	-0.29	-0.83	-1.14
		6.15	-0.21	-0.58	-1.94	-0.68	-2.85	-3.27
CmO_2	PBE	4.00	-0.45	-0.56	-0.78	-0.35	-0.52	-1.00

Combining our newly-acquired PBE + *U* (U_{eff} = 4.00 eV) data on $MAnO_2$ with those we have previously obtained on stoichiometric UO_2 and PuO_2 surfaces allows us to generate Figure 3.6, which plots molecular and dissociative water adsorption energies for all three target surfaces for AnO_2 from U–Cm. Molecular adsorption is weaker on {111} than {110} and {100}, which are more similar to one another ({100} being slightly more favourable). The range of molecular adsorption energies on each surface is quite similar and not very large (c.a. 0.4–0.5 eV across the series from U–Cm) suggesting that AnO_2 have similar abilities to adsorb water molecularly.

The energy sequence for dissociative water adsorption is also {111} < {110} < {100}. Dissociative adsorption energies are very similar on AnO_2 {111}, ranging from -0.27 to -0.50 eV. However, on the {110} and {100} surfaces, the stability of dissociative water adsorption gradually decreases, by a significant amount, from UO_2 to CmO_2. Figure 3.4 reveals a difference between the structures of the dissociative water adsorptions on {111} *vs* {110} and {100}, specifically that the hydroxyl groups and hydrogen atoms dissociated from water retain an interaction with each other on the {111} surface, while they are bonded only with surface An and oxygen on {110} and {100}. As such, the latter surfaces may be better indicators of chemical differences across the AnO_2 series from U to Cm, and Figure 3.6 shows the clear trend towards weaker dissociative adsorption on {110} and {100} surfaces, with the exception of PuO_2 {100}. PuO_2 is known to be very hygroscopic.[58]

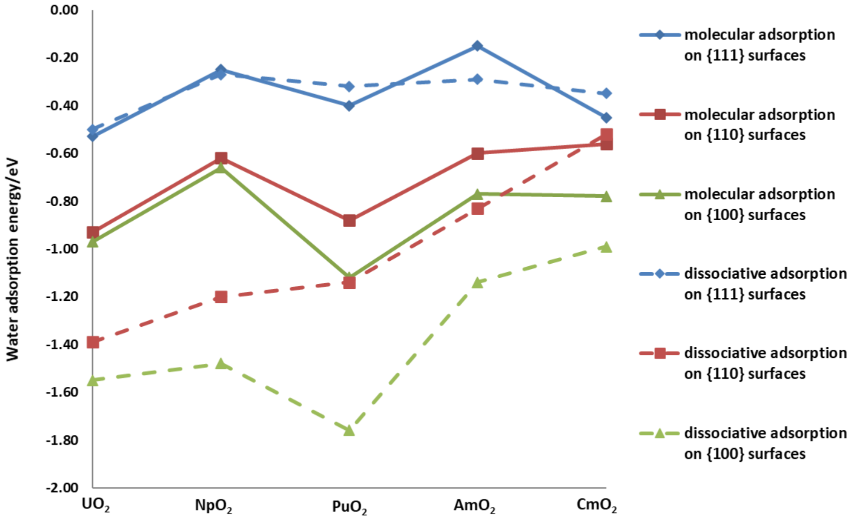

Figure 3.6: Molecular (solid lines) and dissociative (dashed lines) water adsorption energies on AnO_2 (An = U, Np, Pu, Am and Cm) surfaces, calculated at the PBE + *U* (U_{eff} = 4.00 eV) level.

3.3.4 Water adsorption on reduced (oxygen vacancy) surfaces

There are two ways for water to approach reduced surfaces, either above the surface actinide (An_s) or above the surface defect. These two situations will now be discussed for reduced $MAnO_2$ surfaces, after which we discuss water adsorption on reduced AnO_2 surfaces from An = U–Cm, bringing in our previous work on reduced UO_2 and PuO_2. Only data using the PBE + U method (U_{eff} = 4.00 eV) are discussed here; calculations using PBESol and with a larger value of U_{eff} are presented in Table A3.4 and A3.5.

3.3.4.1 Water adsorption above surface actinide of reduced $MAnO_2$ surfaces

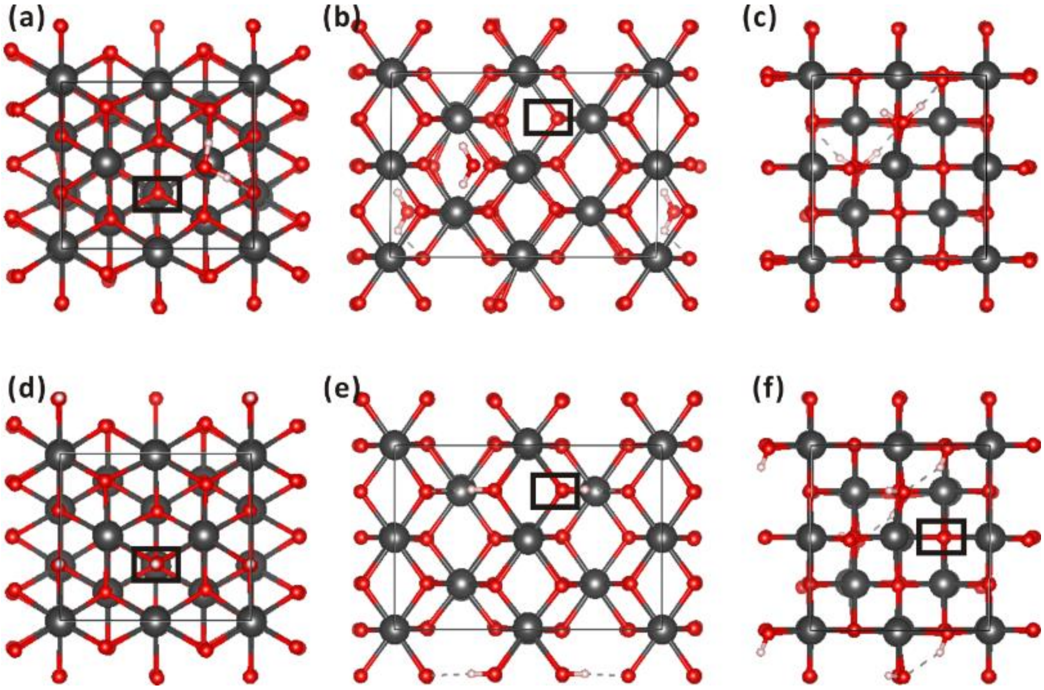

Figure 3.7: Top view of molecular (a) {111}, (b) {110}, (c) {100} and dissociative (d) {111}, (e) {110}, (f) {100} water adsorptions on surface Np of reduced NpO_2 surfaces calculated at the PBE + U level. Water adsorbs on both side of the slabs with 25% coverage. Dark grey, red and white spheres represent neptunium, oxygen and hydrogen atoms, respectively. Black squares mark the positions of the O vacancy.

The structures of molecular and dissociative adsorption on surface Np (Np_s) of reduced NpO_2 are presented in Figure 3.7; the adsorption geometries on reduced AmO_2 and CmO_2 surfaces are similar, and are given in Figure A3.8 and A3.9. The structures of molecular water adsorption on reduced NpO_2 surfaces are similar to the corresponding adsorption structures on the stoichiometric surfaces (compare Figure 3.5 and 3.7) - O_w is bonded with

Np_s and two H_w interact with O_s - although the water molecule is situated a little towards the surface defect. In dissociative adsorption on reduced {111} and {110}, the OH_w adopts the position of the surface defect and H_w bonds to O_s. OH_w and H_w are perpendicular to the {111} surface, while are almost parallel to the {110} surface with H_w forming a hydrogen bond with O_s (Figure 3.7(e)). The structure for dissociative adsorption on reduced {100} surfaces is more similar to the one on the stoichiometric surface (Figure 3.5); OH_w is bonded with two Np_s and does not take the position of the defect, and adsorbed H_w forms a hydrogen bond with OH_w, facilitated by the surface defect-generated movement of Np_s shortening the distance between adsorbed OH_w and H_w. In summary, the surface defects have little influence on the molecular adsorption structures, but rather larger effects on those of dissociative adsorption.

Table 3.5: Energies (eV) for molecular and dissociative water adsorption on reduced NpO_2, AmO_2 and CmO_2 surfaces with O_w approaching surface An, calculated at the PBE + U (U_{eff} = 4.00 eV) level.

AnO_2	Molecular adsorption			Dissociative adsorption		
	{111}	{110}	{100}	{111}	{110}	{100}
NpO_2	-0.24	-0.32	-0.59	-2.07	-1.80	-1.59
AmO_2	-0.62	-0.66	-1.16	-1.90	-1.69	-1.75
CmO_2	-0.60	-0.68	-0.94	-1.70	-1.33	-1.46

The energies for water adsorption above An_s of the reduced surfaces are listed in Table 3.5. As for the stoichiometric surfaces, the sequence of energies for molecular water adsorption is {111} < {110} < {100}. The filling of the oxygen vacancy on dissociative adsorption on $MAnO_2$ {111} and {110} stabilizes the surfaces and results in much more negative adsorption energies than for molecular adsorption. As it is in general the hardest to generate an oxygen defect on {111} surfaces, the filling of the {111} surface defect will stabilize reduced {111} more than {110}, leading to dissociative water adsorption on reduced {111} being more favourable than on reduced {110}. Table 3.4 shows that dissociative adsorption on the stoichiometric {100} surface is more stable than on either {111} or {110}. Here, we find that this trend is either reversed ({111}) or diminished ({110} and {100}), as the {100} surface defect is not filled. Further comparison of Tables 3.4 and 3.5 shows that molecular water adsorption above An_s of reduced surfaces is similar in energy to that on stoichiometric surfaces, while the analogous dissociative adsorptions are much more stable than on the stoichiometric surfaces. Thus, the existence of surface defects greatly promotes dissociation of adsorbed water molecules.

3.3.4.2 Water adsorption above surface defect of reduced $MAnO_2$ surfaces

Attempting to adsorb water molecularly above the oxygen vacancy in reduced NpO_2 {110} and {100} surfaces leads to spontaneous dissociation, as found previously by Bo *et al.* for NpO_2,[33] and by us on reduced UO_2 and PuO_2.[9] This is also the case for the reduced CmO_2 {110} and {100} surfaces here, although stable molecular adsorption is observed on AmO_2 {110} and {100}. As the structures of molecular adsorption on the reduced {111} surfaces, and dissociative adsorption on all three surfaces, are similar for NpO_2, AmO_2 and CmO_2, the structures of molecular and dissociative water adsorption on reduced AmO_2 surfaces are presented in Figure 3.8 (a) – (c) and (d) – (f) respectively; the adsorption structures on NpO_2 and CmO_2 surfaces are presented in Figure A3.10 and A3.11. In molecular adsorption on {111}, which has similar structure to water adsorption on reduced UO_2 and PuO_2 {111} surfaces,[9] the hydrogen atoms point away from the surface, and the lengths of the two O_w-H_w bonds (0.97 and 0.98 Å) are almost the same as in free water (0.98 Å). For AmO_2 {110}, the adsorbed water molecule bonds with the surface through O_w, one H_w forms a hydrogen bond with O_s, and the O_w-H_w bond elongates to 1.06 Å. For AmO_2 {100}, the water molecule stays above the surface defect, one H_w interacts with O_s which moves towards the H_w, and the O_w-H_w bond lengthens to 1.02 Å. In general, the structures of molecular water adsorption on AmO_2 indicate stronger interaction with reduced {110} and {100} surfaces than with {111}; we suggest that these interactions are so strong on reduced UO_2, NpO_2, PuO_2 and CmO_2 {110} and {100} surfaces that they lead to simultaneous dissociation.

OH_w takes up the position of the surface defect on dissociative water adsorption on all three surfaces. The structure of dissociative water adsorption above the {111} surface defect is the same as for dissociative adsorption above An_s. On the {111} and {100} surfaces, as OH_w and H_w are far from each other, there is no interaction between them, while on {110} there is a clear hydrogen bond between OH_w and H_w.

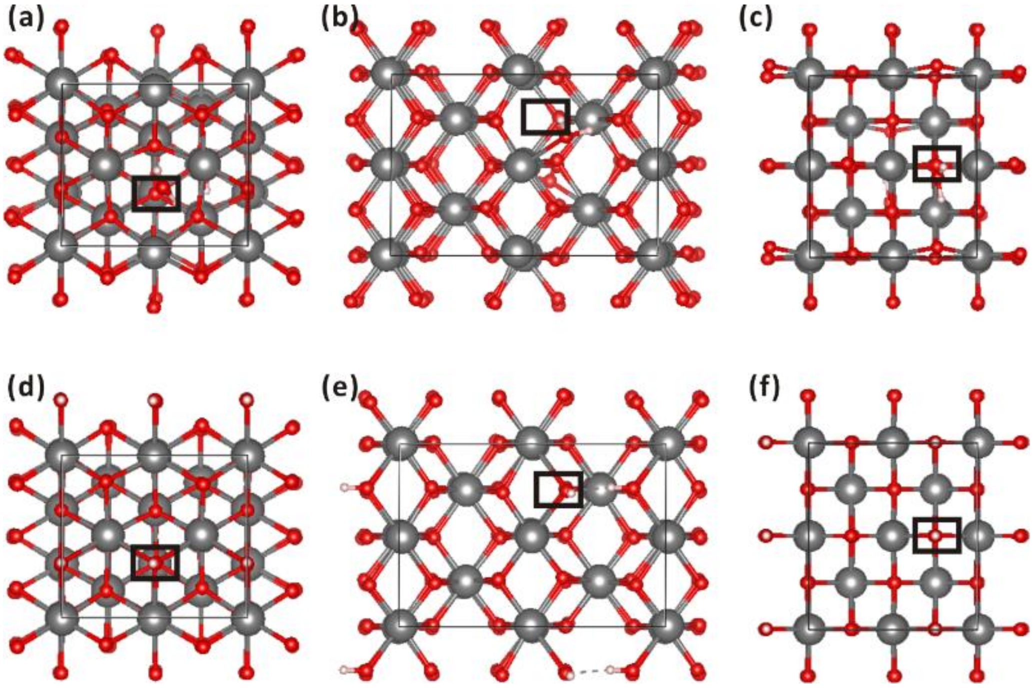

Figure 3.8: Top view of molecular water (a) {111}, (b) {110}, (c) {100} and dissociative water (d) {111}, (e) {110}, (f) {100} adsorption above surface oxygen vacancies of AmO_2 surfaces, calculated at the PBE + *U* level. Water adsorbs on both side of slab with 25% coverage. Light grey, red and white spheres represent americium oxygen and hydrogen atoms, respectively. Black squares mark the positions of the O vacancy.

The energies of water adsorption above the surface defects of reduced $MAnO_2$ surfaces are collected in Table 3.6. The stability of molecular water adsorption on reduced AmO_2 surfaces is {111} < {110} < {100}, the usual sequence, while the stability of dissociative adsorption is {111} > {100} > {110}. As noted above for adsorption above An_s, the filling of the surface defect stabilizes reduced {111} more than reduced {110} and {100} surfaces. In contrast to dissociative adsorption above surface An, here dissociation is significantly more stable on {100} than {110} (compare Tables 3.5 and 3.6), presumably because OH_w now takes up the position of the surface defect on both surfaces. Further comparison of Tables 3.5 and 3.6 indicates that the interaction of water with oxygen vacancy defect surfaces is in general more favourable above the defect than An_s; indeed, molecular water dissociates spontaneously above the {110} and {100} surface defects of NpO_2 and CmO_2.

Table 3.6: Energies (eV) for molecular and dissociative water adsorption on reduced NpO_2, AmO_2 and CmO_2 surfaces with O_w approaching surface defect, calculated at the PBE + U (U_{eff} = 4.00 eV) level. * = water dissociates simultaneously upon adsorption.

AnO_2	Molecular adsorption			Dissociative adsorption		
	{111}	{110}	{100}	{111}	{110}	{100}
NpO_2	-0.57	*	*	-2.07	-1.28	-1.97
AmO_2	-0.71	-0.96	-1.19	-1.90	-1.43	-1.79
CmO_2	-0.46	*	*	-1.70	-1.15	-1.61

Molecular water adsorption above An_s of reduced UO_2 and PuO_2 has not been reported, and leads to dissociation above the oxygen vacancy of reduced UO_2 and PuO_2 {110} and {100}, making it impossible to compare molecular water adsorption across the whole reduced AnO_2 series. However, two kinds of dissociative adsorption structures, similar to the structures in Figure 3.7 (d) – (f) and Figure 3.8 (d) – (f), have been reported on reduced UO_2 and PuO_2 surfaces,[9] allowing us to compare analogous adsorption energies across our series (Figure 3.9). In general, there is a trend toward less negative dissociative adsorption energies from UO_2 to CmO_2 for all surfaces, both above An_s and above the oxygen vacancy. For the reduced {111} surfaces, the same dissociative structures and adsorption energies are found when water approaches either the surface An or the surface defect. For {100}, as we can see in Figure 3.7 (f) and Figure 3.8 (f), and as noted above, there is a structural difference depending on whether water approaches An_s or the surface defect; in the latter case, OH_w adopts the position of the surface defect, while the surface defect remains intact on dissociative adsorption above An_s. Thus, dissociative water adsorption above the surface defect is more stable than above An_s. For {110}, water adsorption on An_s is more stable than above the surface defect. In both situations, the OH_w adopts the position of the surface defect, but the position of H_w is different and leads to different hydrogen bonding situations. Above An_s (Figure 3.7 (e)), the H_w hydrogen bonds with O_s away from OH_w; the two H_w interact with different O_s and form two hydrogen bonds. In contrast, for dissociation above the surface defect (Figure 3.8 (e)), H_w bonds with O_s next to OH_w and forms a hydrogen bond with O_w, leading to OH_w pointing upward and its H_w not forming any hydrogen bond. Finally, as noted for the stoichiometric {100} surface, dissociative adsorption on PuO_2 is significantly more stable than might be expected on the basis of the values for the other AnO_2, for adsorption above An_s and the oxygen vacancy, again showing the special ability of the PuO_2 {100} surface to dissociate water.

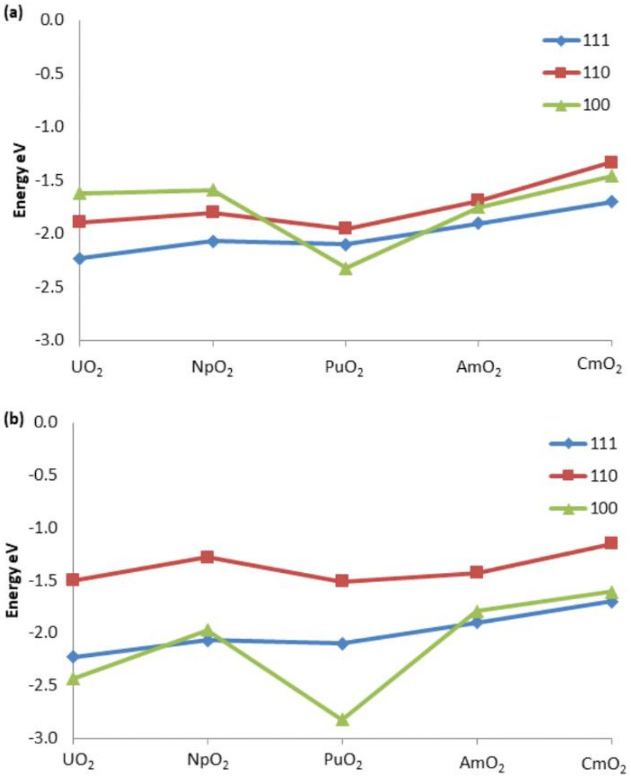

Figure 3.9: Energies (eV) for dissociative water adsorption above (a) surface actinide of

AnO_2 (An = U, Np, Pu, Am and Cm) surfaces and (b) surface defect of AnO_2 surfaces. All energies are calculated at the PBE + U (U_{eff} = 4.00 eV) level.

3.4 Conclusions

In this contribution, we have studied bulk and surface properties of the minor actinide dioxides $MAnO_2$ (MAn = Np, Am, Cm), focusing on the {111}, {110} and {100} surfaces. Comparison of bulk data with experiment allowed us to establish suitable computational parameters to apply to our surface studies of vacancy formation energies and water adsorption. While the PBE and PBESol functionals behave quite similarly for bulk properties, PBE is found to be much better than PBESol for the simulation of surfaces. The Hubbard U value has a clear influence on bulk properties such as lattice constant, band gap and density of states, and surface energies and water adsorption. Overall, we recommend the PBE functional in conjunction with a U_{eff} value of 4.0 eV for the study of the surface properties of these systems.

Oxygen vacancy surface defects not only have clear influence on the geometric structures of $MAnO_2$ surfaces, but also on the electronic distribution at the surface actinides. For NpO_2 and AmO_2, the two electrons left behind on oxygen vacancy creation localise on two surface actinides neighbour the vacancy (more so for NpO_2 than AmO_2), while for CmO_2 these electrons are spread throughout the whole slab. Combining our present data with those we have previously acquired for UO_2 and PuO_2 shows that the oxygen defect generation energy is essentially linearly correlated with the An(IV)/(III) redox potential from U to Cm.

Across the different surfaces and oxides, the geometries of adsorbing water molecules are quite similar. On all stoichiometric $MAnO_2$ {100} surfaces, dissociative water adsorption is more stable than molecular adsorption, as is also the case for dissociative adsorption on stoichiometric NpO_2 and AmO_2 {110} surfaces. By contrast, on all {111} surfaces and CmO_2 {110}, molecular and dissociative adsorption energies are very close. Regardless of whether water approaches a surface actinide or a surface defect, the energies for dissociative adsorption are much larger than molecular; indeed, for the higher index NpO_2 and CmO_2 surfaces, no molecular adsorption could be stabilised above a surface oxygen vacancy. In general, the energies of water adsorptions above surface actinides at reduced surfaces are more negative than surface actinides at stoichiometric surfaces, indicating that the existence of surface defects enhances the activity of the surface actinides. Across the series from UO_2 to CmO_2, there is a slight general tendency towards weaker dissociative water adsorption on oxygen vacancy surfaces, with the exception of the PuO_2 {100} surface, which yields much more stable dissociative water adsorption than the other oxides. This is also true of water adsorptions above stoichiometric PuO_2 {100}, in agreement with the very hygroscopic nature of PuO_2, and warrants further investigation.

References

1. Bo, T.; Lan, J. H.; Zhao, Y. L.; Zhang, Y. J.; He, C. H.; Chai, Z. F.; Shi, W. Q., First-principles study of water adsorption and dissociation on the UO_2 (111), (110) and (100) Surfaces. *J. Nucl. Mater.* **2014**, *454*, 446-454.

2. Cohen, S.; Mintz, M. H.; Zalkind, S.; Seibert, A.; Gouder, T.; Shamir, N., Water chemisorption on a sputter deposited uranium dioxide film - effect of defects. *Solid State Ionics* **2014**, *263*, 39-45.

3. Jomard, G.; Bottin, F.; Geneste, G., Water adsorption and sissociation on the PuO_2(110) Surface. *J. Nucl. Mater.* **2014**, *451*, 28-34.

4. Maldonado, P.; Evins, L. Z.; Oppeneer, P. M., Ab initio atomistic thermodynamics of water reacting with uranium dioxide surfaces. *J. Phys. Chem. C* **2014**, *118*, 8491-8500.

5. Tian, X. F.; Wang, H.; Xiao, H. X.; Gao, T., Adsorption of water on UO_2 (111) surface: density functional theory calculations. *Comput. Mater. Sci.* **2014**, *91*, 364-371.

6. Wellington, J. P. W.; Kerridge, A.; Austin, J.; Kaltsoyannis, N., Electronic structure of bulk AnO_2 (An = U, Np, Pu) and water adsorption on the (111) and (110) surfaces of UO_2 and PuO_2 from hybrid density functional theory within the periodic electrostatic embedded cluster method. *J. Nucl. Mater.* **2016**, *482*, 124-134.

7. Tegner, B. E.; Molinari, M.; Kerridge, A.; Parker, S. C.; Kaltsoyannis, N., Water adsorption on AnO_2 {111}, {110}, and {100} surfaces (An = U and Pu): A density functional theory plus U study. *J. Phys. Chem. C* **2017**, *121*, 1675-1682.

8. Tegner, B. E.; Kaltsoyannis, N., Multiple water layers on AnO_2 {111}, {110}, and {100} surfaces (An = U, Pu): A computational study. *J. Vac. Sci. Technol., A* **2018**, *36*.

9. Wellington, J. P. W.; Tegner, B. E.; Collard, J.; Kerridge, A.; Kaltsoyannis, N., Oxygen vacancy formation and water adsorption on reduced AnO_2 {111}, {110}, and {100} surfaces (An = U, Pu): A computational Study. *J. Phys. Chem. C* **2018**, *122*, 7149-7165.

10. Petit, L.; Svane, A.; Szotek, Z.; Temmerman, W. M.; Stocks, G. M., Electronic Sstructure and ionicity of actinide oxides from first principles. *Phys. Rev. B* **2010**, *81*.

11. Fournier, J. M.; Blaise, A.; Amoretti, G.; Caciuffo, R.; Larroque, J.; Hutchings, M. T.; Osborn, R.; Taylor, A. D., High-energy-neutron spectroscopy of crystal-field excitations in NpO_2. *Phys. Rev. B* **1991**, *43*, 1142-1145.

12. Nishi, T.; Nakada, M.; Itoh, A.; Suzuki, C.; Hirata, M.; Akabori, M., EXAFS and XANES studies of americium dioxide with fluorite structure. *J. Nucl. Mater.* **2008**, *374*, 339-343.

13. Hou, L.; Li, W. D.; Wang, F. W.; Eriksson, O.; Wang, B. T., Structural, electronic, and thermodynamic properties of curium dioxide: Density functional theory calculations. *Phys. Rev. B* **2017**, *96*.

14. Nishi, T.; Itoh, A.; Takano, M.; Numata, M.; Akabori, M.; Arai, Y.; Minato, K., Thermal conductivity of neptunium dioxide. *J. Nucl. Mater.* **2008**, *376*, 78-82.

15. Benes, O.; Gotcu-Freis, P.; Schworer, F.; Konings, R. J. M.; Fanghanel, T., The high temperature heat capacity of NpO_2. *J. Chem. Thermodyn.* **2011**, *43*, 651-655.

16. Arima, T.; Yoshida, K.; Matsumoto, T.; Inagaki, Y.; Idemitsu, K., Thermal conductivities of ThO_2, NpO_2 and their related oxides: molecular dynamics study. *J. Nucl. Mater.* **2014**, *445*, 175-180.

17. Gotcu-Freis, P.; Colle, J. Y.; Hiernaut, J. P.; Konings, R. J. M., The vaporisation behaviour of americium dioxide by use of mass spectrometry. *J. Nucl. Mater.* **2011**, *409*, 194-198.

18. Uchida, T.; Arima, T.; Idemitsu, K.; Inagaki, Y., Thermal conductivities of americium dioxide andsesquioxide by molecular dynamics simulations. *Comput. Mater. Sci.* **2009**, *45*, 229-234.

19. Teterin, Y. A.; Teterin, A. Y.; Ivanov, K. E.; Ryzhkov, M. V.; Maslakov, K. I.; Kalmykov, S. N.; Petrov, V. G.; Enina, D. A., X-Ray photoelectron spectra structure and chemical bond nature in NpO_2. *Phys. Rev. B* **2014**, *89*.

20. McCleskey, T. M., et al., Optical band gap of NpO_2 and PuO_2 from optical absorbance of epitaxial films. *J. Appl. Phys.* **2013**, *113*.

21. Teterin, Y. A.; Maslakov, K. I.; Ryzhkov, M. V.; Teterin, A. Y.; Ivanov, K. E.; Kalmykov, S. N.; Petrov, V. G., X-Ray photoelectron spectra structure and chemical bonding in AmO_2. *Nuclear Technology & Radiation Protection* **2015**, *30*, 83-98.

22. Teterin, Y. A.; Maslakov, K. I.; Ryzhkov, M. V.; Teterin, A. Y.; Ivanov, K. E.; Kalmykov, S. N.; Petrov, V. G., Nature of chemical bond in AmO_2. *Radiochemistry* **2015**, *57*, 565-574.

23. Asprey, L. B.; Ellinger, F. H.; Fried, S.; Zachariasen, W. H., Evidence for quadrivalent curium - X-Ray data on curium oxides. *JACS* **1955**, *77*, 1707-1708.

24. Gubanov, V. A.; Chirkov, A. K., Electronic-structure and ESCA spectra of curium dioxide. *Inorg. Nucl. Chem. Lett.* **1978**, *14*, 139-142.

25. Pegg, J. T.; Aparicio-Angles, X.; Storr, M.; de Leeuw, N. H., DFT plus U study of the structures and properties of the actinide dioxides. *J. Nucl. Mater.* **2017**, *492*, 269-278.

26. Suzuki, M. T.; Magnani, N.; Oppeneer, P. M., Microscopic theory of the insulating electronic ground states of the actinide dioxides AnO_2 (An= U, Np, Pu, Am, and Cm). *Phys. Rev. B* **2013**, *88*.

27. Prodan, I. D.; Scuseria, G. E.; Martin, R. L., Covalency in the actinide dioxides: systematic study of the electronic properties using screened hybrid density functional theory. *Phys. Rev. B* **2007**, *76*.

28. Wang, B. T.; Shi, H. L.; Li, W. D.; Zhang, P., First-principles LDA plus U and GGA plus U Study of Neptunium Dioxide. *Phys. Rev. B* **2010**, *81*.

29. Lu, Y.; Yang, Y.; Zheng, F. W.; Wang, B. T.; Zhang, P., Electronic, mechanical, and thermodynamic properties of americium dioxide. *J. Nucl. Mater.* **2013**, *441*, 411-420.

30. Suzuki, C.; Nishi, T.; Nakada, M.; Akabori, M.; Hirata, M.; Kaji, Y., Core-hole effect on XANES and electronic structure of minor actinide dioxides with fluorite structure. *J. Phys. Chem. Solids* **2012**, *73*, 209-216.

31. Naegele, J. R.; Cox, L. E.; Ward, J. W., Photoelectron-spectroscopy (UPS XPS) study of Np_2O_3 formation on the surface of neptunium metal. *Inorganica Chim. Acta* **1987**, *139*, 327-329.

32. Cakir, P.; Eloirdi, R.; Huber, F.; Konings, R. J. M.; Gouder, T., Surface reduction of neptunium dioxide and uranium mixed oxides with plutonium and thorium by photocatalytic reaction with Ice. *J. Phys. Chem. C* **2015**, *119*, 1330-1337.

33. Bo, T.; Lan, J. H.; Zhao, Y. L.; Zhang, Y. J.; He, C. H.; Chai, Z. F.; Shi, W. Q., Surface properties of NpO_2 and water reacting with stoichiometric and reduced NpO_2 (111), (110), and (100) surfaces from ab initio atomistic thermodynamics. *Surf. Sci.* **2016**, *644*, 153-164.

34. Rak, Z.; Ewing, R. C.; Becker, U., Hydroxylation-induced surface stability of AnO_2 (An = U, Np, Pu) from first-principles. *Surf. Sci.* **2013**, *608*, 180-187.

35. Kresse, G.; Hafner, J., Abinitio molecular-dynamics for liquid-metals. *Phys. Rev. B* **1993**, *47*, 558-561.

36. Kresse, G.; Hafner, J., Ab-initio molecular-dynamics simulation of the liquid-metal amorphous-semiconductor transition in germanium. *Phys. Rev. B* **1994**, *49*, 14251-14269.

37. Kresse, G.; Furthmuller, J., Efficiency of ab-initio total energy calculations for metals and semiconductors using a plane-wave basis set. *Comput. Mater. Sci.* **1996**, *6*, 15-50.

38. Kresse, G.; Furthmuller, J., Efficient iterative dchemes for ab initio total-energy calculations using a plane-wave basis set. *Phys. Rev. B* **1996**, *54*, 11169-11186.

39. Csonka, G. I.; Perdew, J. P.; Ruzsinszky, A.; Philipsen, P. H. T.; Lebegue, S.; Paier, J.; Vydrov, O. A.; Angyan, J. G., Assessing the performance of recent density functionals for bulk solids. *Phys. Rev. B* **2009**, *79*.

40. Perdew, J. P.; Burke, K.; Ernzerhof, M., Generalized gradient approximation made simple (Vol 77, Pg 3865, 1996). *Phys. Rev. Lett.* **1997**, *78*, 1396-1396.

41. Liechtenstein, A. I.; Anisimov, V. I.; Zaanen, J., Density-functional Theory and strong-interactions - orbital ordering in Mott-Hubbard Iinsulators. *Phys. Rev. B* **1995**, *52*, R5467-R5470.

42. Blochl, P. E., Projector augmented-wave method. *Phys. Rev. B* **1994**, *50*, 17953-17979.

43. Monkhorst, H. J.; Pack, J. D., Special points for brillouin-zone integrations. *Phys. Rev. B* **1976**, *13*, 5188-5192.

44. Mannix, D.; Lander, G. H.; Rebizant, J.; Caciuffo, R.; Bernhoeft, N.; Lidstrom, E.; Vettier, C., Unusual magnetism of NpO_2: A study with resonant X-Ray scattering. *Phys. Rev. B* **1999**, *60*, 15187-15193.

45. Tokunaga, Y.; Nishi, T.; Kambe, S.; Nakada, M.; Itoh, A.; Homma, Y.; Sakai, H.; Chudo, H., NMR evidence for the 8.5k phase transition in americium dioxide. *J. Phys. Soc. Jpn.* **2010**, *79*.

46. Tokunaga, Y.; Nishi, T.; Nakada, M.; Itoh, A.; Sakai, H.; Kambe, S.; Homma, Y.; Honda, F.; Aoki, D.; Walstedt, R. E., Self-radiation effects and glassy nature of magnetic transition in AmO_2 revealed by O-17-NMR. *Phys. Rev. B* **2014**, *89*.

47. Momma, K.; Izumi, F., Vesta 3 for Three-dimensional visualization of crystal, volumetric and morphology Data. *J. Appl. Crystallogr.* **2011**, *44*, 1272-1276.

48. Yamashita, T.; Nitani, N.; Tsuji, T.; Inagaki, H., Thermal expansions of NpO_2 and some other actinide dioxides. *J. Nucl. Mater.* **1997**, *245*, 72-78.

49. Hurtgen, C.; Fuger, J., Self-irradiation effects in americium oxides. *Inorg. Nucl. Chem. Lett.* **1977**, *13*, 179-188.

50. Chikalla, T. D.; Eyring, L., Phase relationships in americium-oxygen dystem. *J. Inorg. Nucl. Chem.* **1968**, *30*, 133-&.

51. Noé, M.; Fuger, J., Self-radiation effects on the lattice parameter of $^{244}CmO_2$. *Inorg. Nucl. Chem. Lett.* **1971**, *7*, 421-430.

52. Wu, X. Y.; Ray, A. K., Density-functional study of water adsorption on the PuO_2(110) surface. *Phys. Rev. B* **2002**, *65*.

53. Nolan, M.; Parker, S. C.; Watson, G. W., The electronic structure of oxygen vacancy defects at the low index surfaces of ceria. *Surf. Sci.* **2005**, *595*, 223-232.

54. Somorjai, G. A.; Li, Y., Introduction to surface chemistry and catalysis; John Wiley & Sons, 2010.

55. Bo, T.; Lan, J. H.; Wang, C. Z.; Zhao, Y. L.; He, C. H.; Zhang, Y. J.; Chai, Z. F.; Shi, W. Q., First-principles study of water reaction and H_2 formation on UO_2 (111) and (110) single crystal surfaces. *J. Phys. Chem. C* **2014**, *118*, 21935-21944.

56. Sun, B.; Liu, H. F.; Song, H. F.; Zhang, G. C.; Zheng, H.; Zhao, X. G.; Zhang, P., First-principles study of surface properties of PuO_2: Effects of thickness and O-vacancy on surface stability and chemical activity. *J. Nucl. Mater.* **2012**, *426*, 139-147.

57. Sattonnay, G.; Tetot, R., Bulk, surface and point defect properties in UO_2 from a tight-binding variable-charge model. *J. Phys. Condens. Matter* **2013**, *25*.

58. Stakebake, J. L., The storage behavior of plutonium metal, alloys, and oxide: A review. *J. Nucl. Mater.* **1971**, *38*, 241-259.

DFT + *U* study of $U_{1-y}An_yO_{2-x}$ (An = Np, Pu, Am and Cm) {111}, {110} and {100} surfaces

Jia-Li Chen and Nikolas Kaltsoyannis

Abstract

Mixed dioxides provide a means to recycle the highly radioactive transuranic elements from spent UO_2 fuel. In order to gain a better understanding of such dioxides, knowledge of their geometric and electronic structures is important. However, a systematic study and comparison among uranium-actinide mixed dioxides is lacking. In this work, Hubbard *U*-corrected generalized gradient approximation density functional theory is used to study the surface properties of uranium-actinide mixed dioxides, where actinide = neptunium, plutonium, americium or curium. On stoichiometric surfaces, clear charge transfer is found from uranium to americium and curium, reducing them to An(III), while Np remains tetravalent. Trivalent plutonium may exist on stoichiometric uranium-plutonium surfaces, under limited conditions. On the substoichiometric (oxygen vacancy) mixed dioxide surfaces, all the transuranic elements are trivalent. Both the replacement energies of actinides into uranium dioxide surfaces, and the oxygen vacancy formation energies on uranium-actinide mixed dioxide surfaces, are strongly dependent on the An(IV)/An(III) redox potential. A linear relationship is also found between the replacement energy and the ratio of actinide to uranium in the mixed dioxides.

4.1 Introduction

Nuclear fuel is typically uranium dioxide (UO_2), and the fission of UO_2 in conventional nuclear reactors, as well as, in some countries such as the UK, the reprocessing of UO_2-based spent nuclear fuel, has led to the accumulation of considerable amounts of plutonium, together with smaller quantities of the so-called minor actinides (MAn), neptunium, americium and curium.[1] The plutonium may be blended with uranium to create uranium-plutonium mixed dioxide (U-Pu MOX) nuclear fuel, to be used in either light water reactors or fast breeder reactors.[2-5] The MAn have high radioactivity and they, or their daughters, have long half-lives. Their presence in spent nuclear fuels is thus a non-trivial problem, and it has been proposed to extend the industrial reprocessing technologies in operation today to include a full recycling of all actinides, including the MAn.[6-8] These, in the form of their dioxides, could be mixed into nuclear fuel for use in fast neutron reactors, and hence we must have a clear understanding of the properties of uranium-actinide mixed dioxides, including their surface properties. The latter are particularly important in order to understand the interactions between the fuel pellets and the surrounding cladding. Furthermore, plutonium from reprocessing is stored as PuO_2, in which radioactive decay leads to the build-up of U and Am, and knowledge of the surface chemistry of these mixed dioxides (especially their interactions with water) is important for their safe storage.[9]

U-Pu MOX is the most studied U-An MOX, as MOX with low Pu content ($PuO_2 < 10\%$) is used as nuclear fuel,[2-5] and higher plutonium content is expected to be favourable for fast neutron reactors.[6] U-Pu MOX with Pu to U ratios of up to 0.45:0.55 have been studied;[10-11] the stoichiometric samples are found to be monophasic in the fluorite *Fm-3m* crystalline structure, and the lattice parameters are in good agreement with Vegard's law. An EXAFS-XANES study from Vigier and co-workers confirms the presence of Pu(III) in the substoichiometric sample $U_{0.7}Pu_{0.3}O_{2-x}$.[11] While Pu(III) has not been reported in stoichiometric samples yet, it may well be present. Kato *et al*. found that the oxygen potential of U-Pu MOX increases with Pu content.[12] U(IV)-Pu(III) oxides have been synthesized by Grandjean *et al*. from U(IV) and Pu(III) oxalate precursors.[13]

A much wider range of Np content, from 1% to 85%, has been studied for uranium-neptunium mixed dioxide.[14-15] The fluorite *Fm-3m* crystal structure was found for all the solid solutions, with no residual phases, and all the lattice parameters follow Vegard's law exceptionally well, indicating good mixing in the solid solution. U and Np are tetravalent in MOX with Np: U ratios of up to 0.90:0.10,[14-16] and antiferromagnetic ordering is energetically favourable.[14, 17] XRD analysis of uranium-americium mixed dioxide proves that the MOX is a single-phased fluorite compound whatever the sintering conditions and Am content (10% - 50%).[18-20] In MOX with 10%, 15%, 20% and 50% Am content, Am was found to be exclusively trivalent, while U was found to be mixed valence (IV/V).[18-21] Cm in MOX nuclear fuel has been analysed by Degueldre and co-workers, who found the Cm to be trivalent and embedded in the form of CmO_8^{13-} or CmO_7^{11-} within the fluorite structure of the UO_2 matrix.[22] Grandjean *et al*. synthesized U(IV)-Cm(III) oxides and characterized the mixed dioxide with a Cm to U ratio of 0.10: 0.90 as being face-centred cubic with an oxygen to metal ratio probably less than 2.00:1.00.[13]

Previous work on U-An MOX mainly focuses on bulk properties, and a systematic comparison of their surfaces across the series to Cm is lacking. The high radioactivity of these elements limits experimental studies, and we were therefore motivated to simulate U-An MOX (An = Np, Pu, Am and Cm) {111}, {110} and {100} surfaces with the density functional theory (DFT) + U method, investigating geometric and electronic properties, as well as oxygen vacancy formation on these surfaces. We first discuss stoichiometric and substoichiometric UO_2 {111}, {110} and {100} surfaces, and then present results for Np, Pu, Am or Cm substituted into those surfaces such that the ratio of An to U is 0.08:0.92. We then probe the effects of substituting An into subsurface layers of the stoichiometric and oxygen vacancy UO_2 {111} surface, before finishing by exploring systems with higher concentrations of An. Systematic comparisons across the series are made wherever possible.

4.2 Computational details

All calculations were performed using DFT, as implemented in the Vienna Ab-initio Simulation Package (VASP), version 5.4.1.[23-26] The generalized gradient approximation functional of Perdew, Burke, and Ernzerhof (PBE) was used,[27] with a Hubbard U correction for the 5f electrons (U_{eff} = 4 eV; U = 4.5 eV, J = 0.5 eV).[28] In our previous work on UO_2, PuO_2, and $MAnO_2$, we evaluated the effect of changing the effective Hubbard U (U_{eff}) on bulk lattice parameter and band gap, as well as on surface properties, concluding that a U_{eff} of 4 eV is a good choice for this family of dioxides.[29-30] We also tested the PBESol functional, which has previously been used by other researchers for studying bulk AnO_2, concluding that it is not as good as PBE for surface properties.[30]

Plane wave basis sets and projector augmented wave pseudopotentials were used to describe the ions.[31] A plane wave cutoff of 650 eV was adopted for all calculations. As our cutoff energy is large enough, the Pulay stress can be neglected. Monkhorst-Pack (MP) grids were employed for the k-space integration;[32] a minimum MP grid of 5 × 5 × 1 k points for the Brillouin zone sampling was used for the surface simulations. A 1k colinear magnetic ordering with a net magnetic moment of zero was used,[33] the total system being treated as antiferromagnetic (AFM). Spin−orbit coupling has been neglected; earlier results by Rak and co-workers indicate that spin−orbit coupling has only a very small effect on surface stability.[34]

We have previously minimized UO_2 {111}, {110} and {100} surfaces, constructed from repeating slabs of 24 UO_2 units arranged in six layers, and demonstrated convergence of the UO_2 surface energy with slab depth.[29] The initial structures of the UO_2 surfaces used here are taken from that work, and reoptimized. Each surface is 2 × 2 with 18 Å of vacuum between each slab. The f electrons of U in the first, third, and fifth layers are unpaired and spin up, and spin down in the second, fourth, and sixth layers, in order to keep the whole slab AFM.

For MOX and substoichiometric surfaces, the same slab shape and volume as for the UO_2 surfaces are used, but the ions are allowed to move during optimization (ISIF = 2). This means that the surface lattice parameters can vary. For the {111}, {110}, and {100} surfaces respectively, these are defined as the distances between surface atoms numbered 1 and 2, and 1 and 4 (Figure 4.1 (a)), and 1 and 2, and 1 and 3 (Figure 4.1 (b) and (c)). For UO_2, these distances are 3.86 × 3.87, 5.59 × 3.80, and 3.78 × 4.07 Å, respectively; the distortions arise from the use of the 1k colinear magnetic ordering approximation. No reconstruction was observed.

Substitution of other An (Np, Pu, Am and Cm) is done on both sides of the slab to minimize dipole effects. Thus, the chemical formula of stoichiometric U-An MOX surfaces is $U_{24-2n}An_{2n}O_{48}$ or $U_{1-y}An_yO_2$, where n is the number of substituted An on one side of the UO_2 slab and y:1-y is the ratio of An to U. Substoichiometric UO_2 and U-An MOX are constructed from the stoichiometric surfaces by removing an oxygen atom from both sides of the surface, so the ratio of O to An, or to U and An is 1.92: 1.

All the periodic images were made using VESTA.[35]

Surface energies of UO_2 (E_{sur}) are calculated according to equation 4.1:

$$E_{sur} = \frac{1}{2S}(E_{slab} - 6E_{bulk}) \tag{4.1}$$

where E_{slab} is the energy of the relaxed UO_2 slab, which contains six U_4O_8 formula units, and E_{bulk} is the energy of the bulk, which contains one U_4O_8 formula unit.

The replacement energy of An into UO_2 surfaces (E_{rep}) is calculated according to equation 4.2:

$$E_{rep} = \frac{1}{2}\left[E_{MOX} - \left((1-y)E_{UO_2} + yE_{AnO_2}\right)\right] \tag{4.2}$$

where E_{MOX}, E_{UO2} and E_{AnO2} are the energy of U-An MOX, UO_2 and AnO_2 surfaces, respectively. The energies of AnO_2 surfaces are taken from our previous work. *y*:1-*y* is the ratio of An to U in MOX. The factor of 1/2 is due to the substitution being done on both sides of the slabs.

Oxygen vacancy formation energies (E_{red}) are calculated according to equation 4.3:

$$E_{red} = \frac{1}{2}\left(E_{sub} + E_{O_2} - E_{sto}\right) \tag{4.3}$$

where E_{sub} and E_{sto} are the energies of the relaxed substoichiometric and stoichiometric surfaces, and the E_{O2} is the energy of a single oxygen molecule, in its triplet ground state, in a box with a 20 Å side. The factor of 1/2 is due to the generation of vacancies on both slides of the slab.

Spin density data are reported extensively throughout this work. Spin densities are calculated as the difference between the number of α spin (spin up) and β spin (spin down) electrons, and have units of electron density (i.e. electrons/ $bohr^3$). This can be evaluated on a per-atom basis. For actinides in positive oxidation states, the excess (α-β) spin density is due to unpaired 5f electrons, and the difference between this value and the total number of valence electrons in the neutral atom can be used to establish oxidation state. For example, a formally U(IV) ion will have the electronic configuration {Rn}$5f^2$, so if we calculate a U atom to have a spin density close to two, then we can be confident in assigning it as U(IV), that is, it is tetravalent. For U(III), the electronic configuration will be {Rn}$5f^3$ and, hence, the computed spin density on a U(III) centre will be close to three. The electronic configurations and expected spin densities of all actinides encountered in this work are summarized in Table 4.1.

Table 4.1: Electronic configurations and associated spin densities of actinide ions.

Oxidation state	III		IV	
actinide	Electronic configuration	Spin density	Electronic configuration	Spin density
U	{Rn}5f^3	3	{Rn}5f^2	2
Np	{Rn}5f^4	4	{Rn}5f^3	3
Pu	{Rn}5f^5	5	{Rn}5f^4	4
Am	{Rn}5f^6	6	{Rn}5f^5	5
Cm	{Rn}5f^7	7	{Rn}5f^6	6

4.3 Results and discussion

4.3.1 UO_2 and UO_{2-x} surfaces

Stoichiometric uranium dioxide (UO_2) slabs have been optimized for {111}, {110} and {100} surfaces (Figure 4.1 (a), (b) and (c), respectively). The surface energies (equation 4.1) are calculated to be 0.51, 0.91, and 1.34 J/m^2, in good agreement with our previous periodic simulation (0.65, 1.05 and 1.33 J/m^2, respectively) and the work of Bo *et al.* (0.73 and 1.06 eV for the {111} and {110} surfaces, respectively).[29, 36] Oxygen vacancy (substoichiometric) UO_2 surfaces were also simulated (Figure 4.1 (d), (e) and (f), respectively). Oxygen vacancy formation energies (equation 4.3) are 5.81, 5.47, and 4.98 eV on {111}, {110} and {100} surfaces, respectively, in good agreement with our PBE0 simulations with the Periodic Electrostatic Embedded Cluster Method (5.92, 5.15, and 4.96 eV, respectively).[37] However, we reported larger formation energies in our previous periodic simulation of UO_2 {111}, {110} and {100} surfaces (6.45, 5.69, 5.93, respectively).[29] The difference for the {111} and {100} surfaces is larger than 0.6 eV, even though the same computational parameters were used. It is possible that the disagreement is due to the location of metastable states in our previous work, as the DFT + *U* method is known to suffer from this problem.[38]

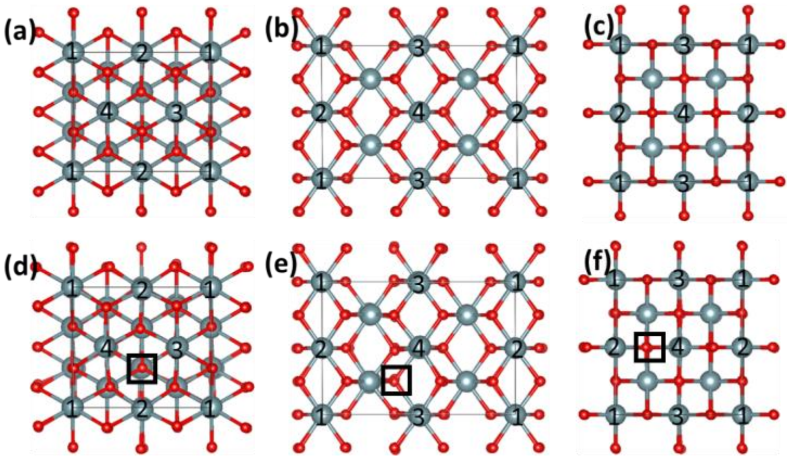

Figure 4.1: Top view of stoichiometric ((a), (b) and (c)) and substoichiometric ((d), (e) and (f)) UO_2 {111}, {110} and {100} surfaces, respectively. Blue-grey and red spheres represent U and O, respectively. The black squares in (d), (e) and (f) mark the position of the oxygen vacancy. The numbers on the surface U atoms are referred to elsewhere in the article.

The spin density of U in the stoichiometric surfaces is about 2 (Table 4.2), indicating that U has 2 unpaired f electrons and is tetravalent, and the spin density of the whole slab is 0, indicating the whole slab is AFM, which is the experimentally reported bulk ground state.[39] For the substoichiometric surfaces, it is important to understand the electron redistribution after the generation of the oxygen vacancies. As a neutral oxygen atom is removed from each side of stoichiometric slab to build the substoichiometric surfaces, two electrons remain at each surface vacancy. The spin density of some surface U ions show clear differences between stoichiometric and substoichiometric surfaces (Table 4.2). On the substoichiometric {111} surface, one surface U has spin density of ~2.9, so one of the electrons has localized on this U, which is reduced to trivalent. Trivalent U has also been found on the substoichiometric {111} surface in previous studies.[36-38] Previous periodic and embedded cluster simulations found that about one electron is delocalized on two other surface U;[36-37] we here find two surface U to have a spin density of ~2.2, but this accounts for only about half an electron in total. Recent PBE + *U* simulations of substoichiometric UO_2 surfaces found that the ground state has some spin density located at the vacancy.[38] We therefore evaluated the difference between the sum of the charge density of the substoichiometric surface and oxygen atoms at the same position as the removed oxygen in a same-sized but empty slab (Appendix 2, Figure A4.1 (b)), and that of the stoichiometric surface represented as the substoichiometric surface with an oxygen atom at the vacancy (Figure A4.1 (c)). The charge differences are given in Figure A4.2, from which it can be seen that we also find charge density located at the vacancy. Therefore, about one electron is localized on a surface U and the other one is delocalized over the vacancy and two other surface U neighbour the vacancy. On the substoichiometric {110} and {100} surfaces, two surface U have increased spin density (Table 4.2), in agreement with previous theoretical simulation. Again, there is also some charge remaining at the O vacancy on these surfaces (Figure A4.2).

Table 4.2: Spin densities of surface U on stoichiometric and substoichiometric UO_2 surfaces. The U number is marked in Figure 4.1.

Spin density		Surface U			
Surface		No. 1	No. 2	No. 3	No. 4
{111}	stoichiometric	2.030	2.037	2.027	2.039
	substoichiometric	2.051	**2.202**	**2.953**	**2.243**
{110}	stoichiometric	2.028	2.028	2.032	2.032
	substoichiometric	2.032	2.031	**2.823**	**2.821**
{100}	stoichiometric	2.033	2.033	2.033	2.033
	substoichiometric	2.042	**2.303**	2.052	**2.959**

4.3.2 $U_{0.92}An_{0.08}O_2$ surfaces with surface An

In this section we discuss the replacement of one surface U by An (Np, Pu, Am, or Cm) on each side of pure UO_2, *i.e.* the ratio of An to U in the MOX is 0.08:0.92 and the chemical formula is $U_{0.92}An_{0.08}O_2$ (designated U-An MOX-8); the $U_{0.92}Np_{0.08}O_2$ (U-Np MOX-8) surfaces are shown as representative examples in Figure 4.2 (a), (b) and (c). The symmetry of the solid solution is the same as in pure UO_2, single-phased fluorite, and the surface lattice constants show only negligible difference between UO_2 and MOX-8 (Table A4.1), so no surface reconstruction is found.

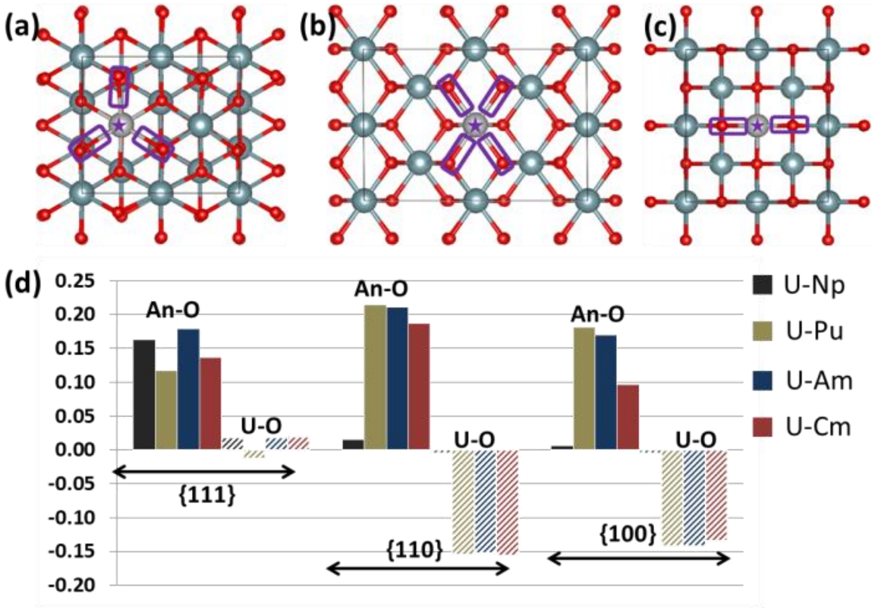

Figure 4.2: Top view of $U_{0.92}Np_{0.08}O_2$ (a) {111}, (b) {110} and {100} surfaces, as well as (d) the average displacement of surface An-O (An = Np, Pu, Am, and Cm) bonds (solid columns) and surface U-O bonds (diagonal columns). Blue-grey, light grey and red spheres represent U, Np and O, respectively. Purple boxes in (a), (b) and (c) mark the surface An-O bonds that are measured to calculate the average displacement in (d).

In order to gain insight into the influence of An substitution on surface geometric structure, the lengths of three, four and two An-O bonds (highlighted in Figure 4.2) are compared for AnO_2 and MOX-8 {111}, {110} and {100} surfaces, respectively. The bond lengths on pure AnO_2 surfaces are taken from our previously calculated results (Table A4.2).[9, 30] The U-O bonds to a surface U, which neighbours a substituted An, on the MOX-8 surface are compared with the corresponding U-O bonds on pure UO_2 surfaces (Table A4.3). The average displacement of surface An-O and U-O bonds are compared in Figure 4.2 (d) for different An and surfaces. Positive displacement means the bond is elongated on the MOX-8 surface compared to pristine UO_2, while negative displacement means the bond is shortened. On the {111} surfaces, substitution of An has little influence on the surface U-O bond length, as the displacements are smaller than 0.02 Å, while significant elongation of the An-O bonds, of about 0.15 Å, is found on all U-An MOX-8. The An-O bond lengths on the pure AnO_2 surfaces are close to the U-O bond length on pure UO_2 surfaces (Table A4.2), and hence the elongation of the An-O bonds on MOX-8 surfaces is mainly due to the substitution (*i.e.* the contribution of the difference between the original An-O and U-O bond lengths is negligible). By contrast, on the {110} and {100} surfaces, the influence of Np is quite different from Pu, Am and Cm. As we can see in Figure 4.2 (d), on U-Np MOX-8, the surface Np-O and U-O bond lengths are almost the same as the corresponding distances on pure NpO_2 and UO_2 surfaces, respectively, while substitution of Pu, Am and Cm causes elongation of the An-O bonds and shortening of the U-O bonds. These displacements influence the surface electronic structure. On U-An MOX-8 {111} and U-Pu, U-Am and U-Cm MOX-8 {110} and {100} surfaces, the overlap between the charge isosurfaces (at the 0.05 $e/\text{Å}^3$ level) of the surface An and O is much smaller than between surface U and O (Figure A4.3). However, on the U-Np MOX-8 {110} and {100} surfaces, the overlap between the charge isosurfaces of Np and O is almost the same as for U and O (Figure A4.3), indicating that Np blends into the UO_2 {110} and {100} surfaces very well, most likely a result of the similar radii of U(IV) and Np(IV).

An substitution has a negligible effect on the spin density of the U ions in subsurface layers. Table 4.3 summarizes the spin density of the An and the three surface U on MOX-8 surfaces, together with analogous U-Zr MOX-8 surfaces. The redox inactivity of Zr(IV) makes U-Zr MOX-8 a useful benchmark to analyse the electron distribution on U-An MOX-8 surfaces, and previous studies of Zr and U mixed oxides suggest that up to 35 mol% of Zr can be incorporated into UO_2, forming a cubic fluorite type $U_{1-y}Zr_yO_2$ solid solution.[40-43] As expected, on U-Zr MOX-8 surfaces, negligible spin density is found on Zr, and the spin density of surface U is almost the same as on pure UO_2 surfaces (Table 4.2), so substitution of Zr has almost no influence on the charge state of surface U.

Table 4.3: Spin density (au) of surface U, An (Np, Pu, Am, and Cm) and Zr on $U_{0.92}An_{0.08}O_2$ and $U_{0.92}Zr_{0.08}O_2$ surfaces. Spin densities with clear changes from the values expected for M(IV) are shown in bold.

MOX	An	{111}			{110)			{100}		
U-Zr	Zr	0.001			0.003			0.001		
	U	2.030	2.036	2.035	2.026	2.036	2.041	2.029	2.038	2.037
U-Np	Np	3.139			3.131			3.131		
	U	1.986	1.988	1.984	1.973	1.970	1.971	1.970	1.972	1.972
U-Pu	Pu	**4.995**			**4.993**			**4.996**		
	U	1.996	**1.125**	1.996	**1.086**	1.967	1.973	1.973	**1.078**	1.973
U-Am	Am	**6.036**			**6.030**			**6.028**		
	U	1.990	1.986	**1.123**	**1.087**	1.968	1.972	1.972	**1.108**	1.968
U-Cm	Cm	**6.858**			**6.841**			**6.851**		
	U	**1.101**	1.993	1.983	**1.075**	1.966	1.978	1.977	**1.091**	1.967

On all three U-Np MOX-8 surfaces, the spin density of surface Np and all surface U are about 3 and 2, so the surface Np and U are tetravalent, in agreement with experiment.[14-16] By contrast, for U-Pu, U-Am and U-Cm MOX-8 surfaces, the spin densities of surface Pu, Am and Cm are about 5, 6, and 7, respectively, so they are all trivalent. In previous experimental studies, only trivalent Am has been found in U-Am MOX containing up to 50% Am, in conjunction with mixed valent U (IV/V), in good agreement with our results.[18-21] As the Cm(IV)/(III) redox potential (3.00 V) is higher than Am(IV)/(III) (2.60 V), and Cm(III) has been found in U-Pu MOX nuclear fuel,[22] it is not surprising that we find trivalent Cm on the U-Cm MOX-8 surfaces. Although Pu (III) has not been reported in stoichiometric U-Pu MOX, Kato *et al.* found that the oxygen potential of U-Pu MOX increases with Pu content,[12] and other previous work confirms the presence of Pu(III) in substoichiometric $U_{0.7}Pu_{0.3}O_{2-x}$.[11] Hence our finding here of Pu(III) may not be unreasonable; the possibility of surface Pu(III) on stoichiometric U-Pu MOX-8 is discussed further below.

If we compare U-Np MOX-8 surfaces with the Zr equivalents, we can see that the three surface U have slightly smaller spin densities in the former system *vs* the latter (and pure UO_2), suggesting that substitution of Np results in the electrons of U becoming more delocalized and partially moving toward Np. The spin densities of two U on U-Pu, U-Am and U-Cm MOX-8 surfaces are similar to U in U-Np MOX-8, while the third U, which is next to An, has a spin density of slightly over 1. Hence substituted Pu, Am and Cm are reduced by obtaining the most part of an electron from a single, neighbour, U and a small part from the other two surface U.

The redox behaviour of the substituted An may well contribute to the displacements seen in Figure 4.2(d). An(III) are larger than An(IV), and should result in greater disruption to the surrounding lattice than substitution of An(IV). This is reflected in the contrasting behaviour of Np (which remains tetravalent) *vs* the heavier An on substitution into the {110} and {100} surfaces. That all four An have a similar structural effect on the {111} surface may reflect its greater inertness *vs* {110} and {100}, perhaps because of its larger metal coordination number (7 *vs* 6).

The replacement energies (equation 4.2) of An in UO_2 surfaces are compared in Figure 4.3 (a), and the energy for optimized UO_2 and AnO_2 surfaces are collected in Table A4.4. The replacement of a surface U with An becomes easier from {111} to {100} surfaces, presumably because the {111} surface is the most stable and the {100} the least, and the extent of the decrease is almost same for all An. For a given surface, the replacement energies decrease from Np to Cm (Figure 4.3 (a)). When we compare the replacement energy with An(IV)/(III) redox potential (0.15, 1.01, 2.60 and 3.00 eV for Np, Pu, Am and Cm, respectively) (Figure 4.3 (b)), for each surface, we find a very strong linear correlation, suggesting that redox potential is an important factor in determining replacement energy.

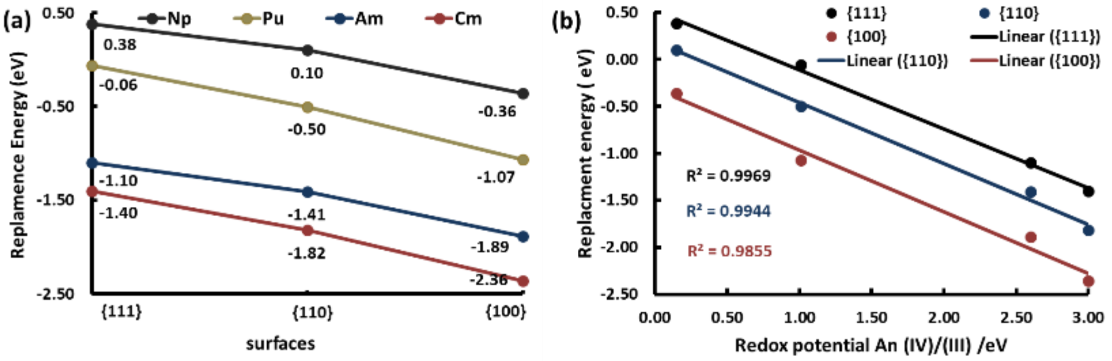

Figure 4.3: (a) Replacement energies for $U_{0.92}An_{0.08}O_2$ (An = Np, Pu, Am and Cm) {111}, {110} and {100} surfaces; (b) Replacement energy vs An (IV)/(III) redox potential. The lines joining the points in (a) are to guide the eye.

4.3.3 $U_{0.92}An_{0.08}O_{1.92}$ surfaces with surface An

Substoichiometric U-An MOX-8 surfaces (An = Np, Pu, Am or Cm) are obtained by removing an oxygen atom from each side of the associated stoichiometric surface, with the resulting chemical formula $U_{0.92}An_{0.08}O_{1.92}$. As we have both U and An on the surfaces, there are two kinds of oxygen vacancy, those next to surface An and those away from surface An. This is illustrated for substoichiometric U-Np MOX-8 surfaces in Figure 4.4; the structures of substoichiometric U-Pu, U-Am, and U-Cm MOX-8 surfaces are similar.

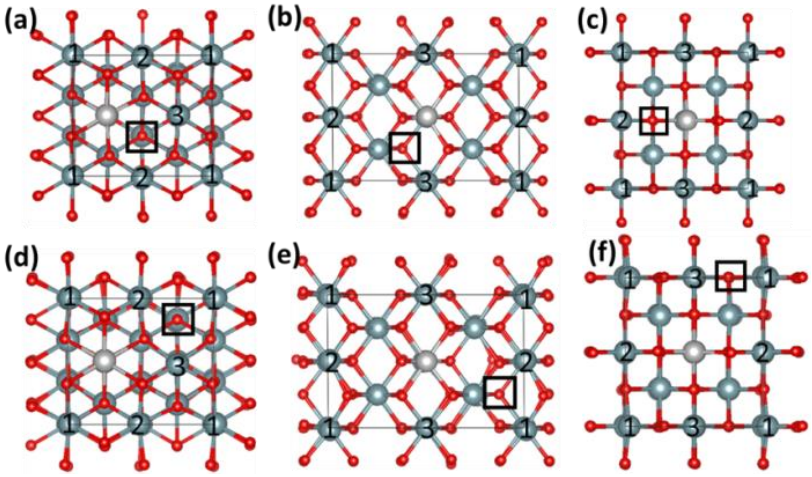

Figure 4.4: Top view of substoichiometric $U_{0.92}Np_{0.08}O_{1.92}$ surfaces, including surfaces with the O vacancy next to Np: (a) {111}, (b) {110} and (c) {100}; and surfaces with the O vacancy away from Np: (d) {111}, (e) {110} and (f) {100}. Blue-grey, light grey and red spheres represent U, Np and O, respectively. Black squares mark the position of the O vacancy.

The generation of O vacancies on MOX-8 surfaces causes distortion of the surface structure. The average displacement of neighbour cations (U and An) and O from the vacancy are presented in Figure 4.5. Positive displacement means the atom moves away from the vacancy, while a negative value indicates the atom moves towards the vacancy. On all surfaces, neighbour cations move away from the vacancy, while neighbour O move towards the vacancy, as is also the case on UO_2 and AnO_2 (An = Np-Cm) and Pu-Am MOX surfaces.[9, 30, 37] Our previous periodic study indicated that, on UO_2 {111}, {110} and {100} surfaces, the average displacement of vacancy-neighbour U is less than 0.2 Å, and less than 0.3 Å for neighbour O.[37] Here, we find similar displacements on U-An MOX-8 surfaces, and conclude that the influence of An on the surface bonds is negligible when compared with the displacements caused by the O vacancy. The average displacements on {111} surfaces are similar for both kinds of vacancy, while on the {110} and {100} surfaces, vacancies away from An result in larger displacements than when next to An, especially for the displacement of neighbour O. That the difference between the two kinds of O vacancy is noticeable only for the {110} and {100} surfaces again indicates the relative inertness of the {111} surfaces vs the {110} and {100}.

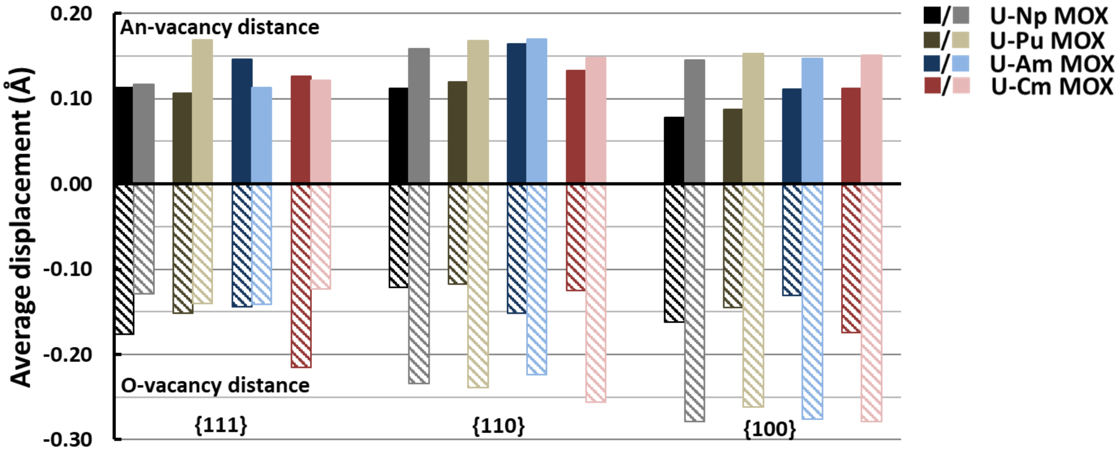

Figure 4.5: Average displacement of nearest neighbour atoms from the O vacancy on U-An MOX-8 surfaces; metal atoms (U, Np, Pu, Am and Cm, solid column) and O (hatched column). Positive displacement indicates the atom moves away from the vacancy site, whereas negative displacement indicates the atom moves toward. Dark and light colours represent O vacancy next to and away from substituted An (Np, Pu, Am and Cm), respectively.

As discussed above, generation of an O vacancy leaves behind two electrons, the distribution of which can be assessed by analysis of spin densities, which we have done for substoichiometric U-An MOX-8, as well as the Zr equivalent. The data for surface U, Zr and An, as well as some U in deeper layers, are collected in Table 4.4. Firstly, we look at U-Zr MOX-8. On all three surfaces, the spin density of the surface Zr is ~ 0.0. When the O vacancy is away from substituted surface Zr (italic), the redistribution of the two electrons is very similar to that found on the pure UO_2 surface (Table 4.2). For example, on the {111} surface, one of the three U neighbour the O vacancy has spin density of ~ 2.9, while the other two are ~ 2.2, and on the {110} and {100} surfaces, the two surface U neighbour the vacancy have increased spin density. The sum of the increased spin density on surface U is less than 2, 1.4, 1.6 and 1.3 on the {111}, {110} and {100} surfaces, respectively. As with the substoichiometric UO_2 surface, we conclude that some of the electron density localises at the O vacancy on U-Zr MOX-8 surfaces.

On the U-Zr MOX-8 {111} surface, when the O vacancy is next to the substituted Zr (Table 4.4, Calibri), all of the three surface U have increased spin density. For {110} and {100}, two U have a clear increase in spin density; one of these is next to the vacancy and on the surface, while the other one is also next to vacancy but in the second layer. That some of the two electrons move to the subsurface layers' U may be explained by the surface structure (Figure 4.4). In Figure 4.4 (a), (b) and (c), we can see that, on the {111} surface, the surface U labelled 1 is only an oxygen away from the vacancy, while, on the {110} and {100} surfaces, the other two surface U are further away from the vacancy than the U in the second layer, which neighbours the vacancy. The sum of the increased spin densities on the three surface U on the {111} surface, and the two U on {110} and {100} surfaces, are smaller than 2, about 1.3, 1.8 and 1.8 on the {111}, {110} and {100} surfaces, respectively, so there will be some electron density at the vacancy.

In contrast to the Zr-substituted systems, surface An can be reduced to the trivalent state. Table 4.4 shows that, on substoichiometric U-Np, U-Pu and U-Cm MOX-8 surfaces, the spin density of substituted Np, Pu or Cm is about 4, 5 and 7, respectively, so about one of the two electrons is localized on the surface An, even when they are away from the vacancy. On the {111} surface, we also find an increase of spin density on two or three surface U, depending on the position of the O vacancy, while on the {110} and {100} surfaces only the surface U next to the vacancy has a clear increase in spin density. Once again, the sum of the increased spin density on the metal ions is smaller than 2 on each substoichiometric U-Np, U-Pu and U-Cm MOX-8 surface, so there will be electron density located at the vacancy.

Table 4.4: Spin density of surface U, Zr or An (Np, Pu, Am, and Cm) on $U_{0.92}Zr_{0.08}O_{1.92}$ or $U_{0.92}An_{0.08}O_{1.92}$ surfaces. Data for surfaces with O vacancy next to substituted Zr or An are Calibri and surfaces with O vacancy away from substituted Zr or An are italic. Spin densities with a clear increase on substoichiometric surface vs the corresponding stoichiometric surface are shown in bold.

MOX-8	An	{111}			{110}			{100}		
U-Zr	Zr	0.022/0.004			0.001/0.014			0.013/0.004		
	U	**2.173** ***2.255***	**2.167** ***2.189***	**2.936** ***2.969***	**2.891** ***2.887***	**2.898**[a] *2.042*	2.014 - 2.030[b] ***2.802***	**2.908** ***2.957***	**2.895**[a] *2.061*	2.009 - 2.052[b] ***2.343***
U-Np	Np	**4.077** / ***4.024***			**4.072** / ***4.206***			**4.297** / ***3.998***		
	U	2.039 ***2.186***	**2.172** ***2.160***	**2.206** ***2.152***	2.033 *2.060*	2.035 ***2.773***	**2.790** *2.047*	2.041 ***2.800***	**2.374** *2.043*	2.046 *2.095*
U-Pu	Pu	**5.025** / ***5.096***			**5.136** / ***5.104***			**5.211** / ***5.087***		
	U	2.040 ***2.154***	**2.189** ***2.166***	**2.176** ***2.156***	2.031 ***2.791***	2.034 *2.055*	**2.618** *2.033*	2.038 *2.084*	**2.266** *2.037*	2.036 ***2.802***
U-Am	Am	**6.494** / ***6.154***			**6.944** / ***6.146***			**7.001** / ***6.137***		
	U	2.074 ***2.160***	**2.146** ***2.164***	**2.137** ***2.169***	2.033 ***2.795***	2.025 *2.057*	2.085 *2.038*	2.031 *2.081*	2.088 *2.032*	2.038 ***2.817***
U-Cm	Cm	**6.788** / ***6.897***			**6.921** / ***6.843***			**6.786** / ***6.841***		
	U	2.042 ***2.111***	**2.201** ***2.177***	**2.121** ***2.162***	2.012 ***2.812***	2.039 *2.038*	**2.502** *2.009*	2.053 *2.087*	**2.255** *2.035*	2.050 ***2.797***

a: spin density of a U in 2nd layer; b: range of spin density for U in 1st and 2nd layers, excluding U with significant change in spin density.

While redistribution on substoichiometric U-Am MOX-8 surfaces with the O vacancy away from Am is similar to that on the U-Np, U-Pu and U-Cm MOX-8 surfaces, that on substoichiometric U-Am MOX-8 surfaces with the O vacancy next to Am is rather different. On {110} and {100}, the Am has clearly been reduced to Am(II) (spin density close to 7), and even on the {111} the Am is mid-way between Am(III) and Am(II). The driver for this is very likely the 5f^7 half-filled shell configuration of Am(II), with the effect manifesting itself most strongly when the Am is next to the vacancy, around which the two electrons tend to localise. When the Am is placed away from the vacancy, its reduction stops at Am(III), with the remaining electron localising partly on the U around the vacancy, and at the vacancy itself.

Oxygen vacancy generation energies (equation 4.3) on U-An MOX-8 surfaces are collected in Table A4.4 and compared in Figure 4.6. Turning first to substoichiometric surfaces with the vacancy next to substituted An (Figure 4.6 (a)), it is clear that vacancy generation is more facile on the MOX-8 surfaces than on the corresponding UO_2 surfaces. This is most likely due to the increasing ease of reduction from M(IV) to M(III) across the series, as the substituted An forms the trivalent state on substoichiometric MOX-8 surfaces, *i.e.* the presence of an An next to the vacancy stabilizes substoichiometric UO_2 surface. O vacancy generation energies for the UO_2 surfaces decrease from {111} to {100}, but do so more gradually on all U-An MOX-8 surfaces. The O vacancy formation energy on U-An MOX-8 surface is not only related to the energy of substoichiometric surfaces, but also to that of the stoichiometric surface. The difference between O vacancy formation energy on UO_2 and MOX surfaces (Δ, equation 4.4) follows from equation 4.3 as:

$$\Delta = E_{red}(UO_2) - E_{red}(MOX) \tag{4.4}$$

$$\Delta = \frac{1}{2}\left(E_{sub}(UO_2) + E_{O_2} - E_{UO_2}\right) - \frac{1}{2}\left(E_{sub}(MOX) + E_{O_2} - E_{MOX}\right) \tag{4.5}$$

$$\Delta = \frac{1}{2}\left(E_{sub}(UO_2) - E_{sub}(MOX)\right) - \frac{1}{2}\left(E_{UO_2} - E_{MOX}\right) \tag{4.6}$$

Substituting for E_{MOX} from equation 4.2 gives:

$$= \frac{1}{2}\left(E_{sub}(UO_2) - E_{sub}(MOX)\right) - \frac{1}{2}\left(E_{UO_2} - (2E_{rep} + (1-y)E_{UO_2} - yE_{AnO_2})\right)$$

$$= \frac{1}{2}\left(E_{sub}(UO_2) - E_{sub}(MOX)\right) - \frac{1}{2}\left(y(E_{UO_2} + E_{AnO_2}) - 2E_{rep}\right)$$

$$= \frac{1}{2}\left(E_{sub}(UO_2) - E_{sub}(MOX)\right) - \frac{y}{2}(E_{UO_2} + E_{AnO_2}) + E_{rep}$$

Thus, the higher the replacement energy the larger Δ. As the replacement energy decreases from the {111} surface to the {100} (Figure 4.3 (a)), the decrease of vacancy formation energy on U-An MOX-8 surfaces is more gentle than on UO_2.

The U-An MOX-8 surfaces can be divided into two groups according to their O vacancy generation energies, U-Np and U-Pu, and U-Am and U-Cm. Within each group, similar O vacancy generation energies are found on the different MOX-8 surfaces. Substituted Np and Pu are trivalent, with c.a. four and five f electrons, respectively, while substituted Am and Cm both have about seven f electrons, *i.e.* a half-filed 5f shell. Thus, the O vacancy generation energies of group two are lower than group one.

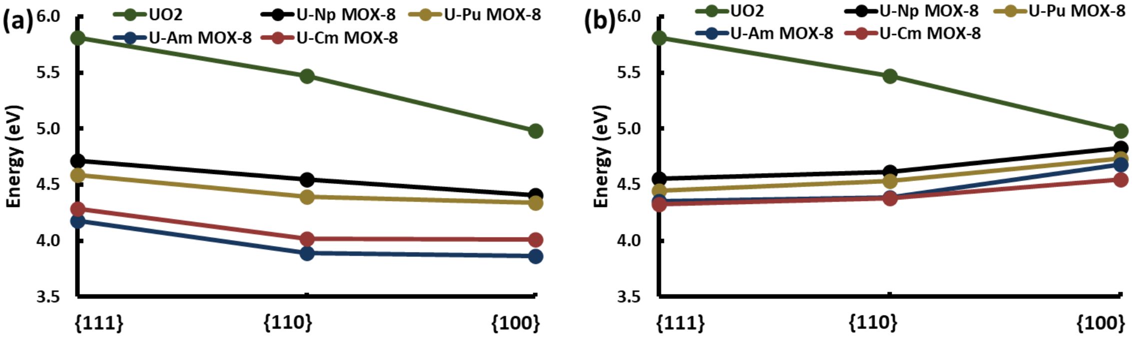

Figure 4.6: O vacancy generation energy (eV) on UO_2 surface and $U_{0.92}An_{0.08}O_2$ (An = Np, Pu, Am or Cm) surfaces, with (a) the vacancy next to substituted An and (b) away from substituted An. The lines joining the points are to guide the eye.

On substoichiometric U-An MOX-8 surfaces with the vacancy away from the substituted An, the vacancy generation energy is also lower than on corresponding $UO_{1.92}$ surface, which we again attribute to the lower redox potential of An(IV)/(III) *vs* that of U. Creating an O vacancy neighbour an An is more favourable than away from An (Figure 4.6 and Table A4.5), *i.e.* higher O vacancy formation energy is found on MOX-8 surfaces with the vacancy away from substituted An than next to it. This may be due to the preferred location of the two electrons left behind on oxygen vacancy formation. We have established that they prefer to remain around the vacancy, yet on MOX-8 surfaces with the An away from the vacancy, about one electron moves to the An, *i.e.* away from the vacancy. In contrast to when the oxygen vacancy is next to a substituted An, the O vacancy formation energies on the {110} and {100} surfaces are slightly larger than on the {111} surface when the An is away from the vacancy (Figure 4.6 (b)). The explanation may be in Figure 4.4 (d) – (f); on the {111} surface (Figure 4.4 (d)), the substituted An and the surface U which neighbours the vacancy bond with the same surface O, and the distance between the substituted An and the surface U is 3.73 - 3.83 Å. While, on the {110} and {100} surfaces, the distance between the An and the U which neighbour the vacancy is 5.53 - 5.59 and 4.06 – 4.08 Å, respectively. We might therefore expect electron transfer on the {111} surface to be easier than on the {110} and {100} surfaces, due to the smaller transfer distance. O vacancy generation energies on MOX-8 {110} and {100} surfaces with the vacancy away from the An are higher than surfaces with the O vacancy neighbour the An (Figure 4.6 and Table A4.5), due to about half of the two electrons transferring away from the vacancy to the An. As the vacancy generation energies are similar on surfaces with different An, redistribution of the two electrons may be the main factor determining vacancy generation energy.

In our previous study, we found that O vacancy generation energies on $Pu_{0.92}Am_{0.08}O_2$ (Pu-Am MOX-8) surfaces with the vacancy next to the surface Am are close to the average value of vacancy generation energies on the corresponding PuO_2 and AmO_2 surfaces.[9] We attributed this to generation of O vacancies on PuO_2 and AmO_2 surfaces reducing, respectively, two surface Pu and Am to the trivalent state, and vacancy generation on Pu-Am MOX-8 surfaces reducing one surface Pu and one Am to the trivalent state. It is interesting to do the same comparison for U-An MOX-8. The O vacancy generation energies on AnO_2 surfaces, and the average values on UO_2 and AnO_2 surfaces, are given in Table A4.6. The energy differences between MOX-8 and the average of the pure substoichiometric dioxides are given in Figure 4.7. For U-Np MOX-8 {110} and {100}, the vacancy formation energies are very close to the average value on the corresponding UO_2 and NpO_2 surfaces, as is the case for the Pu-Am system. From there, the energy differences for U-An MOX-8 {110} and {100} increase steadily across the actinide series. This behaviour is also generally the case for the {111} surface, though that on the U-Np system is an outlier. We therefore suggest that the O vacancy formation energies on mixed dioxide surfaces are close to the average values on the corresponding pure actinide dioxide surfaces only if the two actinides neighbour each other in the periodic table, and this rule becomes less and less applicable when the two actinides are further and further away from each other in the series. Additional insight into this may be gained by examination of the spin densities. On substoichiometric U-Np MOX-8, the surface Np obtains about 1 electron (Table 4.4) and the location of the rest of the electron density is almost the same as on the corresponding substoichiometric UO_2 surfaces (Table 4.2). From U-Pu MOX onwards, for the systems with the An next to the vacancy, the spin density of the surface U with the largest increase reduces, most noticeably for the {110} surface; 2.790, 2.618 and 2.502 for U-Np, U-Pu and U-Cm MOX, respectively, while for U-Am MOX-8 no significant increase in spin density is found for any surface U (Table 4.4). This reflects the greater ease with which the later An are reduced, and O vacancy formation is less and less similar to the situation on pure UO_2 and AnO_2 surfaces.

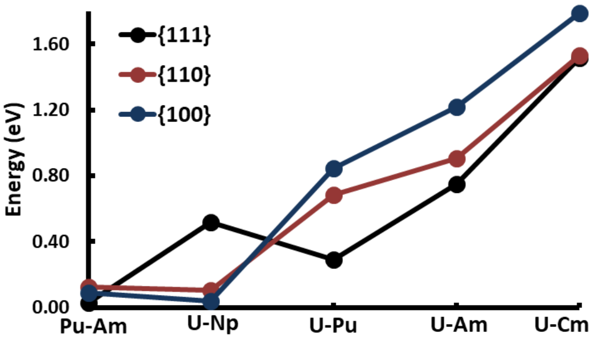

Figure 4.7: Difference between the oxygen vacancy formation energies on $U_{0.92}An_{0.08}O_2$ (An = Np, Pu, Am or Cm) surfaces and the average value on UO_2 and corresponding AnO_2 surfaces, as well as the difference of the energies on $Pu_{0.92}Am_{0.08}O_2$ and the average value on PuO_2 and AmO_2 surfaces. The lines joining the points are to guide the eye.

4.3.4 $U_{0.92}An_{0.08}O_2$ surfaces with subsurface An

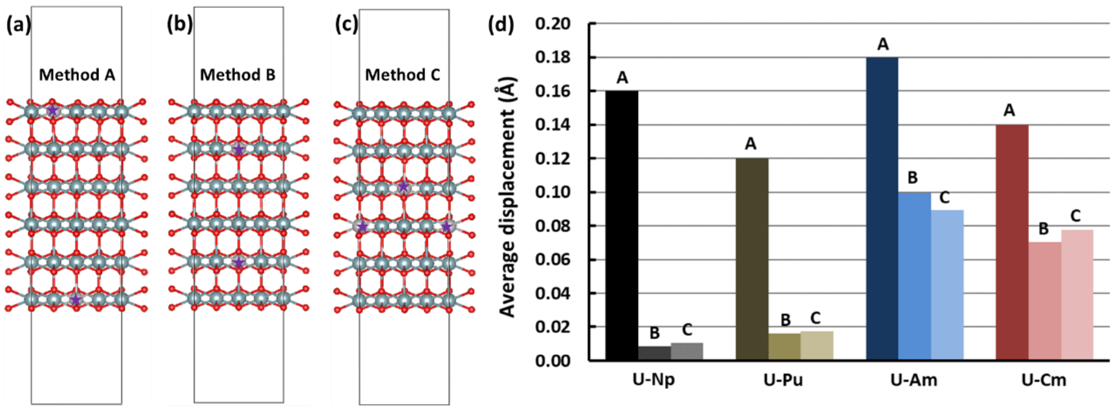

Figure 4.8: Side view of $U_{0.92}Np_{0.08}O_2$ {111} surfaces with Np in (a) 1st and 6th layers (method A), (b) 2nd and 5th layers (method B), and (c) 3rd and 4th layers (method C). Blue-grey, light grey and red spheres represent U, Np and O, respectively, and a purple star marks the position of Np. (d) Average displacement of An-O bonds in $U_{0.92}Np_{0.08}O_2$ (An = Np, Pu, Am and Cm) {111} surfaces with different substitution methods. Dark, medium and light-coloured columns represent substitution methods A, B and C, respectively.

We now consider substitution in the subsurface layers of UO_2 slabs. To keep the MOX-8 slab antiferromagnetic, there are two ways to arrange the An in the deeper layers, either in the 2nd and 5th layers (method B) or the 3rd and 4th layers (method C, denoting substitution on the surface (layers 1 and 6) as method A). We explored methods B and C for the {111} surface, finding that the structures of U-An MOX-8 with these methods are similar for the different An. Figure 4.8 shows the U-Np MOX-8 surfaces as a representative example; the side view of U-Np MOX-8 with Np on the surface (method A) is shown in Figure 4.8 (a), and in deeper layers in (b) and (c). As before, we compare the An-O bonds in the MOX-8 with the corresponding bonds in the pure AnO_2; the average displacements with different substitution methods are collected in Figure 4.8 (d). Displacements caused by subsurface An are much smaller than surface An as surface bonds are more flexible than deeper layer bonds, which are more similar to the bulk. Methods B and C show similar displacements. The MOX-8 slabs divide into two groups according to the size of the displacements in the subsurface layers; for U-Np and U-Pu MOX-8 the displacements are negligible (smaller than 0.02 Å), while those in U-Am and U-Cm MOX-8 are larger, at c. 0.07–0.10 Å.

We evaluated the spin densities, and find that the only significant changes are for An and U in the same layer, so in the following discussion we refer only to U in the same layer as the substituted An (Table 4.5). We have also simulated U-Zr MOX-8 with Zr in deeper layers, and the spin densities of Zr and U in the same layer are also collected in Table 4.5. In the U-Zr system, the spin density of Zr is close to 0, and the spin density of U is about 2.02, so there is no electron transfer between substituted Zr and U. In U-Np and U-Pu MOX-8, the spin density of Np and Pu is about 3 and 4 respectively, *i.e.* tetravalent, while Am and Cm have spin densities of about 6 and 7 (trivalent) in U-Am and U-Cm MOX-8. The U in U-Np and U-Pu MOX-8 have spin densities slightly smaller than the equivalent ions in the Zr system, suggesting a small amount of charge transfer from U in the Np and Pu MOX-8 slabs. Charge transfer is much larger in the Am and Cm systems, with one U in the layer with the substituted Am or Cm having a spin density of about 1.1 and the other two remaining at about 2, *i.e.* the Am or Cm obtain about one electron mainly from a single U in the same layer. The behaviour of the four An once again falls into two groups, with Np and Pu remaining tetravalent and Am and Cm being reduced, which ties in with the An-O bond displacements discussed above (An(III) is larger than An(IV) and will cause larger An-O bond displacements).

Table 4.5: Spin density of substituted An (Np, Pu, Am and Cm) and Zr, and U, in the same layer in $U_{0.92}An_{0.08}O_2$ and $U_{0.92}Zr_{0.08}O_2$ {111} surfaces with substitution method B (M in 2nd and 5th layers) and C (M in 3rd and 4th layers). Spin densities with a clear change from that expected for M(IV) are shown in bold.

MOX	An	Method B (2nd and 5th)			Method C (3rd and 4th)		
U-Zr	Zr	0.002			0.002		
	U	2.018	2.015	2.023	2.017	2.024	2.023
U-Np	Np	3.096			3.089		
	U	2.001	2.007	2.009	2.019	2.023	2.020
U-Pu	Pu	4.247			4.225		
	U	1.997	2.003	1.997	2.004	1.998	2.017
U-Am	Am	**6.123**			**6.113**		
	U	**1.154**	2.017	2.016	2.005	2.012	**1.084**
U-Cm	Cm	**6.835**			**6.832**		
	U	**1.130**	2.007	2.015	2.005	2.012	**1.099**

For stoichiometric MOX-8 with the different substitution methods, we find only tetravalent Np and trivalent Am and Cm, in agreement with experimental results. In contrast, a different charge state is found for Pu with different substitution methods, a trivalent state on the surface (Table 4.3) and tetravalent Pu in deeper layers (Table 4.5). Trivalent Pu has not been reported experimentally for stoichiometric U-Pu MOX-8, but this does not disagree with our results in that if Pu(III) is indeed present in only the surface layer, its concentration overall will be very low and hence difficult to detect experimentally. The low percentage of Pu(III) in U-Pu MOX-8 will be further discussed below, when we consider larger concentrations of An.

The replacement energies (equation 4.2) of An into the UO_2 {111} surface with substitution methods B and C are summarized in Table A4.7 and compared with substitution method A in Figure 4.9. There is relatively little dependence of the substitution energies on the substitution layer, which is perhaps unsurprising for Np, Am and Cm as the charge state of these ions is the same in all layers. For Pu, however, the charge states are not the same, and hence differing final charge states clearly have little effect on substitution energies of Pu into UO_2. The An can again be divided into two groups here, according to the replacement energy. Group one has Np and Pu, as their replacement energies are similar and between c. 0.0–0.5 eV, so the substitution of Np and Pu into UO_2 is energetically neutral or even disfavoured. While, in group two, much more negative replacement energies are found for the substitution of Am and Cm, so it is quite favourable to have trivalent Am and Cm in UO_2 surfaces.

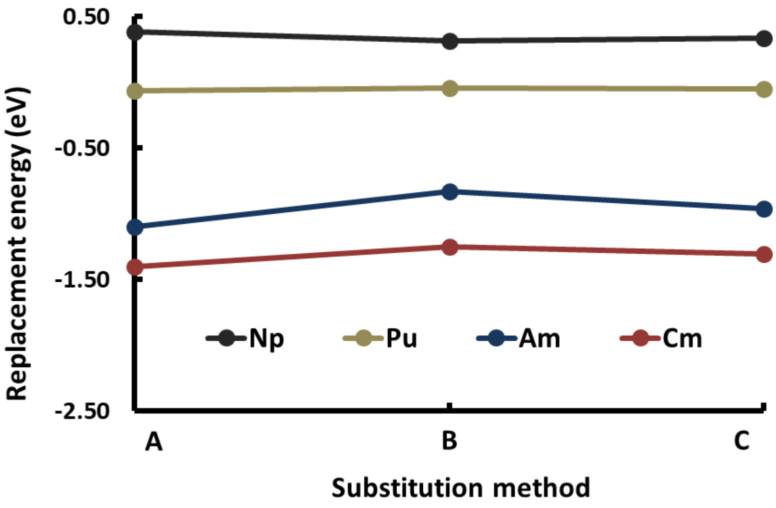

Figure 4.9: Replacement energies for An (Np, Pu, Am and Cm) substituting into the UO_2 {111} surface with substitution method A (An in 1st and 6th layers), B (An in 2nd and 5th layers) and C (3rd and 4th layers), lines are a guide to the eye.

4.3.5 $U_{0.92}An_{0.08}O_{1.92}$ surfaces with subsurface An

We have also considered the generation of surface O vacancies on U-An (An = Np, Pu, Am and Cm) MOX-8 {111} surfaces with subsurface An. As the geometric structures are similar for all substoichiometric U-An MOX-8, we provide the representative example of U-Np MOX-8 in Figure A4.4, and the displacements of the surface atoms caused by generation of the surface O vacancy are compared in Figure 4.10. We choose the O vacancy away from the An in order to facilitate the comparison here, as An does not neighbour the O vacancy when in the subsurface layers. We again see that the neighbour U on the surface move away from the vacancy (positive displacement), while neighbour O move towards (negative displacement). For MOX-8 with different substitution methods, we find similar An-vacancy and similar O-vacancy distances, with the differences smaller than 0.07 and 0.11 Å, respectively, *i.e.* the substitution methods have little influence on O vacancy induced displacement of the surface atoms.

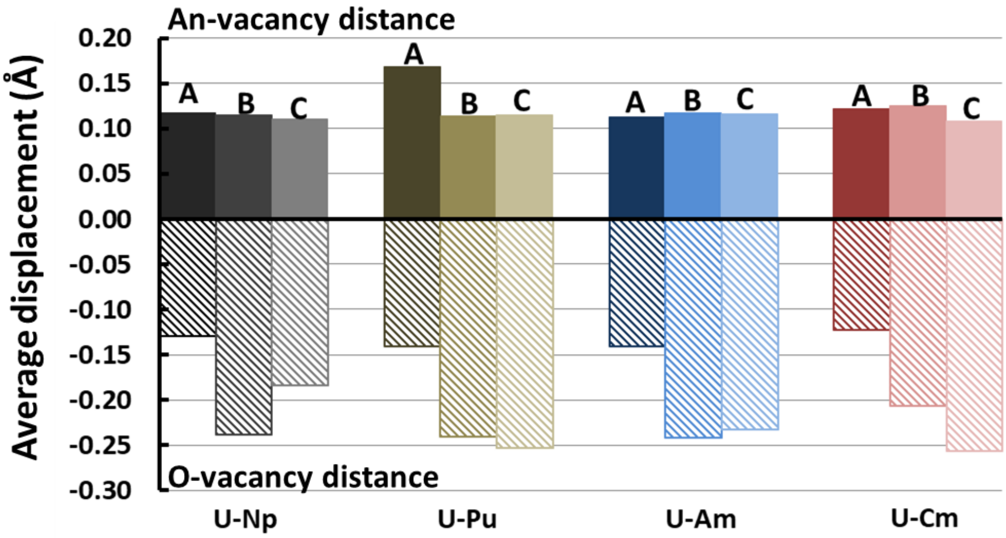

Figure 4.10: Average displacement of nearest neighbour atoms, U (solid column) and O (diagonal column) from the O vacancy in $U_{0.92}An_{0.08}O_{1.92}$ {111} surfaces with subsurface An. Positive displacement indicates the atom moves away from the vacancy site, whereas negative displacement indicates the atom moves toward the site. Dark, medium, and light coloured bars show displacements for substitution methods A, B and C, respectively.

Table 4.6: Spin density of substituted An (Np, Pu, Am and Cm) and Zr, and surface U, in $U_{0.92}An_{0.08}O_{1.92}$ (An = Np, Pu, Am and Cm) and $U_{0.92}Zr_{0.08}O_{1.92}$ {111} surfaces with substitution methods B and C (Figure 4.8 (b) and (c), respectively). Spin densities with a clear change from that expected for M(IV) are shown in bold.

MOX-8		Method B (2nd and 5th layers)				Method C (3rd and 4th layers)			
U-Zr	Zr	0.009				0.001			
	U	2.213	**2.957**	2.228	2.056	2.218	**2.946**	2.229	2.046
U-Np	Np	**4.004**				**4.002**			
	U	2.180	2.178	2.203	2.047	2.197	2.188	2.178	2.041
U-Pu	Pu	**5.069**				**5.072**			
	U	2.200	2.186	2.182	2.040	2.197	2.182	2.186	2.041
U-Am	Am	**6.112**				**6.113**			
	U	2.202	2.184	2.185	2.041	2.106	2.118	2.193	2.017
U-Cm	Cm	**6.836**				**6.836**			
	U	2.197	2.192	2.207	2.017	2.195	2.185	2.177	2.041

Once again we have evaluated the spin densities, and these are collected in Table 4.6, including for substoichiometric U-Zr MOX-8 with Zr in deeper layers. The electron redistribution on substoichiometric U-Zr MOX-8 is very similar for the different substitution methods (Table 4.6 and Table 4.5), and to that on the $UO_{1.92}$ surface (Table 4.2), showing one electron localising on a single U, and the other being distributed on the other surface U and, presumably, partly at the vacancy. The electron redistribution on substoichiometric U-An MOX-8 is also very similar for the different substitution methods, and for the different An, with one electron localising on the substituted An in all cases. The three surface U neighbour the vacancy have a spin density of about 2.2, with the remaining electron density presumably again localising at the vacancy.

O vacancy formation energies (equation 4.3) on {111} surfaces with deep layer An are summarized in Table A4.8, and compared with the energies on surfaces with surface An, with the O vacancy away from the An, in Figure 4.11. On U-Pu, U-Am and U-Cm MOX-8 {111} surfaces, similar formation energies are found for substitution methods A and C, with slightly smaller values for method B. In contrast, there is a significant increase in the vacancy formation energies from substitution methods A to C on the U-Np MOX-8 {111} surface, *i.e.* the deeper the Np the more energy is required to form a surface oxygen vacancy. We speculate that the difference in behaviour of Np *vs* the later An may be due to two competing factors. We know that the two electrons left behind on neutral oxygen vacancy formation prefer to localise around the vacancy, but substitution of An(III) in deeper layers works against this, by localising one electron increasingly far from the vacancy. This would account for the behaviour seen in U-Np MOX-8. Working against this is the driver for An(III) formation, which is increasingly favourable across the An series (as evidenced by the increasingly positive An(IV)/An(III) redox potential), and it may be that these two factors largely counterbalance one another for the later An.

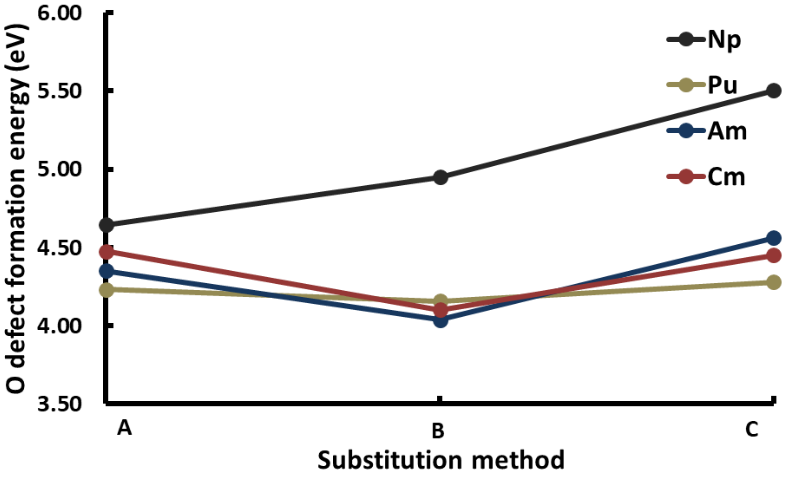

Figure 4.11: O vacancy formation energy on $U_{1.92}An_{0.08}O_2$ (An = Np, Pu, Am and Cm) MOX-8 {111} surfaces with substitution method A (An in 1st and 6th layers), B (2nd and 5th layers) and C (3rd and 4th layers).

4.3.6 $U_{1-y}An_yO_2$ surfaces with surface An (y = 0.08, 0.17, 0.25 and 0.33)

Finally, we simulate the UO_2 {111} surface with higher concentrations of substituted An. As the periodic cell has four U ions on surface, four situations are considered, with, respectively, 1, 2, 3, and 4 surface U replaced with An. As replacement is considered on both sides of slab, the ratio of An to U is 0.08:0.92, 0.17:0.83, 0.25:0.75, and 0.33:0.67, with chemical formulae $U_{0.92}An_{0.08}O_2$ (MOX-8), $U_{0.83}An_{0.17}O_2$ (MOX-17), $U_{0.75}An_{0.25}O_2$ (MOX-25) and $U_{0.67}An_{0.33}O_2$ (MOX-33), respectively. As MOX-8 has been discussed above, we mainly present, in this part, results for MOX-17, MOX-25, and MOX-33, and compare across the An ratios. The surface geometries of U-An MOX-17, MOX-25, and MOX-33 are similar; surface lattice constants are collected in Table A4.9. Note that, as we here consider only surface An substitution, and the displacements of U-O and An-O bonds caused by such substitution are rather different from those of subsurface An, the surface lattice constants and y do not obey Vegard's law, which is obeyed by MOX bulk.[14, 44-45] Representative examples of top views of U-Np MOX-17, MOX-25, and MOX-33 are presented in Figure 4.12 (a), (b) and (c), respectively. For U-An MOX-8, substitution of An into UO_2 surfaces elongates the surface An-O bonds, in comparison with An-O bonds on the corresponding AnO_2 surfaces. With increasing An concentration, the displacement of surface An-O bonds will decrease, and when all surface U are replaced by An, the displacement of surface An-O bonds is close to zero (Figure 4.12 (d)). Interestingly, the An can again be divided into two groups according to the trend in this decrease; group one has Np and Pu and group two has Am and Cm, as when we considered subsurface An (Figure 4.8). We have also checked the interlayer distances, and find that substitution of An has a negligible influence on these (Figure A4.5).

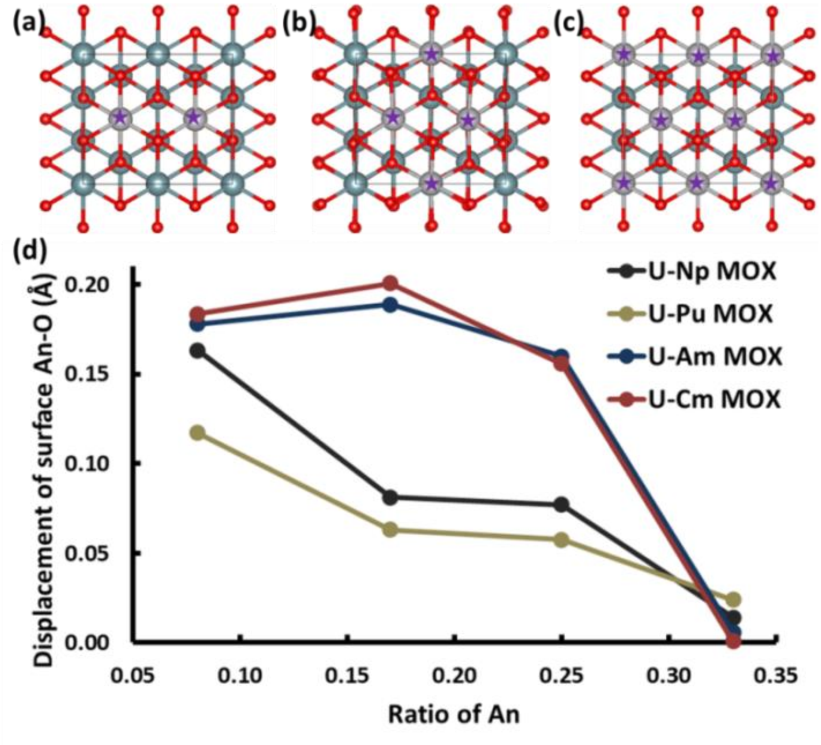

Figure 4.12: Top view of (a) $U_{1.83}Np_{0.17}O_2$, (b) $U_{1.75}Np_{0.25}O_2$ and (c) $U_{1.67}Np_{0.33}O_2$ {111} surface, and (d) displacement of surface An-O bond *vs* An ratio in $U_{1-y}An_yO_2$ (An = Np, Pu, Am and Cm, y = 0.08, 0.17, 0.25 and 0.33) surfaces. In (a), (b) and (c), blue-grey, light grey and red spheres represent U, Np and O, respectively, and purple stars mark the position of substituted Np.

U-Zr MOX-17, MOX-25 and MOX-33 have also been inspected, in order to provide a benchmark for analysing the spin densities of An and U in U-An MOX. Top views of U-Zr MOX-*Y* (= 8, 17, 25 and 33) are presented in Figure A4.6 and the lattice constants are given in Tables A4.1 and A4.9. No matter how many surface U are replaced with Zr, the spin density of the substituted Zr and U are all 0 and 2 respectively (Table A4.10, A4.11 and A4.12), *i.e.* there is no electron transfer between U and substituted Zr. The spin densities of substituted Np in U-Np MOX-*Y* are all about 3.1 (Table A4.10, A4.11 and A4.12), as we found for Np in U-Np MOX-8 (Table 4.3), and the spin densities of U in U-Np MOX-*Y* are slightly smaller than in the corresponding U-Zr MOX-*Y*. Thus, for all the different U-Np MOX studied here, we find no clear charge transfer between U and substituted Np; the Np are all tetravalent, but attract a small amount of electron density from U. By contrast, all Am and Cm are trivalent in all kinds of U-Am and U-Cm MOX, with electrons being transferred from surrounding U ions (Table A4.10, A4.11 and A4.12). For example, on the U-Am MOX-8 {111} surface, the Am obtains an electron from a surface U (Table 4.3), and on the equivalent U-Am MOX-17 surface, the two surface Am obtain electrons from the other two surface U (Table A4.10). As the concentration of Am on the surface increases, there are no longer sufficient surface U from which to obtain electrons, and electrons are transferred from U in the next layer down (Table A4.11). For all U-Pu MOX-*Y*, only one surface Pu is trivalent (Table 4.3, A4.10, A4.11 and A4.12). On U-Pu MOX-8, MOX-17 and MOX-25 surface, this surface Pu acquires an electron from a surface U while, on U-Pu MOX-33, the Pu obtains an electron from a U in a subsurface layer (2nd and 5th). We therefore find that the conditions under which Pu(III) may be formed are quite restricted; the Pu must be on the surface and neighbour Pu must not be reduced. The resulting scarcity of trivalent Pu in U-Pu MOX-*Y* is likely why it has not been detected experimentally.[12]

Replacement energies (equation 4.2) (Table A4.13) are compared for different An and substitution levels in Figure 4.13. In the range studied, substitution of Cm is the easiest, while substitution of Np is the hardest. There is very good correlation of An ratio with replacement energy for Pu, Am and Cm (R^2 = 0.87, 0.97, and 0.97, respectively), though that for Np is poorer (0.58). We further study this by considering the replacement energy per An (Figure 4.13 (b)), and now find a linear relationship for all An. Noticeably, the replacement energy per Np decreases as the amount of Np increases, so Np in a UO_2 slab will favour the further substitution of Np. In contrast, Pu, Am and Cm behave oppositely, so it gets harder and harder to substitute more and more Pu, Am or Cm into UO_2. This may be explained by the charge isosurfaces of U-An MOX-*Y* {111} (Figure A4.7, A4.8, A4.9 and A4.10). For U-Np (Figure A4.7), from MOX-8 to MOX-33, the overlap of the Np and O charge isosurfaces increases, suggesting that the blend of Np into the UO_2 surface becomes better with increasing Np concentration. However, for U-Am/Cm MOX-*Y* (Figure A4.9 and A4.10), the overlap of the charge isosurfaces for surface Am/Cm-O bonds become smaller and smaller. The overlap of the charge isosurfaces for surface Pu-O bonds do not differ much between the different U-Pu MOX surfaces (Figure A4.8), which may relate to the smaller positive slope of the Pu data in Figure 4.13 (b) being rather less than that for the Am and Cm lines.

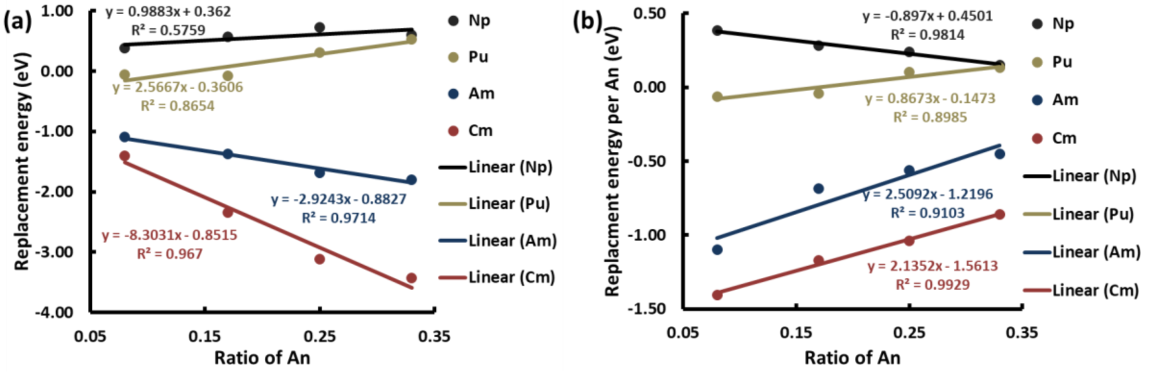

Figure 4.13: (a) Replacement energy of An (Np, Pu, Am and Cm) into the UO_2 {111} surface against ratio of An; (b) Replacement energy per An onto UO_2 {111} surface against ratio of An.

4.4 Conclusions

In this contribution, we have studied the properties of $U_{0.92}An_{0.08}O_2$ MOX (An = Np, Pu, Am and Cm) {111}, {110} and {100} surfaces, in which a surface U is replaced by An, considering also, for the {111} surface, different An substitution positions (surface or subsurface) and increasing the ratio of An to U. Substitution of An into UO_2 surfaces elongates the surface An-O bonds and shortens the U-O bonds, and with increasing An to U ratio, the elongation of the An-O bonds tends to zero as all the surface U are replaced by An. Surface bond displacements are negligible on subsurface substitution of the An, in comparison with surface substitution. In U-Np MOX, the substituted Np is always tetravalent, no matter the substitution position or the ratio of Np to U. By contrast, substituted Am or Cm are always trivalent, with the minor actinides obtaining about 1 electron primarily from a neighbour U, which is oxidised to U(V). The behaviour of Pu is less straightforward than that of Np, Am and Cm. One surface Pu obtains an electron from a neighbour U and forms Pu(III), whereas all the other Pu, either surface or subsurface, remain tetravalent. The energy of replacing a surface U with An is linearly correlated with the An(IV)/(III) redox potential, and decreases from {111} to {100}. For the {111} surface we find little dependence of the replacment energy on whether the An is substituted into the surface or subsurface. Np substitution favours further substitution, while substituted Pu, Am and Cm disfavour further substitution of those elements, especially for Am and Cm.

We have also studied oxygen vacancy formation on $U_{0.92}An_{0.08}O_2$ (An = Np, Pu, Am and Cm) MOX surfaces, to yield $U_{0.92}An_{0.08}O_{1.92}$. After vacancy generation, neighbour An and U move away from the vacancy and neighbour O move towards it, similar to the behaviour on substoichiometric UO_2 and AnO_2 surfaces. The two electrons left behind on removal of a neutral oxygen atom remain partly at the vacancy site, partly delocalise onto neighbour U, and partly localise on the substituted An, even when the vacancy does not neighbour a surface An or when the An is substituted in subsurface layers. On $U_{0.92}An_{0.08}O_{1.92}$ surfaces with the vacancy next to substituted An, the O vacancy generation energy decreases from {111} to {100}, as for the corresponding $UO_{1.92}$ surfaces, but the extent of the decrease is gentler. On $U_{0.92}An_{0.08}O_{1.92}$ surfaces with the vacancy away from substituted An, the O vacancy generation energy increases slightly from {111} to {100}, due to the surface geometric structure and electron redistribution. The vacancy formation energies are similar for $U_{0.92}An_{0.08}O_{1.92}$ (An = Pu, Am and Cm) with subsurface An and with surface An away from the vacancy. By contrast, the surface vacancy formation energy increases with deeper layer Np in $U_{0.92}An_{0.08}O_{1.92}$ {111}, as the two electrons prefer to localize around the vacancy and the electronegativity of Np(IV) is not strong enough to overcome the energy needed for electron transfer from the surface to the subsurface.

References

1. GarciaáAlonso, J. I., Determination of fission products and actinides in spent nuclear fuels by isotope dilution ion chromatography inductively coupled plasma mass spectrometry. *J. Anal. At. Spectrom.* **1995**, *10*, 381-393.

2. Panakkal, J.; Ghosh, J.; Roy, P., Characterisation of uranium-plutonium mixed oxide nuclear fuel pins, using neutron radiography. *British Journal of Non-Destructive Testing* **1985**, *27*, 232-233.

3. Panakkal, J.; Ghosh, J.; Roy, P., Analysis of optical density data generated from neutron radiographs of uranium-plutonium mixed oxide fuel pellets inside sealed nuclear fuel pins. *Nucl. Instrum. Methods Phys. Res., B* **1986**, *14*, 310-313.

4. Hiyama, T.; Takahashi, T.; Kamimura, K., Determination of nitrogen in uranium-plutonium mixed oxide fuel by gas chromatography after fusion in an inert gas atmosphere. *Anal. Chim. Acta.* **1997**, *345*, 131-137.

5. Sato, I.; Furuya, H.; Arima, T.; Idemitsu, K.; Yamamoto, K., Behavior of metallic fission products in uranium–plutonium mixed oxide fuel. *J. Nucl. Mater.* **1999**, *273*, 239-247.

6. Picard, E.; Noirot, J.; Moss, R. L.; Plitz, H.; Richter, K.; Rouault, J., First in-pile experimental results of high-plutonium-content oxide fuel for plutonium burning in fast reactors. *Nucl. Technol.* **2000**, *129*, 1-12.

7. Grouiller, J.-P.; Pillon, S.; de Saint Jean, C.; Varaine, F.; Leyval, L.; Vambenepe, G.; Carlier, B., Minor actinides transmutation scenario studies with PWRs, FRs and moderated targets. *J. Nucl. Mater.* **2003**, *320*, 163-169.

8. Pillon, S.; Somers, J.; Grandjean, S.; Lacquement, J., Aspects of fabrication of curium-based fuels and targets. *J. Nucl. Mater.* **2003**, *320*, 36-43.

9. Chen, J.-L.; Kaltsoyannis, N., Computational study of plutonium–americium mixed oxides ($Pu_{0.92}Am_{0.08}O_{2-x}$); Water adsorption on {111}, {110}, and {100} Surfaces. *J. Phys. Chem. C* **2020**, *124*, 6646-6658.

10. Vauchy, R.; Belin, R. C.; Robisson, A. C.; Hodaj, F., High temperature X-ray diffraction study of the kinetics of phase separation in hypostoichiometric uranium-plutonium mixed oxides. *J. Eur. Ceram. Soc.* **2014**, *34*, 2543-2551.

11. Vigier, J. F.; Martin, P. M.; Martel, L.; Prieur, D.; Scheinost, A. C.; Somers, J., Structural investigation of $(U_{0.7}Pu_{0.3})O_{2-x}$ mixed oxides. *Inorg. Chem.* **2015**, *54*, 5358-5365.

12. Kato, M.; Takeuchi, K.; Uchida, T.; Sunaoshi, T.; Konashi, K., Oxygen potential of $(U_{0.88}Pu_{0.12})O_{2+/-x}$ and $(U_{0.7}Pu_{0.3})O_{2+/-x}$ at high temperatures of 1673-1873 K. *J. Nucl. Mater.* **2011**, *414*, 120-125.

13. Grandjean, S.; Arab-Chapelet, B.; Robisson, A.; Abraham, F.; Martin, P.; Dancausse, J.-P.; Herlet, N.; Léorier, C., Structure of mixed U (IV)–An (III) precursors synthesized by co-conversion methods (where An= Pu, Am or Cm). *J. Nucl. Mater.* **2009**, *385*, 204-207.

14. Martel, L.; Vigier, J. F.; Prieur, D.; Nourry, S.; Guiot, A.; Dardenne, K.; Boshoven, J.; Somers, J., Structural investigation of uranium-neptunium mixed oxides using XRD, XANES, and O-17 MAS NMR. *J. Phys. Chem. C* **2014**, *118*, 27640-27647.

15. Chollet, M.; Martin, P.; Degueldre, C.; Poonoosamy, J.; Belin, R. C.; Hennig, C., Neptunium characterization in uranium dioxide fuel: Combining a XAFS and a thermodynamic approach. *J. Alloys Compd.* **2016**, *662*, 448-454.

16. Chollet, M.; Belin, R. C.; Richaud, J. C.; Reynaud, M.; Adenot, F., High-temperature X-ray diffraction study of uranium-neptunium mixed oxides. *Inorg. Chem.* **2013**, *52*, 2519-2525.

17. Wilkins, S.; Paixão, J.; Caciuffo, R.; Javorsky, P.; Wastin, F.; Rebizant, J.; Detlefs, C.; Bernhoeft, N.; Santini, P.; Lander, G., Resonant X-ray scattering study of magnetic-dipole and electric-quadrupole order in $U_{0.75}Np_{0.25}O_2$. *Phys. Rev. B* **2004**, *70*, 214402.

18. Lebreton, F.; Belin, R. C.; Prieur, D.; Delahaye, T.; Blanchart, P., In situ study of the solid-state formation of $U_{1-x}Am_xO_{2\ +/-\mathrm{delta}}$ solid solution. *Inorg. Chem.* **2012**, *51*, 9369-9375.

19. Lebreton, F.; Horlait, D.; Caraballo, R.; Martin, P. M.; Scheinost, A. C.; Rossberg, A.; Jegou, C.; Delahaye, T., Peculiar behavior of $(U,Am)O_{2-\mathrm{delta}}$ compounds for high americium contents evidenced by XRD, XAS, and Raman spectroscopy. *Inorg. Chem.* **2015**, *54*, 9749-9760.

20. Prieur, D.; Martin, P. M.; Jankowiak, A.; Gavilan, E.; Scheinost, A. C.; Herlet, N.; Dehaudt, P.; Blanchart, P., Local structure and charge distribution in mixed uranium-americium oxides: Effects of oxygen potential and Am content. *Inorg. Chem.* **2011**, *50*, 12437-12445.

21. Horlait, D.; Lebreton, F.; Delahaye, T.; Blanchart, P., Dilatometric study of $U_{1-x}Am_xO_{2\ +/-\mathrm{delta}}$ sintering: Determination of activation energy. *JACS* **2013**, *96*, 3410-3416.

22. Degueldre, C.; Borca, C.; Cozzo, C., Curium analysis in plutonium uranium mixed oxide by x-ray fluorescence and absorption fine structure spectroscopy. *Talanta* **2013**, *115*, 986-991.

23. Kresse, G.; Hafner, J., Ab initio molecular-dynamics for liquid-metals. *Phys. Rev. B* **1993**, *47*, 558-561.

24. Kresse, G.; Hafner, J., Ab initio molecular-dynamics simulation of the liquid-metal–amorphous-semiconductor transition in germanium. *Phys. Rev. B* **1994**, *49*, 14251-14269.

25. Kresse, G.; Furthmuller, J., Efficiency of ab-initio total energy calculations for metals and semiconductors using a plane-wave basis set. *Comput. Mater. Sci.* **1996**, *6*, 15-50.

26. Kresse, G.; Furthmuller, J., Efficient iterative schemes for ab initio total-energy calculations using a plane-wave basis set. *Phys. Rev. B* **1996**, *54*, 11169-11186.

27. Perdew, J. P.; Burke, K.; Ernzerhof, M., Generalized gradient approximation made simple (vol 77, pg 3865, 1996). *Phys. Rev. Lett.* **1997**, *78*, 1396-1396.

28. Liechtenstein, A. I.; Anisimov, V. I.; Zaanen, J., Density-functional theory and strong interactions: Orbital ordering in Mott-Hubbard insulators. *Phys. Rev. B* **1995**, *52*, R5467-R5470.

29. Tegner, B. E.; Molinari, M.; Kerridge, A.; Parker, S. C.; Kaltsoyannis, N., Water Adsorption on AnO2 {111}, {110}, and {100} Surfaces (An = U and Pu): A Density Functional Theory + U Study. *The Journal of Physical Chemistry C* **2017**, *121*, 1675-1682.

30. Chen, J.-L.; Kaltsoyannis, N., Computational study of the bulk and surface properties of minor actinide dioxides $MAnO_2$ (MAn = Np, Am, and Cm); Water adsorption on stoichiometric and reduced {111}, {110}, and {100} Surfaces. *J. Phys. Chem. C* **2019**, *123*, 15540-15550.

31. Blochl, P. E., Projector augmented-wave method. *Phys. Rev. B* **1994**, *50*, 17953-17979.

32. Monkhorst, H. J.; Pack, J. D., Special points for brillouin-zone integrations. *Phys. Rev. B* **1976**, *13*, 5188-5192.

33. Ma, L.; Atta-Fynn, R.; Ray, A. K., Elemental and mixed actinide dioxides: An ab initio study. *J. Theor. Comput. Chem.* **2012**, *11*, 611-629.

34. Rak, Z.; Ewing, R. C.; Becker, U., Hydroxylation-induced surface stability of AnO(2) (An = U, Np, Pu) from first-principles. *Surf. Sci* **2013**, *608*, 180-187.

35. Momma, K.; Izumi, F., VESTA 3 for three-dimensional visualization of crystal, volumetric and morphology data. *J. Appl. Crystallogr.* **2011**, *44*, 1272-1276.

36. Bo, T.; Lan, J.-H.; Wang, C.-Z.; Zhao, Y.-L.; He, C.-H.; Zhang, Y.-J.; Chai, Z.-F.; Shi, W.-Q., First-principles study of water reaction and H_2 formation on UO_2 (111) and (110) single crystal surfaces. *J. Phys. Chem. C* **2014**, *118*, 21935-21944.

37. Wellington, J. P.; Tegner, B. E.; Collard, J.; Kerridge, A.; Kaltsoyannis, N., Oxygen vacancy formation and water adsorption on reduced AnO_2 {111},{110}, and {100} surfaces (An= U, Pu): A computational study. *J. Phys. Chem. C* **2018**, *122*, 7149-7165.

38. Wang, G.; Batista, E. R.; Yang, P., Excess electrons on reduced AnO_2 (111) surfaces (An= Th, U, Pu) and their impacts on catalytic water splitting. *J. Phys. Chem. C* **2019**, *123*, 30245-30251.

39. Amoretti, G.; Blaise, A.; Caciuffo, R.; Fournier, J.; Hutchings, M.; Osborn, R.; Taylor, A., 5f-electron states in uranium dioxide investigated using high-resolution neutron spectroscopy. *Phys. Rev. B* **1989**, *40*, 1856.

40. Wang, H.; Zou, Y.; Zhang, Z.; Wang, K.-Y.; An, H.; Zhan, C.-Y.; Wang, J.; Wu, J.-C., First-principles study of the influence of zirconium on the diffusion of uranium defects in uranium dioxide. *J. Korean Phys. Soc.* **2019**, *74*, 795-800.

41. Kulkarni, N.; Krishnan, K.; Kasar, U.; Rakshit, S.; Sali, S.; Aggarwal, S., Thermal studies on fluorite type $Zr_yU_{1-y}O_2$ solid solutions. *J. Nucl. Mater.* **2009**, *384*, 81-86.

42. Piluso, P.; Trillon, G.; Journeau, C., The UO_2–ZrO_2 system at high temperature (T> 2000 K): Importance of the meta-stable phases under severe accident conditions. *J. Nucl. Mater.* **2005**, *344*, 259-264.

43. Lambertson, M.; Muller, M., Uranium oxide phase equilibrium systems: III, UO_2-ZrO_2. *J. Amer. Cer. Soc.* **1953**, *36*, 367.

44. Dorado, B.; Garcia, P., First-principles DFT plus U modeling of actinide-based alloys: Application to paramagnetic phases of UO_2 and (U,Pu) mixed oxides. *Phys. Rev. B* **2013**, *87*.

45. Nishi, T.; Nakada, M.; Hirata, M., Lattice parameter functions of $(Am_yU_{1-y})O_{2-x}$ based on XRD and XANES measurements. *J. Solid State Chem.* **2017**, *256*, 252-255.

Computational Study of Plutonium-Americium Mixed Oxides ($Pu_{0.92}Am_{0.08}O_{2-x}$); Water Adsorption on {111}, {110} and {100} Surfaces

Jia-Li Chen and Nikolas Kaltsoyannis

Abstract

Hubbard *U*-corrected generalized gradient approximation density functional theory is used to study the surface properties of plutonium-americium mixed dioxides (Pu-Am MOX). Stoichiometric and oxygen vacancy defect {111}, {110} and {100} surfaces are investigated, including the molecular and dissociative adsorptions of water. Comparison with previous work from our group on PuO_2 and AmO_2 leads to the conclusion that substituted Am gains electrons from the PuO_2 slab. In agreement with previous experimental studies, when the oxygen to metal ratio of MOX decreases, substituted Am is reduced to the trivalent state before the reduction of Pu. The geometries of water adsorption are similar to adsorption on PuO_2 and AmO_2 surfaces, while the presence of Am in PuO_2 surfaces promotes water adsorption. Higher temperature is required for dissociation of molecularly adsorbed water on Pu-Am MOX than on the corresponding PuO_2 surfaces, while desorption of dissociatively adsorbed water on PuO_2 is harder than on the corresponding MOX surfaces.

5.1 Introduction

Over many decades, the recycling of spent nuclear fuel in the UK has separated significant quantities of plutonium (Pu, 110.3 tonnes by December 31, 2016).[1] This is currently stored as plutonium dioxide powder while the government agrees a long-term solution, the principal options being re-use in mixed oxide (MOX) fuel or burial in a geological disposal facility. There is evidence for gas build-up in some storage containers, which might be vapour from small residual molecules, such as water desorbing from PuO_2, hydrogen gas from the radiolysis of water or the reaction of water with PuO_2, or helium following alpha decay. To understand the causes of gas generation, and hence to aid prediction of long-term behaviour, the interactions between water and PuO_2 surfaces have been intensively studied experimentally and computationally, and there is generally good agreement between experiment and simulation.[2-6] Water adsorbs in stages, with a first strongly bound, chemisorbed layer producing a hydroxylated surface as a result of dissociation, followed by one or more weakly bound layers of molecular water.[4] Two distinct water desorption temperature ranges have been reported for PuO_2 surfaces, which have been interpreted as being due to these two types of water layer,[2-3] but we have suggested that the ranges may be due to first layer water desorbing from different surfaces.[5]

Over time, americium builds up in the PuO_2 due to the radioactive decay of ^{241}Pu, and so the oldest of the UK's PuO_2 could by now have up to 8% Am. Although Pu and Am are neighbours in the periodic table, a higher oxygen equilibrium potential has been found for americium dioxide than PuO_2, which reflects the different reducibility of Am^{4+} and Pu^{4+}.[7-8] Water adsorption behaviour on AmO_2 and PuO_2 surfaces is also different.[5, 9-10] Thus, the existence of Am in PuO_2 will influence the valence states of Pu ions, water adsorption on its surfaces and, potentially, the way the material interacts with other gaseous species.

Americium-bearing PuO_2 has attracted the attention of experimentalists.[7-8, 11-18] Structural properties of plutonium-americium MOX surfaces, with different ratios of Am : Pu, have been studied by X-ray diffraction.[15] Miwa *et al*. reported that $Pu_{0.91}Am_{0.09}O_2$ has a single phase fluorite structure and the microstructure is homogeneous.[13] Pu-Am MOX with various Am contents (Am to metal ratio = 0.018, 0.077, 0.21, 0.49, 0.80 and 1.00) were studied by Vaych et al.;[8] regardless of the Am content, all the samples remain single phased face-centred cubic (f.c.c.) fluorite. To probe the electronic structure of $Pu_{0.91}Am_{0.09}O_{2-x}$, Osaka *et al*. investigated the oxygen potential of the oxide,[12] and proposed that Am is reduced from a tetravalent to a trivalent state, then after all the Am is reduced, Pu is reduced. Similar valence relationships between Pu and Am have been found for $Pu_{0.5}Am_{0.5}O_{2-x}$ by Jankowiak *et al*.[14] Cation interactions in Pu-Am MOX have been studied by Belin *et al*,[17] providing experimental evidence for Osaka's model,[12] i.e. for $Pu_{1-y}Am_yO_{2-x}$, when the oxygen to metal ratio is larger than 2-y/2, some of the Am(IV) are reduced to Am(III) with all the Pu remaining in the tetravalent state, while when the oxygen to metal ratio is smaller than 2-y/2, all the Am and some of Pu are reduced to the trivalent state, and the rest of the Pu stay in the tetravalent state.[17]

Previous theoretical work in this area mainly focuses on the study of pure PuO_2 and AmO_2,[4-5, 9-10, 19-22] although CeO_2 has also been well studied.[23-27] Not only is CeO_2 interesting in its own right and possesses the same fluorite structure as PuO_2, but it is often used experimentally as a non-radioactive surrogate for PuO_2, and computational evaluations of that similarity are useful. However, there are very few theoretical studies of Pu-Am MOX. Li *et al*. simulated $Pu_{0.5}Am_{0.5}O_2$ bulk, identifying antiferromagnetic ground states.[28] No theoretical studies have simulated Pu-Am MOX surfaces, and to the best of our knowledge, no studies investigate water adsorption on Pu-Am MOX surfaces. Thus, in this paper, we report study of Pu-Am MOX {111}, {110} and {100} surfaces, and water adsorption on these surfaces, and compare our results with previous investigations of PuO_2 and AmO_2. Water desorption temperatures on Pu-Am MOX, and PuO_2, surfaces are also simulated and compared. We organize the paper as follows: we begin with a brief description of the DFT + *U* computational methodology used. We then discuss the structures and energies of stoichiometric and oxygen vacancy defect {111}, {110}, and {100} surfaces, and present molecular and dissociative water adsorption geometries and energies on those surfaces; Corresponding water desorption temperatures are also predicted. We make extensive comparison between the MOX and PuO_2, and thus explore the effects of Am on the properties of PuO_2 surfaces.

5.2 Computational details

All calculations were performed using density functional theory (DFT), as implemented in the Vienna Ab-initio Simulation Package (VASP), version 5.4.1.[29-32] The generalized gradient approximation functional of Perdew, Burke, and Ernzerhof (PBE),[33] with a Hubbard *U* correction for the 5f electrons (U_{eff} = 4 eV; U = 4.5, J = 0.5),[34] was used for the exchange-correlation energy. Plane wave basis sets and projector-augmented wave pseudopotentials were used to describe the ions.[35] A plane wave cutoff of 650 eV was adopted for all calculations. Monkhorst-Pack (MP) grids were employed for the *k*-space integration;[36] a minimum MP grid of 5 × 5 × 1 *k* points was used for the Brillouin zone sampling for the surface simulations. A 1*k* colinear magnetic ordering with a net magnetic moment of zero was used.[28] The total system is treated as antiferromagnetic (AFM). Spin−orbit coupling has been neglected; earlier results by Rák and co-workers indicate that spin−orbit coupling has only a very small effect on surface stability.[21]

In our previous work on UO_2, PuO_2 and AmO_2,[5, 10] we evaluated the effect of changing the effective Hubbard *U* (U_{eff}) on the bulk lattice parameter and band gap, as well as surface properties and water adsorption on those surfaces, concluding that U_{eff} = 4 eV is the best overall approach. We also tested the PBESol functional, as used by other workers for bulk AnO_2,[20] concluding that it is not as good as PBE for the simulation of surfaces.

We have previously minimized the bulk and surface structures of PuO_2,[5] and the PuO_2 surfaces used here are taken from that work. Each surface is constructed from repeating slabs of 24 PuO_2 units arranged in six layers, with 18 Å of vacuum between each slab. The f electrons of Pu in the 1st, 3rd and 5th layers are unpaired and spin up, with spin down electrons in the 2nd, 4th, and 6th layers, in order to keep the whole slab AFM. The same surface model was adopted in our previous studies, in which we demonstrated convergence of the PuO_2 surface energy with slab depth.[5] Each surface is 2 × 2, and the lattice constants of the PuO_2 {111}, {110} and {100} surface are 3.796 × 3.806, 5.534 × 3.737, and 3.710 × 3.989 Å, respectively; the distortions in one direction arise from the use of the 1*k* colinear magnetic ordering approximation, and no reconstruction was found. The defect and water coverage are one-quarter monolayer. Am, defects and adsorbates are introduced on both sides of the slab to minimize the dipole effects. Thus, the chemical formula of stoichiometric Pu-Am MOX surfaces is $Pu_{22}Am_2O_{48}$ or $Pu_{0.92}Am_{0.08}O_2$, and $Pu_{22}Am_2O_{46}$ or $Pu_{0.92}Am_{0.08}O_{1.92}$ for oxygen vacancy defect Pu-Am MOX surfaces. For substoichiometric and Pu-Am MOX surfaces, the same slab shape and volume as for the PuO_2 surfaces are used, only the ions are allowed to move during optimization (ISIF = 2). As our cutoff energy (650 eV) is large enough, the Pulay stress can be neglected. All the periodic images were made using VESTA.[37]

Substitution energies of Am into the PuO_2 surfaces E_{sub} are calculated according to equation 5.1:

$$E_{\mathrm{sub}} = \frac{1}{2}\left[(E_{\mathrm{MOX}} + E_{\mathrm{Pu}}) - (E_{\mathrm{PuO_2}} + E_{\mathrm{Am}})\right] \tag{5.1}$$

where E_{MOX} and $E_{\mathrm{PuO_2}}$ are the energy of the relaxed Pu-Am mixed slab and PuO_2 slab, respectively, and E_{Pu} and E_{Am} is the energy of Pu and Am atoms in the gas phase, calculated in a periodic box with a 20 Å side. The factor of 1/2 is due to substitution on both side of slabs.

E_{reduce}, the surface oxygen defect generation energy, was calculated using equation 5.2:

$$E_{\mathrm{reduce}} = \frac{1}{2}\left(E_{\mathrm{red,slab}} + E_{\mathrm{O_2}} - E_{\mathrm{slab}}\right) \tag{5.2}$$

where E_{slab} is the energy of the stoichiometric slabs $E_{\mathrm{red,slab}}$ is the energy of the relaxed oxygen vacancy defect slab, and $E_{\mathrm{O_2}}$ is the energy of a single oxygen molecule in a box with a 20 Å side. The factor of 1/2 is due to the reduced slab having one vacancy on each side.

E_{ads}, the adsorption energy of water on stoichiometric and oxygen vacancy defect slabs, is given by equations 5.3 and 5.4 respectively:

$$E_{\mathrm{ads}} = \frac{1}{2}\left[E_{\mathrm{slab+mol}} - \left(E_{\mathrm{slab}} + 2E_{\mathrm{H_2O}}\right)\right] \tag{5.3}$$

$$E_{\mathrm{ads}} = \frac{1}{2}\left[E_{\mathrm{red,slab+mol}} - \left(E_{\mathrm{red,slab}} + 2E_{\mathrm{H_2O}}\right)\right] \tag{5.4}$$

where $E_{\mathrm{slab+mol}}$ and $E_{\mathrm{red,slab+mol}}$ are the energies of the stoichiometric and reduced slab with an adsorbed water molecule, respectively, and $E_{\mathrm{H_2O}}$ is the energy of a water molecule in the gas phase, calculated as a single water molecule in a periodic box with a 20 Å side. The factor of 1/2 is due to adsorbing water on both sides of slab.

Molecular thermodynamics was employed to calculate the relationship between the water desorption temperature and the partial pressure of water. The method used is as described in our recently published paper.[22] This is similar to the approach used to calculate the water desorption temperature from AnO_2 (An=U, Pu) surfaces in our previous work,[4] which was itself based on Molinari *et al.*'s work on water desorption from ceria surfaces.[38] Here we adopt a new continuous function for the entropy of the water molecule $S^0_{H_2O}(T)$ (equation 5.5), using the NIST-JANAF thermochemical data,[39] as a higher R^2 value (0.9995) is obtained with the new function (equation 5.5):

$$S^0_{H_2O}(T) \cong 65.086T^{0.1852} \tag{5.5}$$

Spin density data are reported extensively throughout this work. Spin densities are calculated as the difference between the number of α spin (spin up) and β spin (spin down) electrons, and have units of electron density (*i.e.* electrons/bohr^3). This can be evaluated on a per-atom basis. For actinides in positive oxidation states, the excess (α-β) spin density is due to unpaired 5f electrons, and the difference between this value and the total number of valence electrons in the neutral atom can be used to establish oxidation state. For example, a formally Pu(IV) ion will have the electronic configuration {Rn}5f^4, so if we calculate a Pu atom to have a spin density close to four, then we can be confident in assigning it as Pu(IV), *i.e.* it is tetravalent. For Pu(III), the electronic configuration will be {Rn}5f^5, and hence the computed spin density on a Pu(III) centre will be close to 5.

5.3 Results and discussion

5.3.1 $Pu_{0.92}Am_{0.08}O_2$ surfaces

Stoichiometric plutonium dioxide slabs of the {111}, {110} and {100} surfaces, each containing 6 layers including 24 Pu cations and 48 O anions, have been optimized (Figure 5.1). To keep the whole slab antiferromagnetic (AFM), the unpaired f electrons were set as spin up for Pu in 1st, 3rd and 5th layers, and spin down in 2nd, 4th and 6th layers. Surface energies obtained here are 0.67, 1.14, and 1.58 J/m^2 for PuO_2 {111}, {110} and {100} surfaces, respectively in good agreement with previously reported data (0.66, 1.13 and 1.59 J/m^2).[5] The spin densities of the Pu atoms range from 4.192 to 4.258, from 4.158 to 4.327, and from 4.183 to 4.259 in the {111}, {110} and {100} slabs, respectively. The spin density of Pu on the surface (1st and 6th layers) is a little larger than Pu in deeper layers (2nd – 5th layers), suggesting more electrons are localized on surface Pu than Pu in deeper layers, most likely because some Pu-O bonds are cleaved to form the surface, i.e. surface Pu is bonded to 7, 6 and 6 oxygens on {111}, {110} and {100} surface, respectively, but bonded to 8 oxygens in the bulk.

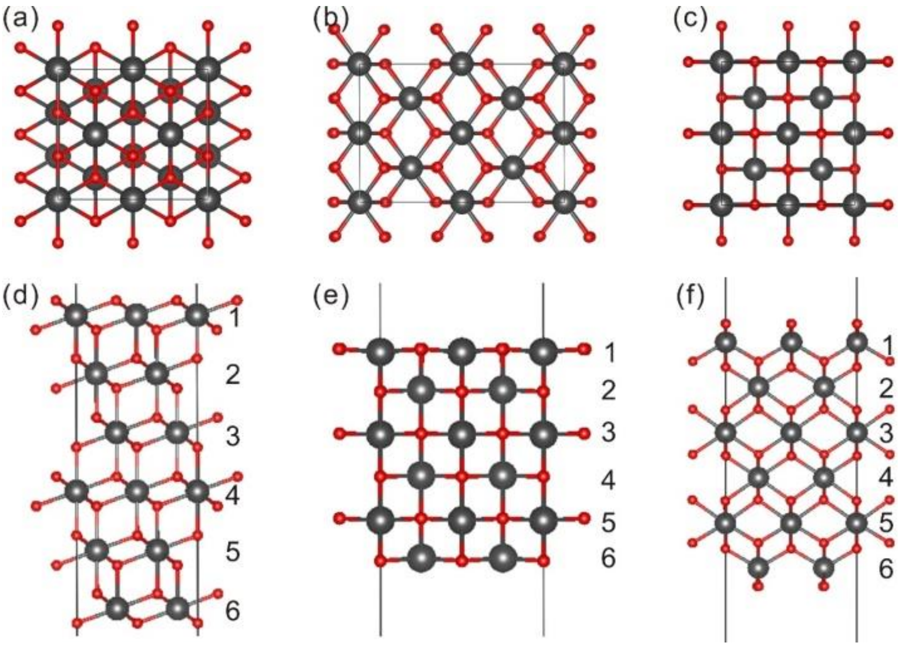

Figure 5.1: Top ((a), (b) and (c), respectively) and side ((d), (e) and (f), respectively) view of stoichiometric PuO_2 {111}, {110}, {100} surfaces. Dark grey and red spheres represent plutonium and oxygen atoms, respectively. the layers of PuO_2 slabs are numbered in (d), (e) and (f).

Substitution of an Am atom has been considered for both sides of the PuO_2 slabs, in order to avoid dipole effects. To keep the MOX slabs AFM, there are three ways to substitute Am; two Am atoms, giving c. 8% Am in the system, in 1st and 6th layers (method A), 2nd and 5th layers (method B), and 3rd and 4th layers (method C). In order to compare substitution of Am at different surfaces, substitution method A has been considered for all three surfaces (Figure 5.2 (a), (b) and (c)). Substitution methods A, B and C have been compared for the {111} surface (Figure 5.2 (d), (e) and (f)), in order to establish how deeply substituted Am affect surface properties and how the interaction between substituted Am affects PuO_2 surfaces.

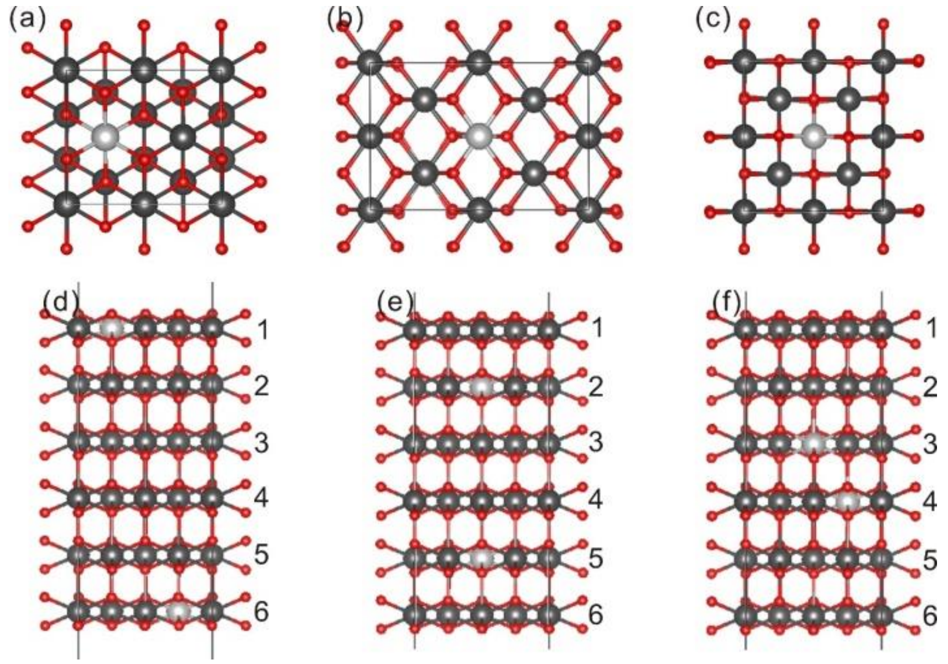

Figure 5.2: Top view of $Pu_{0.92}Am_{0.08}O_2$ (a) {111}, (b) {110} and (c) {100} surfaces with Am substituted in 1st and 6th layers. Side view of $Pu_{0.92}Am_{0.08}O_2$ {111} surfaces with Am in (d) 1st and 6th layers, (e) 2nd and 5th layers, and (f) 3rd and 4th layers. Dark grey, light grey and red spheres represent plutonium, americium and oxygen atoms, respectively.

Substitution of Am has little influence on the geometric structure of all three surfaces for all three substitution methods. For example, the lattice constants of the $Pu_{0.92}Am_{0.08}O_2$ {111}, {110} and {100} surfaces with substitution method A are 3.806 × 3.803, 5.528 × 3.756, and 3.703 × 3.994 Å, respectively; no reconstruction was found. The difference in Am-O bond length between MOX and AmO_2 is not larger than 0.01 Å, as is the change in surrounding Pu-O bonds, which is why there are only small differences between the lattice constants of the PuO_2 and Pu-Am MOX surfaces. However, the electronic structures of $Pu_{0.92}Am_{0.08}O_2$ surfaces show clear differences between AmO_2 and PuO_2. Table 5.1 summarizes the spin densities of the two Am cations and all Pu cations in the same layer. Am and Pu in stoichiometric AmO_2 and PuO_2 are tetravalent with spin densities of c.a. 5 and 4, respectively. However, the spin density of Am cations range from 5.400 to 5.575 (corresponding approximately to the +3.5 charge state) in stoichiometric MOX surfaces, indicating that Am has gone through a reduction process after substitution. As noted in the introduction, previous experimental work on Pu-Am MOX concludes that some Am will be reduced to trivalent, if the oxygen to metal (O/M) ratio in $Pu_{1-y}Am_yO_{2-x}$ is larger than 2-$y/2$.[17] Obviously, $Pu_{0.92}Am_{0.08}O_2$ belongs to this region (2 > 2-0.04), and our model reflects this mixed valence situation *via* Am ions in the c. +3.5 charge state. The spin density of Am on the surface is a little larger than in deeper layers (Table 5.1), in agreement with what is found for surface and deeper layer Pu. The charge states of oxygen anions and Pu cations do not show a clear change after Am substitution, so we compared the charge density of stoichiometric MOX and PuO_2 surfaces (Appendix 3, Figure A5.1). Substitution of Am mainly influences the charge density of atoms in the same layer, and has little influence on neighbour layers, so substituted Am is reduced mainly by surrounding Pu and O atoms and tends to be trivalent.

Table 5.1: Spin density of actinides (An) in $Pu_{0.92}Am_{0.08}O_2$ slabs.

Substitution method	An	{111}	{110}	{100}
A (Am in 1st and 6th layers)	Am	-5.505/ 5.507	-5.553/ 5.556	-5.575/ 5.498
	Pu	4.202 – 4.262	4.198 – 4.314	4.183 – 4.289
B (Am in 2nd and 5th layers)	Am	5.413/ -5.394	-	-
	Pu	4.196 – 4.262	-	-
C (Am in 3rd and 4th layers)	Am	-5.400/ 5.409	-	-
	Pu	4.190 – 4.259	-	-

Calculated Am substitution energies are listed in Table 5.2. When Am is substituted for Pu on the surface (method A), substitution on {111} surfaces is the hardest, and substitution energies on {110} and {100} surfaces are similar. As the {111} surface is the most stable, and the stability of {110} and {100} surfaces are similar, surface activity is likely an important factor in the substitution energy of Am. Substitution energies on the {111} surface are almost the same with methods A, B and C. Interaction between two Am atoms is possible, when they substitute in the 3rd and 4th layers (method C) (Figure 5.2 (f)), but the same energies for substitution methods B and C suggests that the interaction between substituted Am atoms is very small. Distortion of PuO_2 slabs, due to the substitution of Am, is negligible, suggesting size effects on substitution energy are also very small. Overall, we conclude that the substitution energy of Am is mainly related to the activity of the PuO_2 surfaces.

Table 5.2: Substitution energies (eV) of Am into $Pu_{0.92}Am_{0.08}O_2$ slabs

Substitution method	{111}	{110}	{100}
A (Am in 1st and 6th layers)	3.34	3.14	3.16
B (Am in 2nd and 5th layers)	3.35	-	-
C (Am in 3rd and 4th layers)	3.35	-	-

5.3.2 $Pu_{0.92}Am_{0.08}O_{1.92}$ surfaces

As the O/M ratio of Pu-Am MOX may change with environment, such as pressure and temperature, and substoichiometric MOX has been found by experiment,[7, 12] we simulated surfaces with oxygen defects. An O atom was removed from both sides of the slabs to avoid dipole effects, so the chemical formula of the slabs changes to $Pu_{22}Am_2O_{46}$ or $Pu_{0.92}Am_{0.08}O_{1.92}$. For stoichiometric slabs with Am on the surface (method A), there are two kinds of surface oxygen, i.e. bonded with surface Am or not, so there are two kinds of oxygen defect, next to surface Am (Figure 5.3 (a) – (b)) and away from surface Am (Figure 5.3 (d) – (f)), while there is only one kind of defect on surfaces with Am in deep layers (Figure 5.3 (g) and (h)). Surface structures and electronic properties of substoichiometric Pu-Am MOX slabs are discussed in the following section.

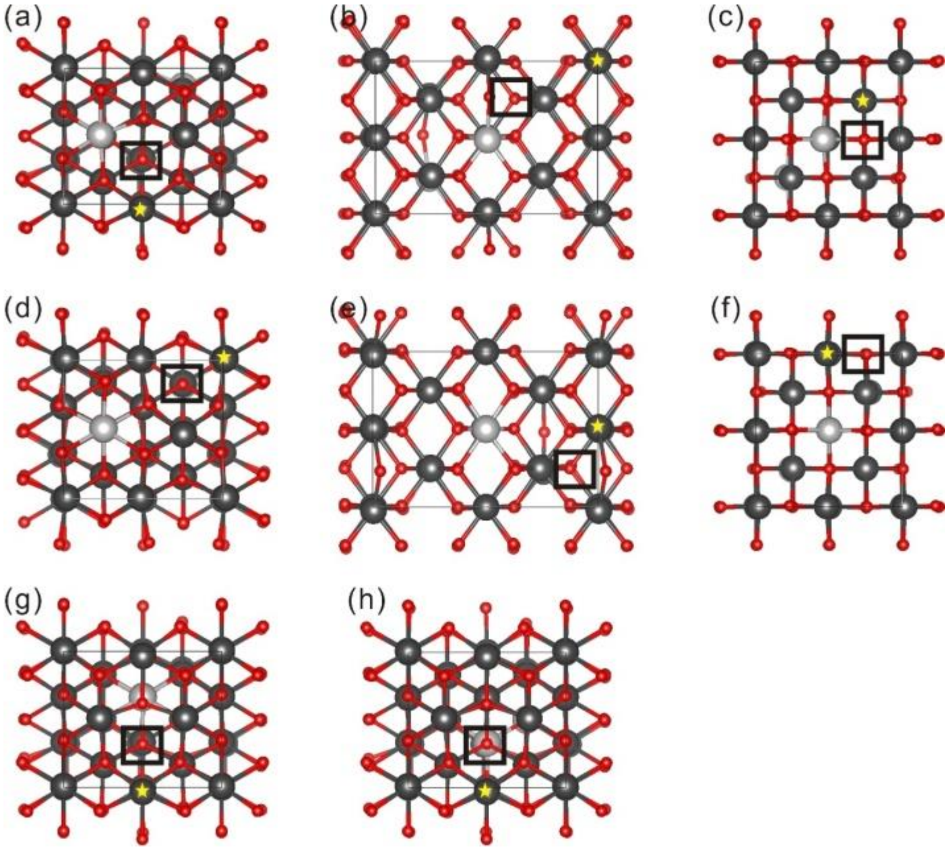

Figure 5.3: Top views of $Pu_{0.92}Am_{0.08}O_{1.92}$ {111}, {110} and {100} surfaces with Am on the surface, with oxygen defects next to surface Am ((a), (b) and (c), respectively) and away from surface Am ((d), (e) and (f) respectively), as well as top views of $Pu_{0.92}Am_{0.08}O_{1.92}$ {111} surfaces with Am in (g) 2nd and 5th layers and (h) 3rd and 4th layers. Dark grey, light grey and red spheres represent plutonium, americium and oxygen atoms, respectively. Black squares mark the positions of oxygen defects. Plutonium atoms marked with yellow stars show clear changes in spin density after generation of the oxygen defect.

Oxygen defect formation influences the surface structures, and the displacement of nearest neighbour An and O atoms from the oxygen vacancy compared to stoichiometric $Pu_{0.92}Am_{0.08}O_2$ surfaces are presented in Figure 5.4. There are three neighbour An and O atoms on the {111} surfaces, and three An and two O on the {110} surfaces. On the {100} surface, the distance to the nearest O is larger than 3.5 Å and the displacement is smaller than 0.1 Å, so only the displacements of the two nearest neighbour An atoms are considered. In all cases, neighbour An move away from the defect, while neighbour O move toward the defect. Larger displacement of neighbour O is found on the {110} surfaces for both kinds of O defect, and comparing Figure 5.3 (b) and (e) with Figure 5.2 (b) show the larger displacement is mainly caused by one of the neighbour O. This O atom in the middle of the triangle of three An in the stoichiometric surface, and moves to the bridge site between two An in the substoichiometric surface. This kind of displacement of neighbour O has not been reported before for substoichiometric PuO_2 surfaces, so the large displacement on the {110} surface is likely to be caused by the substitution of Am. The displacements of An and O on the {111}, and An on {110} and {100} surfaces, are all around 0.2 Å, which is similar to the displacements reported for UO_2 and PuO_2.[9] Thus, excepting the displacement of one surface O (O_s) on the {110} surfaces, similar to what was found for $Pu_{0.92}Am_{0.08}O_2$ surfaces, the existence of Am has little influence on $Pu_{0.92}Am_{0.08}O_{1.92}$ surface structures, i.e. the displacement is mainly caused by the O vacancy. Overall, displacement induced by O vacancies is in broad agreement with our previous findings for substoichiometric AnO_2 (An = U – Cm) surfaces.[9-10]

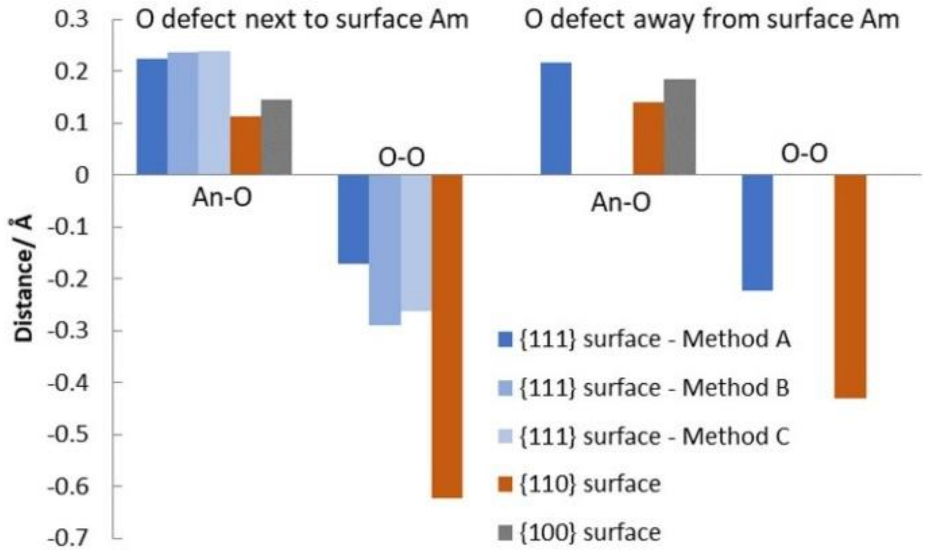

Figure 5.4: Average displacement of nearest neighbour atoms (either An or O) from the oxygen vacancy compared with the stoichiometric slab. Positive displacements indicate movement away from the vacancy site, whereas negative displacements indicate movement toward the site.

Table 5.3: Spin density of americium, and the plutonium atoms marked with a yellow star in Figure 5.3, for $Pu_{0.92}Am_{0.08}O_{1.92}$ surfaces.

Substitution method	O defect	An	{111}	{110}	{100}
A (Am in 1st and 6th layers)	Next to Am	Am	-6.132/ 6.123	-6.101/ 6.113	-6.125/ 6.142
		Pu	-5.060/ 5.061	-5.085/ 5.078	5.057/ 5.059
	Away from Am	Am	-6.128/ 6.128	-6.135/ 6.136	-6.121/ 6.120
		Pu	-5.066/ 5.066	-5.051/ 5.056	-5.081/ 5.073
Substitution method	O defect	An	{111}	{110}	{100}
B (Am in 2nd and 5th layers)		Am	6.104/ -6.107	-	-
		Pu	-5.056/ 5.063	-	-
C (Am in 3rd and 4th layers)		Am	-6.105/ 6.105	-	-
		Pu	-5.063/ 5.063	-	-

The creation of a neutral oxygen vacancy leaves behind two electrons. Table 5.3 summarizes the spin densities of some An that shows clear changes when compared with corresponding $Pu_{0.92}Am_{0.08}O_2$ surfaces (Table 5.1). Comparing Tables 5.1 and 5.3, we find that the two extra electrons on $Pu_{0.92}Am_{0.08}O_{1.92}$ surfaces mainly localize on the substituted

Am cation, and one surface Pu cation, which is indicated by a yellow star in Figure 5.3. The Pu and Am cations are reduced to the trivalent state. The surface Pu cation that gains one electron neighbours the defect, while no matter where the Am cation is located, neighbour the defect or not, it gains another electron, even when substituted in deeper layers, presumably because the Am (IV)/(III) redox potential (2.60 eV) is much higher than Pu (IV)/(III) (1.01 eV). According to previous experimental work,[17] $Pu_{0.92}Am_{0.08}O_{1.92}$ belongs to the region with 2-y/2 ($1.92 < 2-0.04$), and hence our finding about the valence state of the Pu and Am cations agrees with experimental results. Hence, our theoretical simulations support the experimentally proposed cation valence relationship in both stoichiometric and reduced Pu-Am MOX.

O defect generation energies are given in Table 5.4. For substitution method A (Am in 1st and 6th layers), O defect generation on the {111} surface is the hardest, while generation energies on {110} and {100} surfaces are similar, whatever Am is next to the defect or not. This energy sequence, which reflects the relative activity of {111}, {110} and {100} surfaces, is the same as found on stoichiometric AnO_2 surfaces. On each surface, generation energies are similar for both kinds of O defect, as they have similar displacement of neighbour An and O (Figure 5.4) and charge redistribution (Table 5.3). On the {111} surfaces, the O defect generation energy is the smallest for substitution method A, becoming larger for substitution method B and C. The energy sequence for the different substitution methods is related to the charge distribution in the MOX slabs. Substituted Am gains electrons mainly from atoms in the same layer and has only a little influence on neighbour layers (Figure A5.1). In other words, surface atoms are most oxidized with substitution method A, less oxidized with substitution method B, and not oxidized with method C. As the O defect generation process is a reduction process for surface atoms, it is more favourable for more oxidized surface atoms, thus it is easiest to generate O defects on the {111} surface with Am in 1st and 6th layers, and hardest on the surface with Am in the 3rd and 4th layers.

Table 5.4: Oxygen defect generation energies (eV) for Pu-Am MOX surfaces, i.e. on going from $Pu_{0.92}Am_{0.08}O_2$ to $Pu_{0.92}Am_{0.08}O_{1.92}$.

Substitution method	Position of O defect	{111}	{110}	{100}
A (Am in 1st and 6th layers)	Next to Am	1.94	1.10	1.07
	Away from Am	1.97	1.00	1.37
B (Am in 2nd and 5th layers)		2.11	-	-
C (Am in 3rd and 4th layers)		2.27	-	-

O defect generation energies on Pu-Am MOX surfaces with Am on the surface are compared to defect generation energies on stoichiometric PuO_2 and AmO_2 surfaces in Figure 5.5.[9-10] This figure highlights the similar trend in O defect generation energies on stoichiometric AnO_2 and MOX surfaces. On each surface, the O defect generation energy for MOX lies between the corresponding generation energy on PuO_2 and AmO_2 surfaces,[9-10] and close to their average (1.91, 1.22 and 1.16 eV, respectively, for the {111}, {110} and {100} surfaces). In our previous work, we found that O defect generation on AnO_2 surfaces is linearly related with An(IV)/(III) redox potential. As O defect generation energy on Pu-Am MOX surfaces is close to the average generation energy on PuO_2 and AmO_2 surfaces, this again supports the linear relationship between O defect generation energy and An(IV)/(III) redox potential. We conclude that, in addition to surface activity, the redox potential of An(IV)/(III) is an important factor in the O defect generation energy on MOX surfaces.

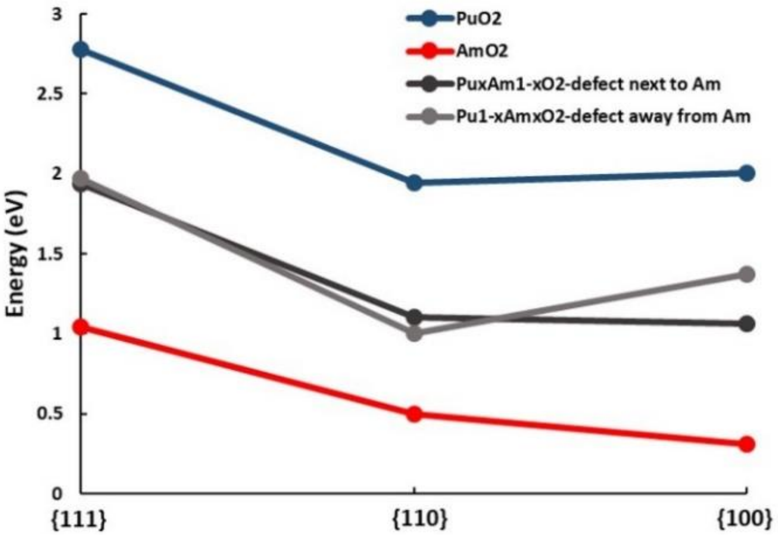

Figure 5.5: Oxygen defect generation energy on pure PuO_2 and AmO_2 surfaces and Pu-Am MOX surfaces.

5.3.3 Water adsorption on $Pu_{0.92}Am_{0.08}O_2$ surfaces

Molecular and dissociative water adsorptions on $Pu_{0.92}Am_{0.08}O_2$ surfaces have also been simulated. If the water stays as an intact molecule during the adsorption process it is termed molecular adsorption, whereas dissociative adsorption breaks an O–H bond and results in one adsorbed hydrogen atom and one adsorbed hydroxyl group. Molecular adsorptions were considered first. On $Pu_{0.92}Am_{0.08}O_2$ surfaces with Am on the surface, there are two approaching routes for a water molecule, approaching surface Am (Am_s) or surface Pu (Pu_s), and the two kinds of molecular adsorption structures on all three surfaces are presented in Figure 5.6 (a) – (f). Adsorption structures are similar on different surface sites on {111}, {110} and {100} surfaces. On the {100} surface, the approach of water to Am_s and Pu_s leads to spontaneous dissociation (Figure 5.6 (c) and (f)), and the adsorption structures are similar to dissociative adsorption structures on stoichiometric AnO_2 {100} surfaces. Molecular adsorption on {111} and {110} surfaces is very similar to taht on the corresponding stoichiometric AnO_2 {111} and {110} surfaces. As the water adsorption structures on PuO_2 and AmO_2 surfaces are almost the same, and no obvious distortion of PuO_2 surfaces is found after the substitution of Am, we conclude that the presence of Am has little influence on the water adsorption geometrics on $Pu_{0.92}Am_{0.08}O_2$ surfaces.

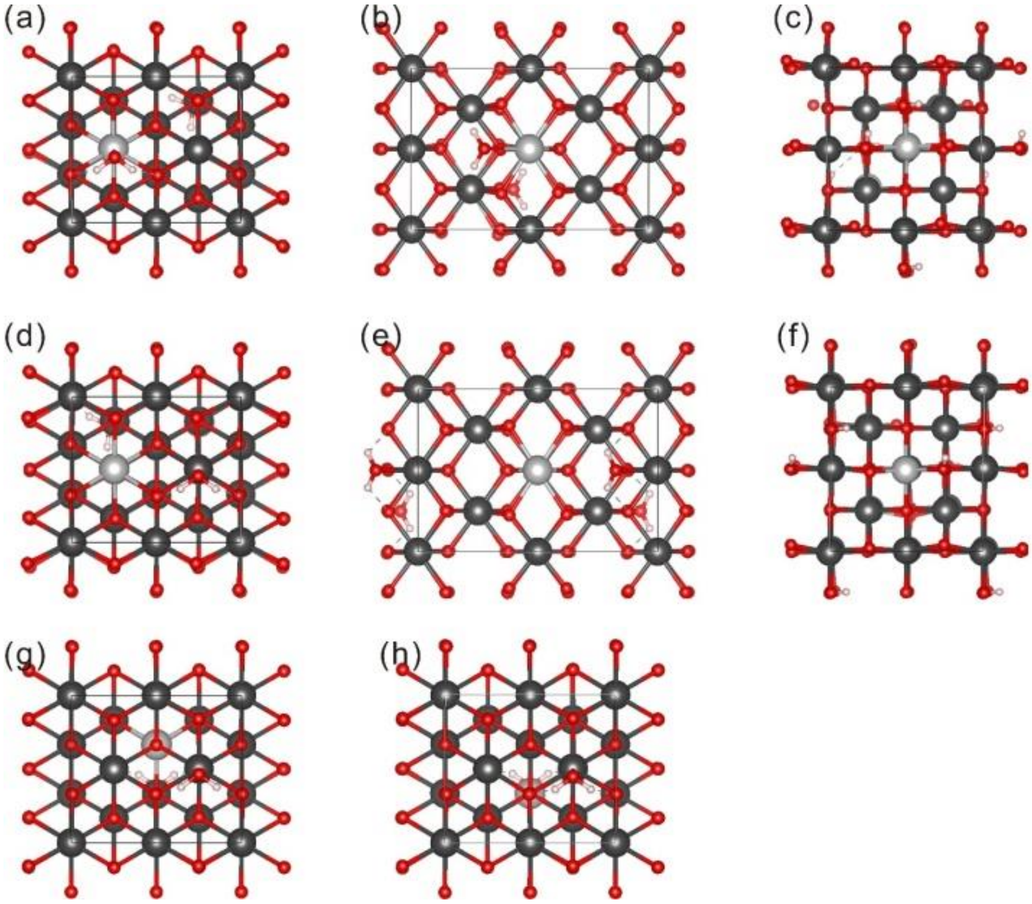

Figure 5.6: Top view of molecular water adsorption on $Pu_{0.92}Am_{0.08}O_2$ {111}, {110} and {100} surfaces, with water approaching surface Am ((a), (b) and (c), respectively) and surface Pu ((d), (e) and (f) respectively), as well as on $Pu_{0.92}Am_{0.08}O_{1.92}$ {111} surfaces with Am in (g) 2nd and 5th layers and (h) 3rd and 4th layers. Dark grey, light grey, red and white spheres represent plutonium, americium, oxygen and hydrogen atoms, respectively.

Molecular adsorption energies on $Pu_{0.92}Am_{0.08}O_2$ surfaces with Am on the surface are compared in Table 5.5. On all three surfaces, water adsorption on Am_s is more stable than on Pu_s. Previous work on water adsorption on stoichiometric PuO_2 and AmO_2 surfaces indicates that molecular water adsorption on stoichiometric PuO_2 is more stable than on the corresponding AmO_2 surfaces.[5, 10] To probe the reason for the reverse activity of Am_s and Pu_s toward water adsorption on Pu-Am MOX surfaces, the spin densities of the surface An cations (An_s) are considered (Table A5.1). On {111} surfaces, the spin density of Am_s and

Pu_s is almost the same as the corresponding Am_s and Pu_s on the clean surface, with a small increase and decrease, respectively. On {110} and {100} surfaces, however, when water adsorbs on Am_s, the spin density of Am_s increases to 6.118 and 6.120, indicating Am is in the trivalent state. The spin density of one Pu_s cation decreases to 3.791 and 3.595 on {110} and {100} surfaces, respectively, but the spin density of An_s cations does not change, when water adsorbs on Pu_s. Thus, adsorption of water on Am_s promotes the reduction of Am to the trivalent state. Overall, the influence of surface electronic structure leads to more stable adsorption on Am_s; this effect is much more obvious for the {110} and {100} surfaces.

Table 5.5: Water adsorption energies (eV) on $Pu_{0.92}Am_{0.08}O_2$ surfaces.

Substitution method	Approaching	Molecular adsorption			Dissociative adsorption		
		{111}	{110}	{100}	{111}	{110}	{100}
Am in 1st and 6th layers	Surface Am	-0.52	-0.96	-1.38	-0.47	-0.91	-1.38
	surface Pu	-0.36	-0.42	-1.03	-0.26	-0.66	-1.03
Am in 2nd and 5th layers		-0.49	-	-	-0.35	-	-
Am in 3rd and 4th layers		-0.45	-	-	-0.36	-	-

Stable dissociative water adsorption structures on the {111} and {110} surfaces are given in Figure 5.7 (a) – (d). Adsorption structures for the two approach routes on each surface are similar, and similar to those on the corresponding stoichiometric AnO_2 surfaces. Thus, substitution of Am also has little influence on dissociative adsorption. Dissociative adsorption energies are given in Table 5.5; as water dissociates spontaneously on the {100} surface, the dissociative and molecular adsorption energies are the same. As with molecular adsorption, dissociative water adsorption on Am_s is more stable than on Pu_s. The spin densities of Am_s and Pu_s cations do not change on dissociative adsorption, except for Am_s on {110} and {100} surfaces, where the Am_s cation is reduced to the trivalent state, and the spin density of one Pu_s decreases to -3.636 and -3.595, respectively (Table A5.2). Again, the influence of surface electronic structure leads to more stable adsorption on Am_s.

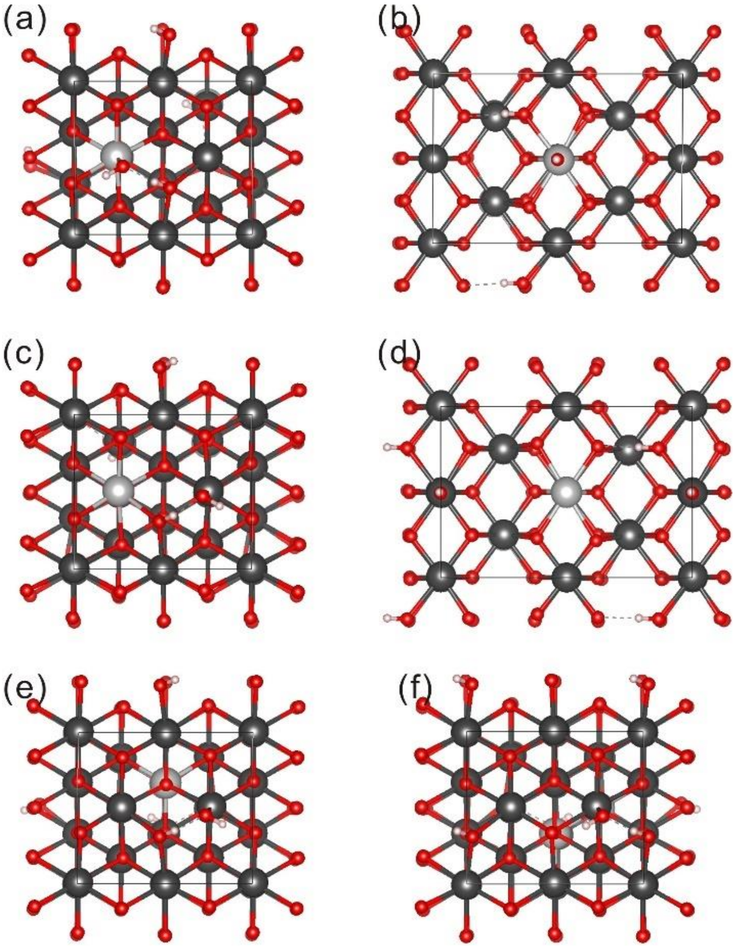

Figure 5.7: Top view of dissociative water adsorption on $Pu_{0.92}Am_{0.08}O_2$ {111} and {110} surfaces, with water approaching surface Am ((a) and (b), respectively) or surface Pu ((c) and (d), respectively), as well as on $Pu_{0.92}Am_{0.08}O_{1.92}$ {111} surfaces with Am in (e) 2nd and 5th layers and (f) 3rd and 4th layers. Dark grey, light grey, red and white spheres represent plutonium, americium, oxygen and hydrogen atoms, respectively.

A similar energy sequence is found for molecular adsorption on $Pu_{0.92}Am_{0.08}O_2$ and stoichiometric PuO_2 and AmO_2 surfaces (Figure 5.8 (a)),[5, 10] i.e. the stability of molecular adsorption increases from {111} to {100}. Adsorption energies on Pu_s of MOX and PuO_2 are similar, as substitution of Am has little influence on surface structure and does not change the charge distribution of Pu_s much. In contrast, the adsorption energies on Am_s in MOX and AmO_2 increasingly differ from {111} to {100}. The Am cation on MOX surfaces is in the c.a. +3.5 charge state, which is liable to be reduced further to the trivalent state, so Am on MOX surfaces is more active than Am on AmO_2 surfaces. The overall activity towards molecular water adsorption of MOX is greater than stoichiometric AnO_2.

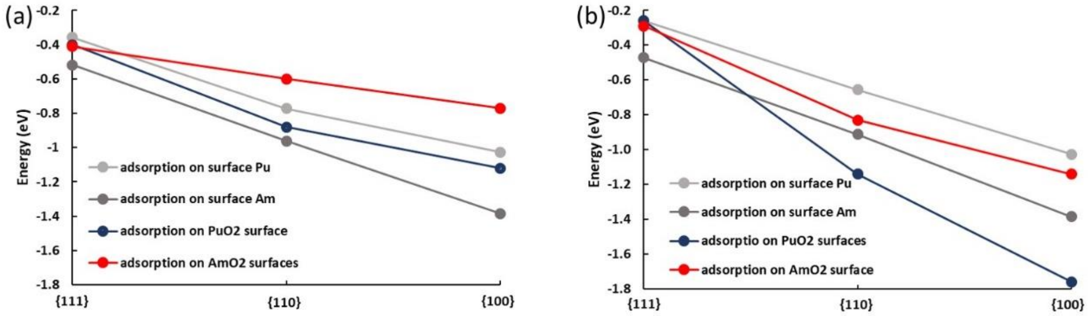

Figure 5.8: (a) Molecular and (b) dissociative adsorption energy on stoichiometric PuO_2 and AmO_2 surfaces, as well as on $Pu_{0.92}Am_{0.08}O_2$ surfaces. Water adsorption energies on PuO_2 and AmO_2 are taken from references 5 and 10, respectively.

Figure 5.8 (b) compares dissociative water adsorption on Pu-Am MOX surfaces with stoichiometric PuO_2 and AmO_2 surfaces. As with molecular adsorption, dissociative adsorption on Am_s on MOX is more stable than on the corresponding AmO_2 surfaces, due to the different charge state of Am_s. Dissociative adsorption on Am_s of $Pu_{0.92}Am_{0.08}O_2$ is the most stable type of adsorption on {111} surfaces, while adsorption on PuO_2 surfaces is the most stable on the {110} and {100} surface. The special activity of PuO_2 surfaces towards dissociative water adsorption was noted in our previous work, where we observed that dissociative water adsorptions on PuO_2 {110} and {100} surfaces have much more negative energies than on UO_2 and minor actinide AnO_2 (An = Np, Am, Cm) surfaces,[5, 10] in agreement with the known high hydrophilicity of PuO_2.

There is only one approach route for water adsorption on $Pu_{0.92}Am_{0.08}O_2$ {111} surface with Am in the 2nd and 5th, and 3rd and 4th layers, i.e. approaching Pu_s. Molecular adsorption structures are present in Figure 5.6 (g) and (h), and dissociative adsorption structures are presented in Figure 5.7 (e) and (f). Both molecular and dissociative adsorption structures are similar to the corresponding adsorption structures on Pu_s of $Pu_{0.92}Am_{0.08}O_2$ {111} surface with Am in the 1st and 6th layers, again showing that substitution of Am little affects water adsorption on PuO_2 surfaces. Adsorption energies are listed in Table 5.5. Molecular and dissociative adsorptions are similar for the three kinds of substitution methods with Am in different layers.

5.3.4 Water adsorption on $Pu_{0.92}Am_{0.08}O_{1.92}$ surfaces

There are three ways for water to approach $Pu_{0.92}Am_{0.08}O_{1.92}$ surfaces with Am on the surface: approaching Am_s, Pu_s or the oxygen defect, while there are two approach routes, Pu_s and defect, on surfaces with Am atoms in deeper layers. Water adsorption on $Pu_{0.92}Am_{0.08}O_{1.92}$ surfaces with Am on the surface will be discussed first, then adsorption on surfaces with Am in deeper layers. For the former, the position of the O defect also has to be considered; adsorptions on surfaces with the O defect next to Am_s are presented, then water adsorption on surfaces with the O defect away from Am_s.

The structures of molecular water adsorption on $Pu_{0.92}Am_{0.08}O_{1.92}$ surfaces with Am on the surface and the O defect next to Am_s, are presented in Figure 5.9. When approaching Am_s, molecular water adsorption structures are similar to structures on the corresponding substoichiometric AmO_2 surfaces ($Am_{24}O_{46}$ or $AmO_{1.92}$).[10] Approaching Pu_s leads to spontaneous dissociation on the {100} surface, while stable molecular water adsorptions are found on {111} and {110} surfaces. The adsorption structures on Pu_s found here are similar to those on the corresponding substoichiometric PuO_2 ($Pu_{24}O_{46}$ or $PuO_{1.92}$) surfaces.[9] All stable molecular adsorption structures on An_s have the oxygen of water (O_w) bonded with one An_s and the two hydrogens of water (H_w) interact with nearby surface oxygens (O_s). Molecular adsorption on the surface defect of {111} is different (Figure 5.9 (g)), with no clear interaction between O_w and An_s, or between H_w and O_s. Approaching the surface defect of {110} and {100} also leads to spontaneous dissociation (Figure 5.9 (h) and (i), respectively); similar dissociative adsorption structures have been reported at the surface defects of $AmO_{1.92}$ and $PuO_{1.92}$.[9-10]

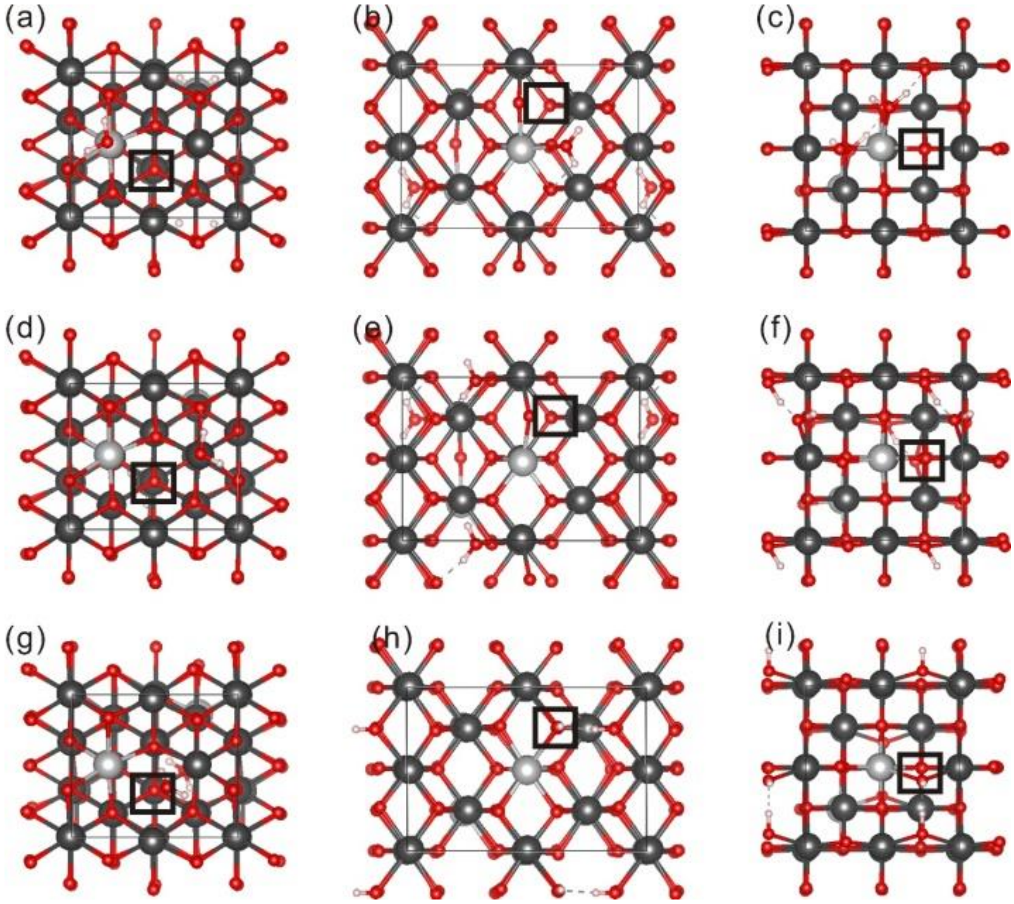

Figure 5.9: Top view of molecular water adsorption on $Pu_{0.92}Am_{0.08}O_{1.92}$ {111}, {110} and {100} surfaces with O defect next to surface Am, with water approaching surface Am ((a), (b) and (c), respectively), surface Pu ((d), (e) and (f), respectively), or on surface defect ((g), (h) and (i), respectively). Dark grey, light grey, red and white spheres represent plutonium, americium, oxygen and hydrogen atoms, respectively.

We now consider dissociative water adsorption on $Pu_{0.92}Am_{0.08}O_{1.92}$ surfaces with Am on the surface and the O defect next to Am_s, except for adsorption on those surfaces on which water dissociates spontaneously. Dissociative adsorption structures are presented in Figure 5.10. The same stable adsorption structure has been found (Figure 5.10 (a)) on the {111} surface for water approaching different surface sites; O_w takes the defect position and a H_w breaks with O_w and forms a new bond with O_s. This conformation has also been found on all $AnO_{1.92}$ {111} surfaces, with O_w 'healing' the surface defect.[9-10] The structure of dissociative adsorption on Am_s of the {110} surface is given in Figure 5.10 (b), which has the hydroxyl groups facing away from each other. The dissociative structure on Pu_s is the same as on the surface defect (Figure 5.9 (h)), with the hydroxyl groups facing each other. These two kinds of dissociative adsorption structures on {110} surfaces have been reported for $AnO_{1.92}$ (An = U – Cm) {110} surfaces.[9-10] Three stable dissociative adsorption structures have been found on the {100} surface, presented in Figure 5.10 (c), Figure 5.9 (f) and (i) for water approaching Am_s, Pu_s and the defect, respectively. For water approaching the Am_s and Pu_s of the {100} surface, O_w does not take the position of the surface defect. O_w bonds with one Am_s and one Pu_s, and H_w bonds with O_s, when water approaches Am_s of the {100} surface (Figure 5.10 (c)), O_w bonds with one Pu_s, and H_w forms a hydroxyl with O_s, when approaching Pu_s. A different adsorption structure has been found, with O_w 'healing' the defect, when approaching the surface defect. Comparing Figure 5.9 (f) and (i), dissociative water adsorption on Pu_s forms the structure in Figure 5.9 (i), which corresponds to dissociative water adsorption on the surface defect. Overall, again, dissociative adsorption structures on $Pu_{0.92}Am_{0.08}O_{1.92}$ surfaces are similar to structures reported on $AnO_{1.92}$ {100} surfaces.[9-10]

To summarise, we report 3, 2 and 1 stable molecular adsorption structures, and 1, 2, and 3 stable dissociative adsorption structures on $Pu_{0.92}Am_{0.08}O_{1.92}$ {111}, {110} and {100} surfaces, respectively, with Am on the surface and the O defect next to Am_s. Both molecular and dissociative adsorption structures on $Pu_{0.92}Am_{0.08}O_{1.92}$ and $AnO_{1.92}$ surfaces are similar. Thus, substitution of Am does not significantly change water adsorption structures on substoichiometric PuO_2 surfaces. That similar adsorption structures are found for substoichiometric MOX and AnO_2 is reasonable given that water adsorption structures are similar on all $AnO_{1.92}$ surfaces. As with clean $Pu_{0.92}Am_{0.08}O_{1.92}$ surfaces, Am_s and one Pu_s are in the trivalent state, and the other Pu_s cations are tetravalent. Thus, the spin density of An_s is not affected by molecular or dissociative water adsorption on $Pu_{0.92}Am_{0.08}O_{1.92}$ surfaces.

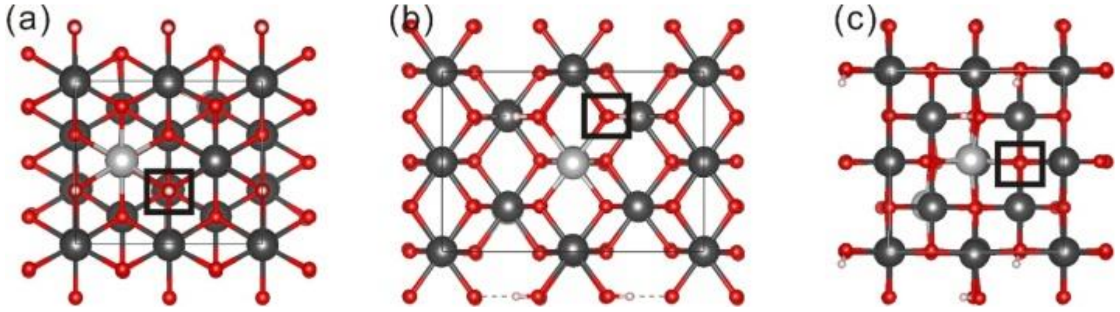

Figure 5.10: Top view of dissociative water adsorption on $Pu_{0.92}Am_{0.08}O_{1.92}$ surfaces, with O defect next to surface Am, (a) on {111} surface with water approaching surface Am, Pu or O defect, (b) on {110} and (c) {100} surfaces approaching surface Am. Dark grey, light grey, red and white spheres represent plutonium, americium, oxygen and hydrogen atoms, respectively.

Water adsorption energies are listed in Table 5.6. The stability of molecular water adsorption on $Pu_{0.92}Am_{0.08}O_{1.92}$ surfaces is {111} < {110} < {100}, which is the same as for water adsorption on $AnO_{1.92}$ surfaces,[9-10] for all three approach routes. Molecular adsorption at the surface defects is much weaker, and water prefers to approach Pu_s atoms than Am_s, as molecular water adsorption on Pu_s is always more stable than on Am_s, and adsorption at Pu_s of the {100} surface leads to spontaneous dissociation. The stability of dissociative adsorption is related to the adsorption structures. On the {111} surface, as the same structures are found on the different surface sites, the adsorption energies are the same for the three approach routes. On the {110} surface, previous studies have found that dissociative adsorption with the hydroxyl groups facing away from each other (Figure 5.10 (b)) is more stable than adsorption with the hydroxyl groups facing each other (Figure 5.9 (h), so dissociative adsorption with water approaching Am_s is the more stable state on the $Pu_{0.92}Am_{0.08}O_{1.92}$ {110} surface. On the {100} surface, as O_w heals the vacancy when water approaches a surface defect, dissociative adsorption on the surface defect is the most stable state among all three stable dissociative states on this surface. Water adsorption energies on $PuO_{1.92}$ and $AmO_{1.92}$ surfaces are also given in Table 5.6. Water adsorption on Am_s of $Pu_{0.92}Am_{0.08}O_{1.92}$ surfaces is more stable than on $AmO_{1.92}$ surfaces. Molecular adsorptions on Pu_s of $Pu_{0.92}Am_{0.08}O_{1.92}$ surfaces are also more stable than on $PuO_{1.92}$ surfaces.

Table 5.6: Molecular (bold) and dissociative (italic) water adsorption energies (eV) on $Pu_{0.92}Am_{0.08}O_{1.92}$, with Am on the surface and the O defect next to the surface Am, $AmO_{1.92}$ and $PuO_{1.92}$ {111}, {110} and {100} surfaces.

Oxides	Adsorption site	{111}	{110}	{100}
$Pu_{0.92}Am_{0.08}O_{1.92}$	Am	**-0.75**/*-2.11*	**-0.88**/*-1.88*	**-1.29**/*-2.22*
	Pu	**-0.80**/*-2.11*	**-0.99**/*-1.43*	*-1.42*
	defect	**-0.29**/*-2.11*	*-1.43*	*-2.34*
$AmO_{1.92}$	Am	**-0.62**/*-1.90*	**-0.66**/*-1.69*	**-1.16**/*-1.75*
$PuO_{1.92}$	Pu	**-0.70**/*-2.10*	**-0.44**/*-1.95*	*-2.59*

Dissociative adsorptions in which O_w heal surface O vacancies result in final geometries similar to the dissociative adsorption of H_2 on the corresponding stoichiometric surfaces (*i.e.* similar to the structures shown for {111} (Figure 5.10 (a), {110} (Figure 5.9 (h) and Figure 5.10 (b)) and {100} (Figure 5.9 (i) and Figure 5.10 (c)) surfaces). In principle, the two adsorbed H may (re)combine to form H_2 and desorb from the surface, a process shown experimentally to occur on substoichiometric UO_2 {111} surfaces following dissociative water adsorption.[40-41] Dissociative adsorption in which O_w heals a surface O vacancy on the $Pu_{0.92}Am_{0.08}O_{1.92}$ {111} surface is almost isoenergetic with that on $PuO_{1.92}$ {111} (-2.11 and -2.10 eV, respectively), while the equivalent process on $Pu_{0.92}Am_{0.08}O_{1.92}$ {110} and {100} surfaces is less stable than on $PuO_{1.92}$ (-1.88/-1.43 and -2.34 vs -1.95 and -2.59 eV, respectively). As the more stable the dissociative adsorption state, the harder H_2 production should be, we predict here that H_2 formation on $Pu_{0.92}Am_{0.08}O_{1.92}$ surfaces is in general easier than on the $PuO_{1.92}$ equivalents.

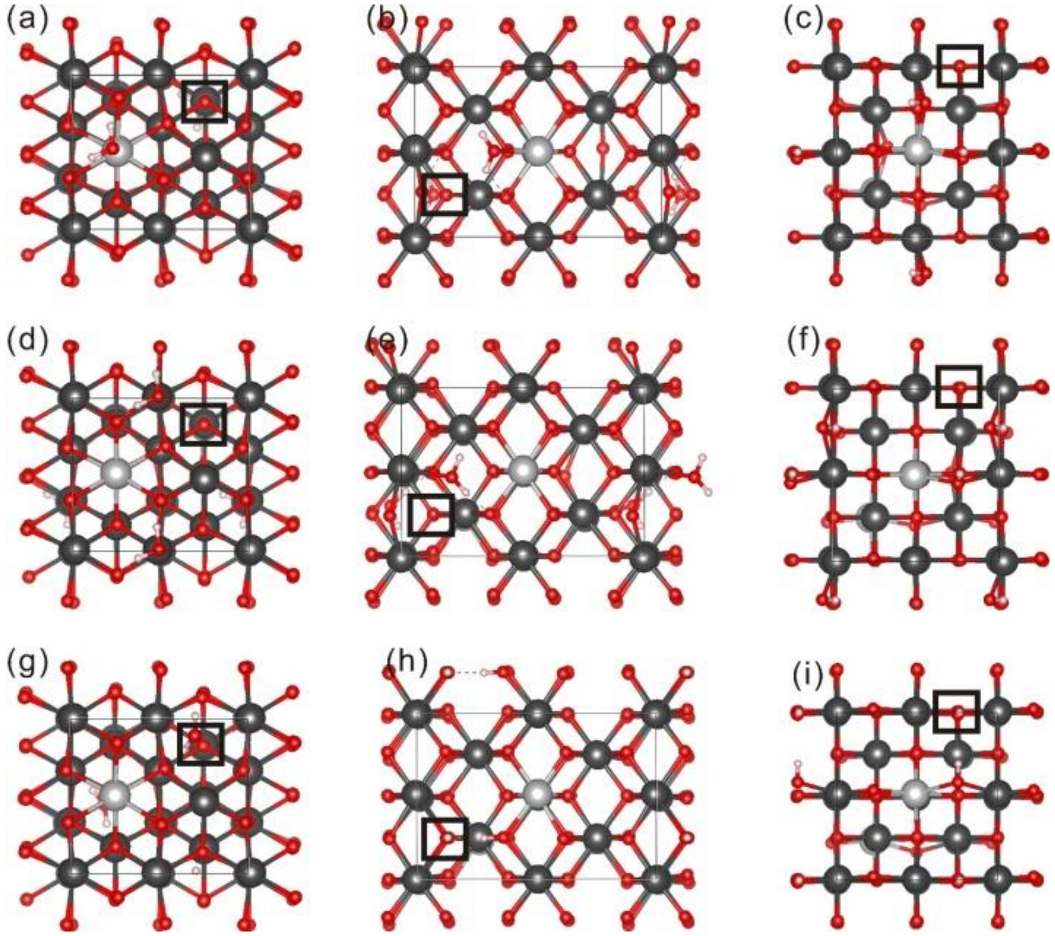

Figure 5.11: Top view of molecular water adsorption on $Pu_{0.92}Am_{0.08}O_{1.92}$ {111}, {110} and {100} surfaces, with the O defect away from surface Am, with water approaching surface Am ((a), (b) and (c), respectively), surface Pu ((d), (e) and (f), respectively), and surface defect ((g), (h) and (i), respectively). Dark grey, light grey, red and white spheres represent plutonium, americium, oxygen and hydrogen atoms, respectively.

Molecular adsorption structures on $Pu_{0.92}Am_{0.08}O_{1.92}$ surfaces, with Am on the surface and the O defect away from Am_s, are presented in Figure 5.11. When approaching Am_s, stable molecular adsorption states are found on the {111} and {110} surfaces (Figure 5.11 (a) and (b), respectively), while a dissociative state is found on {100} (Figure 5.11 (c)). As with water approaching Am_s, adsorption on Pu_s at the {100} surface leads to spontaneous dissociation (Figure 5.11 (f)). A stable molecular adsorption state is found only on the {111} surface when approaching a surface defect (Figure 5.11 (g)); the water molecule dissociates when approaching the surface defect of {110} and {100} (Figure 5.11 (h) and (i), respectively). Adsorption structures on Am_s and Pu_s are similar, and similar to adsorption structures on Am_s and Pu_s of $Pu_{0.92}Am_{0.08}O_2$ surfaces (Figure 5.6 (a)-(f)). The adsorption structures on surface defects reported here are almost the same as on surface defects of $Pu_{0.92}Am_{0.08}O_{1.92}$, with Am on the surface and the O defect next to Am_s (Figure 5.9 (g), (h) and (i)), and we conclude that the position of Am on the surface does not significantly influence the water adsorption structures on the surface defects of $Pu_{0.92}Am_{0.08}O_{1.92}$.

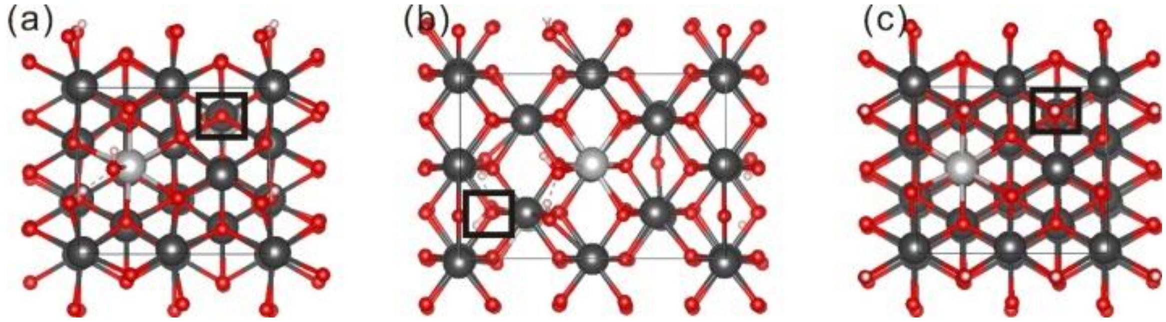

Figure 5.12: Top view of dissociative water adsorption on $Pu_{0.92}Am_{0.08}O_{1.92}$ surfaces, with Am on the surface and the O defect away from Am_s, (a) on {111} surface with water approaching surface Am, Pu or O defect, (b) on {110} and (c) {100} surfaces approaching surfaces Am. Dark grey, light grey, red and white spheres represent plutonium, americium, oxygen and hydrogen atoms, respectively.

Dissociative adsorption structures on $Pu_{0.92}Am_{0.08}O_{1.92}$ surfaces, with Am on the surface and the O defect away from Am_s, are presented in Figure 5.12. Dissociative adsorption on Am_s at the $Pu_{0.92}Am_{0.08}O_{1.92}$ {111} surface (Figure 5.12 (a)) is similar to that on Am_s at the corresponding stoichiometric {111} surfaces (Figure 5.7 (a)). Dissociative adsorption on Am_s at $Pu_{0.92}Am_{0.08}O_{1.92}$ {110} (Figure 5.12 (a)) has the water molecule incompletely dissociated, as a clear hydrogen bond can be found between O_wH_w and O_sH_w (Figure 5.12 (b)). Dissociative adsorption on Pu_s and the defect at {111} and {110} surfaces are the same, with O_w healing the surface defect (Figure 5.12 (c) and Figure 5.11 (h), respectively). The spin densities of An_s have also been calculated for all stable water adsorption structures on

$Pu_{0.92}Am_{0.08}O_{1.92}$ surfaces, with Am on the surface and the O defect away from Am_s (Figure 5.11 and 5.12). Again, the spin densities of Am_s and Pu_s remain the same before and after water adsorption.

Table 5.7: Molecular (Calibri) and dissociative (italic) water adsorption energies (eV) on $Pu_{0.92}Am_{0.08}O_{1.92}$, with Am on the surface and the O defect away from surface Am, and with Am in deep layers.

Substitution method	Adsorption site	{111}	{110}	{100}
A (1st and 6th layers)	Am	-0.53/*-0.45*	-0.69/-0.60	*-0.82*
	Pu	-0.70/*-2.04*	-0.85/-1.35	*-2.40*
	defect	-0.28/*-2.04*	*-1.35*	*-2.08*
Substitution method	Adsorption site	{111}	{110}	{100}
B (2nd and 5th layers)	Pu	-0.52/*-1.45*	-	-
	defect	-0.24/*-1.45*	-	-
C (3rd and 4th layers)	Pu	-0.60/*-1.55*	-	-
	defect	-0.23/*-1.55*	-	-

Molecular and dissociative adsorption energies on $Pu_{0.92}Am_{0.08}O_{1.92}$ surfaces, with Am on the surface and the O defect away from Am_s, are listed in Table 5.7. The energy sequence across the three kinds of surface is as usual, {111} < {110} < {100}, for all three approach routes. On each surface, the stability order is Pu_s > surface defect > Am_s, i.e. water molecules again prefer to approach Pu_s than Am_s, most likely due to the stability of Am (III) and the hygroscopic nature of PuO_2.[42] Water adsorption on Am_s next to the surface defect (Table 5.6) is more stable than on Am_s away from surface defect (Table 5.7). In both cases the Am_s have the same charge state (trivalent) and are surrounded by Pu; the only difference is whether Am_s is next to the surface defect or not, thus, proximity to the defect favours water adsorption on Am_s. Water adsorption energies on Pu_s of $Pu_{0.92}Am_{0.08}O_{1.92}$ surfaces with Am_s next to the defect and away from the defect are similar, as the charge states of Pu_s (trivalent) and surrounding environment are similar for the two kinds of Pu_s. The same reasoning also accounts for similar adsorption energy at the two kinds of surface defect.

Molecular and dissociative adsorption structures on $Pu_{0.92}Am_{0.08}O_{1.92}$ {111} surfaces, with Am in subsurface layers, are presented in Figure 5.13. The adsorption structures are almost the same as water adsorption on $PuO_{1.92}$ surfaces, and thus, deeper substituted Am has negligible influence on water adsorption structures. In agreement with what we found on $Pu_{0.92}Am_{0.08}O_{1.92}$ surfaces, with surface Am, the spin density of substituted Am and Pu_s cations are the same before and after water adsorption. Corresponding adsorption energies are given in Table 5.7. The position of the substituted Am has little influence on the molecular adsorption energies on Pu_s or the surface defect, while dissociative adsorption is more favourable on $Pu_{0.92}Am_{0.08}O_{1.92}$ surfaces with Am on the surface than MOX surfaces with Am in deeper layers. Dissociative water adsorption on $Pu_{0.92}Am_{0.08}O_{1.92}$ {111} surface resembles that on the $Pu_{0.92}Am_{0.08}O_2$ {111} surface with two adsorbed H atoms. As mentioned previously, the $Pu_{0.92}Am_{0.08}O_2$ {111} surface with Am on the surface is slightly more stable than surfaces with Am in subsurface layers. Therefore, we find more stable dissociative water adsorption on the $Pu_{0.92}Am_{0.08}O_{1.92}$ {111} surface with Am in the 1st and 6th layer than Am in deeper layers.

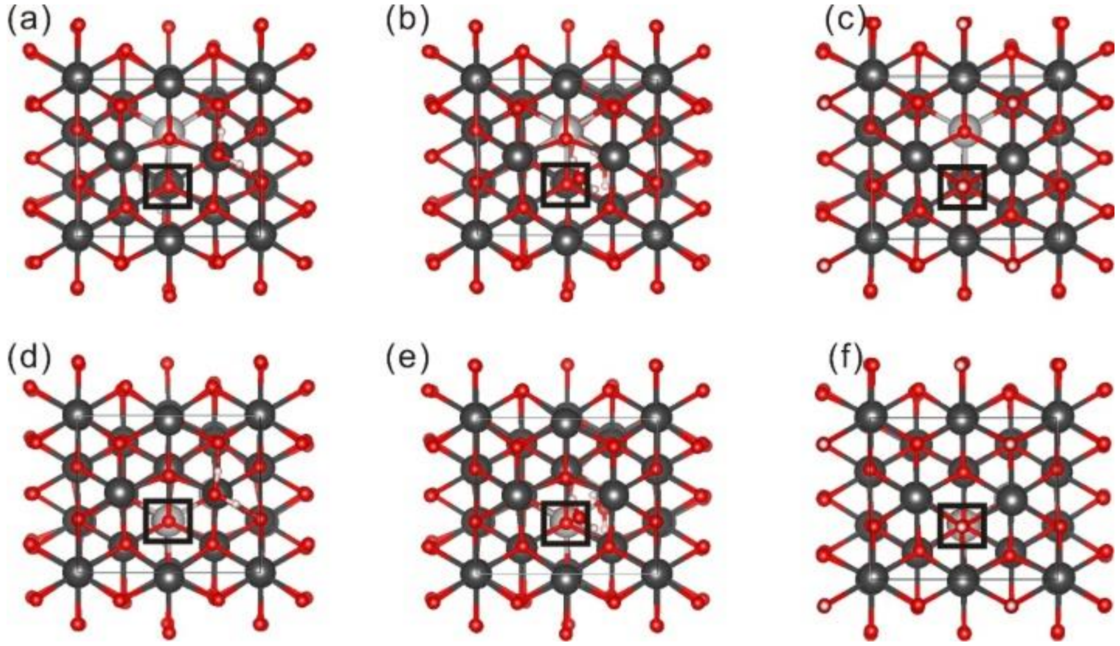

Figure 5.13: Molecular water adsorption on (a) surface Pu and (b) defect, and (c) dissociative adsorption on $Pu_{0.92}Am_{0.08}O_{1.92}$ {111} surface, with Am in 2nd and 5th layers; molecular water adsorption on (d) surface Pu and (e) defect and (f) dissociative adsorption on $Pu_{0.92}Am_{0.08}O_{1.92}$ {111} surface, with Am in 3rd and 4th layers; Dark grey, light grey, red and white spheres represent plutonium, americium, oxygen and hydrogen atoms, respectively.

5.3.5 Water desorption from $Pu_{1-y}AmO_{2-x}$ surfaces

In this section, we consider water desorption from slabs with Am substituted on the surfaces, and in particular focus on calculating the desorption temperatures. Although more than one adsorption configuration has been found on every surface in this work, only the most stable configurations were considered in the desorption temperature simulations. These are the most stable molecular and dissociative water adsorption on stoichiometric {111} (Figure 5.6 (a) and Figure 5.7 (a)), and {110} (Figure 5.6 (b) and Figure 5.7 (b)) surfaces, and substoichiometric {111} (Figure 5.9 (d) and Figure 5.10 (a)), {110} (Figure 5.9 (e) and Figure 5.10 (b)) and {100} (Figure 5.9 (c) and (i)) surfaces, and dissociative water adsorption on the stoichiometric {100} surface (Figure 5.6 (c)). The relationship between water partial pressure and desorption temperature on pure PuO_2 surfaces has also been simulated using the adsorption energies on pure PuO_2 surfaces from our previous work.[9] Comparison of these desorption temperatures on stoichiometric $Pu_{1-y}AmO_{2-x}$, and PuO_2 surfaces can be seen in Figure 5.14, and that on substoichiometric surfaces can be seen in Figure A5.3.

On stoichiometric surfaces (Figure 5.14), the desorption temperatures of molecularly adsorbed water on Pu-Am MOX surfaces are higher than on the corresponding PuO_2 surfaces at the same water partial pressure, *i.e.* desorption of molecularly adsorbed water on MOX surfaces is harder than on the corresponding PuO_2 surfaces, as is the case on substoichiometric surfaces (Figure A5.3). In contrast, the desorption temperatures of dissociatively adsorbed water on MOX surfaces are lower than on the corresponding PuO_2 surfaces, excepting the {111} surface, as it is for the substoichiometric surfaces (Figure A5.3). As we found in our previous work, PuO_2 {110} and {100} surfaces have a special attraction for dissociative water adsorption,[10] due to their very hydroscopic nature.[42] In the present study, we have found that the dissociative adsorption energy on MOX and PuO_2 {111} surfaces are very close, so MOX and PuO_2 {111} surfaces have very similar water desorption behaviour (Figure 5.14 (a)). However, the water desorption temperatures on stoichiometric (Figure 5.14) and oxygen vacancy (Figure A5.3) surfaces increase from {111} to {110} and {100}, and the differences between MOX and PuO_2 surfaces become larger in that order.

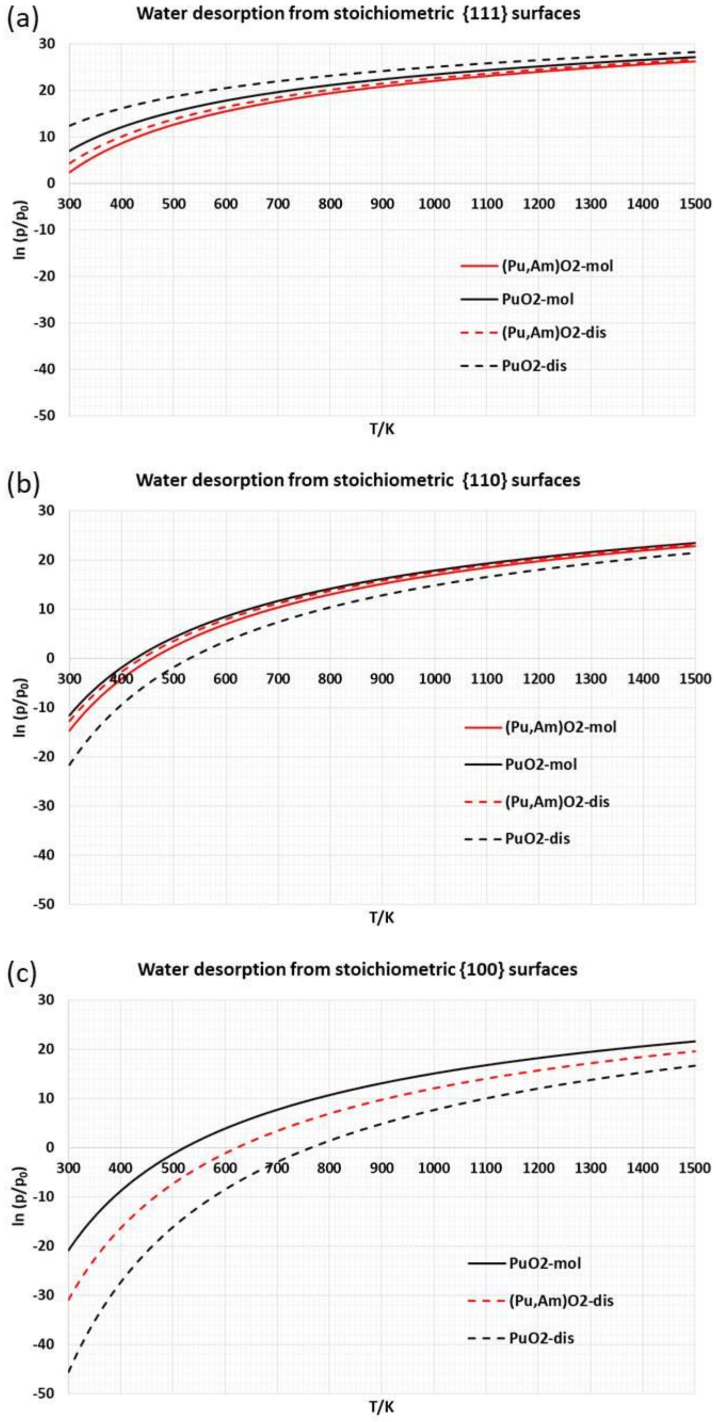

Figure 5.14: Relationship between partial pressure of water (p), and temperature (T) required for thermal desorption of water from stoichiometric (a) {111}, (b) {110} and (c) {100} $Pu_{1-y}AmO_{2-x}$ and PuO_2 surfaces, with molecular (mol) or dissociative (dis) adsorbed water. The equilibrium state between water adsorption and desorption is indicated by the solid (molecular adsorption) and dashed (dissociate adsorption) lines; water will desorb from the surfaces when p/p_0 is below the line, and adsorb when p/p_0 is above the line.

5.4 Conclusions

In this paper, we have studied the surface properties of Pu-Am MOX, focusing on the {111}, {110} and {100} surfaces. Substitution of Am has little influence on the surface structures of stoichiometric and substoichiometric PuO_2 - the displacement of An-O bond length on $Pu_{0.92}Am_{0.08}O_{1.92}$ compared to $Pu_{0.92}Am_{0.08}O_2$ surfaces is mainly caused by the O vacancy - although it does cause clear redistribution of electrons. On stoichiometric surfaces, substituted Am mainly gains electrons from atoms in the same layers and forms a c.a. +3.5 charge state, whereas on substoichiometric surfaces substituted Am is reduced to the trivalent state, both when next to an O vacancy or away from it. We find a valence relationship in good agreement with experiment; Am(IV) will be reduced to the trivalent state prior to any reduction of Pu(IV). The substitution energy of Am in stoichiometric PuO_2 surfaces is closely related to the surface activity. Comparison of oxygen defect generation on MOX and PuO_2, AmO_2 surfaces confirms the linear relationship between oxygen defect generation energies and An(IV)/(III) redox potential, and we conclude that both the redox potential of An(IV)/(III) and the surface activity are important factors in the O defect generation energy on Pu-Am MOX surfaces.

The presence of Am has little influence on water adsorption structures on $Pu_{0.92}Am_{0.08}O_2$ surfaces, although it does affect the adsorption energy. Water is more prone to adsorb on Am_s than Pu_s, as water adsorption on Am_s promotes the formation of the trivalent state on {110} and {100} surfaces. Molecular water adsorption on $Pu_{0.92}Am_{0.08}O_2$ surfaces is more stable than on the corresponding PuO_2 and AmO_2 surfaces, as is dissociative water adsorption on the {111} surface, while dissociative adsorption on PuO_2 {110} and {100} surfaces is much more stable than on corresponding MOX surface, in agreement with the known hydrophilicity of PuO_2. From $Pu_{0.92}Am_{0.08}O_2$ {111} to {100} surfaces, increasing stability is found for molecular and dissociative adsorptions, which is the same energy sequence as on AnO_2 surfaces. Molecular and dissociative adsorption structures and energies are similar on {111} surfaces with Am substituted in different layers.

Molecular and dissociative water adsorption structures on substoichiometric $Pu_{0.92}Am_{0.08}O_{1.92}$ surfaces are similar to those on the corresponding $AnO_{1.92}$ surfaces, and the spin density of An_s is largely unaffected by water adsorption. The energy sequence across the three kinds of surface is the same as $AnO_{1.92}$, {111} < {110} < {100}, for water approaching Am_s, Pu_s or the surface defect. Water adsorption on Pu_s is more stable than on Am_s at $Pu_{0.92}Am_{0.08}O_{1.92}$ surfaces, as Pu is more hydrophilic than Am. Water adsorption on Am_s next to the surface defect is more stable than on Am_s away from surface defect, so proximity to the defect favours water adsorption on Am_s. Similar adsorption energies are found on Pu_s regardless of its proximity to Am_s, as is the case for adsorption on the surface defect. Molecular and dissociative adsorption structures on $Pu_{0.92}Am_{0.08}O_{1.92}$ {111} surfaces with Am in subsurface layers are almost the same as water adsorption on $PuO_{1.92}$ surfaces, so subsurface Am has negligible influence on the water adsorption geometrics. The spin densities of subsurface Am and Pu_s cations in the $Pu_{0.92}Am_{0.08}O_{1.92}$ {111} slab are the same before and after water adsorption.

Desorption temperature simulations indicate that Am in both stoichiometric and substoichiometric PuO_2 hinders desorption of molecularly adsorbed water, while promoting desorption of dissociatively adsorbed water.

The presence of Am promotes O vacancy formation on PuO_2 surfaces. Both surface Am and O vacancies promote molecular water adsorption on these surfaces, but reduce the favourability of dissociative adsorption *vs* PuO_2. The "activity volcanoes" of metal oxide surfaces[32-33] indicate that moderate adsorption favours surface catalysed reactions, and hence the strengthened molecular adsorption and weakened dissociative adsorption on MOX surfaces may promote further chemical reaction, such as H_2 generation, in the storage canisters.

References

1. Tereshina, E. A.; Danis, S.; Springell, R.; Bao, Z.; Havela, L.; Caciuffo, R., Crystal structure and magnetic properties of UO_2/permalloy thin films. *Thin Solid Films* **2015**, *591*, 271-275.

2. Paffett, M.; Kelly, D.; Joyce, S.; Morris, J.; Veirs, K., A critical examination of the thermodynamics of water adsorption on actinide oxide surfaces. *J. Nucl. Mater.* **2003**, *322*, 45-56.

3. Stakebake, J., Thermal desorption study of the surface interactions between water and plutonium dioxide. *J. Phys. Chem.* **1973**, *77*, 581-586.

4. Tegner, B. E.; Kaltsoyannis, N., Multiple water layers on AnO(2) {111}, {110}, and {100} surfaces (An = U, Pu): A computational study. *J. Vac. Sci. Technol. A* **2018**, *36*.

5. Tegner, B. E.; Molinari, M.; Kerridge, A.; Parker, S. C.; Kaltsoyannis, N., Water adsorption on AnO_2 {111}, {110}, and {100} surfaces (An = U and Pu): A density functional theory plus U study. *J. Phys. Chem. C* **2017**, *121*, 1675-1682.

6. Zhang, C.; Yang, Y.; Zhang, P., Thermodynamics study of dehydriding reaction on the PuO_2 (110) surface from first principles. *J. Phys. Chem. C* **2018**, *122*, 7790-7794.

7. Otobe, H.; Akabori, M.; Arai, Y., Oxygen potential measurements of $Am_{0.5}Pu_{0.5}O_{2-x}$ by EMF method. *J. Nucl. Mater.* **2009**, *389*, 68-71.

8. Vauchy, R.; Joly, A.; Valot, C., Lattice thermal expansion of $Pu_{1-y}Am_yO_{2-x}$ plutonium–americium mixed oxides. *J. Appl. Crystallogr.* **2017**, *50*, 1782-1790.

9. Wellington, J. P. W.; Tegner, B. E.; Collard, J.; Kerridge, A.; Kaltsoyannis, N., Oxygen Vacancy Formation and Water Adsorption on Reduced AnO(2){111}, {110}, and {100} Surfaces (An = U, Pu): A Computational Study. *J. Phys. Chem. C* **2018**, *122*, 7149-7165.

10. Chen, J.-L.; Kaltsoyannis, N., Computational study of the bulk and surface properties of the minor actinide dioxides $MAnO_2$ (MAn= Np, Am, Cm); Water adsorption on stoichiometric and reduced {111}, {110} and {100} Surfaces. *J. Phys. Chem. C* **2019**.

11. Ellinger, F. H.; Johnson, K. A.; Struebing, V. O., The plutonium-americium system. *J. Nucl. Mater.* **1966**, *20*, 83-86.

12. Osaka, M.; Kurosaki, K.; Yamanaka, S., Oxygen potential of $(Pu_{0.91}Am_{0.09})O_{2-x}$. *J. Nucl. Mater.* **2006**, *357*, 69-76.

13. Miwa, S.; Osaka, M.; Yoshimochi, H.; Tanaka, K.; Kurosaki, K.; Uno, M.; Yamanaka, S., Phase behavior of PuO2-x with addition of 9% Am. *J. Alloys Compd.* **2007**, *444*, 610-613.

14. Jankowiak, A.; Jorion, F.; Maillard, C.; Donnet, L., Preparation and characterization of $Pu_{0.5}Am_{0.5}O_{2-x}$-MgO ceramic/ceramic composites. *Nucl. Sci. Eng.* **2008**, *160*, 378-384.

15. Jankowiak, A.; Maillard, C.; Donnet, L., Structural study of $Pu_{1-x}Am_xO_2$ (x=0.2; 0.5; 0.8) obtained by oxalate co-conversion. *J. Nucl. Mater.* **2009**, *393*, 87-91.

16. Gotcu-Freis, P.; Colle, J. Y.; Gueneau, C.; Dupin, N.; Sundman, B.; Konings, R. J. M., A thermodynamic study of the Pu-Am-O system. *J. Nucl. Mater.* **2011**, *414*, 408-421.

17. Belin, R. C.; Martin, P. M.; Lechelle, J.; Reynaud, M.; Scheinost, A. C., Role of cation interactions in the reduction process in plutonium-americium mixed oxides. *Inorg. Chem.* **2013**, *52*, 2966-2972.

18. Prieur, D.; Carvajal-Nunez, U.; Vitova, T.; Somers, J., Local and electronic structure of americium-bearing PuO_2. *Eur. J. Inorg. Chem.* **2013**, 1518-1524.

19. Suzuki, M. T.; Magnani, N.; Oppeneer, P. M., Microscopic theory of the insulating electronic ground states of the actinide dioxides AnO_2 (An = U, Np, Pu, Am, and Cm). *Phys. Rev. B* **2013**, *88*, 195146.

20. Pegg, J. T.; Aparicio-Anglès, X.; Storr, M.; de Leeuw, N. H., DFT+U study of the structures and properties of the actinide dioxides. *J. Nucl. Mater.* **2017**, *492*, 269-278.

21. Rak, Z.; Ewing, R. C.; Becker, U., Hydroxylation-induced surface stability of AnO(2) (An = U, Np, Pu) from first-principles. *Surf. Sci* **2013**, *608*, 180-187.

22. Collard, J. C.; Steele, H.; Kaltsoyannis, N., Computational study of HCl adsorption on stoichiometric and oxygen vacancy PuO_2 {111}, {110} and {100} surfaces. *J. Nuc. Mater.* **2019**, https://doi.org/10.1016/j.jnucmat.2019.151951.

23. Chen, H. T.; Choi, Y. M.; Liu, M.; Lin, M., A theoretical study of surface reduction mechanisms of CeO_2 (111) and (110) by H_2. *Chem. Phys. Chem.* **2007**, *8*, 849-855.

24. Fronzi, M.; Piccinin, S.; Delley, B.; Traversa, E.; Stampfl, C., Water adsorption on the stoichiometric and reduced CeO_2 (111) surface: a first-principles investigation. *Phys. Chem. Chem. Phys.* **2009**, *11*, 9188-9199.

25. Yang, Z.; Wang, Q.; Wei, S.; Ma, D.; Sun, Q., The effect of environment on the reaction of water on the ceria (111) surface: a DFT+ U study. *J. Phys. Chem. C* **2010**, *114*, 14891-14899.

26. Fernandez-Torre, D.; Kosmider, K.; Carrasco, J.; Ganduglia-Pirovano, M. V.; Perez, R., Insight into the adsorption of water on the clean CeO_2 (111) surface with van der Waals and hybrid density functionals. *J. Phys. Chem. C* **2012**, *116*, 13584-13593.

27. Chen, B.; Ma, Y.; Ding, L.; Xu, L.; Wu, Z.; Yuan, Q.; Huang, W., Reactivity of hydroxyls and water on a CeO_2 (111) thin film surface: the role of oxygen vacancy. *J. Phys. Chem. C* **2013**, *117*, 5800-5810.

28. Ma, L.; Atta-Fynn, R.; Ray, A. K., Elemental and mied actinide dioxides: An ab initio study. *J. Theor. Comput. Chem.* **2012**, *11*, 611-629.

29. Kresse, G.; Hafner, J., Ab initio molecular-dynamics for liquid-metals. *Phys. Rev. B* **1993**, *47*, 558-561.

30. Kresse, G.; Hafner, J., Ab initio molecular-dynamics simulation of the liquid-metal–amorphous-semiconductor transition in germanium. *Phys. Rev. B* **1994**, *49*, 14251-14269.

31. Kresse, G.; Furthmuller, J., Efficiency of ab-initio total energy calculations for metals and semiconductors using a plane-wave basis set. *Comput. Mater. Sci.* **1996**, *6*, 15-50.

32. Kresse, G.; Furthmuller, J., Efficient iterative schemes for ab initio total-energy calculations using a plane-wave basis set. *Phys. Rev. B* **1996**, *54*, 11169-11186.

33. Perdew, J. P.; Burke, K.; Ernzerhof, M., Generalized gradient approximation made simple (vol 77, pg 3865, 1996). *Phys. Rev. Lett.* **1997**, *78*, 1396-1396.

34. Liechtenstein, A. I.; Anisimov, V. I.; Zaanen, J., Density-functional theory and strong interactions: Orbital ordering in Mott-Hubbard insulators. *Phys. Rev. B* **1995**, *52*, R5467-R5470.

35. Blochl, P. E., Projector augmented-wave method. *Phys. Rev. B* **1994**, *50*, 17953-17979.

36. Monkhorst, H. J.; Pack, J. D., Special points for brillouin-zone integrations. *Phys. Rev. B* **1976**, *13*, 5188-5192.

37. Momma, K.; Izumi, F., VESTA 3 for three-dimensional visualization of crystal, volumetric and morphology data. *J. Appl. Crystallogr.* **2011**, *44*, 1272-1276.

38. Molinari, M.; Parker, S. C.; Sayle, D. C.; Islam, M. S., Water adsorption and its effect on the stability of low index stoichiometric and reduced surfaces of Ceria. *J. Phys. Chem. C* **2012**, *116*, 7073-7082.

39. Chase, M. W., NIST-JANAF Thermochemical Tables, 4th ed. *American Institute of Physics* **1988**, *https://janaf.nist.gov/tables/H-064.html (last accessed October 01, 2019)*.

40. Stultz, J.; Paffett, M.; Joyce, S., Thermal evolution of hydrogen following water adsorption on defective UO_2 (100). *J. Phys. Chem. B* **2004**, *108*, 2362-2364.

41. Bo, T.; Lan, J.-H.; Wang, C.-Z.; Zhao, Y.-L.; He, C.-H.; Zhang, Y.-J.; Chai, Z.-F.; Shi, W.-Q., First-principles study of water reaction and H_2 formation on UO_2 (111) and (110) single crystal surfaces. *J. Phys. Chem. C* **2014**, *118*, 21935-21944.

42. Stakebake, J., The storage behavior of plutonium metal, alloys, and oxide: A review. *J. Nucl. Mater.* **1971**, *38*, 241-259.

Embedded Cluster and Periodic Boundary Condition Study of the Co-Adsorption of HCl and H_2O on PuO_2 Surfaces

Jonathan Collard, Jia-Li Chen, Helen Steele and Nikolas Kaltsoyannis

Abstract

The simultaneous adsorption of HCl and H_2O on the {111} and {110} surfaces of PuO_2 has been studied, using both hybrid density functional theory within the periodic electrostatic embedded cluster method and the GGA+*U* approach using periodic boundary conditions. Excellent agreement is found between the two computational methods. A synergistic effect between co-adsorbed molecules is identified, such that HCl binding energies are enhanced by the presence of water. Higher levels of water also increase the HCl binding energy, forming very stable configurations on both surfaces for first-layer HCl interactions. Second-layer interactions are also explored, in which the HCl molecule is placed above a full monolayer of water on the surfaces. In such circumstances, the HCl reacts with a hydroxyl from the water monolayer to produce molecular water, with the chloride held to the surface via numerous chlorine-acceptor hydrogen bonds.

6.1 Introduction

Over the last several decades, the UK has accumulated the largest stockpile of civil plutonium in the world. For the most part it is currently stored in its fluorite-structured dioxide form within nested stainless-steel canisters, as an intermediate storage system until the government decides on a viable long-term solution. Approximately 5% of these canisters are fitted with a PVC bagging layer around the inner canister which, due to the heat and radioactivity of the contained material, is suspected to have been degrading. Chloride contamination of PuO_2, largely as a result of this degradation, is a significant and relatively poorly understood obstacle to the development of long-term plutonium usage/containment strategies. In order to be viable for repurposing in MOX fuel, the PuO_2 will have to be decontaminated, and for permanent disposal in a geological facility the fundamental chemistry will need to be understood, particularly with regards to corrosion processes.[1]

As the primary product of thermal and radiolytic PVC decay is known to be hydrogen chloride,[2-8] our previous computational work in this area has been focused on the interactions between single HCl molecules and both the pristine (*i.e.* stoichiometric) and reduced surfaces of PuO_2. However, the Magnox canisters containing chloride-contaminated material are not hermetically sealed, and as such are exposed to airborne water vapour in addition to any water remaining from the manufacturing and packaging process. It is therefore important to consider not only the interactions between HCl and PuO_2, but also the co-adsorption of HCl and H_2O.

Although extensive work has been carried out on the interactions between water and the actinide oxides,[9-23] computational literature regarding chloride species is very limited. Our previous study[24] focused on single HCl molecule interactions with both the stoichiometric and substoichiometric {111} {110} and {100} surfaces of PuO_2, finding that interactions with the {110} surface generally yielded far larger adsorption energies than the others. Another notable result was that configurations in which the chlorine atom filled the gap in an oxygen vacancy surface were very stable when compared to pristine surface adsorptions. For the most part it was found that HCl spontaneously dissociates on interaction with the PuO_2 surface, forming structures resembling those of reaction (1) in the work of Parfitt *et. al.* on HCl interactions with rutile surfaces.[25] From these data and molecular thermodynamics calculations we concluded that, owing to the large adsorption energies involved, the heat treatment temperatures required for total desorption of HCl from PuO_2 surfaces would be very high, posing potential difficulties when considering heat treatment as a decontamination option.

We have previously studied interactions between gaseous HCl and CeO_2 experimentally[26] (CeO_2 being a commonly used non-radioactive surrogate for PuO_2[27-29] and, more recently, interactions between HCl and PuO_2.[30-31] We found that chloride species bind tightly to synthetic PuO_2, making it difficult to remove thermally. This was in agreement with our previous computational model,[24] which indicated that chlorine atoms would bind very strongly to defect sites, with correspondingly high desorption temperatures. Our model assumed that once the temperature required to desorb a specific adsorption configuration had been reached, all energetically equivalent geometries would spontaneously desorb. This fit with the experimental findings that the amount of time the chloride-contaminated PuO_2 was held at high temperature had little or no effect on the amount of desorption that occurred.[30] More recently, we performed experiments on chloride-contaminated PuO_2 material retrieved from storage at Sellafield Ltd..[31-32] These results indicated that in addition to adsorbed chloride that could be removed *via* thermal treatment, there appears to exist a more strongly-bound layer which requires temperatures in excess of 950°C to remove. The conclusion drawn from this is that such a layer would not likely be physisorbed to the surface, but rather chemisorbed – a hypothesis that is consistent with our computational findings regarding defect-healing HCl adsorption. Furthermore, our experimental work found that faster gas flow leads to a more rapid desorption of HCl. Since a faster gas flow over the surface during desorption would naturally mean a lower partial pressure of HCl, this could also be explained by the results from our computational work,[24] which concluded that a given adsorption geometry would desorb at a lower temperature if held at a lower HCl partial pressure. Another experimental result was that "drier" samples desorb chloride more readily and that samples with higher water content retain chloride species more readily, implying that there is a synergistic co-adsorption between adsorbed HCl and H_2O.

In this contribution we expand our computational model of the interactions between HCl and PuO_2 by adding explicitly-treated water molecules to the {111} and {110} surfaces in the presence of HCl. The surfaces were chosen as the {111} is the most stable, and the {110} has the most interesting and varied surface morphology. We use both embedded cluster and periodic boundary condition (PBC) density functional theory (DFT). We first study the energetics and geometries of the simultaneous adsorption of single HCl and H_2O molecules. We then explore the case where HCl substitutionally replaces 25% of the water molecules in a full surface monolayer. Finally, we consider the case in which the HCl molecule lies above a full monolayer of water, in order to explore second-layer adsorptions and to gauge whether HCl may still interact with the surface in the absence of direct Pu-Cl contact.

6.2 Computational Details

Using the same methodology and computational parameters in per our previous work, hybrid DFT (PBE0) has been employed in conjunction with the Periodic Electrostatic Embedded Cluster Method (PEECM) to conduct the embedded cluster calculations; the full details of these are described in reference 24.[24] The software used to carry out these calculations was TURBOMOLE 7.3.[33]

Periodic boundary condition (PBC) DFT simulations were performed using the same methodology as we have used in our previous, closely-related work,[11, 17, 22] employing the Vienna Ab-initio Simulation Package (VASP), version 5.4.1.[34-37] The generalized gradient approximation (GGA) functional of Perdew, Burke, and Ernzerhof (PBE) was used,[38] with a Hubbard U correction for the 5f electrons (U_{eff} = 4 eV; U = 4.5 eV, J = 0.5 eV).[39] Plane wave basis sets and projector augmented wave pseudopotentials were used to describe the ions.[40] A plane wave cutoff of 650 eV was adopted for all calculations. Monkhorst-Pack (MP) grids were employed for the k-space integration;[41] a minimum MP grid of 5 × 5 × 1 k points for the Brillouin zone sampling was used for the surface simulations. A 1k colinear magnetic ordering with a net magnetic moment of zero was used and spin−orbit coupling was neglected.[42] PuO_2 {111} and {110} surfaces are constructed from repeating slabs of 24 PuO_2 units arranged in six layers. Each surface is 2 × 2 with 18 Å of vacuum between each slab (Figure A6.1). The net dipole of both the {111} and {110} surfaces is zero, and adsorption is considered on both sides of each surface to avoid adsorbate-induced dipole effects. The f electrons of Pu in the first, third, and fifth layers are unpaired and spin up, while those in the second, fourth, and sixth layers are spin down, in order to keep the whole slab antiferromagnetic – see Figure A6.1 (Appendix 4).

All ball and stick images were generated using VESTA 3, and charge analysis was performed using Multiwfn.[43-44]

When calculating HCl binding energies, the following expressions were used:

$$E_{bind} = E_{PuO_2+H_2O+HCl} - \left(E_{PuO_2+H_2O} + E_{HCl}\right) \qquad (6.1)$$

$$E_{bind} = \frac{1}{2}\left[E_{PuO_2+H_2O+HCl} - \left(E_{PuO_2+H_2O} + 2 * E_{HCl}\right)\right] \qquad (6.2)$$

where $E_{\mathrm{PuO_2+H_2O+HCl}}$ is the total energy of the adsorbed system, $E_{\mathrm{PuO_2+H_2O}}$ is the total energy of the hydrated system in the absence of HCl, and E_{HCl} is the total energy of a free HCl molecule in the gas phase. Equation (1) is used for the PEECM calculations and equation (2) for the PBC, as adsorption is considered on both sides of the surfaces for PBC. This yields the adsorption energy of the HCl molecule binding to the hydrated surface E_{bind}, which can then be compared with our previous adsorption energies in order to deduce the impact of the presence of water on such interactions.

Quantum theory of atoms in molecules (QTAIM) analysis was performed using the AIMAll software package.[45]

6.3 Results and Discussion

6.3.1 Gas Phase HCl + H_2O

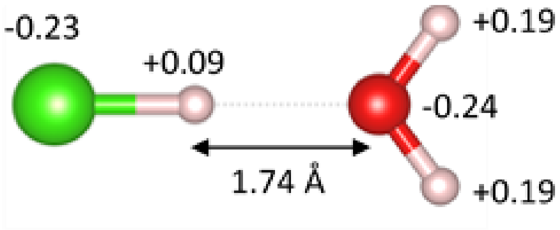

Figure 6.1: Interaction of HCl and H_2O in the gas phase forming a chlorine-donor hydrogen bond. Hirshfeld charges for each atom are shown. Red, green and white spheres represent the O, Cl and H atoms, respectively.

In order to obtain insight into how HCl and H_2O might interact on the surface of PuO_2, the molecules were first placed together, in multiple initial configurations, in the absence of PuO_2. The results from this were that, no matter what the starting configuration, one or both of the molecules rotates to form a chlorine-donor hydrogen bonding geometry, as seen in Figure 6.1, with an interaction energy of -0.35 eV. Analysis of the Hirshfeld charges on each atom reveals a similar charge on the oxygen and chlorine. As oxygen is smaller and harder than chlorine, the chlorine donor orientation is unsurprising.

Considering that HCl is known to dissociate in water, we also investigated the interactions between a chloride ion and water molecules, hydronium (H_3O^+) ions, and clusters containing combinations of the two. Since we will later on discuss HCl adsorbing onto a 1 monolayer (ML) hydrated surface (where 1 ML is defined as consisting of 4 adsorbed H_2O molecules), the aqueous clusters we will consider here are $(H_2O)_4$ (denoted herein as H_8O_4) and H_3O^+-$(H_2O)_3$ (denoted herein as $H_9O_4^+$). Initial structures for the aqueous clusters are adopted from the literature.[46-47] In each case, the chloride ion was initially placed 3 Å away from the optimized aqueous cluster, before being subjected to geometry optimisation. The resulting structures are presented in Figure 6.2.

For Cl^--H_2O (Figure 6.2 (a)), the chloride ion forms an oxygen-donor hydrogen bond with the hydrogen of H_2O with a bond length of 2.05 Å. In this case, Hirshfeld charges show that partial charge transfer occurs from Cl^- to H_2O. In the case where the chloride ion interacts with the H_8O_4 cluster (Figure 6.2 (b)), three hydrogen bonds are formed, with larger bond lengths (2.13, 2.17 and 2.22 Å) than observed for a single water molecule, and with more charge transfer from Cl^- to H_8O_4. For the interaction between the chloride ion and a single hydronium ion (not pictured) the chloride ion abstracts one of the hydrogen atoms, forming HCl in much the same configuration as seen in Figure 6.1. When in the presence of several water molecules in addition to a hydronium ion (as is the case in Figure 6.2(c)), chloride does not remove a hydrogen from the hydronium. Instead, the hydronium ion forms three identical hydrogen bonds of length 1.48 Å with the three water molecules. These water molecules also form three oxygen-donor hydrogen bonds of length 2.01 Å with the chloride ion, which are shorter than the equivalent hydrogen bonds in Cl^--H_8O_4 system. 0.61 charge transfers from Cl^- to $H_9O_4^+$. The bonding energies of Cl^--H_2O, Cl^--H_3O^+, Cl^--H_8O_4 and Cl^--$H_9O_4^+$ are -1.12, -8.30, -2.20 and -6.54 eV, respectively. The notably higher bonding energy of Cl^--H_3O^+ and Cl^--$H_9O_4^+$ is clearly due to the interaction of two formally charged species.

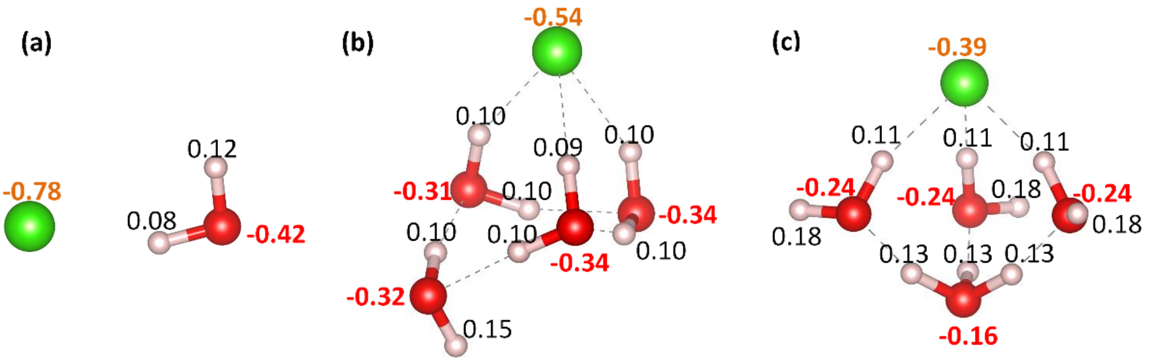

Figure 6.2: Interaction of Cl^- with (a) H_2O, (b) H_8O_4 and (c) $H_9O_4^+$ in the gas phase. Hirshfeld charges for Cl (green), each O (red) and H (black) are shown. Red, green and white spheres represent the O, Cl and H atoms, respectively

6.3.2 Singly Co-adsorbed HCl + H_2O

Following on from the gas phase results, PEECM and PBC co-adsorption calculations were set up by adding an intact HCl molecule (with H-Cl bond length 1.27 Å) to the most energetically stable geometry of a single water molecule on either the {111} or {110} surfaces. These geometries were taken from our previous PEECM[11] and PBC[12] work. The HCl was placed approximately 2.80 Å above a plutonium atom, and arranged such that a chlorine-donor hydrogen bonding configuration would be favoured.

Upon interaction with the singly hydrated {111} surface, both the PEECM and the PBC predict similar geometric structures. The HCl molecule dissociates, donating its hydrogen atom to the water molecule. The water molecule subsequently ejects a different hydrogen atom from the other side, hydroxylating the surface and forming a chlorine-acceptor hydrogen bond of length 1.98 Å and 2.09 Å for PEECM and PBC respectively, as shown in Figure 6.3. The HCl binding energy for this configuration is -1.10 eV (PEECM) and -0.87 eV (PBC).

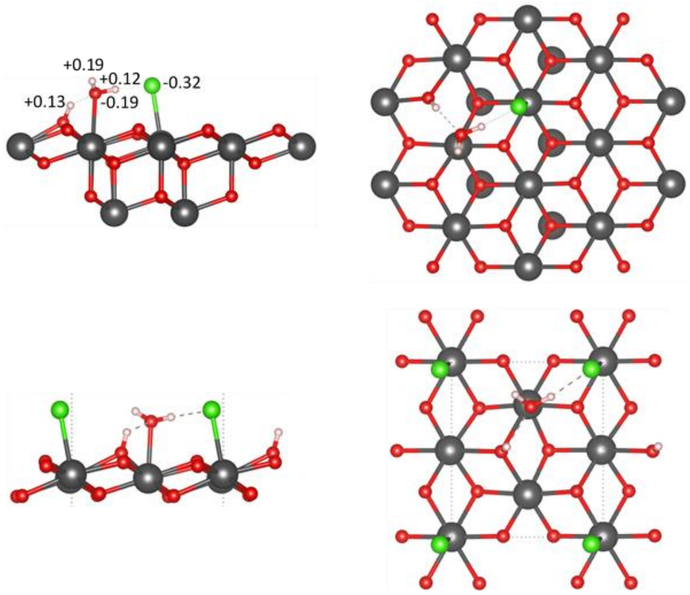

Figure 6.3: Side (left) and top-down (right) views of the co-adsorption of HCl and H_2O on the PuO_2 {111} surface, produced from an initial chlorine-donor hydrogen bonding configuration; PEECM (top) and PBC (bottom). Hirshfeld charges from the PEECM calculation are shown for each adsorbing atom. Grey, red, green and white spheres represent the Pu, O, Cl and H atoms, respectively.

Since our H_2O/HCl gas-phase calculations suggested that a chlorine-acceptor hydrogen bond was unlikely, QTAIM analysis of the chlorine-acceptor hydrogen bond critical point (BCP) was performed to deduce the nature of this bond. From this, ρ_{BCP} and $\nabla^2\rho|_{\mathrm{BCP}}$ values of 0.043 a.u. and +0.086 a.u. were calculated, similar to the hydroxyl-water hydrogen bond BCP values of 0.038 a.u. and +0.135 a.u. respectively, suggesting that this interaction is indeed closed-shell and indicative of hydrogen bonding.

Water preferentially binds to the {110} surface in a dissociative manner and, when HCl is added, the HCl donates its hydrogen atom to the adsorbed hydroxyl, forming molecular water. As seen for the {111} surface, this water molecule forms a chlorine-acceptor bond of length 2.15 Å (PEECM) and 2.17 Å (PBC), seen in Figure 6.4. With a HCl binding energy of -2.39 and -2.64 eV for the PEECM and PBC simulations respectively, this is a significantly stronger interaction than on the {111} surface, following the same trend as in our previous work regarding single HCl adsorption on PuO_2.[24] QTAIM analysis of the H⋯Cl BCP on the

{110} surface yields ρ_{BCP} and $\nabla^2\rho|_{\mathrm{BCP}}$ values of 0.030 a.u. and +0.070 a.u. Comparing these to the water-surface hydrogen bond, 0.027 a.u. and +0.092 a.u. respectively, we again conclude that these clearly closed-shell interactions are hydrogen bonds.

The explanation for this change in the type of hydrogen bonding when adsorbing onto the PuO_2 surface comes from the Hirshfeld partial atomic charges. In the gas phase these are very similar for oxygen and chlorine (Figure 6.1), but when adsorbed onto the surfaces, the chlorine becomes more negatively charged than the oxygen (Figures 6.3 and 6.4) and hence becomes the preferred for the δ^+ charge of a hydrogen atom.

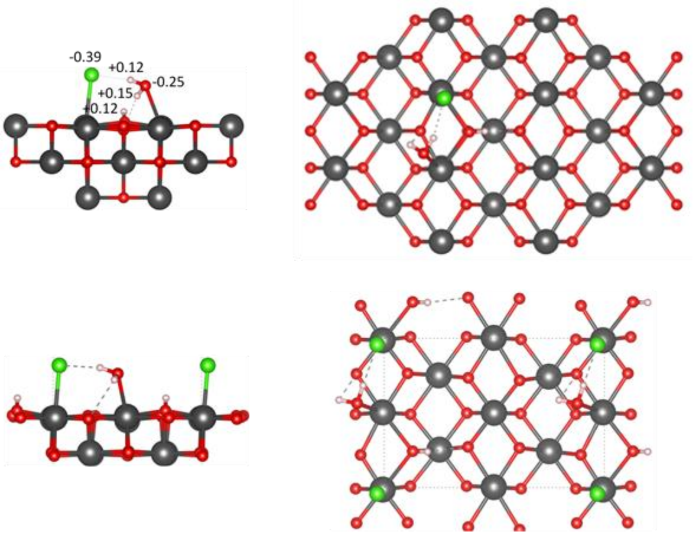

Figure 6.4: side (left) and top-down (right) view of the co-adsorption of HCl and H_2O on the PuO_2 {110} surface, produced from an initial chlorine-donor hydrogen bonding configuration; PEECM (top) and PBC (bottom). Hirshfeld charges from the PEECM calculation are shown for each adsorbing atom. Grey, red, green and white spheres represent the Pu, O, Cl and H atoms, respectively.

Given that, when dissociated on the PuO_2 surface, chlorine-acceptor hydrogen bonding configurations are more favourable, several new configurations were considered, with an initial bias towards chlorine-acceptor hydrogen bonding. The most energetically stable of these on the {111} surface, in which a total of three hydrogen bonds are formed, is depicted in Figure 6.5, with HCl binding energies of -1.80 eV and -1.79 eV for PEECM and PBC simulations, respectively. PEECM finds chlorine-acceptor hydrogen bond lengths of 2.19 Å and 2.05 Å between the adsorbed water molecule and surface hydroxyls, respectively, with the corresponding bond lengths from PBC calculation being 2.20 Å and 2.15 Å.

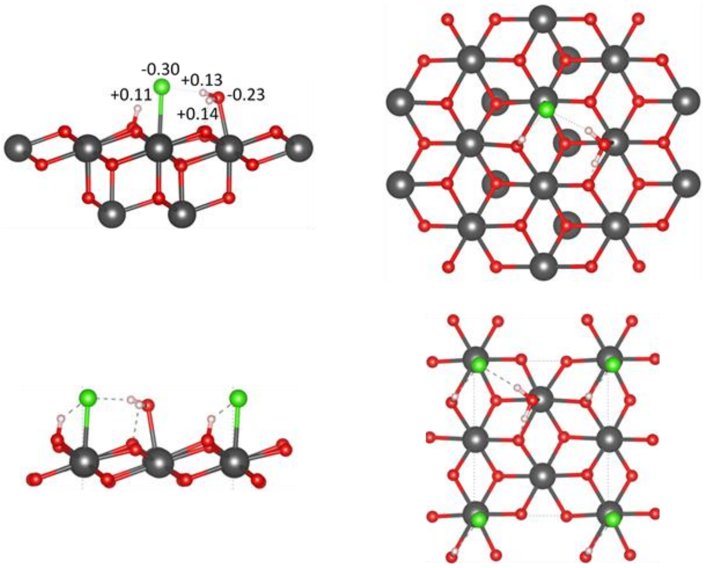

Figure 6.5: Side (left) and top-down (right) view of the co-adsorption of HCl and H_2O on the PuO_2 {111} surface, produced from an initial chlorine-acceptor hydrogen bonding configuration; PEECM (top) and PBC (bottom). Hirshfeld charges from the PEECM calculation are shown for each adsorbing atom. Grey, red, green and white spheres represent the Pu, O, Cl and H atoms, respectively.

QTAIM analysis of the PEECM again confirms their hydrogen bonding nature, with ρ_{BCP} and $\nabla^2\rho|_{\mathrm{BCP}}$ values of 0.028 a.u. and +0.066 a.u. for the water-chlorine and 0.038 a.u. and +0.093 a.u. for the surface hydroxyl-chlorine hydrogen bond critical points, respectively.

One notable aspect of this configuration is that on the {111} surface a water-surface hydrogen bond is broken in order to form the water-chlorine hydrogen bond, hinting that the co-adsorbed geometry is more stable than the sum of its parts which, comparing to the single HCl adsorption energy of -1.51 eV calculated in our previous work,[24] is the case. This finding is in agreement with our experimental work which found "{PuO_2} samples with higher water contents to retain chloride species more readily".[32]

For the analogous calculation on the {110} surface, depicted in Figure 6.6, the HCl was positioned in its most energetically stable configuration (found from our previous work)[24] while the water molecule was adsorbed dissociatively nearby, with a bias towards forming a chlorine-acceptor hydrogen bond. This configuration was also found to be more stable than the chlorine-donor one, with HCl binding energies of -2.78 eV and -2.83 eV, and chlorine-acceptor hydrogen bond lengths of 2.60 Å and 2.47 Å from PEECM and PBC simulations, respectively. QTAIM analysis of this system revealed a weak chlorine-acceptor hydrogen bond, with PEECM ρ_{BCP} and $\nabla^2\rho|_{\mathrm{BCP}}$ values of 0.012 a.u. and +0.034 a.u. This is not unexpected, as a H$\cdots$Cl separation of 2.60 Å is quite large for the formation of a hydrogen bond, and explains with the increase in stability when compared to single HCl molecule adsorptions[24] is less significant for the {110} surface (≈ 0.11 eV) than the {111} surface (≈ 0.29 eV) at the PEECM level.

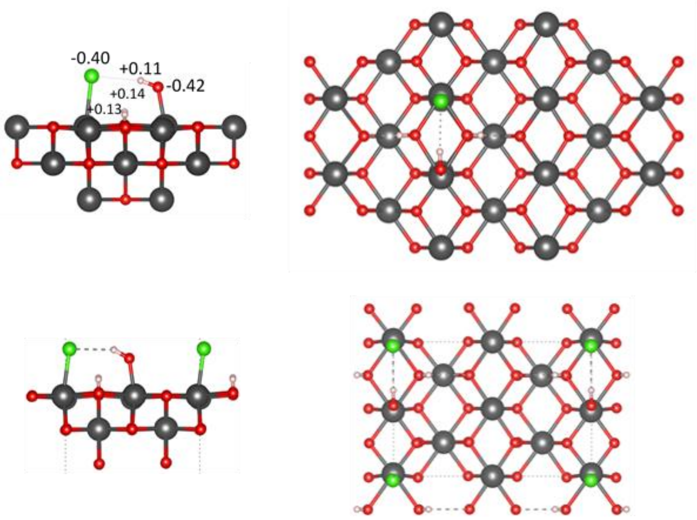

Figure 6.6: Side (left) and top-down (right) view of the co-adsorption of HCl and H_2O on the PuO_2 {110} surface, produced from an initial chlorine-acceptor hydrogen bonding configuration; PEECM (top) and PBC (bottom). Hirshfeld charges from the PEECM calculation are shown for each adsorbing atom. Grey, red, green and white spheres represent the Pu, O, Cl and H atoms, respectively.

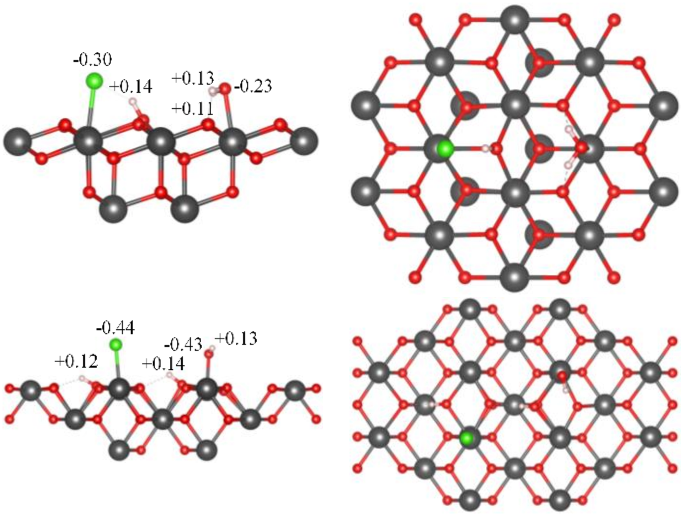

Figure 6.7: Side (left) and top-down (right) view of the non-interacting co-adsorption of HCl and H_2O on the PuO_2 {111} (top) and {110} (bottom) surfaces. Hirshfeld charges are shown for each adsorbing atom. Grey, red, green and white spheres represent the Pu, O, Cl and H atoms, respectively.

In addition to configurations where the H_2O and HCl were placed such that they could interact on the surface, two “control” geometries were also calculated, in which the HCl and H_2O were placed at opposite ends of the PEECM surface cluster and hence did not directly interact. The purpose of this was to give a reference against which we can compare other geometries, *i.e.* to deduce whether the H_2O-HCl interaction stabilises or destabilises the overall system. These configurations are shown in Figure 6.7, for which the HCl binding energy was calculated to be -1.16 eV and -2.58 eV for the {111} and {110} surfaces respectively. Comparing this to our previous work[24] we see two things: firstly, when HCl and H_2O interact on the {111} surface of PuO_2, the configuration in which both a water-chlorine and a water-surface hydrogen bond are formed (Figure 6.5) is more favourable than HCl adsorbing by itself or far away from a water molecule, indicating that combined adsorption increases stability. However, the -1.16 eV bonding energy for the HCl binding in the control geometry is significantly weaker than previously found for the solo adsorption of HCl, which could suggest that the presence of water on the surface has an indirect effect on HCl adsorptions elsewhere on the surface. The implication of this would be that, for less saturated surfaces, the presence of H_2O on the surface acts to destabilise bound HCl. This effect is not observed on the {110} surface, where the HCl binding energy for the configuration given in Figure 6.7 is not significantly different to that when bound in the absence of water.

Table 6.1: HCl binding energy E_{bind}, for the systems depicted in Figures 6.3 – 6.7, plus H···Cl separation distance $d_{\mathrm{H\cdots Cl}}$; PEECM data are in Calibri text, and PBC in italics. The electron density at the bond critical point ρ_{BCP} and the Laplacian of the electron density evaluated at the bond critical point $\nabla^2\rho|_{\mathrm{BCP}}$ for each H···Cl bond, are also summarised.

Surface	Initial Configuration	E_{bind} / eV	$d_{\mathrm{H\cdots Cl}}$ / Å	ρ_{BCP} / a.u.	$\nabla^2\rho\|_{\mathrm{BCP}}$ / a.u.
{111}	Cl-Donor H-Bond	-1.10/ -0.87	1.98/2.09	0.043	+0.086
	Cl-Acceptor H-Bond	-1.80/ -1.79	2.05/2.15	0.038	+0.093
			2.19/2.20	0.028	+0.066
	Control	-1.16	2.00	0.042	+0.099
{110}	Cl-Donor H-Bond	-2.39/ -2.64	2.15/2.17	0.030	+0.070
	Cl-Acceptor H-Bond	-2.78/ -2.83	2.60/2.47	0.012	+0.034
	Control	-2.58	---	---	---

Key data from the singly co-adsorbed calculations are collected in Table 6.1. The agreement between the PEECM/PBE0 and PBC/PBE+U approaches is generally very good indeed, yielding confidence in our conclusions. In addition, this agreement allows us to focus solely on the PEECM technique for the remainder of this study.

6.3.3 Co-adsorption with Multiple H_2O Molecules

Table 6.2: HCl binding energy E_{bind}, for the configurations in which a HCl molecule replaces one molecule in the 1ML hydrated system, plus H···Cl separation distances $d_{\mathrm{H\cdots Cl}}$. Electron density at the bond critical point ρ_{BCP} and the Laplacian of electron density evaluated at the bond critical point $\nabla^2\rho|_{\mathrm{BCP}}$ are given for each H···Cl bond.

Surface Index	E_{bind} / eV	$d_{\mathrm{H\cdots Cl}}$ / Å	ρ_{BCP} / a.u.	$\nabla^2\rho\|_{\mathrm{BCP}}$ / a.u.
{111}	-2.93	2.14	0.032	+0.084
		2.19	0.028	+0.065
{110}	-4.25	2.56	0.013	+0.037

Due to the atmospheric composition within Magnox canisters, it is likely that the PuO_2 would already have a significant amount of water on its surface by the time a HCl molecule comes into contact with it. We therefore now consider HCl interactions with a water-saturated surface. As described previously,[24] our PEECM clusters feature four surface Pu interaction sites. When all four sites interact with an adsorbing molecule, this corresponds to a single monolayer (ML) surface coverage. To begin with we examine the case where a HCl molecule replaces one water molecule on such a saturated surface. In order to evaluate all possible configurations, the initial geometries were constructed as follows. First, the most stable configuration of four water molecules adsorbing onto the surface in question was taken. Then, a set of calculations was performed where a HCl molecule replaces each one of the four water molecules on said surface, in four different orientations, for a total of 16 geometries per surface. Four initial orientations of HCl on each adsorption site were chosen such that interactions between the dissociated HCl hydrogen atom and each of the three remaining water molecules could be investigated – in addition to one configuration where this hydrogen atom migrates away from the water molecules – to maximise the likelihood that a global energy minimum would be reached. Key data for the most stable geometries resulting from these calculations on {111} and {110} are collected in Table 6.2, and are shown in Figures 6.8 and 6.9.

6.3.3.1 {111} Surface

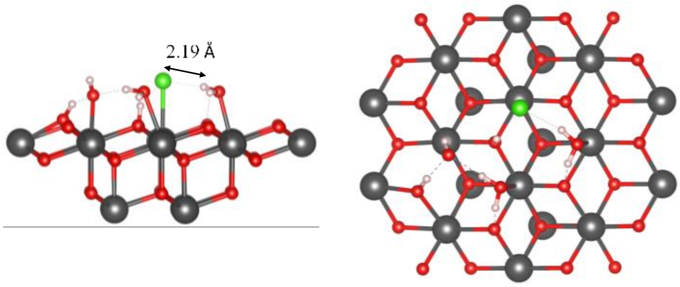

Figure 6.8: Side (left) and top-down (right) view of the most stable configuration for HCl replacing a H_2O molecule from 1ML of water on the PuO_2 {111} surface. The dissociated hydrogen from the HCl forms a surface hydroxyl, the interaction with which draws the chlorine into interaction range of the adjacent water molecule, forming a hydrogen bond. Grey, red, green and white spheres represent the Pu, O, Cl and H atoms, respectively.

Of all configurations tested for the {111} surface, the most energetically stable configurations by far arise when the HCl replaces a dissociatively adsorbed water molecule from a hydrated surface with a 50:50 mixture of dissociatively and molecularly adsorbed water. This is in agreement with our previous work, which found that when 3 water molecules were adsorbed onto the PuO_2 surface (*i.e.* 75% coverage), the most favourable proportion of molecular:dissociative adsorption was 2:1.[11] For this adsorption, the most stable orientation has the dissociated hydrogen atom from the HCl in a position such that the H···Cl interaction draws the chlorine atom towards the centre of the cluster, with ρ_{BCP} and $\nabla^2\rho|_{\mathrm{BCP}}$ values of 0.032 a.u. and +0.084 a.u., respectively. This is seen in Figure 6.8.

This attraction minimises the distance between the chlorine atom and its adjacent water molecule, forming a hydrogen bond of length 2.19 Å, with ρ_{BCP} and $\nabla^2\rho|_{\mathrm{BCP}}$ values of 0.028 a.u. and +0.065 a.u., respectively. The HCl binding energy for this interaction is -2.93 eV, which is significantly stronger than for HCl binding by itself or co-adsorbing with a single water molecule.

6.3.3.2 {110} Surface

The morphology of the {111} surface facilitates dissociation of molecular HCl when it is introduced to the hydrated surface, hydroxylating an adjacent surface oxygen atom. In contrast, the {110} surface is such that the adsorbed HCl molecule is not close enough to an oxygen atom to dissociate immediately. Instead the molecule remains intact for much of the geometry optimisation, migrating across the surface until in locates a suitable oxygen atom, be that from the surface or adsorbed water. Only once such an oxygen atom has been reached does the HCl molecule dissociate, the liberated chlorine atom subsequently finding the nearest suitable adsorption site. The optimum geometry located was that in which hydrogen bonding is maximised across the cluster, between the adsorbed chlorine atom and hydroxyl groups. Although QTAIM analysis reveals such hydrogen bonds to be weak (with ρ_{BCP} and $\nabla^2\rho|_{\mathrm{BCP}}$ values of 0.009 a.u. and +0.031 a.u. for the hydroxyl-hydroxyl and 0.013 a.u. and +0.037 a.u. for the hydroxyl-chlorine interactions, respectively, again due to the relatively large separation between the adsorbed groups) the configuration displayed in Figure 6.9 is very stable, with a HCl binding energy of -4.25 eV. This result exceeds even the stability of our most stable defect-healing configuration on the substoichiometric {111} surface, whilst reinforcing the idea that the formation of bridging surface hydrogen bonds on the {110} surface is particularly energetically favourable given the morphology of the surface.[24]

As seen for the {111} surface, the optimum configuration contains only dissociatively adsorbed water molecules. This is again in agreement with our previous work, which found that, for three water molecules adsorbing onto the stoichiometric {110} surface of PuO_2, the most favourable adsorption mode was that in which all water molecules adsorbed dissociatively.

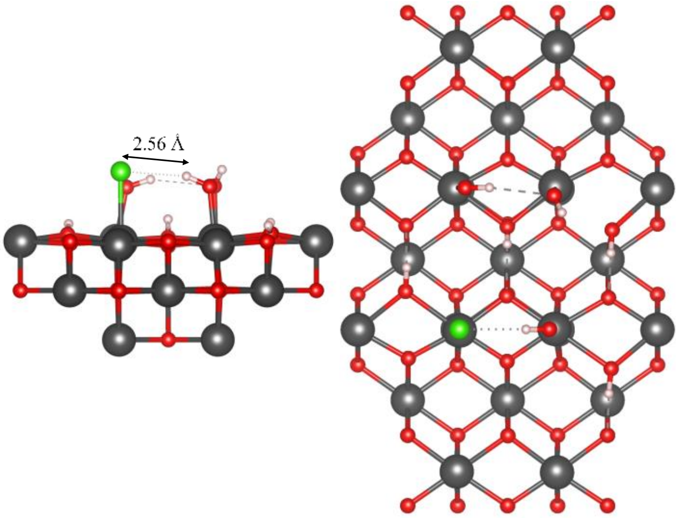

Figure 6.9: Side (left) and top-down (right) view of the most stable configuration for HCl adsorbing into 1ML of water on the PuO_2 {110} surface. Grey, red, green and white spheres represent the Pu, O, Cl and H atoms, respectively.

6.3.4 HCl Adsorbing onto 1ML Hydrated Surface

In an abundance of water, HCl may not have a direct path to a surface plutonium atom. Hence, we also consider the case where the HCl molecule interacts with surface-adsorbed water. In order to explore this a HCl molecule was placed above 1ML of adsorbed water.

6.3.4.1 {111} Surface

Upon interaction with the 1ML hydrated {111} surface, the HCl molecule spontaneously dissociates, with the hydrogen atom binding to a surface hydroxyl and forming molecular water. However, without a surface plutonium atom available to interact with the dissociated chlorine atom remains above the water layer, bound entirely by hydrogen bonds from the water (Figure 6.10). The HCl binding energy of this interaction is -1.32 eV, slightly less stable than a single HCl molecule binding to the dry surface.[24]

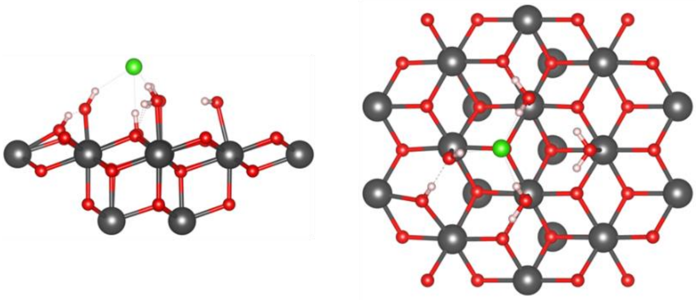

Figure 6.10: Side (left) and top-down (right) view of the adsorption of HCl onto the 1ML hydrated {111} surface of PuO_2. Grey, red, green and white spheres represent the Pu, O, Cl and H atoms, respectively.

Each of the four chlorine-acceptor hydrogen bonds has a similar ρ_{BCP} and $\nabla^2\rho|_{\mathrm{BCP}}$, with values ranging from 0.030 to 0.040 a.u. and from +0.065 to +0.090 a.u., respectively (Table 6.3). These values are close to those of the chlorine-acceptor hydrogen bonds we found in the Cl^{-}-$H_9O_4^{+}$ cluster described in section 3.1 (data collected in Figure A6.2). The existence of these four hydrogen bonds explains how the configuration can be relatively stable, despite lacking the Pu-Cl interaction we have seen previously.

Table 6.3: H···Cl separation $d_{\mathrm{H\cdots Cl}}$, electron density at the bond critical point ρ_{BCP} and the Laplacian of electron density evaluated at the bond critical point $\nabla^2\rho|_{\mathrm{BCP}}$ for each H···Cl bond in Figure 6.10.

$d_{\mathrm{H\cdots Cl}}$ / Å	$\boldsymbol{\rho}_{\mathbf{BCP}}$ / a.u.	$\boldsymbol{\nabla}^{\mathbf{2}}\boldsymbol{\rho}|_{\mathbf{BCP}}$ / a.u.
2.01	0.040	+0.090
2.03	0.039	+0.087
2.16	0.030	+0.074
2.18	0.030	+0.065

6.3.4.2 {110} Surface

A similar configuration to the {111} surface is found for the interaction of HCl with the fully hydrated {110} surface, as is seen in Figure 6.11. In this configuration the dissociated chlorine atom, with no surface plutonium atom to interact with, again binds solely via hydrogen bonding, this time with six hydrogen bonds, yielding an HCl binding energy of -2.58 eV. This energy is similar to that of a single HCl molecule binding directly to the {110} surface. QTAIM analysis reveals little variation in the characteristics of the chlorine-acceptor hydrogen bonds; the range of ρ_{BCP} is 0.020 to 0.029 a.u., whereas the range of $\nabla^2\rho|_{\mathrm{BCP}}$ is +0.053 to +0.068 a.u. (Table 6.4). These values are close to those of the chlorine-acceptor hydrogen bonds we find in the Cl^--H_8O_4 cluster described in section 3.1 (data collected in Figure A6.3). Comparison of these ρ_{BCP} and $\nabla^2\rho|_{\mathrm{BCP}}$ data with those of the hydrogen bonds formed on the {111} surface suggests that the interaction between the water layer and {110} surface is stronger than on the {111}, as the chlorine-acceptor hydrogen bonds are stronger above the latter. It has been previously shown that molecular water binds more strongly to PuO_2 {110} than {111}.[12]

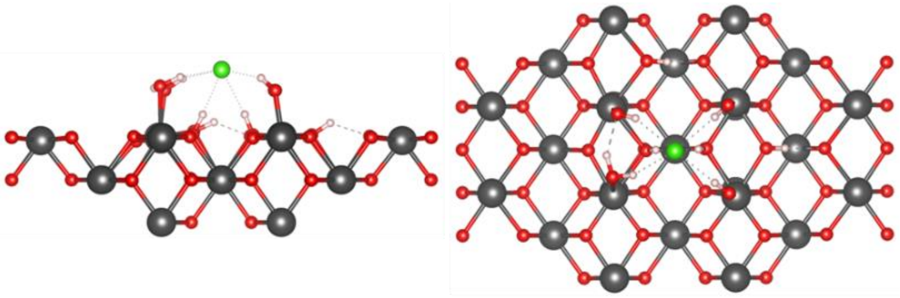

Figure 6.11: Side (left) and top-down (right) view of the adsorption of HCl onto the 1ML hydrated {110} surface of PuO_2. Grey, red, green and white spheres represent the Pu, O, Cl and H atoms, respectively.

Comparing these findings with our previous work regarding multiple water molecules interacting with the stoichiometric surfaces of PuO_2[11] we find that, in the presence of HCl, the optimum proportions of molecular: dissociative water adsorption modes differ. In the case of the {111} surface, we found that, for a full monolayer of adsorbed water, a 1:1 split of molecular to dissociative adsorptions is preferred. However, in the presence of HCl these proportions change, with a ratio of 3:1 being preferred. Similarly, we previously found that, for the {110} surface, a fully dissociative adsorption configuration was preferred, whereas in the presence of HCl we find the optimum ratio to be 1:3.

Table 6.4: H···Cl distance $d_{\mathrm{H\cdots Cl}}$, electron density at the bond critical point ρ_{BCP} and the Laplacian of the electron density evaluated at the bond critical point $\nabla^2\rho|_{\mathrm{BCP}}$ for each H···Cl bond in Figure 6.11.

$d_{\mathrm{H\cdots Cl}}$ / Å	$\boldsymbol{\rho}_{\mathbf{BCP}}$ / a.u.	$\boldsymbol{\nabla^2\rho}|_{\mathbf{BCP}}$ / a.u.
2.18	0.029	+0.068
2.20	0.029	+0.066
2.27	0.024	+0.059
2.30	0.022	+0.057
2.32	0.022	+0.056
2.36	0.020	+0.053

To further validate these findings, geometries were constructed for both the {111} and {110} surfaces which mirrored the expected distribution of molecularly and dissociatively adsorbed water molecules based on our previous work.[11] In both cases, these were found to be less stable than their counterparts in Figures 6.10 and 6.11. This is likely because, when unable to interact with a surface plutonium atom, the HCl instead interacts with the hydrated surface *via* an acid-base type interaction: neutralising one of the adsorbed Pu-OH groups and forming molecular water. This finding is consistent with the first part of reaction (2) in the work of Parfitt *et. al.*, who proposed that for HCl interacting with hydroxylated rutile surfaces, the HCl would neutralise a surface hydroxyl, forming physisorbed molecular water.[25] The next proposed step in this reaction mechanism is for the chloride to replace the physisorbed water on the TiO_2 surface, which based on the energetic favourability of direct Pu-Cl bonds, would likely also be the case for PuO_2.

6.3.5 HCl Desorption Temperatures from PuO_2 {111} and {110} Surfaces

In our previous work, we presented data which show the desorption temperature of either H_2O[12,48] or HCl[24] from actinide dioxide surfaces as a function of H_2O or HCl partial pressure. Deriving similar data in the present case is less straightforward, as we are considering the co-adsorption of two species. Nevertheless, in order to get some measure of the effect of co-adsorption on the desorption temperature of HCl, we have employed the methodology described in reference 24 to generate Figures 6.12 and 6.13. The vertical axis spans $-90 < \ln(p/p_0) < 20$, as this represents a reasonably wide range of partial pressures, and an upper limit for temperature of 1500 K was chosen because it is unlikely that temperatures in excess of this would be achieved in practice. Note that the zero-Kelvin adsorption energies used in this process are the HCl binding energies obtained in the present work from both the PEECM and PBC approaches, which reflect the modification to HCl adsorption caused by co-adsorption with a single water molecule. For {111} the desorption curves from both PEECM and PBC are extremely similar to one another, while for {110} there is a slight difference between them, reflecting the zero-Kelvin adsorption energies. Also presented in Figures 6.12 and 6.13 are the data from our previous study of HCl which show that, for a given partial pressure of HCl, the co-absorption with water results in a higher HCl desorption temperature.

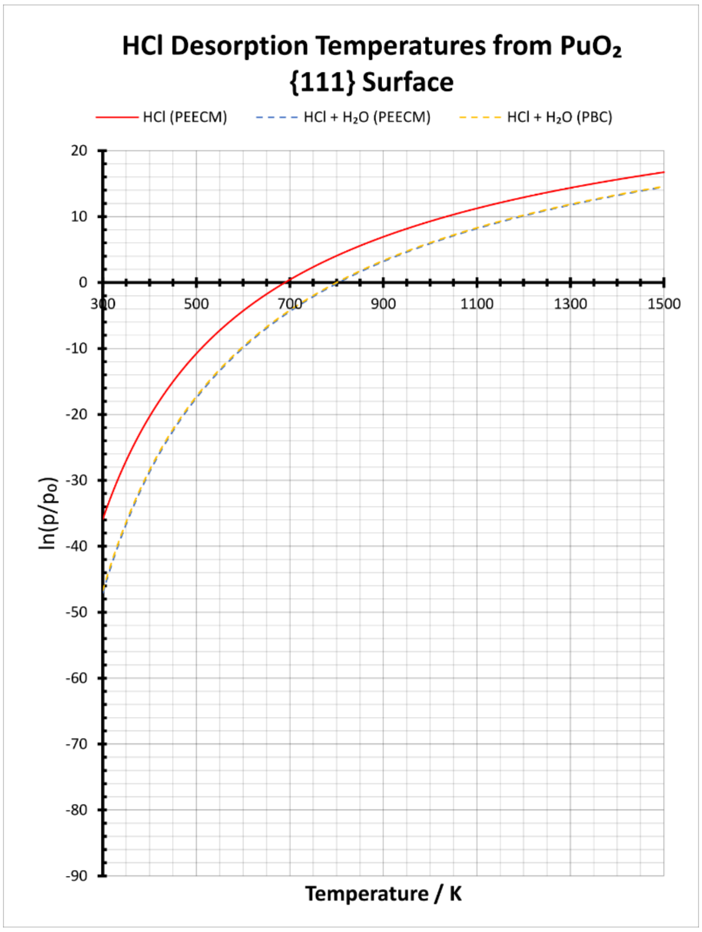

Figure 6.12: Relationship between partial pressure of HCl *p*, and temperature *T* required for thermal desorption of HCl co-adsorbed with a single water molecule from the PuO_2 {111} surface. Data in red from are taken reference 24.

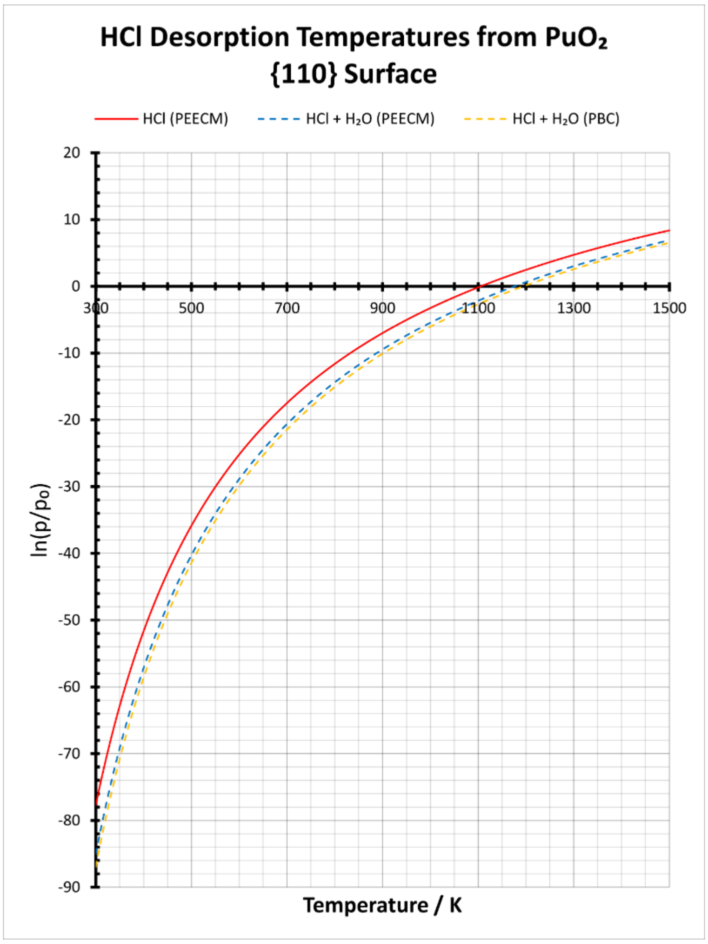

Figure 6.13: Relationship between partial pressure of HCl *p*, and temperature *T* required for thermal desorption of HCl co-adsorbed with a single water molecule from the PuO_2 {110} surface. Data in red are taken from reference 24.

6.4 Conclusions

In this contribution, we have used both embedded cluster and periodic boundary condition DFT to explore the impact of co-adsorption with water on the geometry and strength of HCl binding to the {111} and {110} surfaces of PuO_2. Excellent agreement is found between the two computational approaches. Different levels of water coverage have been explored, ranging from a single co-adsorbed molecule, to a full monolayer. Results for single molecule co-adsorptions indicate that due to the formation of chlorine-acceptor hydrogen bonds, closely bound HCl and H_2O have a synergistic effect on HCl binding energy. However, when there is a large separation between the molecules, there is evidence to suggest that the binding of HCl on the {111} surface may instead be weakened. This could have implications for surfaces with lower saturation levels of water – including those which have been dried *via* heat treatment – making bound HCl in such systems easier to remove.

Substitution of HCl into a full monolayer of water on surface of PuO_2 compounds these synergistic effects, yielding far more stable configurations than those found for single HCl molecule adsorptions on the dry surfaces. In all cases, the optimum distribution of molecularly and dissociatively adsorbed H_2O matches that found in our previous work on multiple water molecule adsorptions in the absence of HCl.[11]

The adsorption of HCl above a full monolayer of water further confirms the strong nature of the chlorine-acceptor hydrogen bonds formed. Despite the fact that the chlorine atom cannot interact directly with surface Pu, the configurations produced still have reasonably strong HCl binding energies, stabilised by the numerous hydrogen bonds formed with adsorbed water. On both surfaces, we find the optimum distribution of molecularly and dissociatively adsorbed H_2O over the four adsorption sites to have one additional molecular water than we found previously in the absence of HCl.[11] This is attributed to an acid-base-like reaction between the HCl molecule and an adsorbed hydroxyl group from dissociatively adsorbed water, stabilising the overall system and matching the first step in reaction (2) proposed by Parfitt *et. al.* for HCl interactions with hydroxylated rutile surfaces.[25]

From this work it is clear that the interactions between HCl and the surface of PuO_2 are greatly influenced by the presence of water. Taking into consideration the well-known hygroscopicity of PuO_2, this is likely of significance in the context of long-term storage solutions for such material – particularly with regards to chloride removal for potential future fuel repurposing – and would benefit from future studies, both theoretical and experimental. In our previous work regarding the adsorption of solely HCl we concluded that the temperatures required to thermally desorb HCl from PuO_2 surfaces would likely be very high; this conclusion is here further reinforced by the discovery of a synergistic co-adsorption between HCl and water.

References

1. Taylor, R.; Webb, K.; Gregson, C.; Orr, R.; Sims, H.; Mason, C.; Hobbs, J.; Bernard, R., *Stabilisation of chloride contaminated plutonium oxide for long term storage*, 2014.

2. Nitta, S. I. O. Y. N. I., Mechanism of discoloration of irradiated polyvinyl chloride. *J. Appl. Polym. Sci.* **1962**, *6*, 629*638.

3. Decker, C., Oxidative degradation of poly(vinyl chloride). *J. Appl. Polym. Sci.* **1976**, *20*, 3321-3336.

4. Miller, A. A., Radiation chemistry of poyvinyl chloride. *J. Phys. Chem.* **1959**, *63*, 1755-1759.

5. Zahran, A. H.; Hegazy, E. A.; Ezz Eldin, F. M., Radiation effects on poly (vinyl chloride)—I. gas evolution and physical properties of rigid PVC films. *Radiat. Phys. Chem.* **1985**, *26*, 25-32.

6. Arakawa, K.; Seguchi, T.; Yoshida, K., Radiation-induced gas evolution in chlorine-containing polymer. Poly(vinyl chloride), chloroprene rubber, and chlorosulfonated-polyethylene. *Int. J. Radiat. Appl. Instrum. C* **1986**, *27*, 157-163.

7. Machi, E. S. A. H. T. S. S., Radiation ‐ induced oxidative degradation of poly(vinyl chloride). *J. Appl. Polym. Sci.* **1981**, *26*, 2947-2957.

8. LaVerne, J. A.; Carrasco-Flores, E. A.; Araos, M. S.; Pimblott, S. M., Gas production in the radiolysis of poly(vinyl chloride). *J. Phys. Chem. A* **2008**, *112*, 3345-3351.

9. Maldonado, P.; Evins, L. Z.; Oppeneer, P. M., Ab initio atomistic thermodynamics of water reacting with uranium dioxide surfaces. *Journal of Physical Chemistry C* **2014**, *118*, 8491-8500.

10. Tian, X.-f.; Wang, H.; Xiao, H.-x.; Gao, T., Adsorption of water on UO_2 (111) surface: Density functional theory calculations. *Comput. Mater. Sci.* **2014**, *91*, 364-371.

11. Chen, J.-L.; Kaltsoyannis, N., Computational study of the bulk and surface properties of minor actinide dioxides $MAnO_2$ (MAn = Np, Am, and Cm); Water adsorption on stoichiometric and reduced {111}, {110}, and {100} Surfaces. *J. Phys. Chem. C* **2019**, *123*, 15540-15550.

12. Wu, X. Y.; Ray, A. K., Density-functional study of water adsorption on the PuO_2 (110) surface. *Phys. Rev. B* **2002**, *65*.

13. Wellington, J. P. W.; Kerridge, A.; Austin, J.; Kaltsoyannis, N., Electronic structure of bulk AnO_2 (An = U, Np, Pu) and water adsorption on the (111) and (110) surfaces of UO_2 and PuO_2 from hybrid density functional theory within the periodic electrostatic embedded cluster method. *J. Nucl. Mater.* **2016**, *482*, 124-134.

14. Bo, T.; Lan, J.-H.; Zhao, Y.-L.; Zhang, Y.-J.; He, C.-H.; Chai, Z.-F.; Shi, W.-Q., First-principles study of water adsorption and dissociation on the UO_2 (111), (110) and (100) surfaces. *J. Nucl. Mater.* **2014**, *454*, 446-454.

15. Bo, T.; Lan, J.-H.; Wang, C.-Z.; Zhao, Y.-L.; He, C.-H.; Zhang, Y.-J.; Chai, Z.-F.; Shi, W.-Q., First-principles study of water reaction and H_2 formation on UO_2 (111) and (110) single crystal surfaces. *J. Phys. Chem. C* **2014**, *118*, 21935-21944.

16. Sims, H. E.; Webb, K. J.; Brown, J.; Morris, D.; Taylor, R. J., Hydrogen yields from water on the surface of plutonium dioxide. *J. Nucl. Mater.* **2013**, *437*, 359-364.

17. Wellington, J. P. W.; Tegner, B. E.; Collard, J.; Kerridge, A.; Kaltsoyannis, N., Oxygen vacancy formation and water adsorption on reduced AnO_2 {111}, {110}, and {100} surfaces (An = U, Pu): A computational study. *J. Phys. Chem. C* **2018**, *122*, 7149-7165.

18. Haschke, J. M.; Allen, T. H.; Morales, L. A., Reactions of plutonium dioxide with water and hydrogen-oxygen mixtures: Mechanisms for corrosion of uranium and plutonium. *J. Alloys Compd.* **2001**, *314*, 78-91.

19. Senanayake, S. D.; Waterhouse, G. I. N.; Chan, A. S. Y.; Madey, T. E.; Mullins, D. R.; Idriss, H., The reactions of water vapour on the surfaces of stoichiometric and reduced uranium dioxide: A high resolution XPS study. *Catal. Today* **2007**, *120*, 151-157.

20. Bo, T.; Lan, J.-H.; Zhao, Y.-L.; Zhang, Y.-J.; He, C.-H.; Chai, Z.-F.; Shi, W.-Q., Surface properties of NpO_2 and water reacting with stoichiometric and reduced NpO_2 (111), (110), and (100) surfaces from ab initio atomistic thermodynamics. *Surf. Sci.* **2016**, *644*, 153-164.

21. Jomard, G.; Bottin, F.; Geneste, G., Water adsorption and dissociation on the PuO_2(110) surface. *Journal of Nuclear Materials* **2014**, *451*, 28-34.

22. Tegner, B. E.; Molinari, M.; Kerridge, A.; Parker, S. C.; Kaltsoyannis, N., Water adsorption on AnO(2) {111}, {110}, and {100} surfaces (An = U and Pu): A density functional theory plus U study. *Journal of Physical Chemistry C* **2017**, *121*, 1675-1682.

23. Senanayake, S. D.; Idriss, H., Water reactions over stoichiometric and reduced UO_2 (111) single crystal surfaces. *Surf. Sci.* **2004**, *563*, 135-144.

24. Collard, J.; Steele, H.; Kaltsoyannis, N., Computational study of HCl adsorption on stoichiometric and oxygen vacancy PuO_2 {111}, {110} and {100} surfaces. *Journal of Nuclear Materials* **2020**, *530*, 151951.

25. Parfitt, G. D.; Ramsbotham, J.; Rochester, C. H., Infra-red study of hydrogen chloride adsorption on rutile surfaces. *Trans. Faraday Soc.* **1971**, *67*, 3100-+.

26. Sutherland-Harper, S., et al., Surface speciation and interactions between adsorbed chloride and water on cerium dioxide. *J. Solid State Chem.* **2018**, *262*, 16-25.

27. Drera, S. S.; Björk, K. I.; Sobieska, M., Ceria-thoria pellet manufacturing in preparation for plutonia-thoria LWR fuel production. *J. Nucl. Mater.* **2016**, *479*, 184-188.

28. J.C. Marra, A. D. C., R.A. Pierce, J.M. Pareizs, A.R. Jurgensen, D.M. Missimer, Cerium as a surrogate in the plutonium immobilized form, in: environmental issues and waste management technologies in the ceramic and nuclear industries VII (eds G.L. Smith, S. Sundaram and D.R. Spearing).

29. Sweet, L. E.; Corbey, J. F.; Gendron, F.; Autschbach, J.; McNamara, B. K.; Ziegelgruber, K. L.; Arrigo, L. M.; Peper, S. M.; Schwantes, J. M., Structure and bonding

investigation of plutonium peroxocarbonate complexes using cerium surrogates and electronic Structure Modeling. *Inorg. Chem.* **2017**, *56*, 791-801.

30. Sutherland-Harper, S., et al., Characterisation and heat treatment of chloride-contaminated and humidified PuO_2 samples. *J. Nucl. Mater.* **2018**, *509*, 654-666.

31. Sutherland-Harper, S.; Livens, F.; Pearce, C.; Hobbs, J.; Orr, R.; Taylor, R.; Webb, K.; Kaltsoyannis, N., Interactions of HCl and H_2O with the surface of PuO_2. *J. Nucl. Mater.* **2019**, *518*, 256-264.

32. Webb, K., et al., Thermal processing of chloride-contaminated plutonium dioxide. *ACS Omega* **2019**, *4*, 12524-12536.

33. Ahlrichs, R.; Bär, M.; Häser, M.; Horn, H.; Kölmel, C., Electronic structure calculations on workstation computers: The program system turbomole. *Chem. Phys. Lett.* **1989**, *162*, 165-169.

34. Kresse, G.; Hafner, J., Ab initio molecular dynamics for liquid-metals. *Phys. Rev. B* **1993**, *47*, 558-561.

35. Kresse, G.; Hafner, J., Ab initio molecular-dynamics simulation of the liquid-metal-amorphous-semiconductor transition in germanium. *Phys. Rev. B* **1994**, *49*, 14251-14269.

36. Kresse, G.; Furthmüller, J., Efficiency of ab-initio total energy calculations for metals and semiconductors using a plane-wave basis set. *Computational Materials Science* **1996**, *6*, 15-50.

37. Kresse, G.; Furthmüller, J., Efficient iterative schemes for ab initio total-energy calculations using a plane-wave basis set. *Physical Review B* **1996**, *54*, 11169-11186.

38. Perdew, J. P.; Burke, K.; Ernzerhof, M., Generalized gradient approximation made simple. *Physical Review Letters* **1996**, *77*, 3865-3868.

39. Liechtenstein, A. I.; Anisimov, V. I.; Zaanen, J., Density-functional theory and strong interactions: Orbital ordering in Mott-Hubbard insulators. *Phys. Rev. B* **1995**, *52*, R5467-R5470.

40. Blöchl, P. E., Projector augmented-wave method. *Physical Review B* **1994**, *50*, 17953-17979.

41. Monkhorst, H. J.; Pack, J. D., Special points for Brillouin-zone integrations. *Physical Review B* **1976**, *13*, 5188-5192.

42. Ma, L.; Atta-Fynn, R.; Ray, A. K., Elemental and mixed actinide dioxides: An ab initio study. *Journal of Theoretical & Computational Chemistry* **2012**, *11*, 611-629.

43. Lu, T.; Chen, F. W., Multiwfn: A multifunctional wavefunction analyzer. *J. Comput. Chem.* **2012**, *33*, 580-592.

44. Momma, K.; Izumi, F., VESTA 3 for three-dimensional visualization of crystal, volumetric and morphology data. *Journal of Applied Crystallography* **2011**, *44*, 1272-1276.

45. Kieth, T. A., AIMALL. *aim.tkgristmill.com* **2019**.

46. Sobolewski, A. L.; Domcke, W., Ab initio investigation of the structure and spectroscopy of hydronium−water clusters. *J. Phys. Chem. A* **2002**, *106*, 4158-4167.

47. Shields, R. M.; Temelso, B.; Archer, K. A.; Morrell, T. E.; Shields, G. C., Accurate predictions of water cluster formation, $(H_2O)_{n=2-10}$. *J. Phys. Chem. A* **2010**, *114*, 11725-11737.

48. Chen, J.-L.; Kaltsoyannis, N., Computational study of plutonium–americium mixed oxides ($Pu_{0.92}Am_{0.08}O_{2-x}$); Water adsorption on {111}, {110}, and {100} surfaces. *The Journal of Physical Chemistry C* **2020**, *124*, 6646-6658.

Conclusion

In this thesis, actinide oxide systems have been extensively investigated with DFT methods, vie. DFT + *U* and hybrid DFT, with periodic boundary and embedded cluster models. These two methods both give reasonable results, which are in good agreement with experiment, and similar predictions are made with the two methods.

Minor actinides dioxides, NpO_2, AmO_2, and CmO_2, were studied with DFT + *U* method, similar bulk and surface properties were observed, as well as water adsorption behaviour at their surfaces. Comparisons for pure actinide dioxides, from UO_2 to CmO_2, give an overall view of actinide dioxides, for example, surface properties, like surface O vacancy formation, closely related to An (IV/III) redox potential.

Uranium-actinide mixed oxides, from U-Np MOX to U-Cm MOX, were also investigated with DFT + *U* method. Although the mixing of other actinides (Np, Pu, Am, and Cm) into UO_2 has minor effects on geometric structure, obvious influences have been found on the electronic structure, surface properties, and water adsorption behaviour, thus, mixing of other actinides should be carefully controlled for the safe usage of actinide MOX fuel.

Simplified PuO_2 + H_2O system could not precisely describe the long-term storage PuO_2 stockpiles, as Am build up have been observed in PuO_2 stockpiles and other residual molecules, like HCl. In order to find out the influence of Am on PuO_2, Pu and Am MOXs were extensively studied with DFT + *U* method. Simulations indicate Am has an influence on PuO_2 surface properties and water adsorption, and could lead to accelerated gas build up in PuO_2 stockpiles.

Both PBE + U and PBE0 methods were used for simulating HCl and H_2O co-adsorption on PuO_2 surfaces. Adsorption of HCl onto wet PuO_2 surface, from a single co-adsorbed molecule, to a full monolayer, indicates desorption of HCl is easier for surfaces with lower saturation levels of water

The work in this thesis takes a further step for the theoretical investigation of actinide nuclear fuel and wastes from previous studies, which have mainly focused on pure UO_2 and

PuO_2. Even small ratios of other actinides in UO_2 and Am in PuO_2, as well as different types of residual molecules, can influence on the properties of UO_2 and PuO_2 and cannot be neglected. Therefore, further studies could investigate more complicated systems, like U-Pu-MAn and Pu-Am-U MOX systems, to bring simulations closer to actual MOX fuel and aged PuO_2 stockpiles. Other residual molecules, such as nitrogen oxides and carbon oxides, should also be considered in future simulations.

Appendix 1

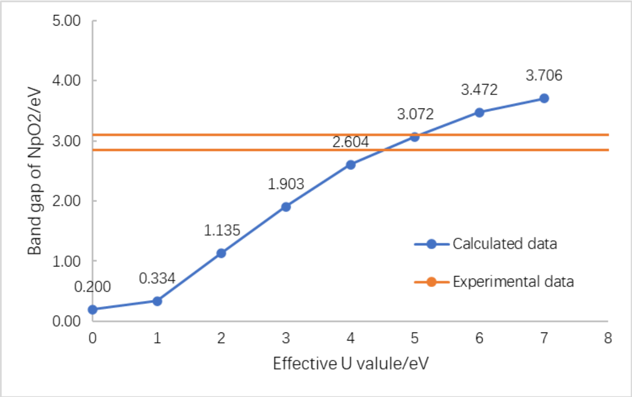

Figure A3.1: The band gap of NpO_2.

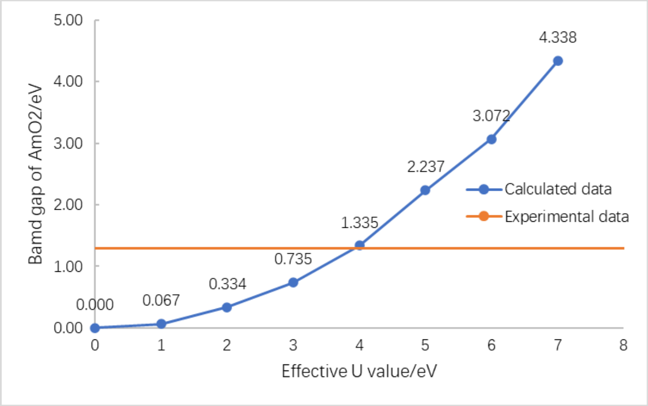

Figure A3.2: The band gap of AmO_2.

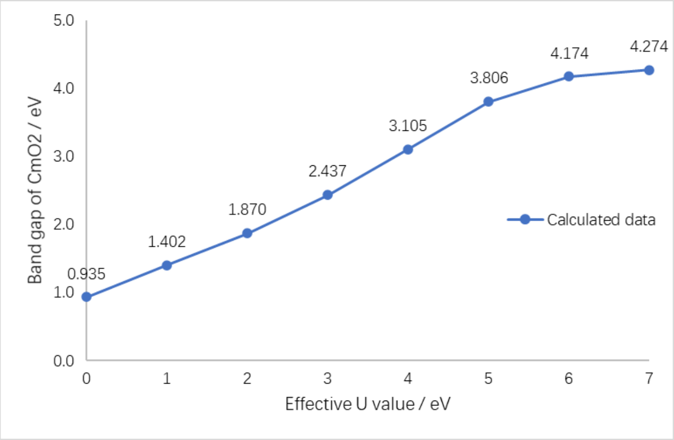

Figure A3.3: The band gap of CmO_2.

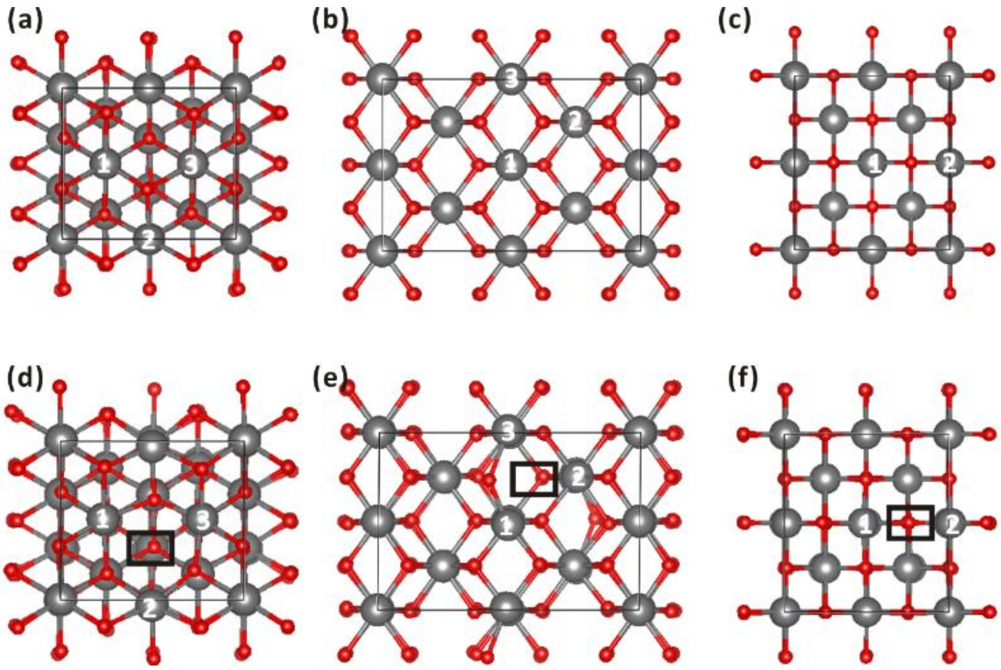

Figure A3.4: Top view of stoichiometric (a) {111}, (b) {110}, (c) {100} and reduced (d) {111}, (e) {110}, (f) {100} AmO_2 surfaces calculated at PBE+U level with U_{eff} = 4.00 eV (the corresponding U_{eff} = 6.15 eV images, not shown, are very similar). Light grey and red spheres represent americium and oxygen atoms, respectively, black squares mark the position of oxygen vacancy defects, and the labelled americium atoms were bonded to the removed oxygen.

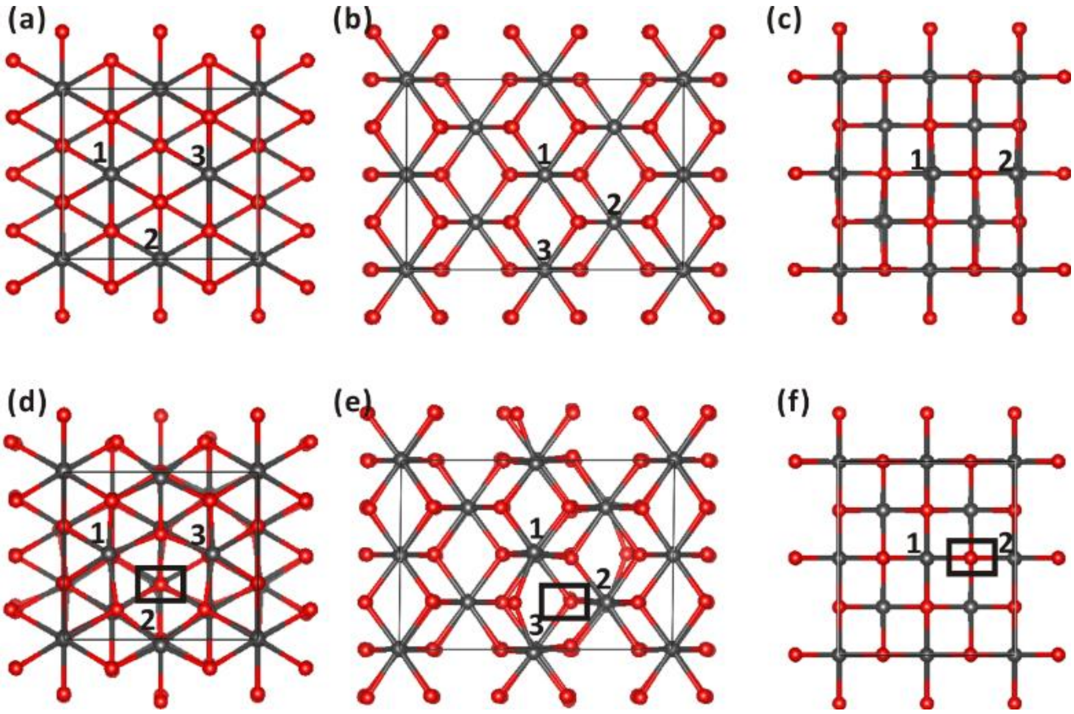

Figure A3.5: Top view of stoichiometric (a) {111}, (b) {110}, (c) {100} and reduced (d) {111}, (e) {110}, (f) {100} CmO_2 surfaces calculated at PBE+U (U_{eff} = 4.5eV) level. Small dark grey and red spheres represent curium and oxygen atoms, respectively, black squares mark the position of oxygen vacancy defects, and the labelled curium atoms were bonded to the removed oxygen.

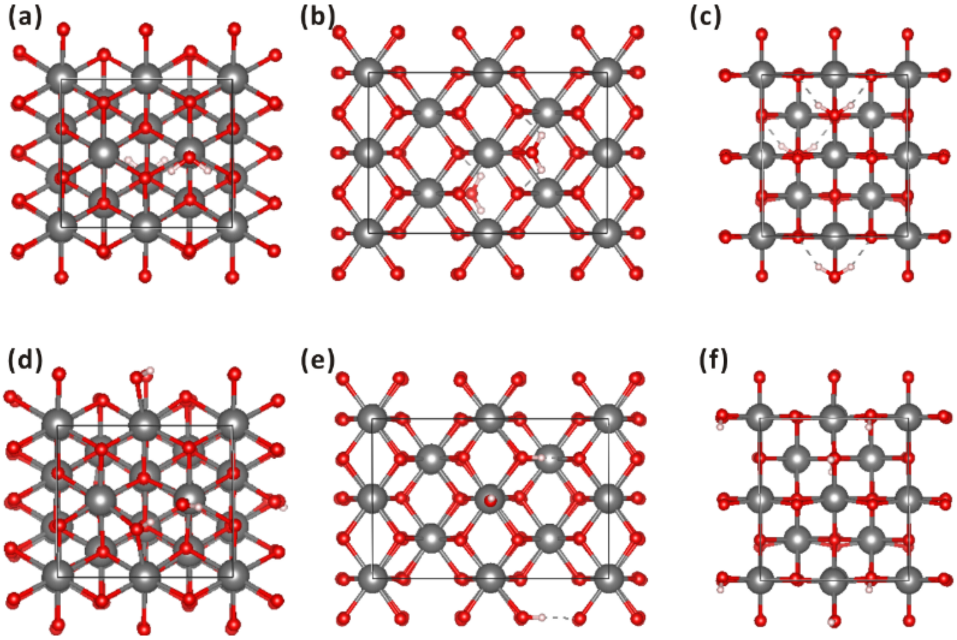

Figure A3.6: Top view of molecular (a) {111}, (b) {110}, (c) {100} and dissociative (d) {111}, (e) {110}, (f) {100} water adsorption on stoichiometric AmO_2 surfaces calculated at PBE+U level with U_{eff} = 4.00 eV (the corresponding U_{eff} = 6.15 eV images, not shown, are very similar). Water adsorbs on both sides of the slab with 25% coverage. Light grey, red and white spheres represent americium, oxygen and hydrogen atoms, respectively.

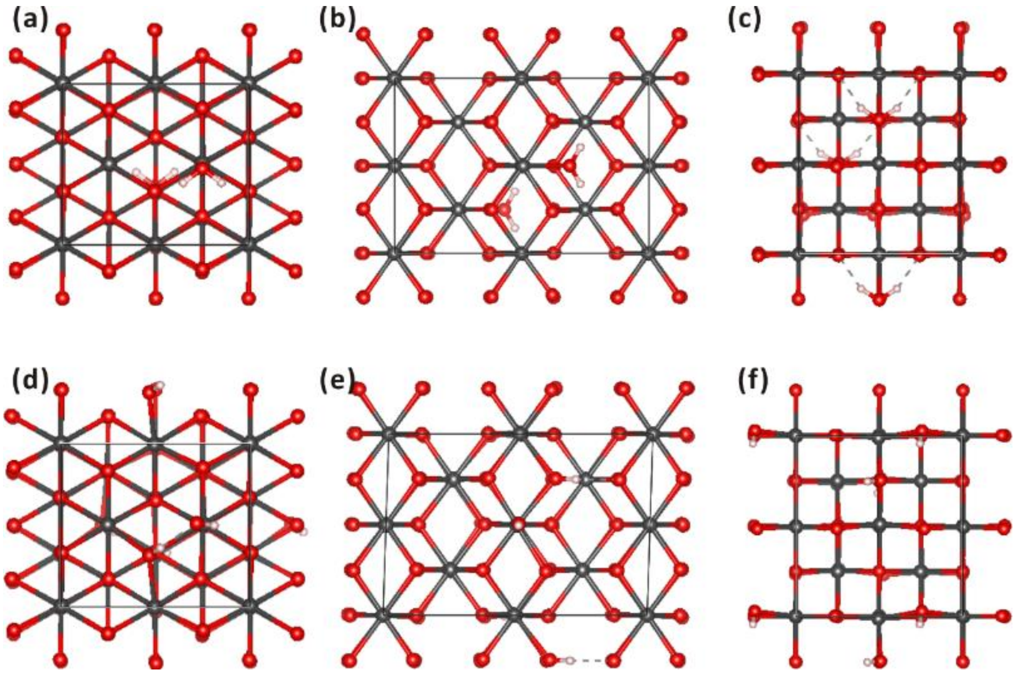

Figure A3.7: Top view of molecular (a) {111}, (b) {110}, (c) {100} and dissociative (d) {111}, (e) {110}, (f) {100} water adsorption on stoichiometric CmO_2 surfaces calculated at PBE+U (U_{eff} = 4.5eV) level. Water adsorbs on both sides of the slab with 25% coverage. Small dark grey, red and white spheres represent curium oxygen and hydrogen atoms, respectively.

Table A3.1: O_w-Np_s and H_w-O_s bond lengths for molecular and dissociative water adsorption on NpO_2 surfaces calculated at the PBE + *U* and PBESol + *U* levels (U_{eff} = 4.5eV).

Adsorption	Bond length (Å)	{111}		{110}		{100}	
	Method	PBE	PBESol	PBE	PBESol	PBE	PBESol
molecular	O_w-Np_s	2.60	2.53	2.68	2.61	2.60/2.68	2.55/2.59
	H_w-O_s	2.14/2.13	2.01/1.99	2.07/2.08	2.01/2.06	1.94/1.97	1.01/1.01
dissociative	O_w-Np_s	2.24	2.22	2.13	2.12	2.34/2.35	2.30/2.32
	H_w-O_s	1.01	1.03	0.99	0.99	0.97	0.97

Table A3.2: O_w-Am_s and H_w-O_s bond lengths for molecular and dissociative water adsorption on AmO_2 surfaces calculated at the PBE + *U* level with U_{eff} = 4.00 and 6.15 eV.

Adsorption	Bond length (Å)	{111}		{110}		{100}	
	U_{eff} (eV)	4.00	6.15	4.00	6.15	4.00	6.15
molecular	O_w-Am_s	2.59	2.64	2.70	2.68	2.57/2.73	2.57/2.76
	H_w-O_s	2.10/2.12	2.18/2.14	2.10/2.11	2.10/2.19	1.93/1.90	1.90/1.90
dissociative	O_w-Am_s	2.23	2.34	2.13	2.12	2.36/2.31	2.34/2.41
	H_w-O_s	1.02	0.99	0.99	0.99	0.98	0.97

Table A3.3: O_w-Cm_s and H_w-O_s bond lengths for molecular and dissociative water adsorption on CmO_2 surfaces (PBE + *U*, U_{eff} = 4.5 eV)).

Adsorption	Bond length (Å)	{111}	{110}	{100}
molecular	O_w-Cm_s	2.62	2.68	2.62 / 2.75
	H_w-O_s	2.11 / 2.14	2.16 / 2.16	2.01 / 2.01
dissociative	O_w-Cm_s	2.29	2.18	2.40 / 2.43
	H_w-O_s	0.99	0.98	0.97

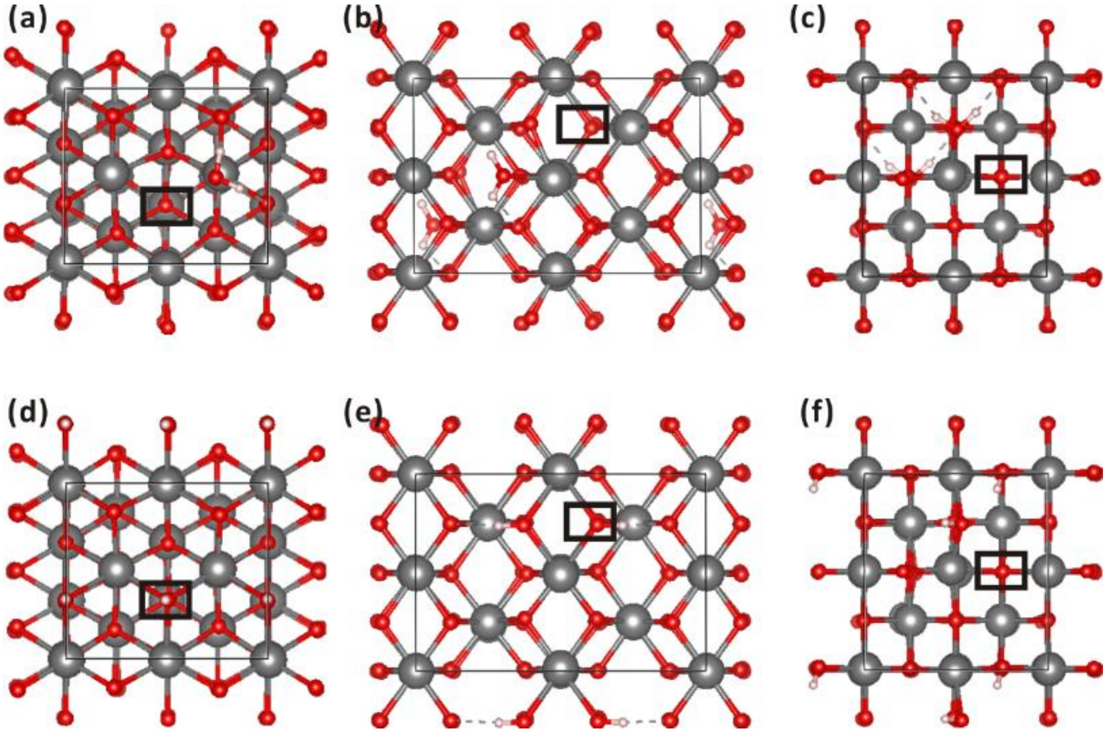

Figure A3.8: Top views of molecular (a) {111}, (b) {110}, (c) {100} and dissociative (d) {111}, (e) {110}, (f) {100} water adsorptions at the surface Am of reduced AmO_2 surfaces calculated at the PBE+*U* (U_{eff} = 4.5eV) level. Water adsorbs on both side of the slabs with 25% coverage. Light grey, red and white spheres represent americium oxygen and hydrogen atoms, respectively. The black square marks the position of the defect.

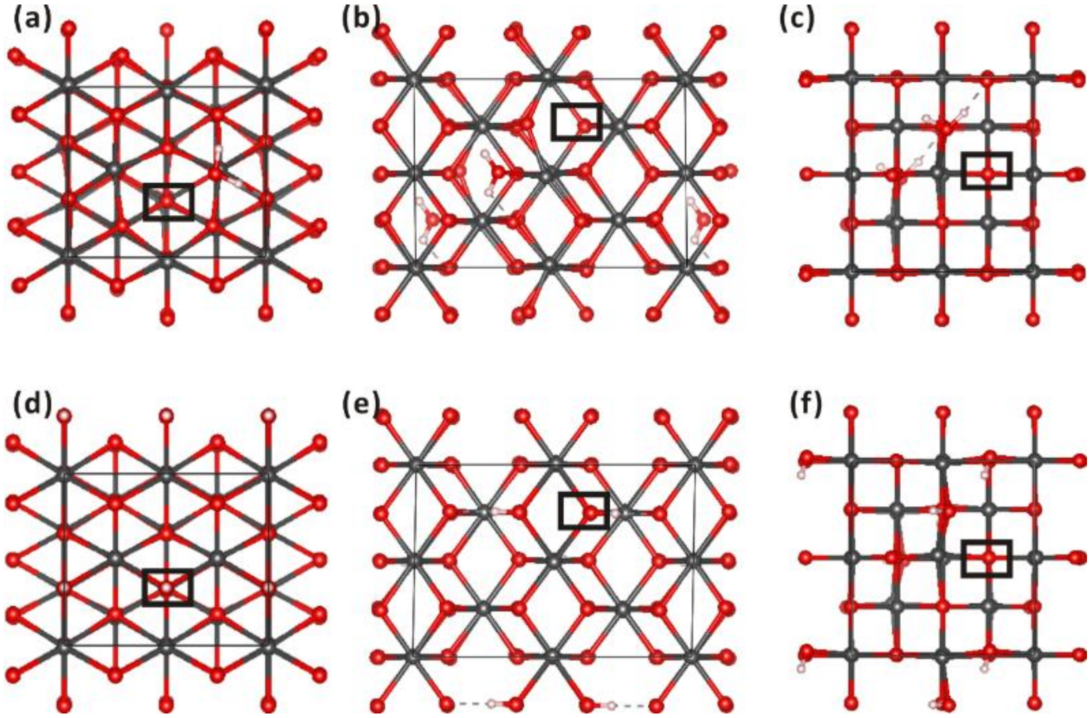

Figure A3.9: Top view of molecular (a) {111}, (b) {110}, (c) {100} and dissociative (d) {111}, (e) {110}, (f) {100} water adsorptions at the surface Cm of reduced CmO_2 surfaces calculated at the PBE+U (U_{eff} = 4.5eV) level. Water adsorbs on both side of the slabs with 25% coverage. Small dark grey, red and white spheres represent curium oxygen and hydrogen atoms, respectively. the black square marks the position of the defect.

Table A3.4: Energies (eV) for molecular and dissociative water adsorption on reduced NpO_2 surfaces, which are calculated at PBESol + U (U_{eff} = 4.00 eV) level, and AmO_2 surfaces, which are calculated at PBE + U (U_{eff} = 6.15 eV) level, with O_w approaching surface An.

AnO_2	Molecular adsorption			Dissociative adsorption		
	{111}	{110}	{100}	{111}	{110}	{100}
NpO_2	-0.03	-0.56	dis*	-2.18	-1.59	-1.23
AmO_2	-0.61	-1.62	-1.54	-2.91	-1.69	-2.37

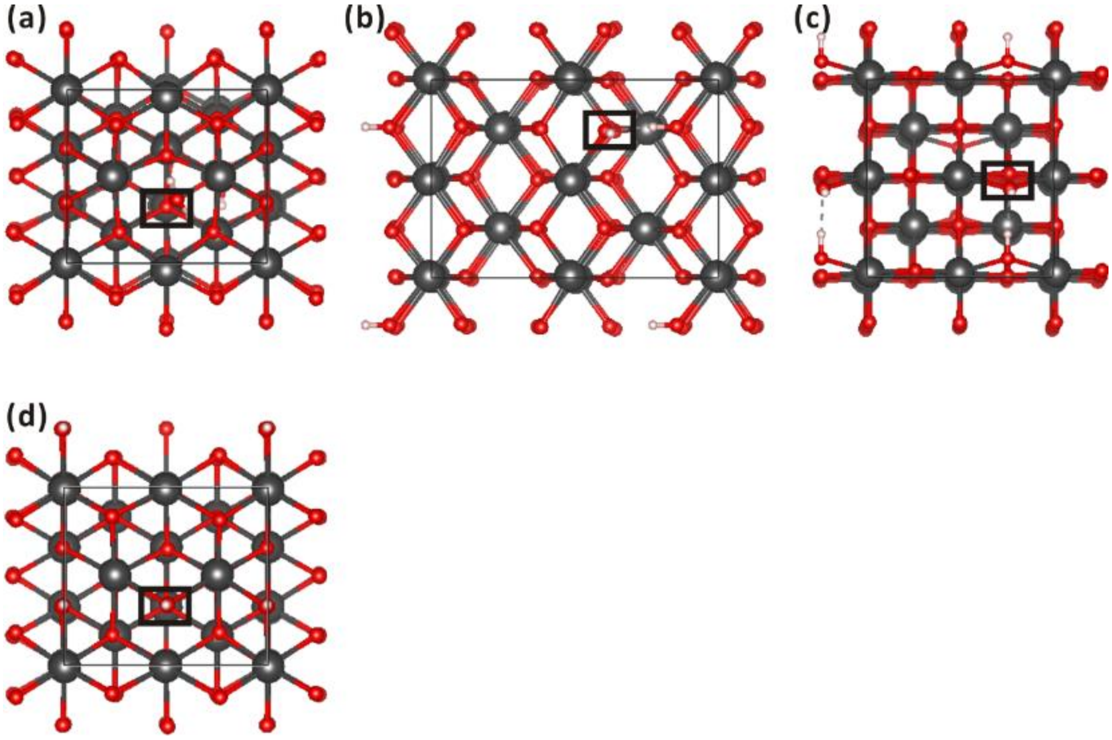

Figure A3.10: Top views of molecular water (a) {111}, (b) {110}, (c) {100} and dissociative water (d) {111}, (e) {110}, (f) {100} adsorption above surface oxygen vacancies on NpO_2 surfaces, calculated at the PBE+U (U_{eff} = 4.5eV) level. Water adsorbs on both side of slab with 25% coverage. Dark grey, red and white spheres represent neptunium oxygen and hydrogen atoms, respectively. the black square makes the position of defect.

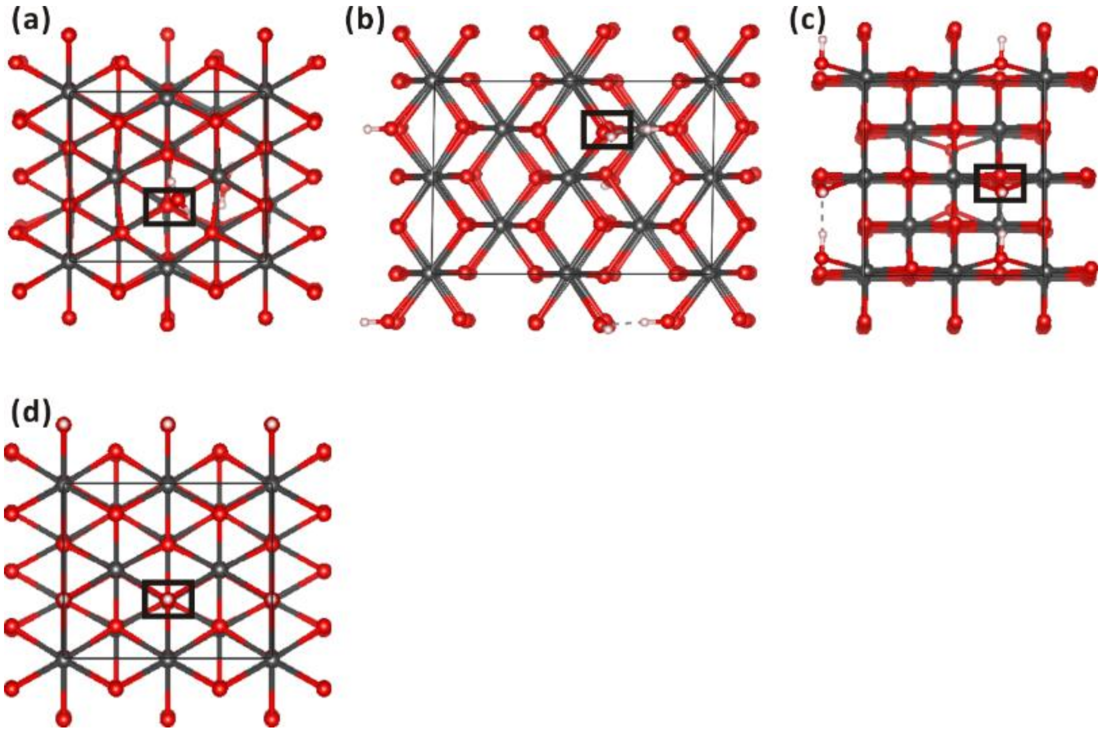

Figure A3.11: Top view of molecular water (a) {111}, (b) {110}, (c) {100} and dissociative water (d) {111}, (e) {110}, (f) {100} adsorption above surface oxygen vacancies at CmO_2 surfaces, calculated at the PBE+U (U_{eff} = 4.5eV) level. Water adsorbs on both side of slab with 25% coverage. Small dark grey, red and white spheres represent curium oxygen and hydrogen atoms, respectively. the black square makes the position of defect.

Table A3.5: Energies (eV) for molecular and dissociative water adsorption on reduced NpO_2 surfaces, which are calculated at PBESol + U (U_{eff} = 4.00 eV) level, and AmO_2 surfaces, which are calculated at PBE + U (U_{eff} = 6.15 eV) level, with O_w approaching surface defect.

AnO_2	Molecular adsorption			Dissociative adsorption		
	{111}	{110}	{100}	{111}	{110}	{100}
NpO_2	-1.41	dis	dis	-2.18	-1.17	-2.05
AmO_2	-0.61	-1.62	-1.54	-2.91	-1.84	-2.42

Appendix 2

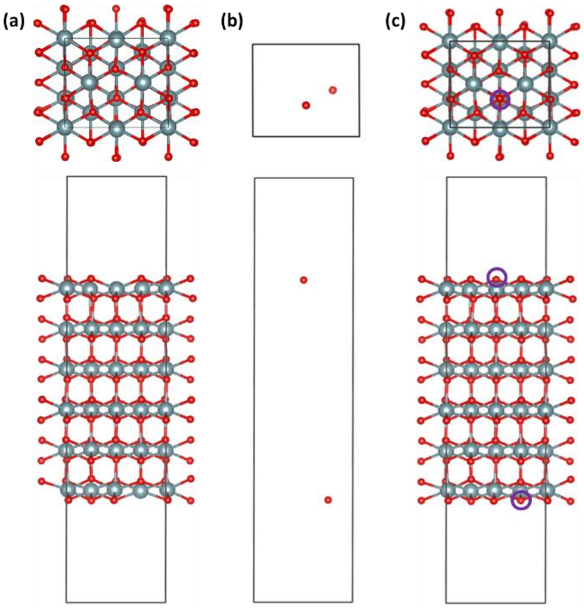

Figure A4.1: Top and side view of (a) substoichiometric UO_2 {111} surfaces; (b) two oxygen atoms in the {111} surface slab, with the same position as the oxygens removed from the {111} surface; and (c) the substoichiometric UO_2 {111} surfaces in (a) with the oxygens in (b) inserted on the top and bottom surfaces.

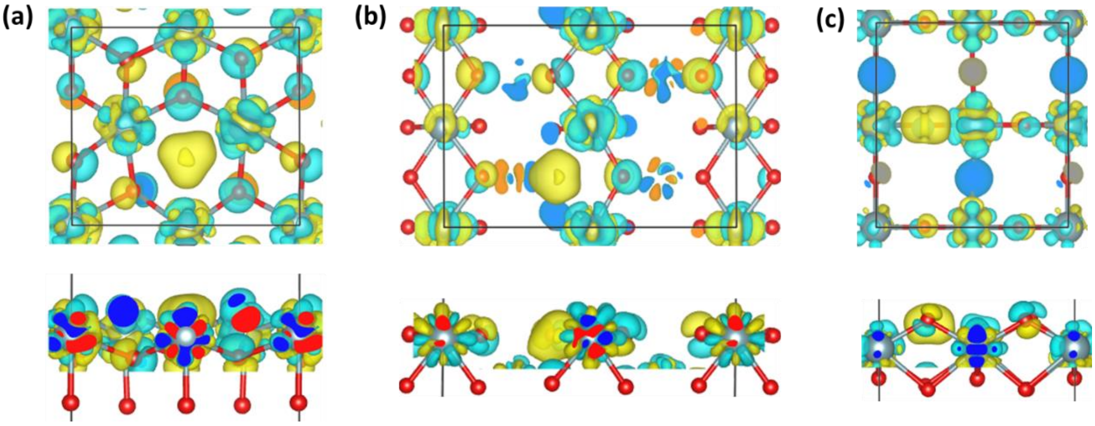

Figure A4.2: Charge difference isosurface (0.05 e/Å^3) on (a) {111}, (b) {110} and (c) {100} surfaces with and without oxygen vacancies.

Table A4.1: Surface lattice constant (Å) of stoichiometric UO_2, $U_{0.92}Zr_{0.08}O_2$, and $U_{0.92}An_{0.08}O_2$ (An = Np, Pu, Am and Cm) surfaces

MOX	{111}	{110}	{100}
UO_2	3.86 × 3.87	5.59 × 3.80	3.78 × 4.07
U-Zr	3.82 × 3.81	5.58 × 3.81	3.77 × 4.05
U-Np	3.87 × 3.87	5.58 × 3.80	3.78 × 4.07
U-Pu	3.77 × 3.77	5.59 × 3.78	3.77 × 4.07
U-Am	3.86 × 3.89	5.59 × 3.80	3.78 × 4.07
U-Cm	3.87 × 3.88	5.59 × 3.79	3.77 × 4.07

Table A4.2: Surface bond lengths (Å) on stoichiometric UO_2 and AnO_2 (An = Np, Pu, Am and Cm) surfaces. Bond lengths on AnO_2 surfaces are collected from our previous work[1-3]

AnO_2	Bonds	{111}			{110}			{100}		
U	U-O	2.383	2.350	2.358	2.315	2.331	2.331	2.315	2.190	2.187
Np	Np-O	2.352	2.349	2.360	2.307	2.310	2.307	2.297	2.170	2.182
Pu	Pu-O	2.343	2.332	2.335	2.216	2.240	2.254	2.328	2.169	2.166
Am	Am-O	2.370	2.335	2.268	2.253	2.257	2.257	2.253	2.177	2.176
Cm	Cm-O	2.396	2.365	2.368	2.287	2.298	2.298	2.287	2.238	2.231

Table A4.3: Surface An-O and U-O bond lengths (Å) on $U_{0.92}An_{0.08}O_2$ (An = Np, Pu, Am and Cm) surfaces.

An	Bonds	{111}			{110}				{100}	
Np	Np-O	2.484	2.514	2.552	2.322	2.310	2.332	2.317	2.177	2.188
	U-O	2.455	2.323	2.366	2.321	2.306	2.316	2.327	2.178	2.188
Pu	Pu-O	2.477	2.461	2.424	2.484	2.467	2.456	2.489	2.348	2.349
	U-O	2.420	2.290	2.342	2.158	2.168	2.172	2.177	2.046	2.047
Am	Am-O	2.533	2.479	2.496	2.485	2.451	2.444	2.484	2.344	2.348
	U-O	2.478	2.372	2.294	2.182	2.152	2.159	2.188	2.046	2.047
Cm	Cm-O	2.545	2.510	2.484	2.490	2.474	2.460	2.493	2.338	2.323
	U-O	2.474	2.302	2.372	2.165	2.164	2.159	2.180	2.057	2.051

Table A4.4: Energy (eV) of optimized UO_2 and AnO_2 (An = Np, Pu, Am and Cm) {111}, {110} and {100} surfaces; data for AnO_2 are from our previous work.[3]

UO_2	-694.9295672	-688.5309638	-687.9364861
NpO_2	-720.5084397	-712.9054981	-713.0381213
PuO_2	-750.7981867	-743.2075467	-743.3287318
AmO_2	-789.8163775	-783.1766196	-783.595617
CmO_2	-836.4200286	-830.59216	-831.7653421

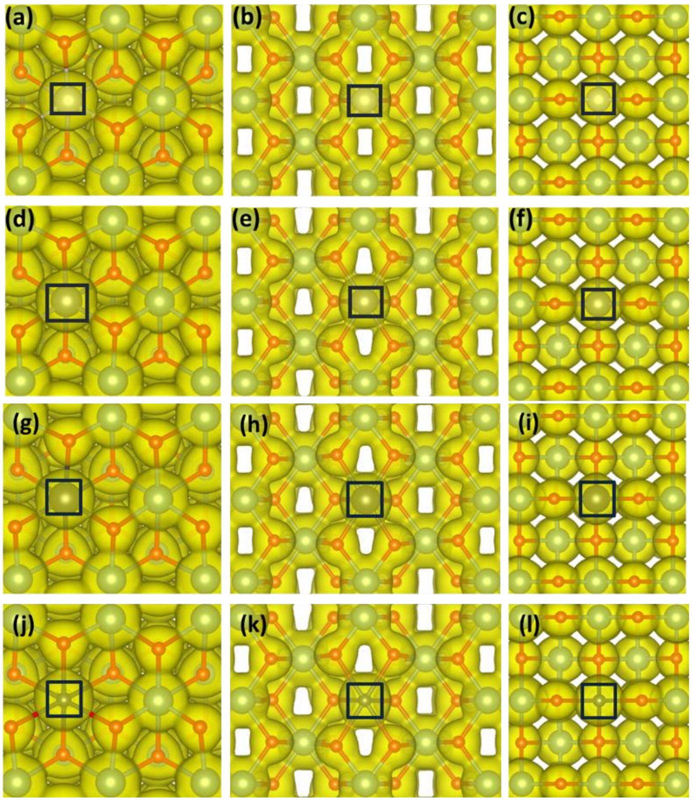

Figure A4.3: Charge density isosurface (0.05 e/Å^3), in yellow, of $U_{0.92}Np_{0.08}O_2$ (a) {111}, (b) {110} and (c) {100} surfaces, $U_{0.92}Pu_{0.08}O_2$ (d) {111}, (e) {110} and (f) {100} surfaces, $U_{0.92}Am_{0.08}O_2$ (g) {111}, (h) {110} and (i) {100} surfaces and $U_{0.92}Cm_{0.08}O_2$ (j) {111}, (k) {110} and (l) {100} surfaces. Blue grey, light grey, grey, dark grey, small dark grey and red spheres represent U, Np, Pu, Am, Cm and O, respectively. The black square in each figure marks the position of substituted An (Np, Pu, Am and Cm).

Table A4.5: O vacancy generation energy (eV) on $U_{0.92}An_{0.08}O_2$ (An = Np, Pu, Am or Cm) surfaces with O vacancy next to An and away from An.

MOX	O vacancy	{111}	{110}	{100}
U-Np	Next to Np	4.71	4.54	4.41
	Away from Np	4.55	4.61	4.83
U-Pu	Next to Pu	4.60	4.39	4.34
	Away from Pu	4.44	4.53	4.73
U-Am	Next to Am	4.18	3.89	3.86
	Away from Am	4.35	4.39	4.68
U-Cm	Next to Cm	4.28	4.02	4.01
	Away from Cm	4.33	4.38	4.55

Table A4.6: O vacancy generation energy on AnO_2 (an =Np, Pu, Am and Cm) surfaces, from our previous work,[3] and the average number of O vacancy generation on pure UO_2 and AnO_2 surfaces.

AnO_2	{111}	{110}	{100}
NpO_2	4.65	3.83	3.76
Aver. on UO_2 + NpO_2	5.23	4.65	4.37
PuO_2	2.78	1.94	2.00
Aver. on UO_2 + PuO_2	4.30	3.71	3.49
AmO_2	1.04	0.50	0.31
Aver. on UO_2 + AmO_2	3.43	2.98	2.65
CmO_2	-0.28	-0.49	-0.53
Aver. on UO_2 + CmO_2	2.77	2.49	2.23

Table A4.7: Replacement energies (eV) of An into UO_2 {111} surface with substitution method B, which has An in 2nd and 5th layers, and method C, which has An in 3rd and 4th layers.

Substituted An	Method B	Method C
Np	0.32	0.34
Pu	-0.05	-0.05
Am	-0.83	-0.96
Cm	-1.25	-1.82

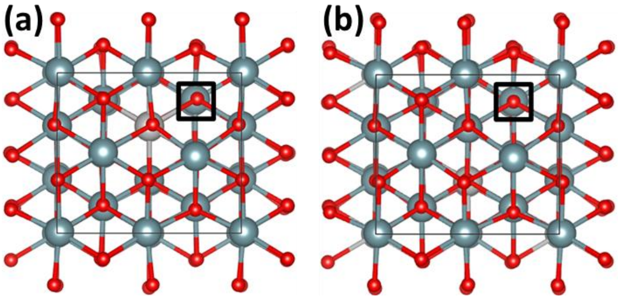

Figure A4.4: Top views of $U_{0.92}Np_{0.08}O_{1.92}$ with Np in (a) 2nd and 5th layers and (b) 3rd and 4th layers. Blue grey, light grey and red spheres represent U, Np and O, respectively. The black squares in the figures mark the position of the O vacancy.

Table A4.8: O vacancy formation energy (eV) on $U_{0.92}An_{0.08}O_{1.92}$ (An = Np, Pu, Am and Cm) with substitution method B, which has An in 2nd and 5th layers, and method C, which has An in 3rd and 4th layers

Substituted An	Method B	Method C
Np	4.95	5.50
Pu	4.15	4.26
Am	4.04	4.56
Cm	4.10	4.45

Table A4.9: Surface lattice parameters (Å) of $U_{0.83}Zr_{0.17}O_2$/$U_{0.83}An_{0.17}O_2$ (MOX-17), $U_{0.75}Zr_{0.25}O_2$/$U_{0.75}An_{0.25}O_2$ (MOX-25) and $U_{0.67}Zr_{0.33}O_2$/$U_{0.67}An_{0.33}O_2$ (MOX-33) (An = Np, Pu, Am and Cm) {111} surfaces

MOX	MOX-17	MOX-25	MOX-33
U-Zr	3.84X3.75	3.71X3.84	3.46X3.74
U-Np	3.87X3.86	3.87X3.87	3.88X3.87
U-Pu	3.77X3.81	3.77X3.78	3.89X3.87
U-Am	3.86X3.89	3.88X3.90	3.87X3.87
U-Cm	3.86X3.89	3.87X3.90	3.87X3.87

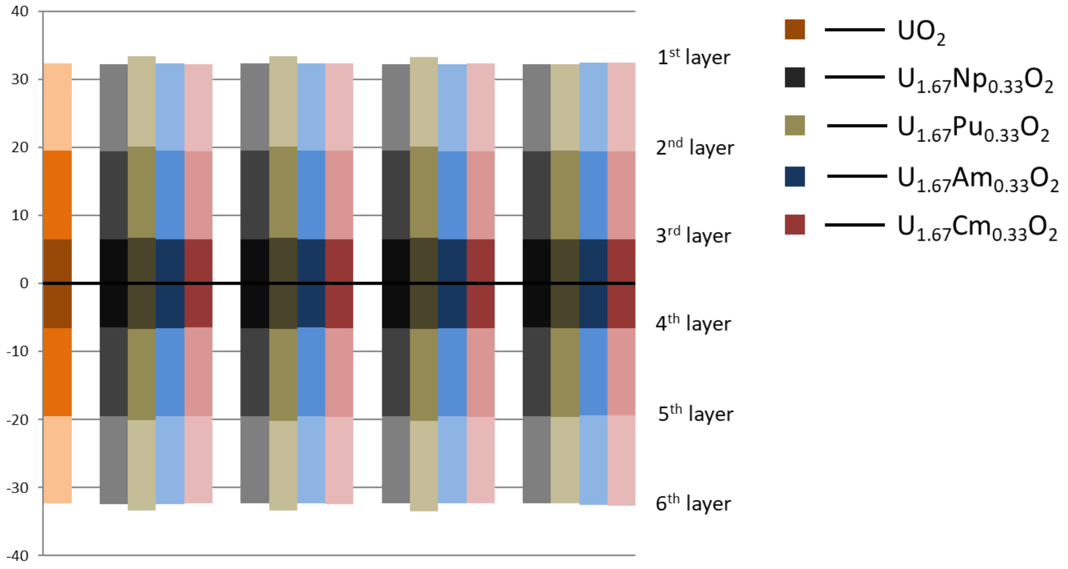

Figure A4.5: Layer distance between the layer of cation (U or An: Np, Pu, Am or Cm), the height of the middle of the slab is set as zero.

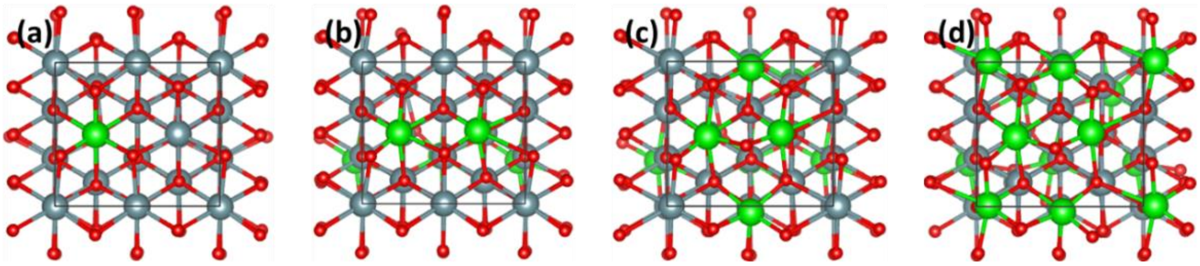

Figure A4.6: Top views of (a) $U_{0.92}Zr_{0.08}O_2$, (b) $U_{0.92}Zr_{0.17}O_2$, (c) $U_{0.92}Zr_{0.25}O_2$ and (d) $U_{0.92}Zr_{0.33}O_2$ {111} surfaces

Table A4.10: Spin density of Zr or An and surface U in $U_{0.83}Zr_{0.17}O_2$ or $U_{0.83}An_{0.17}O_2$ (An = Np, Pu, Am and Cm)

$U_{0.83}Zr_{0.17}O_2$	Zr	0.000	0.001
	U in 1st layer	2.034	2.032
$U_{0.83}Np_{0.17}O_2$	Np	3.111	3.118
	U in 1st layer	2.013	2.003
$U_{0.83}Pu_{0.17}O_2$	Pu	5.088	4.248
	U in 1st layer	1.149	2.004
$U_{0.83}Am_{0.17}O_2$	Am	6.131	6.132
	U in 1st layer	1.138	1.076
$U_{0.83}Cm_{0.17}O_2$	Cm	6.837	6.839
	U in 1st layer	1.149	1.093

Table A4.11: Spin density of Zr or An and U in 1st and 2nd layer in $U_{0.75}Zr_{0.25}O_2$ or $U_{0.75}An_{0.25}O_2$ (An = Np, Pu, Am and Cm)

$U_{0.75}Zr_{0.25}O_2$	Zr	0.003	0.003	0.000	
	U in 1st layer	2.050			
	U in 2nd layer	2.024	2.021	2.037	2.015
$U_{0.75}Np_{0.25}O_2$	Np	3.112	3.128	3.115	
	U in 1st layer	2.021			
	U in 2nd layer	2.009	2.019	2.000	1.999
$U_{0.75}Pu_{0.25}O_2$	Pu	4.253	4.277	5.074	
	U in 1st layer	1.083			
	U in 2nd layer	2.017	2.032	2.022	2.011
$U_{0.75}Am_{0.25}O_2$	Am	6.130	6.130	6.134	
	U in 1st layer	1.145			
	U in 2nd layer	2.002	1.073	1.018	2.001
$U_{0.75}Cm_{0.25}O_2$	Cm	6.838	6.835	6.838	
	U in 1st layer	1.101			
	U in 2nd layer	1.099	2.011	2.002	1.093

Table A4.12: Spin density of Zr or An and U in 2nd layers in $U_{0.67}Zr_{0.33}O_2$ or $U_{0.67}An_{0.33}O_2$ (An = Np, Pu, Am and Cm)

$U_{0.67}Zr_{0.33}O_2$	Zr	0.002	0.003	0.003	0.001
	U in 2nd layer	2.025	2.016	2.031	2.012
$U_{0.67}Np_{0.33}O_2$	Np	3.108	3.117	3.118	3.110
	U in 2nd layer	2.003	2.026	2.024	2.003
$U_{0.67}Pu_{0.33}O_2$	Pu	4.290	4.280	4.283	5.072
	U in 2nd layer	2.010	2.005	1.073	2.023
$U_{0.67}Am_{0.33}O_2$	Am	6.121	6.119	6.121	6.119
	U in 2nd layer	1.038	1.040	1.117	1.130
$U_{0.67}Cm_{0.33}O_2$	Cm	6.763	6.771	6.773	6.828
	U in 2nd layer	1.097	1.098	1.094	1.091

Table A4.13: Replacement energy (E_{rep}, eV) and replacement energy per An (Np, Pu, Am and Cm) into UO_2 {111} surface with the ratio of An to U of 0.17: 0.83. 0.25: 0.75 and 0.33: 0.67.

Ratio	0.17: 0.83		0.25: 0.75		0.33: 0.67	
MOX	E_{rep}	E_{rep} per An	E_{rep}	E_{rep} per An	E_{rep}	E_{rep} per An
U-Np	0.56	0.28	0.72	0.24	0.60	0.15
U-Pu	-0.08	-0.04	0.30	0.10	0.53	0.13
U-Am	-1.37	-0.69	-1.69	-0.56	-1.80	-0.45
U-Cm	-2.34	-1.17	-3.12	-1.04	-3.43	-0.86

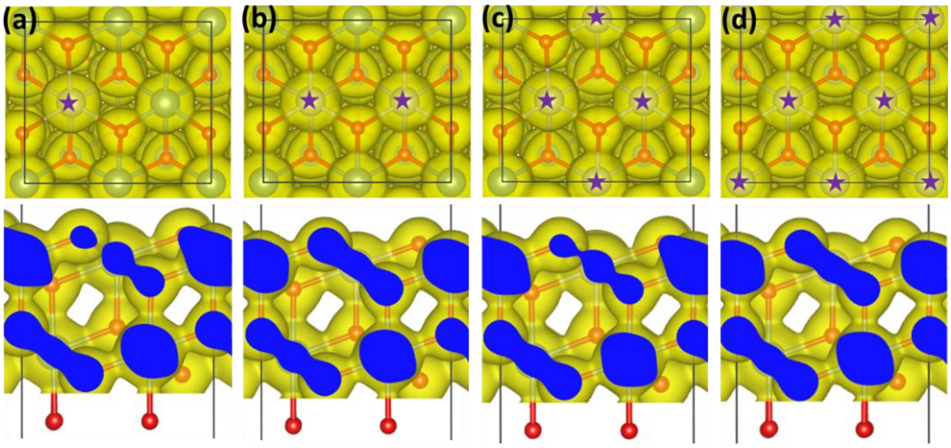

Figure A4.7: Charge density isosurface (0.05 e/Å^3), in yellow, of $U_{1-y}Np_yO_2$ {111} surface with y = (a) 0.08, (b) 0.17, (c) 0.25 and (d) 0.33, top and side views. The purple stars in the figures mark the positions of substituted Np atoms.

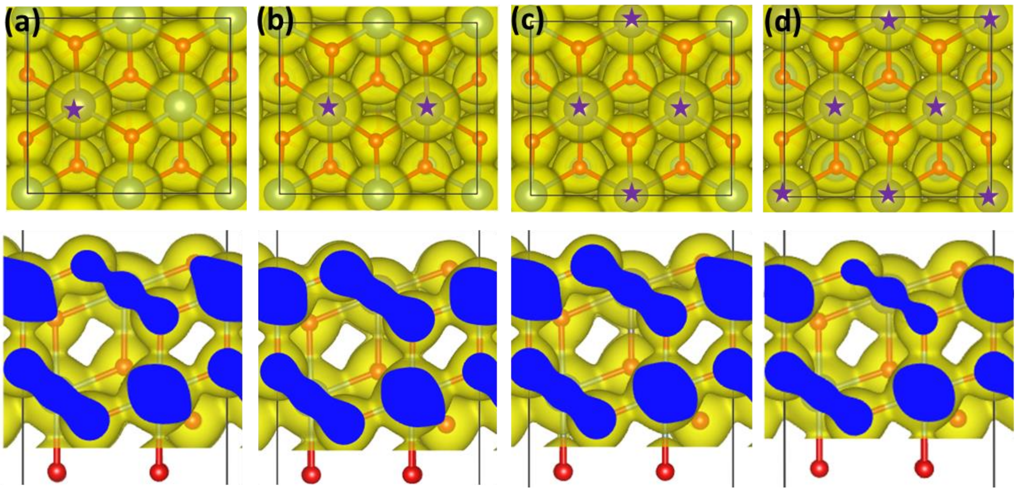

Figure A4.8: Charge density isosurface (0.05 e/Å^3), in yellow, of $U_{1-y}Pu_yO_2$ {111} surface with y = (a) 0.08, (b) 0.17, (c) 0.25 and (d) 0.33, top and side views. The purple stars in the figures mark the position of substituted Pu atoms.

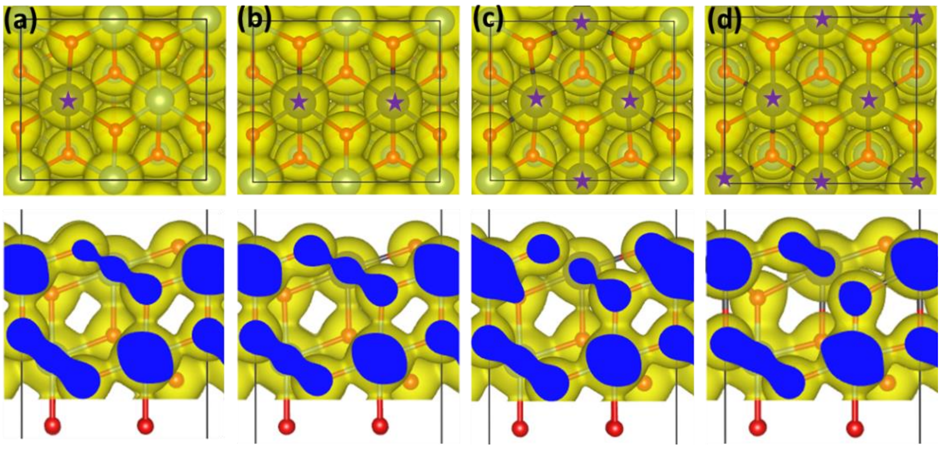

Figure A4.9: Charge density isosurface (0.05 e/Å^3), in yellow, of $U_{1-y}Am_yO_2$ {111} surface with y = (a) 0.08, (b) 0.17, (c) 0.25 and (d) 0.33, top and side views. The purple stars in the figures mark the position of substituted Am atoms.

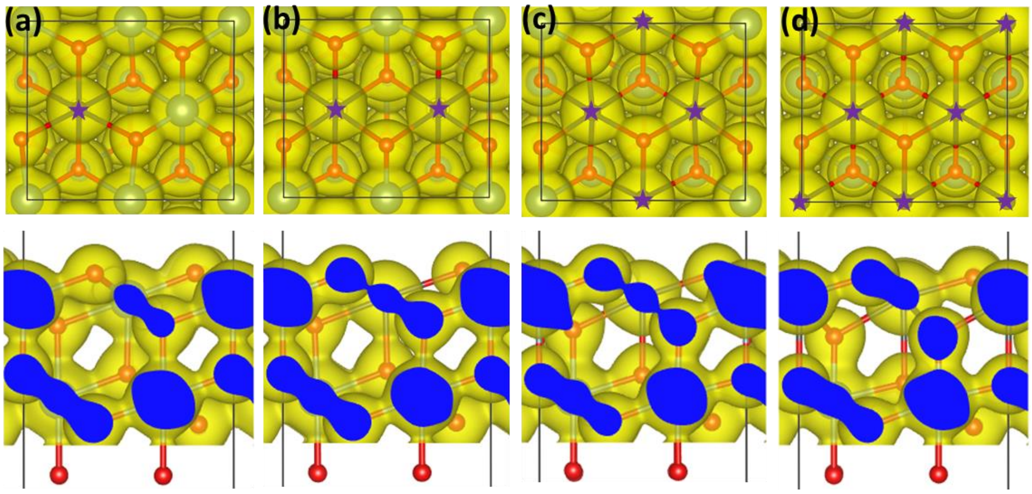

Figure A4.10: Charge density isosurface (0.05 e/Å^3), in yellow, of $U_{1-y}Am_yO_2$ {111} surface with y = (a) 0.08, (b) 0.17, (c) 0.25 and (d) 0.33, top and side views. The purple stars in the figures mark the position of substituted Cm atoms.

References

1. Tegner, B. E.; Molinari, M.; Kerridge, A.; Parker, S. C.; Kaltsoyannis, N., Water Adsorption on AnO2 {111}, {110}, and {100} Surfaces (An = U and Pu): A Density Functional Theory + U Study. *The Journal of Physical Chemistry C* **2017**, *121*, 1675-1682.

2. Chen, J.-L.; Kaltsoyannis, N., Computational study of plutonium–americium mixed oxides ($Pu_{0.92}Am_{0.08}O_{2-x}$); Water adsorption on {111}, {110}, and {100} Surfaces. *J. Phys. Chem. C* **2020**, *124*, 6646-6658.

3. Chen, J.-L.; Kaltsoyannis, N., Computational study of the bulk and surface properties of minor actinide dioxides $MAnO_2$ (MAn = Np, Am, and Cm); Water adsorption on stoichiometric and reduced {111}, {110}, and {100} Surfaces. *J. Phys. Chem. C* **2019**, *123*, 15540-15550.

Appendix 3

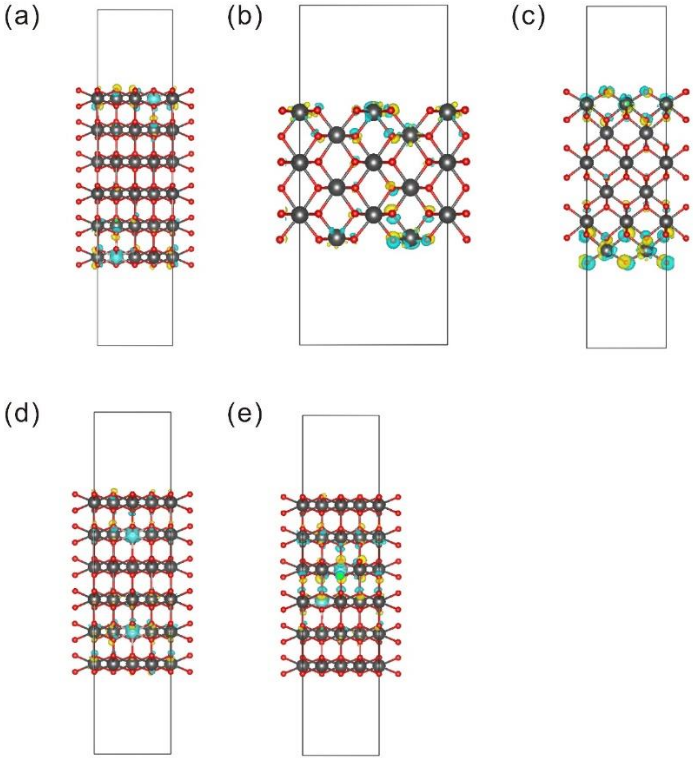

Figure A5.1: Charge density difference between $Pu_{0.92}Am_{0.08}O_2$ and PuO_2 surfaces, (a), (b) and (c) are $Pu_{0.92}Am_{0.08}O_2$ {111}, {110} and {100} surfaces with Am in 1st and 6th layers, respectively. (d) and (e) are $Pu_{0.92}Am_{0.08}O_2$ {111} surfaces with Am on 2nd and 5th, and 3rd and 4th layers, respectively. Dark grey, light grey and red spheres represent plutonium, americium and oxygen atoms, respectively. Blue and yellow represent charge increase and decreases, respectively.

Table A5.1: Spin density of surface Pu and substituted Am on $Pu_{0.92}Am_{0.08}O_2$ surface before and after molecular water adsorption.

Spin density of:	Surface	{111}	{110}	{100}
Pu in top layer	Clean surface	-4.254 – -4.262	-4.244 – -4.264	-4.261 – -4.274
	Adsorb on Pu	-4.241 – -4.254	-4.261 – -4.274	-4.231 – -4.275
	Adsorb on Am	-4.250 – -4.256	-3.791, -4.297, -4.301	-3.595, -4.034, -4.124
Am	Clean surface	-5.505	-5.553	-5.575
	Adsorb on Pu	-5.500	-5.549	-5.530
	Adsorb on Am	-5.483	-6.118	-6.120

Table A5.2: Spin density of surface Pu and substituted Am on $Pu_{0.92}Am_{0.08}O_2$ surface before and after dissociative water adsorption.

Spin density of:	Surface	{111}	{110}	{100}
Pu in top layer	Clean surface	-4.254 – -4.262	-4.244 – -4.264	-4.261 – -4.274
	Adsorb on Pu	-4.230 – -4.251	-4.205 – -4.267	-4.231 – -4.275
	Adsorb on Am	-4.236 – -4.252	-3.636, -4.289, -4.292	-3.595, -4.034, -4.124
Am	Clean surface	-5.505	-5.553	-5.575
	Adsorb on Pu	-5.490	-5.549	-5.530
	Adsorb on Am	-5.481	-6.091	-6.120

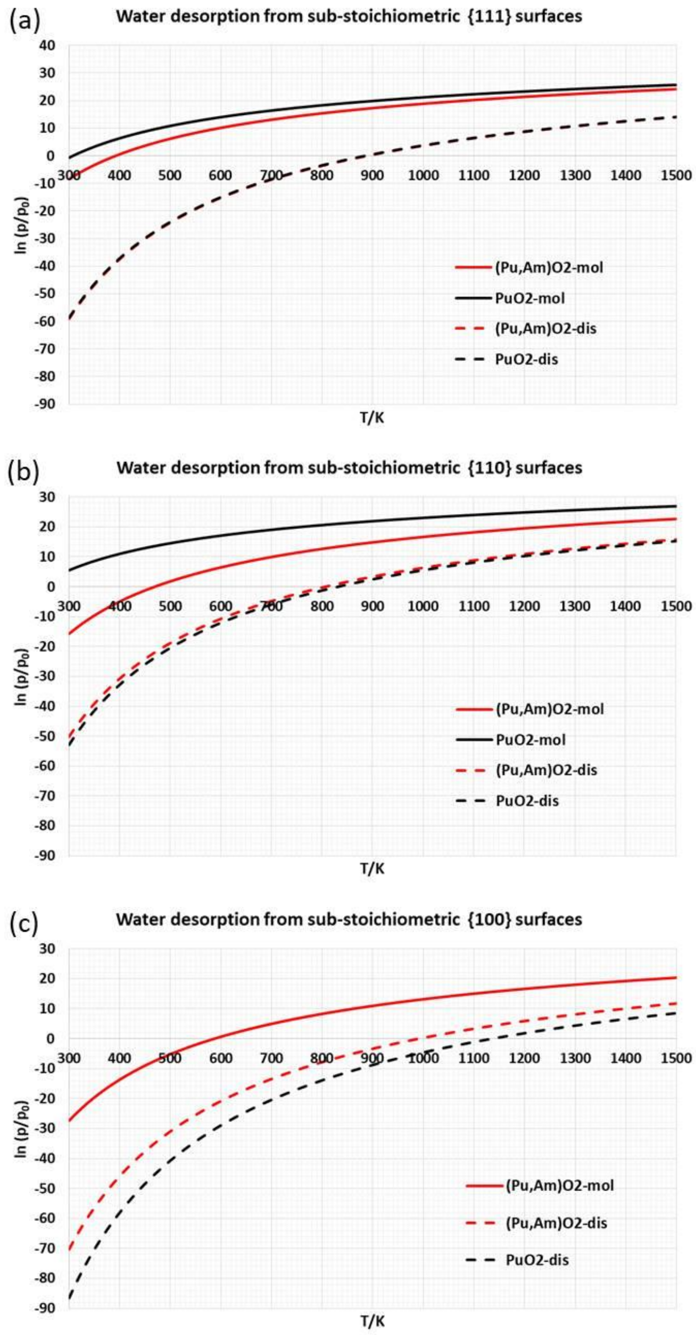

Figure A5.2: Relationship between partial pressure of water (p), and temperature (T) required for thermal desorption of water from sub-stoichiometric (a) {111}, (b) {110} and (c) {100} $Pu_{1-y}AmO_{2-x}$ and PuO_2 surfaces, with molecular (mol) or dissociative (dis) adsorbed water. The equilibrium state between water adsorption and desorption is indicated by the solid (molecular adsorption) and dashed (dissociate adsorption) lines; water will desorb from the surfaces when p/p_0 is below the line, and will adsorb when p/p_0 is above the line.

Appendix 4

Table A6.1: Spin densities (au) of Pu and O in PuO_2 {111} and {110} slabs; a positive value indicating spin up and negative value indicating spin down. The layer numbers are marked in Figure A6.1.

	{111}		{110}	
Layer	Pu	O	Pu	O
1st	4.256, 4.257, 4.256, 4.257	-0.105, -0.105 -0.105, -0.105 -0.062, -0.062 -0.061, -0.066	4.327, 4.326, 4.277, 4.277	-0.102, -0.102, -0.074, -0.074, -0.102, -0.102, -0.079, -0.079
2nd	-4.192, -4.204, -4.192, -4.211	0.047, 0.044 0.042, 0.042 0.049, 0.045 0.046, 0.046	-4.192, -4.191, -4.191, -4.191	0.003, 0.003 0.002, 0.002 0.003, 0.003 0.006, 0.006
3rd	4.204, 4.204, 4.205, 4.204	-0.049, -0.051 -0.049, -0.053 -0.052, -0.052 -0.052, -0.052	4.188, 4.189, 4.185, 4.185	-0.007, -0.007 -0.007, -0.007 -0.007, -0.007 -0.007, -0.007
4th	-4.206, -4.202, -4.205, -4.201	0.052, 0.052 0.052, 0.052 0.049, 0.051	-4.187, -4.187, -4.188, -4.188	0.006, 0.006 0.007, 0.007 0.006, 0.006

		0.051, 0.050		0.006, 0.006
5th	4.195, 4.197, 4.198, 4.195	-0.047, -0.043 -0.048, -0.041 -0.046, -0.045 -0.040, -0.039	4.191, 4.191, 4.191, 4.191	-0.002, -0.002 -0.005, -0.005 -0.002, -0.002 -0.006, -0.006
6th	-4.258, -4.258, -4.256, -4.254	0.061, 0.063 0.063, 0.063 0.106, 0.105 0.105, 0.105	-4.292, -4.292, -4.295, -4.294	0.080, 0.080 0.087, 0.087 0.084, 0.084 0.088, 0.088

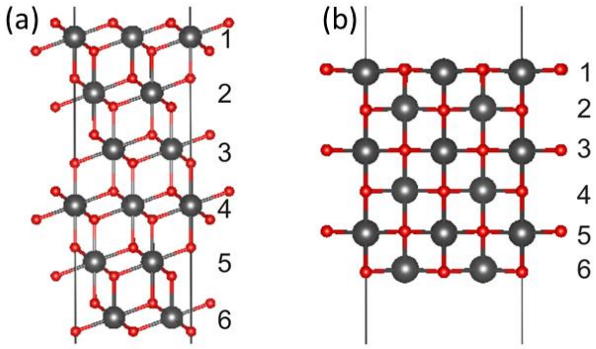

Figure A6.1: Side view of PuO_2 {111} and {110} surfaces.

Table A6.2: H···Cl separation $d_{\mathrm{H\cdots Cl}}$, electron density at the bond critical point ρ_{BCP} and the Laplacian of electron density evaluated at the bond critical point $\nabla^2\rho|_{\mathrm{BCP}}$ for each H···Cl bond of Cl^{-}-$H_9O_4^{+}$ system (Figure 2 (c)).

$d_{\mathrm{H\cdots Cl}}$ / Å	$\boldsymbol{\rho}_{\mathbf{BCP}}$ / a.u.	$\boldsymbol{\nabla^2\rho}|_{\mathbf{BCP}}$ / a.u.
2.01	0.043	0.086
2.01	0.043	0.086
2.01	0.043	0.086

Table A6.3: H···Cl separation $d_{\mathrm{H\cdots Cl}}$, electron density at the bond critical point ρ_{BCP} and the Laplacian of the electron density evaluated at the bond critical point $\nabla^2\rho|_{\mathrm{BCP}}$ for each H···Cl bond in the Cl^{-}-H_8O_4 system display in Figure 2 (b).

$d_{\mathrm{H\cdots Cl}}$ / Å	$\boldsymbol{\rho}_{\mathbf{BCP}}$ / a.u.	$\boldsymbol{\nabla^2\rho}|_{\mathbf{BCP}}$ / a.u.
2.17	0.031	0.067
2.22	0.029	0.065
2.13	0.034	0.072

Acknowledgment

My deepest gratitude is first to Professor Nikolas Kaltsoyannis, my supervisor. Under his constant and enlightening guidance, I have had an enriched and happy PhD life for the past three years. His patience and kindness have built my confidence in scientific research and faith in my research.

Secondly, I would like to express my heartfelt thanks to Dr. Bengt E. Tegner and Dr. Jonathan Collard. Bengt led me to the world of VASP, and shared his experience on periodic simulation of actinide oxides with me generously. Jonathan showed me another way to simulate solid state actinide oxides, and cooperation with him was a precious experience. I am also grateful to Dr. Helen Steele of Sellafield Limited for her helpful comments on each of my works. I would like to thank all group members for helping me and the great time we had, especially Sophie Cooper, who helped me with English writing, which is a lot for a non-native speaker like me.

I am grateful to the China Scholarship Council and The University of Manchester for a PhD studentship for me. I also thank the HEC Materials Chemistry Consortium, which is funded by the EPSRC (EP/L000202, EP/R029431), for access to ARCHER, the UK's National Supercomputing Service (http://www.archer.ac.uk).

Finally, I would like to thank my dear family for their love and great faith in me for many years. I also want to thank my boyfriend, Song Yu. We have similar experiences and know each other well, and he is always there for me when I lose myself.